Transport Properties and Magnetoresistance of Cluster-Assembled Fe-Ge and Fe-Ag Nanocomposites

Transport Properties and Magnetoresistance of Cluster-Assembled Fe-Ge and Fe-Ag Nanocomposites

Transporteigenschaften und Magnetowiderstand von Cluster-basierten Fe-Ge- und
Fe-Ag–Nanokompositen

Dissertation von Nicolas Sebastian Gack

Darmstadt, Technische Universität Darmstadt

Tag der mündlichen Prüfung: 17. Februar 2023

Jahr der Veröffentlichung der Dissertation auf TUprints: 2023

Erklärung zur Dissertation

Hiermit versichere ich, dass ich meine Dissertation selbstständig und nur mit den angegebenen Quellen und Hilfsmitteln angefertigt habe. Diese Arbeit hat in gleicher oder ähnlicher Form noch keiner Prüfungsbehörde vorgelegen.

Darmstadt, den 25. August 2022

Nicolas Sebastian Gack

Abstract

Granular nanocomposites are composite materials in which grain-like particles with dimensions on the order of nanometers form one of the phases. These nanoparticles are embedded in a second phase, the matrix. Such granular nanocomposites constitute a very promising class of materials with great potential for novel and tailorable properties, making granular nanocomposites especially interesting for scientific endeavor. In the simplest case, granular nanocomposites are synthesized via co-deposition of two immiscible chemical elements. In this approach, nanoparticles grow via incorporation of diffusing atoms of one of the elements forming the prototype material; the remaining atoms of the other element constitute the matrix. This phase segregation process may be assisted by thermal annealing. Another approach used to form granular nanocomposite prototype materials is to ion-implant nanoparticle-type atoms into already grown films or wafer surfaces. However, since these two approaches utilize the immiscibility of the combined materials, they can be applied to such immiscible material systems only. Furthermore, the range of achievable elemental compositions and particle sizes is limited.

An interesting alternative strategy to synthesize granular nanocomposites is to deposit the matrix material simultaneously with preformed, spherical nanoparticles. In this approach, the nanoparticles are embedded into the matrix in a direct fashion. The preformed, spherical nanoparticles are called clusters, correspondingly, the created nanomaterials are called cluster-assembled nanocomposites. The great advantage of this special co-deposition approach is that it allows for the creation of nanocomposites out of elements that are at least partially miscible or that can form crystallographic mixed phases—that is, for the creation of so-called nonequilibrium compositions. Embedding the nanoparticles as preformed constituents instead of letting them segregate during the deposition process also increases the degree of control over the deposition process. An ultimate degree of control over the composition is achieved when the clusters are size-selected prior to deposition. This is the strategy pursued in the present thesis. Here, a cluster ion beam deposition system that features a narrow cluster size distribution of $\pm 10\%$ is used to synthesize films of cluster-assembled nanocomposites. Two different nanocomposites are prepared and examined: nanocomposites made of Fe-clusters embedded in Ge-matrices and nanocomposites of Fe-clusters embedded in Ag-matrices. The created Fe-clusters are only a few nanometers in size and, therefore, of superparamagnetic kind. The study of the physical properties of the prepared nanocomposites as a function of cluster size and cluster concentration, in particular, of their transport and magnetoresistive properties, is the central aim of this thesis.

First, the Fe-Ge nanocomposites are examined. In this course, also the process of sample preparation and the various performed measurements are discussed. Embedding magnetic Fe nanoparticles into a semiconductor aims for a synthesis of the magnetic and the semiconducting properties, that is, for the creation of so-called magnetic semiconductors. Magnetic semiconductors define a class of materials whose properties can be controlled by means of a magnetic field in addition to—or even instead of—an electric field. For this reason, magnetic semiconductors represent an essential component for the emerging field of spintronics.

Two series of Fe-Ge nanocomposites are prepared: one with clusters consisting of 500 ± 50 Fe atoms and one with clusters consisting of 1000 ± 100 Fe atoms. In the course of the analysis, Ge is found to grow in an amorphous structure under the conditions of the co-deposition experiments. A co-deposition sample layout that consists of a co-deposition mask and a complementing sample chip layout is developed. The deposited nanocomposite samples are studied by means of resistance and magnetoresistance measurements in a cryostat, by means of scanning electron microscopy including energy-dispersive X-ray spectroscopy, and by means of SQUID magnetometry. Besides tunneling magnetoresistance, which is negative, of saturating kind, and observed with a magnitude on the order of 1% here, at least one other effect not saturating within the examined magnetic field range of $|\mu_0 H| \leq 6\,\text{T}$ is observed. Several effects that may explain the observed non-saturating behavior are discussed, however, the origin remains unsolved. Furthermore, the resistivity of the Fe-Ge nanocomposites as well as the tunneling magnetoresistance are each found to be a function of the average distance between the surfaces of neighboring clusters rather than the average distance between their centers of mass. Finally, some of the Fe-Ge nanocomposite samples are thermally annealed in vacuum, under the presence of hydrogen gas, and at two different temperatures in various steps. Thermal annealing alters the structure of the as-deposited nanocomposites, which is reflected by changes in the measured physical properties. These changes are identified and discussed.

Secondly, the Fe-Ag nanocomposites are examined. In comparison to the Fe-Ge system, the Fe-Ag system is represented in the literature rather well. In particular, it is well-known that the giant magnetoresistance effect can occur in layered as well as in granular Fe-Ag structures. Here, the aim is to confirm that the applied methods give results comparable to those found in the literature and to perhaps even improve upon existing data. Again, two series of nanocomposite samples with clusters consisting of 500 and 1000 Fe atoms, respectively, are fabricated. In addition, a third series of Fe-Ag nanocomposite samples with clusters consisting of 1500 ± 150 Fe atoms is prepared. Giant magnetoresistance of maximum -6% is observed. The giant magnetoresistance effect increases in magnitude with decreasing size of the embedded clusters. Furthermore, an optimum composition of clusters and matrix material for a maximum magnitude of the giant magnetoresistance effect seems to exist. However, no clear

dependence of the measured properties on neither the Fe concentration nor the average distance between the surfaces of neighboring clusters is observed.

Besides the examination of Fe-Ge and Fe-Ag nanocomposites, a setup that combines laser ablation and inert gas condensation is designed and assembled. In contrast to other techniques, laser ablation features a large fraction of uncharged output particles. Further, laser ablation also allows for the creation of nanoparticles made of electrically insulating materials. Accordingly, the original application considered for the setup lies in the field of matter-wave diffraction experiments. In principle, the setup may be used for the deposition of cluster-assembled materials as well. However, it has never been used for experiments in any of these fields. Nevertheless, the present state of the setup as well as its principle of operation are reviewed. The review is completed with a brief analysis of a test sample of collected Ag clusters prepared with the setup.

Zusammenfassung

Granulare Nanokomposite sind Verbundmaterialien, bei denen eine der Phasen aus nanometergroßen, kornartigen Partikeln gebildet wird. Diese Nanopartikel sind in eine zweite Phase, die Matrix, eingebettet. Granularen Nanokompositen wird ein großes Potential für das Hervorbringen neuartiger, per Herstellungsprozess einstellbarer Eigenschaften zugeschrieben, was sie zu einer für die Forschung sehr interessanten und vielversprechenden Materialklasse macht. Im einfachsten Fall lassen sich granulare Nanokomposite mittels Co-Deposition zweier nicht mischbarer chemischer Elemente erzeugen. Die Nanopartikel bilden sich dann aus den Atomen eines der beiden aufgebrachten chemischen Elemente; die zurückbleibenden Atome des anderen Elements bilden die Matrix. Dieser Prozess des Seigerns kann durch Anlassen der Probe unterstützt werden. Die Atome, die die Nanopartikel bilden sollen, können auch mittels Ionenimplantation in einen bereits fertig aufgewachsenen Film oder in die Oberfläche eines Wafers eingebracht werden. Der Nachteil dieser beiden Herangehensweisen ist aber, dass sie eben nur auf solche nicht mischbaren Materialsysteme angewendet werden können. Des Weiteren sind auch den einstellbaren Mischungsverhältnissen und den erzielbaren Partikelgrößen Grenzen gesetzt.

Eine interessante Alternative zu Co-Deposition und Ionenimplantation ist, das Matrixmaterial auf ein Substrat aufwachsen zu lassen während gleichzeitig vorgefertigte, kugelförmige Nanopartikel auf dieses abgeschieden und so in das Matrixmaterial eingebettet werden. Solche vorgefertigten Nanopartikel werden als Cluster bezeichnet, die erzeugten Nanomaterialien entsprechend als Cluster-basierte Nanokomposite. Der große Vorteil dieses speziellen Co-Depositions–Ansatzes ist, dass sich mit ihm auch Nanokomposite aus Elementen, die ineinander zumindest teilweise löslich sind oder miteinander kristallographische Phasen bilden können, erzeugen lassen – sogenannte Nichtgleichgewichtskompositionen. Dass die Nanopartikel bereits als solche deponiert werden anstatt dass sie sich im Film erst noch bilden müssen, macht den Herstellungsprozess zudem kontrollierbarer. Ein Höchstmaß an Kontrollierbarkeit wird erreicht, wenn die vorgefertigten Cluster unmittelbar vor der Deposition noch eine Größenselektion durchlaufen. Genau dieser Ansatz findet in der vorliegenden Thesis Anwendung. Hier werden Nanokompositfilme aus Fe-Clustern in Ge-Matrix und Nanokompositfilme aus Fe-Clustern in Ag-Matrix untersucht, die mit einem Clusterionenstrahl-Depositionssystem erzeugt werden, das mit lediglich $\pm 10\%$ Massenabweichung vom Sollwert eine hohe Größenselektivität aufweist. Die erzeugten Fe-Cluster sind nur wenige

Nanometer groß und aufgrund dessen superparamagnetisch. Das zentrale Ziel der Thesis ist, die Abhängigkeit der physikalischen Eigenschaften der erzeugten Cluster-basierten Nanokomposite von der Größe der eingebetteten Cluster und deren Konzentration zu untersuchen, allen voran die der Transporteigenschaften und die der magnetoresistiven Eigenschaften.

Als erstes werden die Fe-Ge–Nanokomposite untersucht. In diesem Zuge werden auch der Herstellungsprozess und die verschiedenen Messungen beschrieben. Das Einbetten der magnetischen Fe-Nanopartikel in einen Halbleiter zielt darauf ab, die magnetischen und die halbleitenden Eigenschaften zu verschmelzen, um auf diese Weise magnetische Halbleiter zu erzeugen. Solche magnetischen Halbleiter definieren eine Klasse an Materialien, deren Eigenschaften zusätzlich zu – oder sogar anstelle von – einem elektrischen Feld mit einem Magnetfeld kontrolliert werden können. Sie sind deshalb essentiell wichtig für zukünftige Anwendungen im Bereich der Spintronik.

Es werden zwei Serien Fe-Ge–Nanokomposit–Proben hergestellt. Eine, die Cluster aus 500 ± 50 Fe-Atomen enthält, und eine, die Cluster aus 1000 ± 100 Fe-Atomen enthält. Wie sich herausstellen wird, wächst das Ge unter den während der Co-Deposition herrschenden Bedingungen amorph auf. Des Weiteren wird ein auf die Herstellung mit dem Clusterionenstrahl-Depositionssystem abgestimmtes Probenlayout, das sich aus einer Co-Deposition–Maske und einem entsprechend angepassten Probenchip-Layout zusammensetzt, entwickelt. Die hergestellten Nanokompositproben werden mittels Widerstands- und Magnetowiderstandsmessungen in einem Kryostaten, mittels Rasterelektronenmikroskopie inklusive energiedispersiver Röntgenspektroskopie und mittels SQUID-Magnetometrie untersucht. Neben dem negativen, sättigenden magnetischen Tunnelwiderstandseffekt, der in der Größenordnung von 1% vorliegt, wird mindestens ein weiterer magnetoresistiver Effekt beobachtet, der im untersuchten Magnetfeldbereich $|\mu_0 \, \mathrm{H}| \leq 6 \, \mathrm{T}$ nicht sättigt. Einige magnetoresistive Effekte, die eine Erklärung für die gemachten Beobachtungen liefern könnten, werden diskutiert, jedoch bleibt der Ursprung des nicht sättigenden Effekts ungeklärt. Wie sich herausstellt, hängen der spezifische Widerstand und der magnetische Tunnelwiderstand der Fe-Ge–Nanokomposite vom gemittelten Abstand zwischen den Oberflächen benachbarter Cluster und nicht vom gemittelten Abstand zwischen ihren Schwerpunkten ab. Abschließend werden einige der Fe-Ge–Nanokompositproben im Vakuum sowie in wasserstoffgashaltiger Atmosphäre bei zwei verschiedenen Temperaturen schrittweise thermisch angelassen. Das Anlassen ändert die Struktur der Nanokomposite, was mit Veränderungen in den gemessenen Eigenschaften einhergeht. Die Veränderungen werden identifiziert und diskutiert.

Als zweites werden die Fe-Ag–Nanokomposite diskutiert. Verglichen mit dem Fe-Ge–System ist das Fe-Ag–System ein in der Fachliteratur recht gut dokumentiertes Materialsystem. Insbesondere ist der Fachliteratur bekanntermaßen zu entnehmen, dass sowohl in geschichteten als auch in granularen

Fe-Ag–Strukturen der Riesenmagnetowiderstandseffekt auftritt. Es gilt also zu untersuchen, ob sich die in der Fachliteratur dokumentierten Eigenschaften bestätigen lassen und ob sich dort zu findende Ergebnisse eventuell sogar verbessern lassen. Zusätzlich zu zwei Probenserien mit den bereits bei den Fe-Ge–Nanokompositen verwendeten Clustern aus 500 bzw. 1000 Fe-Atomen wird eine dritte Probenserie mit Clustern aus 1500 ± 150 Fe-Atomen hergestellt. In der Tat wird in diesen auch der Riesenmagnetowiderstandseffekt beobachtet – in Höhe von bis zu -6%. Der Effekt fällt stärker aus, je kleiner die eingebetteten Cluster sind. Zudem scheint es, als gäbe es ein Optimum hinsichtlich Größe und Konzentration der Cluster in der Matrix, bei dem ein maximaler Riesenmagnetowiderstandseffekt erzielt wird. Im Gegensatz zu den Fe-Ge–Nanokompositen kann hier aber keine eindeutige Abhängigkeit der gemessenen Eigenschaften weder von der Fe-Konzentration noch vom gemittelten Abstand zwischen den Oberflächen benachbarter Cluster beobachtet werden.

Zusätzlich zur Herstellung und Erforschung der Fe-Ge– und Fe-Ag–Nanokomposite wird eine Anlage, die Laserablation und Inertgaskondensation kombiniert, entworfen und aufgebaut. Im Gegensatz zu anderen Herstellungstechniken sind per Laserablation erzeugte Partikel größtenteils ungeladen. Zudem lassen sich per Laserablation auch Nanopartikel aus elektrisch nicht leitenden Materialien herstellen. Entsprechender Weise liegt die ursprünglich für die Anlage vorgesehene Verwendung im Forschungsfeld der Beugungsexperimente mit Materiewellen. Prinzipiell kann die Anlage aber auch für die Herstellung Cluster-basierter Materialien verwendet werden. Jedoch wurden mit der Anlage bis dato weder Experimente in dem einen noch in dem anderen Forschungsfelder durchgeführt. Daher werden lediglich ihre Funktionsweise und ihr momentaner Zustand beschrieben. Der Beschreibung folgt abschließend eine kurze Analyse einer Testprobe aus Ag-Nanopartikeln, die mit der Anlage erzeugt wurden.

Acknowledgments

My favorite bakery is acknowledged for the countless *Nervennahrung* that mysteriously found its way into my shopping bag again and again.

At this point, I would also like to thank my comrades from the fire department of the city of Ettlingen for keeping me grounded especially during coronavirus lockdown times when urgently needed social interactions were hardly possible.

And last, to my family and friends: Thank you for your enduring and unconditional support.

Table of Content

1 Introduction

Granular nanocomposites are multiphase materials that consist of at least two distinct phases. One phase is formed by nanometer-sized grains, another phase forms the matrix that encloses them [1]. The goal of combining these phases is either the symbiosis of their individual physical properties or the creation of materials with new properties that result from the nanogranular structure. Classically, granular nanocomposites are grown, e.g., via simultaneous deposition of two immiscible elements by electron beam evaporation or sputtering, or by ion implantation. In these approaches, segregation due to the immiscibility of the constituting chemical elements leads to the formation of precipitates either directly during deposition or in a subsequent annealing step.

An interesting alternative strategy is the simultaneous deposition of preformed, spherical nanoparticles with a matrix material. As in this process, the spherical nanoparticles, which are also called clusters, are formed prior to deposition, this strategy allows for a more precise control of the composition of these granular nanocomposites [2–4], i.e., the size distribution of the clusters and their separation in the host matrix. An ultimate degree of control is achieved when the clusters are deposited from a size-selected beam. This approach is followed in the present thesis. The cluster ion beam deposition system (CIBD) [5–7] used to grow nanocomposite films of this cluster-assembled kind features a narrow size-selectivity of only 10%. For this reason, the CIBD system is well qualified for the preparation of samples suitable for studies of the dependence of sample properties on cluster size. In general, simultaneous deposition of preformed clusters together with the matrix material further extends the palette of materials, since even nonequilibrium compositions of elsewise at least partially miscible elements can be fabricated. In the present thesis, transport and magnetoresistive properties of films of single-domain magnetic Fe clusters embedded in Ge and Ag matrices are studied under the above-mentioned aspect. Henceforth, these nonequilibrium cluster-assembled nanocomposites are referred to as Fe-Ge and Fe-Ag, respectively.

Magnetic nanometer-sized clusters consist of one single magnetic domain only. The constituting atomic moments rotate coherently and add up to a giant paramagnetic moment. Such nanoparticles are desirable because of the low energy barrier that has to be overcome in order to reverse the direction of the magnetic moment [8]. The phenomenon related to thermal-energy-induced flipping of isolated magnetic moments of such kind is called superparamagnetism [9]. Magnetic nanoparticles exhibit larger

spin relaxation times [10–12] than their bulk counterparts. For this reason, magnetic nanoparticles are interesting candidates for nanoscale spintronic devices. Giant and tunneling magnetoresistance effect can be employed, e.g., in layered structures to act as spin valves. The structural conditions for these effects to appear can also be met in granular materials [13–16]. Therefore, magnetic nanoparticles can be applied in spintronic devices as well [17]. In superconducting circuits spin valve structures as a part of a Josephson junction allow to control the phase shift across the junction [18,19]. This effect has potential applications in neuromorphic computing [20] and in quantum computing, where π-qubits are expected to exhibit reduced decoherence [21,22].

However, there are limits for magnetic-nanoparticle-induced properties because of finite-size effects. Finite-size effects occur, for example, because the number ratio of surface to core magnetic moments increases with decreasing nanoparticle size. Since surface moments may be misaligned with respect to the core moments for energetic reasons the fraction of misaligned magnetic moments increases with decreasing cluster size [23,24]. Furthermore, the dipole moments of magnetic nanoparticles start to interact with each other when the nanoparticles are arranged in close vicinity to each other [25,26].

Classically, it is the electric field that is used to control the functional state of an electronic device, working on the electric charge of the carriers only. However, the shrinking size of integrated circuits in electronic devices is limited by the increase of dissipation and leakage within the devices. These limitations are promised to be overcome when the spin degree of freedom of the carriers is used in addition to or even instead of their electric charge [27,28]. Adding magnetic properties via magnetic particles allows the control of the transport properties of a nonmagnetic matrix by applying a magnetic field, i.e., by using the spin degree of freedom of the charge carriers. The development of materials and, consequently, devices where the application of a magnetic field controls conductivity or where the magnetic permeability can be manipulated by an electric field is of great desire [29]. To achieve the former, materials with adjustable magnetoresistive properties are needed.

The combination of magnetic nanoparticles with semiconductors can result in intriguing phenomena like injection magnetoresistance, as documented by Lutsev et al. [30,31]. There, Co nanoparticles were deposited onto GaAs substrates as conducting, ferromagnetic component of films of granular $SiO_2(Co)$. In the prepared $SiO_2(Co)$/GaAs heterostructures the Co nanoparticles cause the formation of accumulation layers with two field-dependent spin-split sublevels in the semiconducting substrates on the one hand, and are used to inject electrons into the semiconducting substrate on the other. Positive magnetoresistance of up to $10^5\%$ was observed at room temperature, which makes the heterostructures ideally suited for being used as magnetic field sensors. As a further example, ferromagnetism in semiconductors has been applied to build functional elements with a gate-tunable proximity

magnetoresistance effect [32]. Lutsev et al. [30,31] used a gated bilayer structure of a nonmagnetic InAs and a ferromagnetic (Ga,Fe)Sb semiconductor to this end.

Research into magnetic semiconductors like (Ga,Fe)Sb started more than two decades ago. The aim of introducing ferromagnetism to a semiconductor while preserving its useful transport properties has slowly been approached by these dilute magnetic semiconductors (DMSs) [33]. A DMS is synthesized by substituting few percent of the semiconductor atoms by atoms that exhibit a finite magnetic moment when built into the crystal lattice of the semiconductor. Then, ferromagnetism is established by carrier-mediated coupling of ferromagnetic dopant atomic moments. Also, ferromagnetic inclusions can form. In this case, dipole-dipole interaction between the inclusions determines the magnetic properties of the DMS. One challenge is to achieve ferromagnetism above room temperature, a basic requirement for a wide range of applications. Recently, an amorphous metal-oxide magnetic semiconductor was synthesized from a ferromagnetic metallic glass that exhibits a Curie temperature higher than 600 K [34,35]. In contrast, the highest Curie temperature achieved in (Ga,Mn)As, a meanwhile well-established crystalline DMS, is 200 K only [35,36]. In crystalline DMSs the increase of the Curie temperature is limited by the amount of dopant atoms that can be dissolved in the lattice of the semiconductor without changing its crystal structure [35].

Standard technologies like molecular beam epitaxy, ion implantation, co-sputtering, and pulsed laser deposition have been used to create DMSs out of elemental and multicomponent semiconductors embedding both 3d and 4f magnetic elements, e.g., Ge:Mn [37–39] and ZnO:Fe [40,41]. In DMSs, ferromagnetic inclusions are not necessarily composed of the pure ferromagnetic dopant only, but can also be formed of a ferromagnetic alloy, e.g., $ZnSnAs_2$:MnAs [42,43]. Moreover, thermite reactions have also been employed to synthesize DMSs [44].

In the present thesis, size-selective CIBD is used to combine magnetic Fe clusters with the elemental semiconductor Ge. The Fe-Ge samples are used to study the transport properties and the magnetoresistance of this nonequilibrium cluster-assembled material.

Fe-Ag, the second cluster-assembled material system studied in the present thesis, is known to exhibit granular giant magnetoresistance [45–47]. This effect is caused by spin-dependent scattering of electrons by Fe atoms located at the surfaces of the Fe clusters [45]. Since Fe and Ag are immiscible elements and since the Fe-Ag system has been well-researched in the literature, cluster-assembled Fe-Ag nanocomposites are particularly suitable for size and concentration dependence studies.

An additional technical development made in the course of this thesis is the design and construction of a setup that uses laser ablation in an inert gas atmosphere in order to synthesize clusters via inert gas

condensation with diameters on the order of 10 nm and 100 nm. This special source, henceforth referred to as pulsed laser – buffer gas condensation (PL-BGC) setup, features a large fraction of neutral particles in its output. In contrast to the order of chapters chosen in this thesis, the PL-BGC setup was the initial project of this thesis. The application originally considered for the PL-BGC setup lies in the field of matter-wave diffraction experiments [48–51]; such experiments require beams of neutral particles. Nonetheless, the setup may be used for the preparation of cluster-assembled materials as well. Although the PL-BGC setup has neither been used for diffraction experiments nor for film depositions, an introduction to the laser ablation technique, a description of the PL-BGC setup and its benefits, and some experimental results are added to this thesis as a reference for future research.

1.1 Motivation

Simultaneous deposition of preformed nanometer-sized clusters and matrix material is a promising strategy to synthesize cluster-assembled nanocomposites, a special type of granular nanomaterial. The advantages of this strategy are the ability to select the clusters that are used for deposition by size and that even nonequilibrium compositions of elsewise at least partially miscible elements can be fabricated. On the one hand, combining two elements can aim for the symbiosis of their individual, already existing properties. This is, for example, the case, when clusters of a ferromagnetic material are co-deposited with a semiconducting matrix material. Such combinations aim for the synthesis of DMSs [33]. These materials are of great interest for techniques that combine traditional semiconductor-based nanoelectronics with magnetization or magnetic-field-sensitive devices and building blocks. On the other hand, co-depositions can aim for the creation of new materials with properties that are a consequence of the repeating pattern of clusters and matrix material. When ferromagnetic clusters are co-deposited with an insulating matrix the resulting nanocomposite may exhibit a tunneling magnetoresistance effect [13]. Similarly, giant magnetoresistance may be observed when a non-ferromagnetic metallic matrix is used [14–16].

The advantage of the CIBD technique used in the present work lies in the high degree of control over the deposited clusters. The used CIBD system includes a sector magnet with which the cluster ions in the beam are selected by their size. This way, very narrow cluster size distributions are achieved in the prepared films. Furthermore, the impact energy of the cluster ions on a growing film can be controlled. For these reasons, the CIBD system is well qualified to produce samples for studies of cluster size dependence effects in these cluster-assembled nanocomposites.

To test the capabilities of the CIBD system to synthesize potential DMS films, samples of Fe clusters embedded in matrices of Ge are prepared. In addition, samples of Fe clusters embedded in Ag matrices are prepared. The Fe-Ag system has been examined in the literature quite frequently and is known to exhibit granular giant magnetoresistance.

1.2 Objectives

The used CIBD system offers a very high degree of control over the co-deposition process and features a very narrow cluster size distribution. For these reasons, the transport properties of the prepared nanocomposite films cannot only be studied as a function of the volume fraction of the clusters in the films but also as a function of the size of the embedded clusters. Consequently, this allows to distinguish between effects that are related to the volume fraction and effects that depend on the size of the clusters.

Two nanocomposite systems are studied: Fe clusters embedded in Ge matrices and Fe clusters embedded in Ag matrices. The combination of magnetic clusters (Fe) and a semiconducting matrix (Ge) results in nanocomposites with both semiconducting and magnetic properties, with their properties depending on the size of the clusters. Fe-Ag is chosen as a second combination because it is a well-studied system known for its giant magnetoresistance. For this reason, cluster-assembled Fe-Ag nanocomposites are suitable to study the dependence of the granular giant magnetoresistance on cluster size and cluster concentration.

A strategy how to electrically connect the Fe-Ge films for transport measurements has to be developed in advance. This is of particular importance since the resistivities of the semiconducting sample films are expected to vary by several orders of magnitude when measured as a function of temperature. For this reason, an appropriate sample chip layout and, closely related, a compatible co-deposition sample layout have to be developed. Besides the examination of the properties of the as-deposited films, thermal annealing and hydrogenation are subsequent strategies to alter the as-deposited Fe-Ge nanocomposite films after the initial measurements in order to create films with different properties.

In addition to the research on Fe-Ge and Fe-Ag nanocomposites, a cluster source based on laser ablation is developed. Laser ablation features a low fraction of ionized particles and can be applied to a wide range of materials, including strongly magnetic ones that cannot be sputtered easily as well as oxides that are not suitable for ion-deposition-based systems.

1.3 Outline of the Thesis

Chapter 2: Starting with the magnetic dipole moment, the phenomenon of magnetism is reviewed, with the focus on the ferromagnetism of Fe. Subsequently, a review on ordinary, anisotropic, tunneling, and giant magnetoresistance effect is given.

Chapter 3: The CIBD system used to prepare cluster-assembled Fe-Ge and Fe-Ag nanocomposites is reviewed in this chapter. It combines deposition of cluster ions from a size-selected cluster ion beam with deposition of matrix material from a constant flux of atoms emitted from an effusion cell.

Chapter 4: This chapter contains the research on cluster-assembled Fe-Ge nanocomposite films. Transport and magnetoresistance data of the nanocomposite samples are analyzed and the influence of the Fe concentration is studied. The Ge matrices turn out to be of amorphous structure and tunneling magnetoresistance is found to occur. Furthermore, the tunneling magnetoresistance effect is superimposed by at least one other magnetoresistance effect that varies with the magnetic field within the range accessible with the device used for transport measurements. Finally, some of the as-prepared samples are thermally annealed at two different temperatures. The observed changes in sample properties are discussed and related those observed in DMSs.

Chapter 5: In this chapter, the second material system, Fe-Ag, is studied. As expected, the cluster-assembled Fe-Ag nanocomposite samples exhibit granular giant magnetoresistance.

Chapter 6: In addition to the CIBD system used to synthesize cluster-assembled nanocomposites, another stand-alone cluster source based on laser ablation is designed and assembled. The principle of laser ablation, the current state of the setup, and its principle of operation are reviewed in this chapter. Finally, a test sample of aggregated Ag clusters is presented.

2 Theory of Magnetism and Magnetoresistance

Already in the 19th century electric transport through metals was found to be influenced by magnetic fields and to even depend on the direction of the electric current relative to the magnetization in case of ferromagnets. These two effects, ordinary and anisotropic magnetoresistance, are intrinsic magnetoresistance effects in the sense that they originate from the atomic and crystal structure. By combining materials with different transport and magnetic properties, artificial structures with magnetoresistive properties can be designed and prepared. Tunneling magnetoresistance occurs when two ferromagnetic domains are separated by a tunneling barrier, giant magnetoresistance occurs when a non-ferromagnetic metallic spacer material separates the two domains. In both structures, the resistivity depends on spin-dependent scattering, i.e., it depends on the relative magnetization between the two ferromagnetic domains to each other. The conditions for these two effects can be met both in layered and granular structures.

This chapter covers the theoretical background relevant for the magnetoresistance measurements performed in this thesis. Since Fe is the ferromagnetic ingredient of both nanocomposites studied in this thesis, first, the ferromagnetism of Fe is derived. It is generally known that the magnetic dipole moments associated with the orbital momentum and the spin of the electron are the sources of magnetism. Consequently, the chapter starts with the description of the magnetic dipole moment of the electron. As the Fe nanoparticles discussed in the present work exhibit superparamagnetism, this type of magnetism is discussed following the section on ferromagnetism. Last, the four magnetoresistance effects introduced above—ordinary, anisotropic, tunneling, and giant magnetoresistance—are explained. The required theoretical considerations are well described in many textbooks on solid state physics or magnetism. The discussions of this chapter are based on the textbooks by J. M. D. Coey [52], W. Nolting [53], T. Fließbach [54], H. Ibach & H. Lüth [55], and R. Gross & A. Marx [56] if not stated otherwise.

2.1 Magnetic Dipole Moment and Paramagnetism

2.1.1 The Magnetic Dipole Moment of the Electron

In his fourth equation, J. C. Maxwell related a stationary current density $\vec{j}$ with the curl of a static magnetic flux density: $\text{curl}\,\vec{B} = \mu_0 \vec{j}$. With the vector potential $\vec{A}$ chosen in Coulomb gauge ($\text{div}\,\vec{A} = 0$), this transforms to Poisson's equation for the components of the vector potential: $\triangle \vec{A} = -\mu_0 \vec{j}$. Treating the current as being contained in a finite volume V, the general solution of Poisson's equation can be expanded in orders of distance from that volume. This is called the multipole expansion, the leading term of which is the magnetic dipole moment

$$\vec{\mu} = \frac{1}{2} \int_V \vec{r} \times \vec{j}(\vec{r})\, d^3r, \qquad\qquad [2\text{-}1]$$

where the integral runs over the volume V associated with the current density.

An electron orbiting a nucleus with a classical angular momentum $\vec{l}$ represents a current running in a loop, and generates a magnetic moment $\vec{\mu} = -e/2m_e\,\vec{l}$. $-e$ and m_e are the electron's charge and mass, respectively. Expressing the orbital momentum in terms of quantum mechanics, only one component, usually chosen as the z-component, can be measured precisely. This component is quantized by the orbital magnetic quantum number m_l. Therefore, the corresponding magnetic moment is also quantized, namely, in units of the Bohr magneton μ_B: $\mu_z^l = -\mu_B m_l$.

The magnetic moment induced by the nonclassical intrinsic angular momentum of the electron, by its spin $\vec{s}$, can be expressed in a similar way: $\mu_z^s = -g_e \mu_B m_s$. However, the ratio g_e of $\vec{\mu}_s$ expressed in units of μ_B and spin angular momentum $\vec{s}$ expressed in units of $\hbar$ is different from unity. For the spinning electron it is $g_e \approx 2$. The total angular momentum of an electron is $\vec{j} = \vec{l} + \vec{s}$.

2.1.2 Magnetic Moments and the Single-Electron Hamilton Operator

The properties related to the electron spin have to be added 'artificially' to the Schrödinger equation in form of magnetic moments interacting with the magnetic field when needed for the system to be modeled. However, the electron spin is respected by the relativistic Dirac equation. The Dirac equation ascribes a factor $g_e = 2$ to the electron spin. Among others, the 'artificial' terms are obtained from the Dirac equation in its nonrelativistic limit. The important terms in the resulting Hamilton operator are the Zeeman interaction

$$\mathcal{H}_Z = \frac{\mu_B}{\hbar}\left(\hat{l} + 2\hat{s}\right)\mu_0 \vec{H} \qquad\qquad \text{[2-2]}$$

and the coupling of the electron spin to the orbital angular momentum of the electron

$$\widehat{\mathcal{H}}_{SO} = \frac{1}{2m_e^{\,2}c^2}\,\frac{1}{r}\,\frac{dU}{dr}\,\hat{l}\cdot\hat{s}. \qquad\qquad \text{[2-3]}$$

$\hat{l}$ and $\hat{s}$ are the quantum mechanical single-particle angular momentum operators, $\hbar$ is the reduced Planck's constant, c is the speed of light in vacuum and r is the distance from the center of the electrostatic potential U, which is assumed to have spherical symmetry here.

The Zeeman term, Equation [2-2], represents the coupling of a single electron to an external magnetic field. Depending on its orbital momentum and its spin, the energy of an electron is either lowered or increased. For (quasi-)free electrons ($l = 0$) the Zeeman shift by a magnetic field causes a surplus of electrons with one spin orientation because electrons shifted upward in energy can flip their spin in order to reduce their energy again. This yields a net magnetization of the electron gas. The corresponding Pauli susceptibility is

$$\chi_P = \mu_0\,\mu_B^{\,2}\,D(E_F), \qquad\qquad \text{[2-4]}$$

where $D(E_F) = D_\uparrow(E_F) + D_\downarrow(E_F)$ is the density of states at the Fermi level of the 3D electron gas including both spin polarizations.

In a many-particle system the single-particle operators are replaced by the corresponding many-particle operators $\hat{L}$ and $\hat{S}$. The total angular momentum of a many-particle system is $\vec{J} = \vec{L} + \vec{S}$ and its magnetic moment is

$$\vec{\mu} = -g\,\mu_B\,\vec{J}/\hbar \qquad\qquad \text{[2-5]}$$

with the Landé factor in LS-coupling $g = \frac{3}{2} + \left(S(S+1) - L(L+1)\right)/2J(J+1)$. The Zeeman energy becomes

$$E_Z = g\,\mu_0\,\mu_B\,M_J\,H. \qquad\qquad \text{[2-6]}$$

Regarding the coupling of spin and orbital momentum, Equation [2-3], the potential of a nucleus with charge Ze is $U = -Ze^2/4\pi\varepsilon_0 r$. For a single 3d electron ($r \sim 0.1$ nm) in an otherwise 'empty' atom

the energy of the effect can be estimated to be on the order 1 meV for 3d transition elements ($Z \approx 25$). Hence, spin-orbit coupling plays a minor role here. However, the effect becomes " …more important for heavy elements and especially for inner shells." [52]

2.1.3 Paramagnetism of Localized Electrons

In an assumed ideal paramagnet the electrons of a many-particle system do not interact via their charges or their magnetic moments. Their number is constant and so is the occupied volume. Hence, they represent a canonic ensemble and the expectation value for any quantity q in this type of ensemble is $\langle q \rangle = \sum_i q_i \exp(-E_i/k_B T)/\mathcal{Z}$, where $\mathcal{Z} = \sum_i \exp(-E_i/k_B T)$ is the partition function of the canonic ensemble, i runs over all possible energy states, and E_i symbolizes the corresponding energies.

According to the addition rules for quantum mechanical angular momenta, the component of the total angular momentum of the system projected to the direction of an external magnetic field $M_J \in \{-J, \dots, J\}$ can take $2J + 1$ discrete values. The corresponding energies are $E_{M_J} = g\mu_0\mu_B M_J H$, according to the Zeeman energy, Equation [2-6]. Evaluating the thermodynamic average, one obtains

$$\langle \mu_Z \rangle = \mu_{max}\, \mathcal{B}_J(x) = \mu_{max} \left(\frac{2J+1}{2J} \coth\left(\frac{2J+1}{2J}x\right) - \frac{1}{2J}\coth\left(\frac{x}{2J}\right) \right) \qquad [2\text{-}7]$$

for the component of the magnetic moment pointing into the direction of the external magnetic field, where $x = g\mu_B J\,(\mu_0 H)/k_B T$, $\mu_{max} = g\mu_B J$ is the maximum possible magnetization, and where $\mathcal{B}_J(x) = \langle \mu_Z \rangle / \mu_{max}$ is called the Brillouin function. Expanding the Brillouin function in the limit $x \ll 1$ yields $\mathcal{B}_J(x) \approx x\, J(J+1)\,/\,3J$ as the leading term. In this limit, the susceptibility $\chi = n\langle \mu_Z \rangle / H$ of an ensemble with number density n is $\chi = C/T$. This is the Curie law with the Curie constant

$$C = ng^2\mu_0\mu_B{}^2\, J(J+1)/3k_B = \mu_0 n\mu_{eff}^2/3k_B. \qquad [2\text{-}8]$$

The classical form given here is obtained via the effective moment $\mu_{eff}^2 = g^2\mu_B{}^2|\vec{J}|^2/\hbar^2 = g^2\mu_B{}^2 J(J+1)$. In the limit $J \to \infty$ the Brillouin function reduces to the Langevin function

$$\mathcal{L}(x) = \coth(x) - \frac{1}{x}. \qquad [2\text{-}9]$$

2.2 The Ferromagnetism of Iron

In the previous section, the magnetic moment of an electron and the paramagnetic behavior of a free electron gas were discussed. In this section, the properties of electrons bound to single atoms are discussed, followed by the changes that occur when a crystal lattice is built out of these atoms. The effect of exchange interaction is introduced and the occurrence of ferromagnetism is motivated by the Stoner criterion.

2.2.1 The Atom — A Many-Electron System

Two examples for a many-electron system are, first, single atoms that possess a spherically symmetric electric potential, and secondly, lattices of atoms with a periodic potential, generated by the superposition of atomic potentials. For the mathematical formulation of the many electron problem one of the electrons is 'singled out for calculation'. All other electrons form an electric potential which is experienced by this electron. Let i label the electron singled out, and let j be the index used to count through the remaining electrons. Then, the corresponding Coulomb potential is $U_2 = e^2 / 4\pi\varepsilon_0 r_{ij}$, where r_{ij} is the distance between electrons i and j, and where (i, j) runs over all possible combinations.

The many-electron wave function has to be antisymmetric under pairwise particle permutations in order to respect the Pauli principle. Following the Hartree-Fock method, the many-particle problem can be transformed into equations that effectively represent single-particle problems. The demand for asymmetry brings about another term in the effective single-particle operator. It represents a potential experienced by electron i that is caused by all other electrons j with their spin oriented parallel to that of electron i. Because of the indistinguishability of the electrons electron i can be exchanged with any of these electrons while the many-particle state remains unchanged. For this reason, the additional term is called exchange interaction.

Regarding the single Fe atom ($Z = 26$), the electronic configuration is [Ar] $3d^6\, 4s^2$, i.e., there are six electrons to be distributed among the ten states available in the 3d shell. All other shells are filled completely. Intra-atomic exchange interaction demands five of the six 3d electrons to occupy the available states with their spins aligned parallel (Hund's second rule). The remaining electron occupies the $m_l = 2$ state with its spin aligned antiparallel to the other 3d electrons. The state with highest possible orbital momentum in direction of quantization is occupied because the electron is then further away from the nucleus and, thus, from the other 3d electrons. In this configuration it experiences less Coulomb repulsion (Hund's third rule).

2.2.2 Lattices of Iron Atoms

When atoms are arranged in a lattice the valence shells of the atoms start to overlap. The outermost shell of an Fe atom is the 4s shell, the next deeper shell is formed by the 3d orbitals. Now, that atoms are close enough to allow their outermost orbitals to overlap to smaller or larger extents, the energies of the valence states need to split. This way, valence and conduction bands form. For Fe, the 4s band is wide because of the large overlap of the 4s wave functions. The overlap is less for the 3d orbitals, hence, the corresponding bands are much narrower.

The electrons in the nonspherical 3d orbitals experience the charge distribution caused by the electrons of their nearest neighbors, called the crystal field. The orbitals are deform by the crystal field, which comes along with an energetic splitting of the 3d levels. This splitting is reflected by the highly structured 3d bands in the density of states of bulk Fe, see Figure 2-1(a) (replot from Reference [57]). In Figure 2-1(a), the density of states is plotted per spin orientation, which are symbolized by ↑ and ↓. Note, that '↑' and '↓' are only used to distinguish between the two spin orientations, without referring to any axis of quantization.

Bulk Fe possesses a bcc structure (α-Fe) at room temperature, i.e., there are 8 nearest neighbors per lattice site. α-Fe is a ferromagnet with a Curie temperature of 1043 K. There are both 4s and 3d states at the Fermi level. Therefore, 4s and 3d electrons intermix, which causes a redistribution of the valence electrons among the 3d and 4s states. In fact, for α-Fe only 0.6 electrons retain their 4s character while the number of electrons with 3d character increases to 7.4 on average. The 0.6 4s electrons are largely spin-paired, i.e., there are each 0.3 electrons with spin ↑ and ↓ on average. For the 3d electrons it is 4.8 with spin ↑ and 2.6 with spin ↓. Therefore, the magnetic moment per Fe atom is 2.2 μ_B [58], and not 4 μ_B as one could think regarding the electronic configuration of the single Fe atom. As there are more electrons with spin ↑, these are called majority spin electrons. Consequently, electrons with spin ↓ are called minority spin electrons.

Above 1184 K bulk Fe possesses an fcc structure (γ-Fe), with 12 nearest neighbors per lattice site. Since the deformation of orbitals caused by the crystal field and the degree of orbital overlapping are different here, γ-Fe possesses a different electronic structure and, consequently, different magnetic properties. However, since γ-Fe is a high temperature phase the following trick has to be used to examine its magnetic properties: The fcc phase can be stabilized by letting granules of γ-Fe precipitate in a matrix of Cu [59–62]. This is because there is only little mismatch between the fcc lattices of the γ-Fe particles and the fcc Cu host. Keeping the high-temperature fcc structure is energetically favored over the formation of fcc–bcc interfaces that would inevitably come to existence in case the Fe particles adopt the low-temperature bcc structure. Moreover, the lattice parameter of the γ-Fe precipitates matches the one
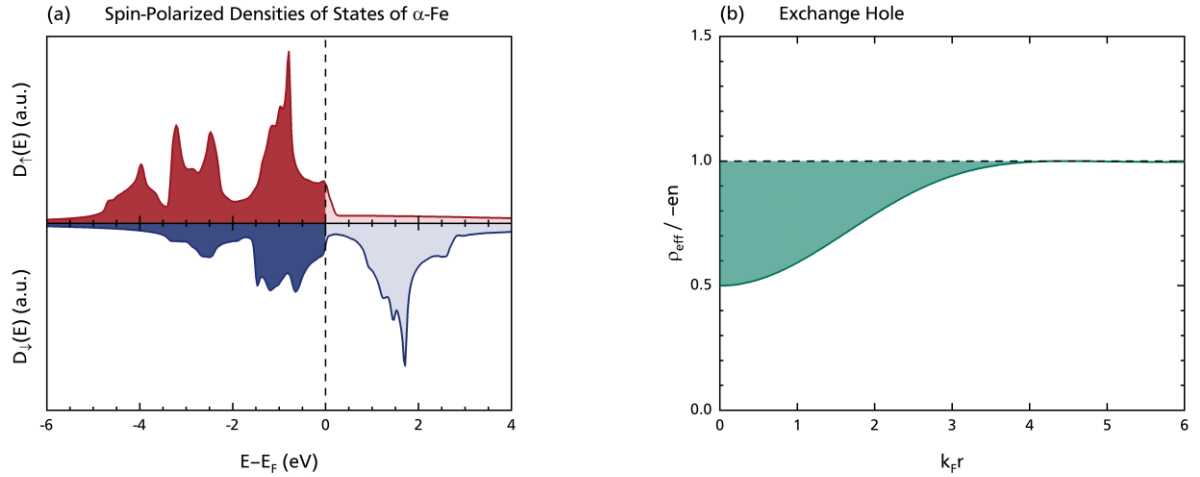
Figure 2-1: Spin-Polarized Density of States of α-Fe and Exchange Hole of the (Quasi-)Free Electron Gas

(a) Spin-polarized density of α-Fe. The upper half (red) shows the distribution of majority (↑) spin electrons, the lower half (blue) that of minority ones (↓). α-Fe has some unfilled 3d↑ states at the Fermi level and, therefore, is a weak ferromagnet. The graph is a replot from Reference [57], i.e., a plot of the numerical data available there.

(b) Effective charge distribution seen by a (quasi-)free electron. The reduced amount of charge in the vicinity of the electron is called the exchange hole. The charge distribution is normalized to the homogeneous distribution of charge $-en$.

of bulk γ-Fe. Samples of this kind were, e.g., produced and examined by means of neutron scattering at room temperature and at several cryogenic temperatures using liquid He (LHe) as coolant by Abrahams et al. [59]. The authors find their samples, which they describe as dispersed single crystals of fcc Fe, to possess antiferromagnetic ordering up to a Néel temperature of 8 K and a magnetic moment per Fe atom of 0.7 μ_B. The existence of an antiferromagnetic state is also confirmed by simulations of γ-Fe lattices. According to these simulations, γ-Fe may also exhibit a ferromagnetic ground state if the lattice parameter was larger [62–64].

2.2.3 The Way to Ferromagnetic Ordering

2.2.3.1 Exchange Interaction and the Exchange Hole

In the periodic lattice of bulk Fe the 3d and 4s electrons are bound only weakly and, therefore, can be treated as quasi-free. Consequently, the 3d and 4s electrons are well approximated by the free electron gas model. In the free electron gas a parallel alignment of spins is favored because of exchange interaction. The spatial part of the two-particle wave function of a pair of electrons with parallel spins (i, j) has to be antisymmetric: $\Psi_{ij} \propto \varphi_i(\vec{r}_i)\varphi_j(\vec{r}_j) - \varphi_i(\vec{r}_j)\varphi_j(\vec{r}_i)$. Integrating the probability

to find electron j at a position $\vec{r}$ relative to electron i, $\left|\Psi_{ij}\right|^2 \propto 1 - \cos\left(\left(\vec{k}_i - \vec{k}_j\right)\vec{r}\right)$, over the whole, spin-polarized Fermi sea yields an effective charge distribution experienced by electron i

$$\rho_{eff}(\vec{r}) = -en\left(1 - \frac{9}{2}\frac{\left(\sin(k_F r) - k_F r \cos(k_F r)\right)^2}{(k_F r)^6}\right)$$
[2-10]

with $(\hbar k_F)^2 = 2m_e E_F$. $-e$ is the charge of the electron and n is the homogeneous number density of electrons. The distribution Equation [2-10] is plotted in Figure 2-1(b). The color-highlighted deviation from a constant charge distribution below $k_F r \approx 4$ is called the exchange hole. The lack of electric charge in the vicinity of electron i reduces the effective shielding of the ion core potential (nucleus + inner electrons), i.e., the attraction by the ion core effectively increases. Therefore, the energy of electron i is reduced—the exchange interaction is of attractive kind. The higher the spin polarization in the electron gas, the higher the energy bonus. For electrons in a covalent bond, i.e., localized electrons, exchange interaction favors antiparallel alignment of spins. This is the famous two-electron example of the diatomic hydrogen molecule that is found in many textbooks.

2.2.3.2 The Stoner Criterion for Ferromagnetic Ordering

The reduction in energy per electron due to exchange interaction depends on the spin-polarized number of electrons n_σ. Therefore, the single-electron energies become spin polarized, too: $E_\sigma(\vec{k}) = E(\vec{k}) - I\,n_\sigma/N$. Here, $E(\vec{k})$ is a single-electron band energy, N is the number of atoms, $\sigma \in \{\uparrow, \downarrow\}$ is the spin index, and I is the Stoner parameter that represents the strength of the energetic reduction. The Fourier transformed function of Equation [2-10] is constant in $\vec{k}$-space to good approximation. Therefore, the Stoner parameter can be assumed constant, too [65].

In a ferromagnet, a surplus of electrons with one spin orientation exists: $R = (n_\uparrow - n_\downarrow)/N > 0$. This surplus can be expressed via Fermi-Dirac occupation probabilities $f\left(E_\sigma(\vec{k})\right)$ with the spin-polarized single-electron energies given above. This leads to a self-consistency equation for the ratio R. Demanding solutions with $R > 0$ yields the Stoner criterion:

$$I\,N(E_F) > 1,$$
[2-11]

where $N(E_F)$ is the density of states per atom for each spin state. The magnetization of the exchange-interacting quasi-free electron gas in an external magnetic field H is

$$M = \frac{\chi_P}{1 - I\,N(E_F)}\,H. \tag{2-12}$$

It can be seen that exchange interaction increases the susceptibility of the quasi-free electron gas. Moreover, the susceptibility diverges when $I\,N(E_F) \to 1$. In particular, when a magnetic material fulfills the Stoner criterion the splitting of spins happens spontaneously. To fulfill the criterion a large density of states at the Fermi level, i.e., narrow bands are required. Besides Fe, only Co and Ni fulfill the Stoner criterion, and in fact, these elements are known for their ferromagnetic properties.

The shifted spin-polarized densities of states are shown in Figure 2-1(a). As can be seen, most of the majority spin 3d states are located below the Fermi level, however, not all of them. Therefore, the average number of 3d majority spin-electrons per atom is 4.8, which makes Fe a weak ferromagnet. In a strong ferromagnet the exchange interaction is strong enough to push all 3d majority spin states below the Fermi level. This is the case for Ni and Co.

2.2.3.3 The Ferromagnet at Finite Temperatures and the Curie Temperature

So far, ferromagnetism was discussed at zero temperature. The behavior at nonzero temperatures is well explained in terms of the mean field theory on ferromagnetism by Weiss, which is as follows. The magnetic field inside a ferromagnet is a superposition of an external field $\vec{H}$ and a contribution proportional to its own magnetization: $\vec{H}_{int} = n_W\vec{M} + \vec{H}$, where the Weiss constant n_W is the corresponding proportionality factor. The argument of the Langevin function, Equation [2-9], is replaced according to $\vec{H} \to n_W\vec{M} + \vec{H}$. For zero external field the magnetization is equal to the spontaneous magnetization of the ferromagnet M_S. This leads to a self-consistency equation for M_S. Nontrivial solutions exist when $T < T_C$, where

$$T_C = n_W\,C \tag{2-13}$$

is the Curie temperature, and C is the Curie constant from Equation [2-8]. The Curie temperature of α-Fe is 1043 K. Above this temperature magnetic moments still exist, but spontaneous ferromagnetic ordering is suppressed. The moments remain disordered, forming a paramagnetic state. The corresponding paramagnetic susceptibility is calculated analogous to the one of the paramagnetic ensemble. One obtains

$$\chi = \frac{C}{T - T_C}. \tag{2-14}$$

2.2.3.4 Anisotropy

In a single-crystalline sample, the direction of the ferromagnetic magnetization usually lies along a preferred crystal direction. This behavior is called anisotropy and the preferred direction is called the easy axis. The easy axis is not to be mixed up with the easy direction defined by the direction of an external magnetic field. Also, the easy axis offers two equivalent possibilities of magnetization alignment. There is an energy cost associated with deviations from alignment to the easy axis. The anisotropy can have a number of different origins: anisotropy in the shape of the magnetic particle, anisotropy in its magnetocrystalline structure, anisotropy of its surface, and induced anisotropy. The first three are discussed in brief next.

Shape anisotropy originates from the magnetostatic energy a sample with finite magnetization gains in its own demagnetizing field. In an ellipsoid of revolution with homogeneous density of magnetic moment the easy direction is the semimajor axis. The difference in magnetostatic energy density between parallel and perpendicular alignment to the easy direction of the magnetization of a sample is $\Delta E = 1/4 \, \mu_0 M_S (1 - 3\mathcal{N})$. M_S is the saturation magnetization of the ferromagnet and $\mathcal{N}$ the demagnetizing factor. In general, the energy density due to misalignment is $E_{sh} = K_{sh} \sin^2(\theta)$, where θ is the angle between the direction of magnetization and the easy direction and $K_{sh} = \Delta E$ is the anisotropy constant. For a perfect sphere it is $\mathcal{N} = 1/3$, hence, the shape anisotropy of a perfect sphere is zero—as expected. The clusters used in this work are assumed to be of spherical shape. However, since they consist of 'only' a few hundred atoms and since they may deform in the moment they are soft-landed on a sample, it is well possible that the spherical shape is modified to an oblate one.

The origin of magnetocrystalline anisotropy is the crystal field, which is generated by the ion cores forming the lattice and experienced by the electrons in the orbitals that contribute to the finite magnetic moment of the solid. The moment of the electron in an orbital that is stabilized by the crystal field is aligned in a particular crystallographic direction by spin-orbit interaction. This kind of anisotropy causes, e.g., the cube edges $\langle 100 \rangle$ to be the easy directions of bcc α-Fe. The leading term of magnetocrystalline anisotropy is $E_{mc} = K_1 \sin^2(\theta)$. Merging both sources of anisotropy into a single expression, an effective anisotropy constant can be defined so that $E_{eff} = K_{eff} \sin^2(\theta)$.

For particles in the nanometer range, the number of moments located on the surface of a particle is not negligible compared to the number of moments forming the particle. This is taken into account by the surface anisotropy $E_S = \int K_S (1 - (\vec{e}_M \cdot \vec{e}_n)^2) \, d^2r$, where the integral runs over the surface of a particle, K_S is the corresponding anisotropy constant, $\vec{e}_M$ is the direction of magnetization, and $\vec{e}_n$ is the surface normal direction. In micro-SQUID measurements of single Co clusters in Nb matrices, the clusters consisted of about 1000 atoms, Jamet et al. [26] found that in this case "… it seems that the cluster-matrix interface provides the main contribution to the magnetic anisotropy."

2.2.3.5 The Stoner-Wohlfarth Ferromagnet in a Magnetic Field

The simplest model of an isolated ferromagnetic particle is the one proposed by Stoner & Wohlfarth [66,67]. It is based on a prolate, uniformly magnetized ellipsoid with saturated magnetization $|\vec{M}| = M_S$ and with shape or magnetocrystalline anisotropy $E_A = K\sin^2(\theta)$, see Section 2.2.3.4. θ is the angle of the magnetization towards the easy axis. The model assumes that all moments within the particle remain aligned parallel, hence, rotate coherently when the magnetization changes direction. When the model is restricted to two dimensions, the prolate ellipsoid reduces to an ellipse, as it is shown in Figure 2-2(a). The semimajor axis is the easy axis and the angle θ is added accordingly.

The magnetostatic energy of the particle in a magnetic field $\vec{H}$ is $E_M = -\mu_0 \vec{M}\vec{H}$. The direction of the magnetic field with respect to the easy axis is represented by the angle towards the easy axis, ϕ. Then it is $\vec{M}\vec{H} = M_S H\cos(\phi - \theta)$. Similarly, the component of the relative magnetization $m = M/M_S$ parallel to the magnetic field is given by $m_\parallel = \cos(\phi - \theta)$. Hence, the total energy of the particle is

$$E = K\sin^2(\theta) - \mu_0 M_S H\cos(\phi - \theta). \qquad [2\text{-}15]$$

To find the direction of the magnetization, i.e., the angle θ that results when a magnetic field of strength H and direction ϕ is present, the minimum of Equation [2-15] with respect to θ has to be found. The governing pair of (in)equations is $dE/d\theta = 0$ and $d^2E/d\theta^2 \geq 0$. A positive second derivative represents a stable minimum, the second derivative being equal to zero represents a saddle point.

In general, these equations have to be numerically solved for solutions $m_\parallel(h)$. Therefore, it is common practice to normalize the magnetic field to the anisotropy field via $h = \mu_0 M_S H/2K$. Some of the resulting $m_\parallel(h)$ curves are plotted in Figure 2-2(b). Only the two limiting cases $\phi = 0$ (red, magnetic field parallel to the easy axis) and $\phi = \pi/2$ (green, magnetic field parallel to the hard axis) as well as the case $\phi = \pi/4$ (not shown) can be solved analytically. The numerically solved cases $\phi = \pi/6$ and $\phi = \pi/3$ are added in blue and yellow, respectively.

The Stoner-Wohlfarth model explains the occurrence of hysteresis as follows. Starting at a large positive field $h \gg 1$ the magnetization in direction of the magnetic field is saturated in good approximation, $m_\parallel = 1$. When h decreases, the angle θ minimizing the energy also changes. Below a certain field h_{sw} another minimum starts to coexist in the $E(\theta)$ curve, indicating a second solution and, hence, a second possibility of magnetization alignment. At $-h_{sw}$, i.e., at a field pointing into the reverse direction of the current magnetization, the so-far stable minimum changes to a saddle point, and vanishes for larger negative fields. Until this point the magnetization is reversible. However, the
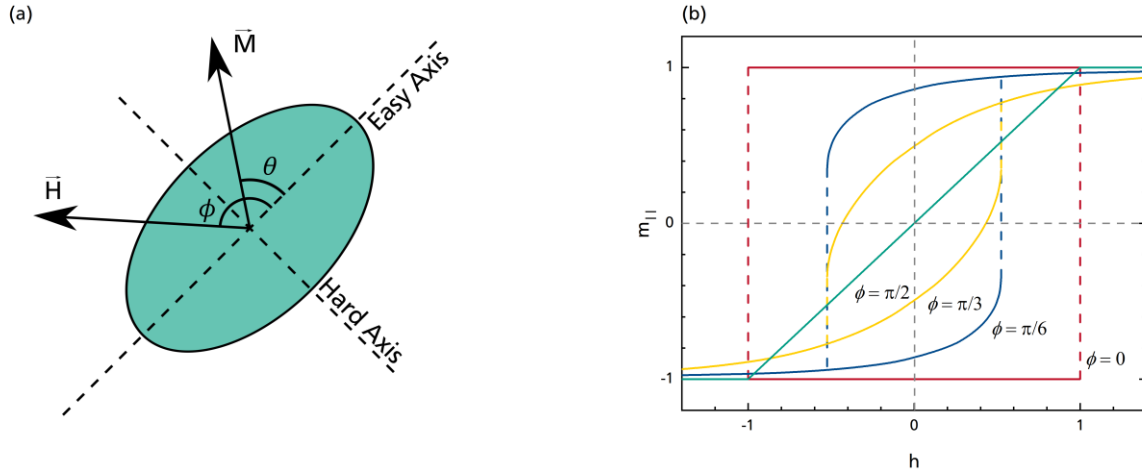
Figure 2-2: Hysteresis in the Stoner-Wohlfarth Model

(a) Stoner-Wohlfarth ellipsis. The semimajor axis is the easy axis, the semiminor axis the hard axis. The magnetic field $\vec{H}$ is applied at an angle ϕ with respect to the easy axis, which causes the magnetization $\vec{M}$ to take an angle θ towards the easy axis.

(b) $m_\parallel(h)$ curves calculated with the Stoner-Wohlfarth model for different orientations of the magnetic field. The hysteresis is of rectangular shape when the magnetic field is applied parallel to the easy axis (red curve). When it is applied parallel to the hard axis, no hysteresis but full reversibility is observed (green curve).

magnetization switches to the other minimum at $h = -h_{sw}$ because there the energy required to do so becomes zero. For $\phi = \pi/6$ and $\phi = \pi/3$ (blue and yellow curves) the Stoner-Wohlfarth model yields $h_{sw} = 0.524$. For the case $\phi = 0$, no deviation of the magnetization from the easy axis occurs since the magnetic field is oriented parallel to the easy axis. Consequently, the magnetic field has to compensate the full anisotropy in order to switch the magnetization. Therefore, $h_{sw} = 1$ in this case and $m_\parallel$ switches from 1 directly to -1 (red curve). When the magnetic field is applied along the hard axis of the ellipsoid ($\phi = \pi/2$), $m_\parallel$ varies linearly with h when $|h| \leq 1$, and remains saturated $\left(|m_\parallel| = 1\right)$ when $|h| \geq 1$. Within the magnetic field range $|h| < 1$ the magnetization vector progressively rotates towards the reverse direction without switching. Hence, no hysteresis occurs; the corresponding magnetization curve (green) is fully reversible.

An ensemble of ferromagnetic domains can be interpreted as an ensemble of randomly oriented, noninteracting Stoner-Wohlfarth particles. The relative remanence of such an ensemble is $m_r = 1/2$, its coercivity is $h_c = 0.482$, and the remnant coercivity is $h_{rc} = 0.524$.

2.3 Superparamagnetism of Nanoparticles

Superparamagnetism is a form of magnetism that appears in single domain ferromagnetic particles with dimensions smaller than the radius for coherent rotation of magnetization corresponding to the ferromagnetic material. Coherent rotation was discussed in the context of the Stoner-Wohlfarth model in Section 2.2.3.5. The radius for coherent rotation of Fe is 12 nm. While the moments of a superparamagnetic particle are exchange-coupled, the particle itself can be treated as a paramagnetic macrospin for the following reason. Such a superparamagnetic particle has an energy barrier that depends on anisotropy aspects and this barrier has to be overcome in order to reverse the direction of the magnetic moment of the particle. However, a reversal needs to be induced by thermal energy in order to overcome the energy barrier. Therefore, superparamagnetism appears when the thermal energy is on the order of the energy barrier. A detailed review on superparamagnetism is given in, e.g., Reference [9].

For nanoparticles with the shape of an ellipsoid of revolution the direction of magnetization is twofold degenerated. Hence, a nanoparticle can reverse the direction of its macrospin in case the maximum anisotropy energy $E_A = K_1 V$ is overcome by thermal energy, where V is the particle volume. The flipping frequency $\tau^{-1} = \tau_0^{-1} e^{-E_A/k_B T}$ is the product of an attempt frequency τ_0^{-1} and the Boltzmann factor $e^{-E_A/k_B T}$. As long as no magnetic field is applied both directions of magnetization are equally favored in terms of energy. Hence, the flipping frequencies are the same for both directions. Both magnetic orientations exist for the same time on average. For this reason, the net magnetic moment of an ensemble of superparamagnetic particles is zero. However, the barrier becomes asymmetric when a magnetic field is applied, i.e., one of the two directions is favored over the other. Then, a net magnetization can be measured.

When the magnetization of an ensemble of such nanoparticles is measured within a time span much smaller than the magnetic moment reversal time τ, the moments appear as being frozen. In this blocked state magnetization vs. magnetic field curves recorded from an ensemble show ferromagnetic behavior, i.e., magnetic hysteresis. In the opposite case, where the time for reversal is smaller than the measurement time, flipping happens many times within one measurement period. Then, the ensemble shows a finite magnetization because each nanoparticle has its magnetic moment aligned parallel to a favored direction for a longer time compared to antiparallel alignment. Here, the ensemble of nanoparticles behaves similarly to an ensemble of paramagnetic atomic moments, however, with a much larger magnetic susceptibility due to the ferromagnetic base material. For this reason, the magnetic behavior of such particles is called 'superparamagnetic'.

Choosing the ferromagnetic resonance frequency $\tau_0^{-1} \sim 1\,\text{GHz}$ as the attempt frequency and the inverse flipping frequency as an approximate measurement period of $100\,\text{s}$, the superparamagnetic ensemble appears blocked when the temperature is below the blocking temperature

$$T_B \approx \frac{K_1 V}{25 k_B}.$$ [2-16]

When an ensemble is cooled in a small magnetic field, the magnetization increases with $1/T$ as expected for an ensemble of paramagnetic moments. When the temperature is sufficiently low, the moments appear blocked, consequently, the magnetization saturates. This measurement procedure is called field-cooled magnetization vs. temperature curve or, briefly, field-cooled (FC). The warming up of a demagnetized ensemble in a small magnetic field starts with an increase of the magnetization until all magnetic moments are unblocked, i.e., their anisotropy energy barrier can be overcome by thermal energy. Then, the moments align in accordance with the applied field. With further increasing temperature the magnetization decreases with $1/T$. Ideally, this part of the zero-field-cooled (ZFC) curve overlaps with the FC curve in the paramagnetic temperature range, where the magnetization of the ensemble is reversible.

Because a superparamagnetic moment represents a paramagnetic moment in the classical limit $J \to \infty$, the magnetization of a superparamagnetic ensemble follows a Langevin function (Equation [2-9]). In the ideal case, the superparamagnets do not interact with each other, i.e., there are no dipolar interactions between isolated superparamagnetic moments or exchange interactions between touching particles. Then, the relative magnetization $m = M/M_S$ is a function of H/T according to the argument of the Langevin function. The argument changes when dipolar interactions within an ensemble of interacting superparamagnets are taken into account. Then, the temperature is replaced by an apparent temperature $T \to T_a = T + T^*$, which is the sum of the real temperature T and a constant T^* that is related to the dipole energy of the superparamagnetic particles [25], and the relative magnetization is no longer a function of H/T.

In reality, the nanoparticles of an ensemble are distributed in size and interact with other superparamagnetic moments. Hence, the magnitude of their magnetic moments, their anisotropy barriers and, consequently, their blocking temperatures are distributed in magnitude. In real ZFC curves the maximum peak is of finite width and broadens with increasing interaction strength and cluster size distribution, while the peak simultaneously shifts to higher temperatures. At a certain temperature some smaller nanoparticles may already be unblocked, while the magnetic moments of larger nanoparticles are still frozen. This distribution of blocking temperatures may also be found for samples in which the

spatial distribution of superparamagnetic moments is not uniform. Different strength of interaction between nanoparticles depending on their separation may have a similar effect.

The magnetic properties of the nanometer-sized superparamagnetic Fe clusters examined in the present thesis are discussed in Sections 4.5.2 and 5.2.3.

2.4 Magnetoresistance Effects

In this theory section, the four magnetoresistance effects mentioned in the introduction are explained: ordinary, anisotropic, tunneling, and giant magnetoresistance.

2.4.1 Ordinary Magnetoresistance

In the Sommerfeld picture of electronic transport the electrons are treated as a gas of free particles. The conduction electrons move freely between scattering events, which happen continuously and cause a progressive redistribution of momentum $\vec{k}$ among the electrons. The Fermi surface of the free electron gas is a sphere with its center at $\vec{k} = 0$. Scattering happens only in an energy range $\sim k_B T$ around the Fermi energy, i.e., only in a thin layer around the Fermi surface, because only here unoccupied but thermally accessible states exist. Electrons at the Fermi level move with the Fermi velocity v_F, which is on the order of 10^6 m/s for metals, and scattering happens at a frequency on the order of $\tau^{-1} = 10^{14}$ s^{-1}. The corresponding average distance between two scattering events is the mean free path $\lambda_0 = v_F \tau$, which can be estimated as being on the order of 10 nm with the values given above.

When an electric field E is applied along the x-direction the Fermi sphere is shifted by $\delta k = eE\tau/\hbar$ into this direction. For symmetry reasons, the shift of the Fermi sphere δk becomes also the average momentum of the conduction electrons. Accordingly, the average velocity of the electrons is different from zero: The electrons drift with a small velocity $v_D = \hbar\, \delta k / m_e = eE\tau/m_e$ opposite to the direction of the applied electric field, which results in a current $j = nev_D$ in x-direction. Here, m_e and $-e$ are the electron mass and charge, respectively, and n is the number of conduction electrons per unit volume. The quantity $\mu = e\tau/m$ that relates the drift velocity of a charge carrier to the applied electric field as $v_D = \mu E$ is called mobility. Assuming an electric field $E = 100$ V/m, a drift velocity on the order of 10^{-1} m/s can be estimated. Hence, the drift velocity is very small compared to the Fermi velocity. The resistivity is obtained via Ohm's law $E = \rho_0 j$:

$$\rho_0 = \frac{m_e}{ne^2\tau} = \frac{m_e v_F}{ne^2 \lambda_0}. \qquad \text{[2-17]}$$

When a magnetic field is applied along the z-direction in addition, electrons propagate along circular arcs rather than straight lines due to the Lorentz force $\vec{F}_L = -e(\vec{E} + \vec{v} \times \vec{B})$. Note, that the Lorentz force acts on the real velocity of the electrons, i.e., the Fermi velocity. The radii of the arcs are equal to the cyclotron radius $r_C = \omega_C / v_F = eB/m_e v_F$, where ω_C is the cyclotron angular velocity. The propagation length along the arc remains unchanged, i.e., remains equal to λ_0. However, the distance between two scattering locations is now the length of the chord spanned by the angle $\varphi = \lambda_0 / \omega_C$ defined by the arc. Consequently, the effective mean free path reduces. It becomes

$$\lambda_{eff} = 2\, r_C\, \sin\left(\frac{\varphi}{2}\right) \approx \lambda_0 \left(1 - \frac{(\omega_C \tau)^2}{24}\right) \qquad \text{[2-18]}$$

for small φ. The resistivity becomes

$$\rho = \frac{m_e v_F}{ne^2 \lambda_{eff}} = \frac{m_e v_F}{ne^2 \lambda_0 \left(1 - \frac{(\omega_C \tau)^2}{24}\right)} \approx \rho_0 \left(1 + \frac{(\omega_C \tau)^2}{24}\right). \qquad \text{[2-19]}$$

Hence, the relative change of resistivity due to the applied magnetic field, $\Delta\rho/\rho_0$, is positive and $\propto B^2$ in first approximation. This Lorentz-force induced type of magnetoresistance is universal to all conductors, therefore, it is called ordinary magnetoresistance. Its magnitude is on the order of 1% at 1 T in metals. The effect may be larger in semimetals and semiconductors owing to the higher carrier mobilities characterizing these materials.

Note, that the Hall field only compensates a drift off the direction of the applied electric field so that the original direction of average movement is maintained. Therefore, when the individual movement of the electrons is disregarded the resistivity is independent of the magnetic field. Consequently, the magnetoresistance of the electron gas is zero.

However, the above calculations are still a too simple model for the ordinary magnetoresistance in real conductors. This is because the Fermi surface of real conductors may differ a lot from the shape of a perfect sphere. Moreover, the electrons are organized in bands with dispersion relations $E_n(\vec{k})$ (n is the band index). An electron moves with a velocity $\vec{v}_n(\vec{k}) = 1/\hbar\, \vec{\nabla}_k E_n(\vec{k})$ and is assigned an effective mass $m^*(\vec{k}) = \hbar^2 \left(d^2 E_n(\vec{k})/dk^2\right)^{-1}$. In momentum space the electron trajectories follow surfaces of constant energy (the Fermi surface) and lie on planes oriented perpendicular to the applied magnetic

field. The trajectories result from the intersections of these planes. Because the magnetic part of the Lorentz force is $\propto \vec{B} \times \vec{\nabla}_k E_n(\vec{k})$ the sense of rotation along these trajectories is determined by whether $\vec{\nabla}_k E_n(\vec{k})$ points to the inside of or away from the enclosed area. Moreover, even open trajectories can result, depending on the orientation of the magnetic field relative to the crystallographic directions of the (single-crystalline) sample [68]. This is in contrast to the spherical Fermi surface of free electrons, where $\vec{\nabla}_k E_n(\vec{k})$ always points away from the enclosed area. For the reason of the dependence on orientation, the trajectories can be divided into electron- and hole-like trajectories. In a more-advanced model, the two-band model, one electron- and one hole-like band are assumed to contribute to charge transport. Accordingly, each 'type' of carrier requires a different Hall field to have its drift movement compensated. This leads to a compensation effect of the carriers because only one Hall field can exist, of course. When the resistivity resulting from this model is calculated via a projection of the current density $\vec{j}$ on the electric field $\vec{E}$ a term $\propto B^2$ appears in the expression. In general, ordinary magnetoresistance is always $\propto B^2$ in small magnetic fields and tends to saturate at large fields.

2.4.2 Anisotropic Magnetoresistance

The basic principle of magnetoresistance caused by spin-orbit interaction in conductors with a spin-polarized density of states was proposed by Smit [69]. His model for anisotropic magnetoresistance is further discussed and extended in, e.g., References [70–73]. Anisotropic magnetoresistance occurs as follows, according to these references.

In a strong ferromagnet the 3d↑ states are completely filled—that is, ↑ represents the majority spin. The 3d states are localized to a higher degree than the 4s states. However, they contribute to charge transport with delocalized states, too. For simplicity, the 3d states are now assumed to only represent localized states, while the delocalized states are all represented by the 4s states. In this picture, spin-preserving scattering of 4s↑ electrons into 3d↑ states is suppressed, while scattering of 4s↓ electrons into 3d↓ states is possible. Spin-preserving scattering between 4s states is possible for both spin orientations, of course. In a weak ferromagnet, such as Fe, the 3d↑ states are almost filled, so that scattering into 3d↑ states is not fully suppressed.

The product of orbital and spin angular momentum operator appearing in the Hamiltonian for spin-orbit interaction, Equation [2-3], can be written as $\hat{L}\hat{S} = \frac{1}{2}\left(\hat{L}_-\hat{S}_+ + \hat{L}_+\hat{S}_-\right) + \hat{L}_z\hat{S}_z$. Here, $\hat{J}_\pm = \hat{J}_x \pm i\hat{J}_y$ are the angular momentum ladder operators. From this form it is visible that spin-orbit interaction mixes majority and minority spin 3d states. The axis of quantization is the z-direction here, i.e., the direction of magnetization.

Spin-orbit interaction mixes 3d↑ states to the states available for scattering, i.e., holes in the 3d↑ states are created by the operator $\hat{S}_-$ in the second term. On the other hand, the operator $\hat{L}_+ = \hat{L}_x + i\hat{L}_y$ in the second term is not symmetrical in position space, i.e., the holes in the 3d states are not equally distributed over the 3d states. In particular, there is a deficit of holes in 3d states oriented perpendicular to the magnetization direction. Therefore, 4s electrons are scattered more often when moving parallel to the direction of magnetization and less when moving perpendicular to it. Hence, $\rho_\parallel > \rho_\perp$: The resistivity of a single-crystalline ferromagnet is anisotropic.

When a magnetic field is applied to a demagnetized polycrystalline ferromagnet the magnetic moments become aligned. Then, resistivity increases in case it is measured in direction of the magnetic field and decreases in case it is measured in a direction perpendicular to it [74].

2.4.3 Tunneling Magnetoresistance

A trilayered structure consisting of two ferromagnetic metal layers (1) and (2) that are separated by a nonmagnetic tunneling barrier exhibits a dependence of its resistance on whether the directions of magnetization of the two ferromagnetic layers are aligned parallel or antiparallel. The difference is due to the spin-polarized density of states. Assuming the electron spin to be conserved during tunneling, the current through the junction can be split into two spin-polarized currents I_σ with $\sigma \in \{\uparrow, \downarrow\}$, in the sense of the model by Jullière [75]. Here, the arrows denote whether an electron has its spin aligned parallel or antiparallel to the direction of magnetization of electrode (1). In general, electrons tunnel across the barrier in both directions and only a shift in energy of the two Fermi levels by an applied voltage V creates a net current $I_\sigma = I_\sigma^{(1)\to(2)} - I_\sigma^{(2)\to(1)}$. Here, electrode (1) is set to a voltage V with respect to electrode (2). Each current can be expressed in terms of the spin-polarized densities of states of the electrodes, the occupation probability of initial states $f(E)$, and the probability of the target states to be unoccupied $1 - f(E)$, where $f(E)$ is the Fermi function. For the net current, integration over energy yields

$$I_\sigma \propto \int\limits_{-\infty}^{+\infty} D_\sigma^{(1)}(E - eV)\, D_\sigma^{(2)}(E)\, \big(f(E - eV) - f(E)\big)dE. \qquad \text{[2-20]}$$

Assuming the densities of states $D_\sigma^{(i)}(E)$ to be constant, i.e., replacing them by their values at the Fermi level $D_\sigma^{(i)} = D_\sigma^{(i)}(E_F)$, and since the integral over the difference of Fermi functions yields eV, the conductivity of each spin channel is: $\sigma_\sigma \propto D_\sigma^{(1)} D_\sigma^{(2)}$. The total conductivity is the sum of the conductivities of the two spin channels: $\sigma = \sigma_\uparrow + \sigma_\downarrow$. In case the directions of magnetization of the two electrodes are

parallel, it is $\sigma_P \propto D_+^{(1)} D_+^{(2)} + D_-^{(1)} D_-^{(2)}$, where $D_\pm^{(i)}$ denotes the majority/minority spin density of states in electrode (i). For the antiparallel alignment the majority spin of one electrode is the minority spin in the other and, hence, the conductivity is $\sigma_{AP} \propto D_+^{(1)} D_-^{(2)} + D_+^{(1)} D_-^{(2)}$. With the spin polarization of the density of states $P_i = \left(D_+^{(i)} - D_-^{(i)} \right) / \left(D_+^{(i)} + D_-^{(i)} \right)$ the relative change in tunneling conductivity and resistivity $\rho = 1/\sigma$ can be written as

$$\frac{\sigma_P - \sigma_{AP}}{\sigma_P} = \frac{\rho_{AP} - \rho_P}{\rho_{AP}} = \frac{2P_1 P_2}{1 + P_1 P_2}. \qquad [2\text{-}21]$$

The conclusion from this simple model is that the observed change in conductivity is directly related to the spin polarization of the ferromagnetic electrodes. However, the model does not take into account any tunneling barrier properties, i.e., there is no dependence on tunneling barrier height ϕ and thickness s. Barrier properties were first included by Slonczewski [76], who treated the tunneling junction by means of wave functions of electrons that tunnel between two simple spin-polarized parabolic bands, where each band represents one of the ferromagnetic electrodes. The Fermi wave vector for electrons in electrode (i) with spin σ is denoted as $k_\sigma^{(i)}$. The relative angle between the magnetization directions of the two electrodes is θ. While the width s of the tunneling barrier enters via the continuity conditions of the wave functions, its height ϕ is included via the imaginary wave vector within the barrier $\hbar\kappa = \sqrt{2m(\phi - E_F)}$. Slonczewski found for the effective spin polarization of electrode (i) being coupled to the tunneling barrier

$$P_i = \frac{k_+^{(i)} - k_-^{(i)}}{k_+^{(i)} + k_-^{(i)}} \frac{\kappa^2 - k_+^{(i)} k_-^{(i)}}{\kappa^2 + k_+^{(i)} k_-^{(i)}}, \qquad [2\text{-}22]$$

where $k_\sigma^{(i)} \propto D_\sigma^{(i)}$ because of the free electron assumption. Therefore, the first fraction is identical to the result observed by Jullière. It is noteworthy that the sign of the second fraction depends on the height of the tunneling barrier. The conductivity through the tunnel junction is $\sigma = \sigma_0 (1 + P_1 P_2 \cos(\theta))$, where σ_0 is the conductivity of the unmagnetized metal ($P_i = 0$). For further reading, the tunneling magnetoresistance models are well discussed in, e.g., References [77,78].

Besides Jullière, Maekawa & Gäfvert [79] discovered the effect in layered structures. Mentionable tunneling magnetoresistance of several percent in effect at room temperature was first observed by Miyazaki et al. [80] and Moodera et al. [81]. Later, the effect was also discovered in granular structures of spatially isolated ferromagnetic nanoparticles embedded in insulating matrices [13]. A first theory of tunneling magnetoresistance in such granular films was proposed by Inoue & Maekawa [82]. In such

films, the angle θ between the magnetic moments of two isolated nanoparticles are randomly distributed and so are the barrier widths s. However, tunneling preferably happens between pairs of close-up nanoparticles. Another effect arising with insulated metallic particles is Coulomb blocking: A particle carrying a negative net charge is unlikely to get occupied by another electron. After averaging over θ, Inoue & Maekawa find

$$\sigma = \sigma_0(1 + P^2 m^2)e^{-2\sqrt{2\kappa C/k_B T}}, \qquad\qquad [2\text{-}23]$$

where P is the polarization as defined above (as all nanoparticles are made of the same material index i was dropped), κ is the imaginary wave vector defined above, $C = sE_C$ is argued to be a constant, where E_C is the charging energy of one nanoparticle, and $m^2 = \langle\cos(\theta)\rangle$ is the square of the relative magnetization and results from averaging over $\theta \in [0; \pi]$.

The tunneling magnetoresistance is a consequence of the average alignment of the magnetic moments of the nanoparticles. A magnetic field primarily improves the degree of alignment by favoring parallel alignment to the external magnetic field. The magnetoresistance is a result of the lifted magnetic disorder and, thus, correlated to the resulting magnetization.

2.4.4 Giant Magnetoresistance

2.4.4.1 Phenomenology and Theory

When two single-domain ferromagnetic electrodes are separated by a non-ferromagnetic conducting spacer layer the conductance through the resulting trilayered structure depends on whether the ferromagnetic electrodes have their directions of magnetization aligned parallel or antiparallel. Here, the discussion is limited to charge transport in direction of layer alternation (CPP, abbreviation for current perpendicular to plane). Figure 2-3 depicts a trilayered structure with (a) antiparallel alignment of the directions of magnetization of the layers and (b) with parallel alignment. The spacer layers are drawn in gray, the ferromagnetic layers are colored blue and red. Blue means the magnetization points upward with respect to the drawing plane, red means the magnetization points downward, as indicated by the large arrows in the lower right corners of the ferromagnetic layers. Accordingly, the blue electron with spin down is a majority spin electron in the blue ferromagnetic layers but a minority spin electron in the red ferromagnetic layer. Vice versa, the red electron with spin up is a minority spin electron in the blue layers but a majority spin electron in the red layer. The scattering in the ferromagnetic layers is spin dependent. In a hard ferromagnet there are more minority spin states at the Fermi level than majority spin states. Therefore, minority spin electrons are scattered more often than majority spin electrons, as
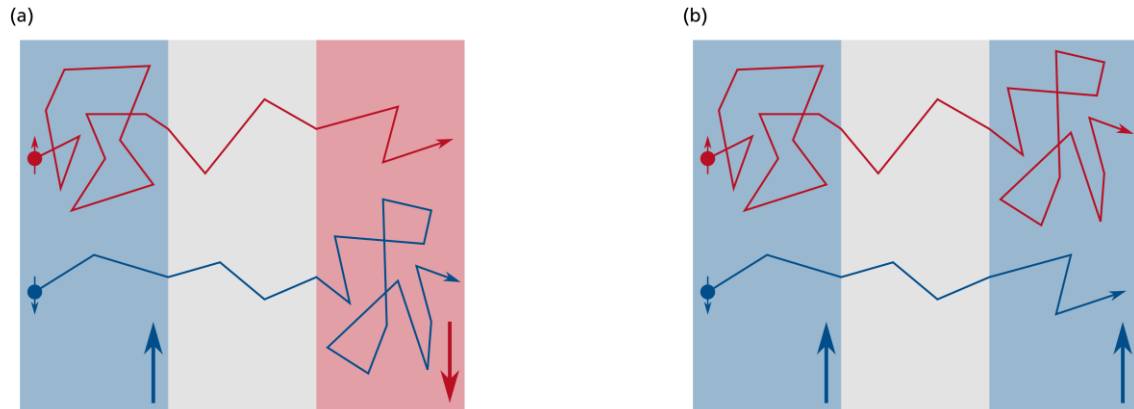
Figure 2-3: Giant Magnetoresistance Effect in a Trilayered Structure in the CPP Orientation

(a) Antiparallel alignment of directions of magnetization.
(b) Parallel alignment of directions of magnetization.

As indicated by the arrow in the lower right corner of each layer the magnetization of a blue ferromagnetic layer points upward and that of a red layer points downward. Because the spin down electron is a majority spin in a blue layer the electron and its trajectory are colored blue. The same holds for the red electron, its trajectory, and the red layer. The non-ferromagnetic spacer layer is colored gray. The trajectories depict that in each layer the minority spin electron scatters at a higher rate than the majority spin electron. This results in a higher resistance in case of antiparallel alignment.

indicated by the schematic electron trajectories indicated in Figure 2-3. This results in a higher resistivity for the minority spin channel. Minority and majority spin channel can be treated as parallel conduction via two independent resistors. Because of the different resistivities of minority and majority channels the total resistivity is lower when the directions of magnetization of the layers are aligned parallel. The base unit for the effect to occur is the trilayered sandwich structure of two ferromagnetic metallic layers with a non-ferromagnetic metallic spacer between them. However, the magnetoresistance increases in magnitude when more spacer/ferromagnet bilayers are added.

The giant magnetoresistance effect was first observed in Fe/Cr tri- and multilayered structures [83,84] in the current-in-plane (CIP) geometry. First models for this effect are presented in References [85,86]. After its discovery, the effect was also observed in the CPP geometry in Co/Ag multilayered structures [87] as well as in granular Co-Cu [14] and Co-Ag structures [15,16]. A general review of the history of the giant magnetoresistance effect is given in Reference [47].

Focusing on the CPP orientation, Valet & Fert [88] developed a model starting from the linearized Boltzmann equation under the assumption that the spin diffusion length l_{sf} is much larger than the electron mean free paths λ_σ. Assume, the three basic layers are parallel to the xy-plane and the current crosses through the layers along the z-direction. For simplicity, the ferromagnetic and the non-ferromagnetic conductors are assumed to each have a single parabolic conduction band with the

same effective electron mass m^* and Fermi velocity v_F. According to Valet & Fert, the basic principle of the effect is that the spin-asymmetry $\beta = (\rho_- - \rho_+)/(\rho_- + \rho_+)$ in a ferromagnetic layer needs to adapt to the one in the non-ferromagnetic layer, namely to zero. Let $\pm$ denote majority and minority spin, respectively. Further, $\rho_\sigma = 1/\sigma_\sigma$ is the spin-polarized resistivity in the ferromagnet. In a strong ferromagnet the density of states at the Fermi level is higher for minority spin electrons. Therefore, their mean free path is shorter and, consequently, the resistivity of the minority spin channel is higher.

In a junction of two semi-infinite electrodes the spin-asymmetry adjusts within a zone defined by the average spin diffusion length $l_{sf} = \left(l_\uparrow^2 + l_\downarrow^2\right)^{1/2}$. The $l_\sigma = \left(1/3\, v_F \lambda_\sigma \tau_{sf}\right)^{1/2}$ are the spin-polarized diffusion lengths with the spin-polarized electron mean free paths $\lambda_\sigma = v_F(1/\tau_\sigma + 1/\tau_{sf})$ and the scattering rates for spin-conserving and spin-flipping scattering events $1/\tau_{\sigma,sf}$, respectively. Within a distance l_{sf} away from the interface the spin polarization decreases by $1/e$ into both directions. In this region around the interface spin-flip scattering events progressively change the spin polarization of the total current.

The required adjustment of spin polarization leads to a spin accumulation on both sides of the interface. The accumulation, in turn, alters the electro-chemical potential and the alteration of the chemical potential leads to a voltage drop across the interface. Hence, the interface can be assigned an area resistance r_{SI}, independent of interface scattering. In a trilayered structure, and generally in multilayered structures, the interface resistance depends on whether two separated ferromagnetic layers are magnetized into the same direction or into opposite directions. Because majority spin electrons have to be decimated in the antiparallel configuration such that they adapt to the minority spin concentration in the counter-ferromagnet, much more adjustment by scattering has to be performed in the antiparallel configuration. Therefore, it is $r_{SI}^{AP} > r_{SI}^P$. The area resistance adds to the material resistances $\rho_F t_F$ and $\rho_N t_N$ for the ferromagnet and non-ferromagnetic layers, respectively, and to a resistance related to electron scattering by the interface. $\rho_{F,N}$ and $t_{F,N}$ denote the resistivity and the thickness of the ferromagnetic and the non-ferromagnetic layers, respectively. Taking the antiparallel alignment as the one to which a multilayered system returns when an applied magnetic field is switched off again, the relative change of the total resistance compared to antiparallel alignment $(r - r^{AP})/r^{AP}$ is the giant magnetoresistance. It is maximum negative when $r = r^P$. In the limit $t_{F,N} \ll l_{sf}$, the resistance of a multilayered structure reduces to that of two parallel spin-polarized currents $I_{tot} = I_\uparrow + I_\downarrow$, namely, $(r^{P,AP})^{-1} = \left(r_\uparrow^{P,AP}\right)^{-1} + \left(r_\downarrow^{P,AP}\right)^{-1}$. The Valet-Fert model is extended in Reference [89] and reviewed in, e.g., Reference [90].

In the CPP orientation, electrons subsequently pass through all the layers in order to pass through the structure, i.e., the electrons always sample all the layers. This is the key difference in comparison

with the CIP orientation. In the latter case, the electron mean free path has to exceed the thicknesses of the non-ferromagnetic layers. This relation is mandatory because an electron has to sample at least two ferromagnetic layers that can change their relative magnetic orientation in order for giant magnetoresistance to appear [91].

2.4.4.2 Interface Exchange Coupling

There are several possibilities for the creation of giant magnetoresistance elements in which the directions of magnetization of the ferromagnetic layers relative to each other can be switched by an external magnetic field. The use of different ferromagnetic materials and, thus, different coercivities is one approach. Another option regarding the trilayered structure only is to pin the magnetization of one ferromagnetic electrode by exchange coupling it with an adjacent antiferromagnetic layer, while the other one remains 'free'. In both cases, a sufficiently small magnetic field switches the easy (free) layers only while the harder (exchange-coupled) layers keep their direction of magnetization.

The giant magnetoresistance effect was discovered first in multilayered structures. There, the mechanism by which the antiparallel alignment of the films was achieved was a quantum mechanical effect called interlayer exchange coupling. The coupling strength of the effect was found to oscillate with the non-ferromagnetic spacer layer thickness t_N. The period is about 1 nm for all transition metals, except for Cr, where it is almost 2 nm [92–94]. The effect is related to RKKY indirect exchange [95–97], however, the period for RKKY interaction is much shorter, i.e., about 1 to 3 atomic layers. In fact, Unguris et al. [93] found a superposition of a long-period and a short-period coupling in an extremely well ordered Fe/Cr/Fe trilayered sample. The reason for this behavior is found in the origin of interface exchange coupling as described in the next paragraph [98–100].

When a parallel alignment of the two ferromagnetic layers is assumed, good agreement between the densities of states of the majority spin electrons of both sides is achieved. This is because both the ferromagnetic layers, which are assumed to be made of a strong ferromagnet, and the metallic spacer metal only have s-like majority spin electrons at the Fermi level. In the ferromagnetic layers, the minority spin electrons are intermixed with d-like electrons. Therefore, minority spin electrons experience higher potential steps at the ferromagnet/spacer interfaces than majority spin electrons and are reflected by the interface with a higher probability. The incoming, reflected, and re-reflected minority spin electrons interfere and standing-wave states form within the spacer layer. Similarly to electrons in a 1D potential well, here, discrete quantum well states exist for wave vectors $k_\perp^{(n)} = n\pi/t_N$ in the non-ferromagnetic spacer, where $n \in \mathbb{N}$ and $k_\perp^{(n)}$ is the wave vector component in the direction perpendicular to the interface. As the corresponding energy levels of the quantum well $E_n = \left(\hbar k_\perp^{(n)}\right)^2/2m^*$, where m^* is the

effective electron mass, vary with the spacer layer thickness t_N, the lowest unoccupied state of the well is populated as soon as its energy is lowered down to the Fermi level E_F at a certain spacer layer thickness. When parallel coupling of the ferromagnetic layers is energetically preferred over antiparallel coupling because of this quantum well effect the layers align parallel. In case the effect results in a higher energy, the layers align antiparallel. The formation of a quantum well is not possible in the antiparallel case since a minority spin electron needs to be reflected by both interfaces the spacer layer forms with the neighboring ferromagnetic layers. As explained above, the quantum well energy states vary with the spacer layer thickness. Therefore, the states are occupied in steps. Hence, the alignment oscillates in order to keep the energy of the structure as low as possible.

In real metals, oscillatory coupling is related to critical spanning vectors Q_i across the Fermi surface of the spacer layer material. A critical spanning vector possesses the following properties: It "… points perpendicular to the [ferromagnet/spacer] interface; … connects two sheets of the Fermi surface, which are coplanar to each other; and … is in the first Brillouin zone." [98] Since several of these wave vectors can exist, the coupling of the ferromagnetic layers varies as the superposition of several oscillations, each with a period $2\pi/Q_i$ corresponding to a different critical spanning vector. Moreover, the spacer layer thickness can only be increased or decreased in steps of atomic layer thicknesses. This leads to an aliasing effect in the real oscillatory behavior.

2.4.4.3 Giant Magnetoresistance in Granular Materials

According to Ferrari et al. [101] the phenomenology of giant magnetoresistance in granular films of magnetic particles embedded in nonmagnetic matrices is quite similar to that of giant magnetoresistance in CPP-oriented multilayered structures in case the resistivity of the granules is much smaller than the resistivity of the matrix. In the opposite case, the current tends to bypass the granules. Then, given that the mean free path of the electrons, the distances between the granules, and the size of the granules are on the same order, the situation is similar to giant magnetoresistance of CIP-oriented multilayered structures.

Zhang & Levy applied the formalism already used to model CIP and CPP giant magnetoresistance in multilayered structures [86,91,102] to granular films in a similar way [103,104]. Moreover, the authors published a general formalism for "Electron transport in magnetic inhomogeneous media" in Reference [105]. Following the formalism of CPP giant magnetoresistance in multilayered structures, Zhang & Levy present a model for granular materials, which is characterized by the following parameters. Spin-independent scattering both at the surface and in the bulk of a magnetic granule in the matrix are governed each by a corresponding mean free path. Spin-dependent scattering is accounted for by spin-dependent mean free paths, which are each related to their spin-independent instances by

dependent-to-independent ratio parameters. Last, scattering in the matrix is always spin independent and, accordingly, accounted for by a fifth mean free path. However, the distribution of magnetic and nonmagnetic material can no longer be characterized by the two well-defined layer thicknesses as in multilayered structures. Instead, the distribution of ferromagnetic and non-ferromagnetic constituents is now random and, therefore, characterized by the concentration of granules in the matrix and a size distribution function for the magnetic granules. The distribution function is the analog of the layer thicknesses in multilayered structures. In a subsequent publication, Ferrari et al. [101] confirm from the analysis of their model that the equations observed by Zhang & Levy represent the CPP limit of giant magnetoresistance in granular materials.

Besides other authors, Zhang & Levy deduce the following properties of giant magnetoresistance in granular films from their model [104]. The magnetoresistance increases with increasing spin-dependent to spin-independent scattering ratios and with increasing quality of the matrix, i.e., with increasing mean free path, as a consequence of a lower impurity concentration in the matrix. The magnetoresistance increases also when the spin-dependent scattering at the surfaces intensifies, i.e., when the corresponding mean free path decreases. When the granules are superparamagnetic, i.e., very small in size, the ratios of spin-dependent to spin-independent surface and bulk scattering are greatly reduced, which leads to a smaller magnetoresistance.

The magnetoresistance increases with increasing concentration of magnetic granules, and is larger for smaller granules in case the applied magnetic field is strong enough to saturate the magnetization. This is not the case for superparamagnetic granules: When the granules are small enough to exhibit superparamagnetic properties, the magnetoresistance decreases instead.

Zhang & Levy claim that a broad distribution of granule sizes reflects the nature of real granular films best. In particular, deviations from a $\Delta\rho/\rho_0 \propto M^2$ dependence, M is the total magnetization, which is obtained for isolated, identical, spherical granules appears "… because the contribution to the magnetoresistance from aligning smaller granules is larger while their contribution to the total magnetization is small." [104] Interaction between the magnetic granules can cause deviations from the parabolic dependence as well [106]. Another, more general model that takes into account short-range particle interaction in form of a correlation angle of the magnetic moments of nearest neighbor granules is presented in Reference [107].

3 Review of the Cluster Ion Beam Deposition System

For the aggregation and (co-)deposition of cluster-based nanocomposites the cluster ion beam deposition (CIBD) system described in References [5–7] was used. The system was designed and constructed by Dr. Arne Fischer as part of his PhD thesis [5] in the group of Prof. Horst Hahn. In this chapter, the CIBD system is reviewed in the state as it was employed to synthesize the Fe-Ge and Fe-Ag nanocomposite films of the present work. A CAD drawing [5] of the CIBD system is presented in Figure 3-1.
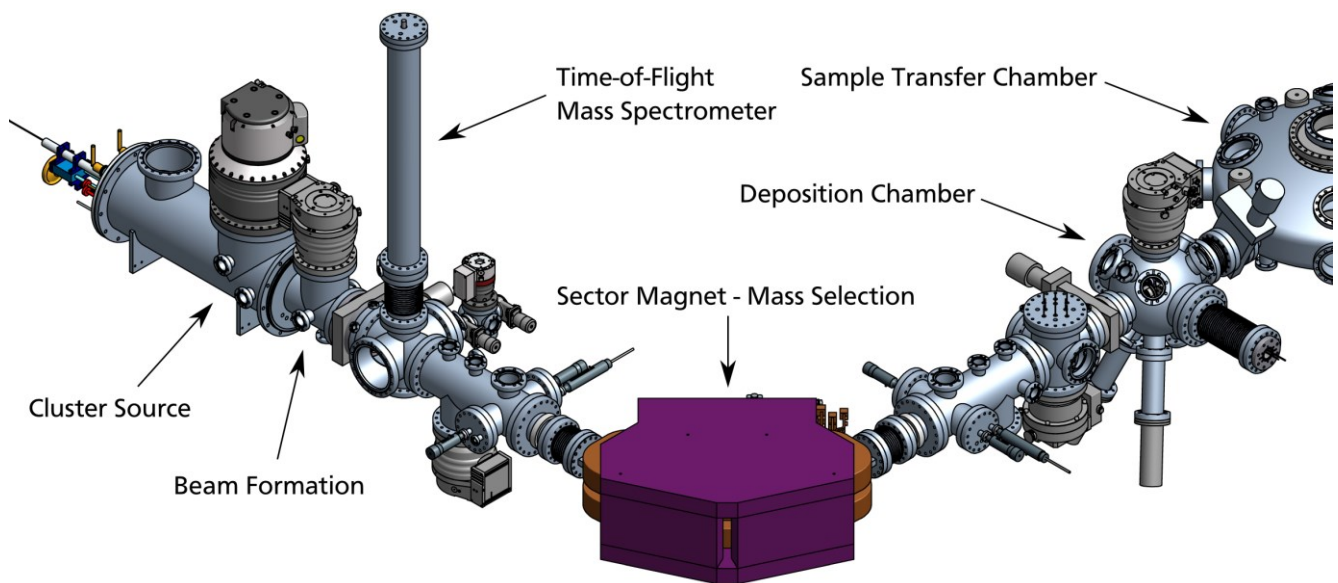
Figure 3-1: CAD Drawing of the Used CIBD System

The clusters aggregate within the cluster source located at the left side of the image. A subsequent skimmer and electrostatic lens system forms a cluster ion beam from the negatively charged output of the cluster source. Right behind this section, a time-of-flight mass spectrometer is installed. However, this spectrometer was not used in case of the present thesis. Subsequently, a 90° sector magnet is installed, working as a mass selector element on the cluster ion beam. After passing the sector magnet, the size-selected ion beam is deposited onto the sample installed inside the spherical deposition chamber on the right side of the image. The UFO-like shaped chamber on the very right side is used to transfer samples between a load lock (not shown) and the deposition chamber. The CAD drawing originates from the pool of images, i.e., was rendered from the CAD model, available to scientists working with the system. In particular, the image was also used in Reference [5]. In the present case, it was modified by adding the labels.

Following the highlighted components from the left-hand to the right-hand side of the graph, the major components of the system are described in brief as follows. In the cluster source clusters aggregate from magnetron sputtered material in an inert gas atmosphere. The source is described in detail in Section 3.1. Right after the cluster source two skimmer stages and a system of electrostatic lenses form a beam of cluster ions from the output of the source. At this location, also a time-of-flight mass spectrometer is installed. However, this component was not used in the course of the present thesis. Subsequent to the beam formation, cluster ions of desired size are selected from the beam with the help of a sector magnet. Together, beam formation, mass selection, and cluster ion beam guidance through the system form the cluster ion beam optics, which is explained in more detail Section 3.2. The beam of size-selected cluster ions is deposited onto a sample located inside the deposition chamber. Two additional sources are attached to the deposition chamber and serve as co-deposition sources: an effusion cell and a triple electron beam evaporator. In the course of the present work the effusion cell was used to provide the matrix material for the synthesized nanocomposites. Details about the deposition chamber are given in Section 3.3. On the back side, a sample transfer chamber is connected to the deposition chamber. With the help of the manipulator arm installed inside this transfer chamber, CIBD samples can be transferred between the deposition chamber and a separately pumped load lock (not shown).

To test the capabilities of the newly constructed system, Dr. Fischer prepared nanocomposite films of Fe clusters of 1000 atoms embedded in Ag matrices in order to study the magnetic interaction between the clusters [5]. Moreover, Dr. Fischer examined the magnetic coupling of the Fe clusters via exchange interaction by embedding them in antiferromagnetic Cr matrices [5,6]. To examine the influence of the size of the clusters on the magnetic properties Dr. Fisher synthesized Fe-Cr films containing Fe clusters with either 500, 1000 or 2000 atoms. Besides these two cluster-assembled nanocomposites also purely cluster-composed FeSc films were deposited [5], however, with a not size-selected cluster ion beam and at an alternative deposition stage in front of the sector magnet. Dr. Fischer only studied the magnetic properties of the deposited films.

In the present work, samples of cluster-assembled Fe-Ge nanocomposites containing either clusters with 500 ± 50 or 1000 ± 100 Fe atoms were synthesized. In addition, Fe-Ag nanocomposites containing 500 ± 50, 1000 ± 100, or 1500 ± 150 Fe atoms were prepared. Henceforth, the clusters belonging to these ranges of size are referred to as Fe_{500}, Fe_{1000}, and Fe_{1500}, respectively.

3.1 Cluster Source

The cluster ion beam of the CIBD system is generated using of a Haberland-type cluster source [108,109], which combines magnetron sputtering with inert gas condensation. The parameters of the source can be optimized in order for the source to have maximum output at the desired cluster size. A cross-sectional schematic drawing of the source of the CIBD system is presented in Figure 3-2.
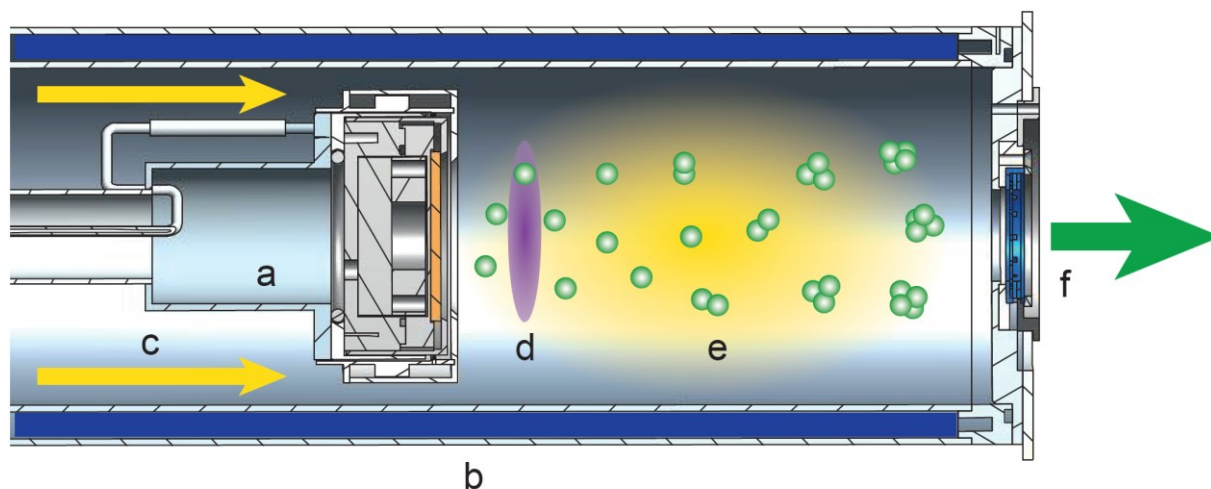
Figure 3-2: Cross-Sectional View of the Cluster Aggregation Tube of the Cluster Source

The magnetron sputter head (a) carrying the target (orange colored disk) is contained in a LN$_2$ cooled aggregation tube (b). A mixture of He and Ar gas is showered directly onto the target feeding the plasma discharge (d). The option to let carrier gas also enter from the back side of the sputter head (c) was not used. After the plasma region the cluster aggregate (e) on their way to the iris (f). Here, a supersonic expansion terminates the aggregation process. The drawing originates from the pool of images available to scientists working with the CIBD system; it is also used in Reference [5].

The depicted elements are as follows. The 2″ target of the desired metal is mounted onto a magnetron sputter head (a) inside the aggregation tube (b). The walls of the aggregation tube are cooled by a constant flow of liquid nitrogen (LN$_2$) to a temperature of about 100 K. A mixture of Ar and He gas (both Air Liquide, N6 Purity) is used as sputter gas and fed into the aggregation tube with the use of two mass flow controllers (MFCs) through a shower head right in front of the sputter target. He gas is used to dilute the Ar gas in the subsequent cluster aggregation step. Additionally, carrier gas can also be delivered from the back side of the sputter head as indicated by the yellow arrows (c), however, this option was not used in the present case. Behind the region of plasma discharge, illustrated by the purple disk (d), atoms and aggregates of target material are cooled by transfer of thermal energy when colliding

with cold carrier gas atoms (e). Cluster generation with the above cluster source is limited to well-conducting materials as otherwise the ion optics would become contaminated too quickly.

Keeping the aggregation tube and the carrier gas mixture at low temperatures by cooling with LN_2 is crucial for cluster growth. For continuous cluster growth (see, e.g., References [110,111] for classical nucleation theory) the increase in thermal energy a cluster experiences during aggregation needs to dissipate, and this happens in collisions with cold carrier gas atoms. When the process of heat dissipation is too slow the hot cluster can fragment again. The rate of collisions and the average amount of thermal energy taken off a growing cluster depends on the ratio of cooling-efficient Ar atoms to diluting He atoms.

Since free electrons and ionized particles are widely present in the region the growth of clusters happens, charge transfer processes during collisions are very likely. For this reason, a large fraction of clusters carries a net charge after aggregation [108,112,113]. However, clusters remain either singly charged or neutral. Doubly charged clusters, which could be identified by a second peak in the mass distribution, were never observed in earlier cluster ion beam experiments according to Reference [5].

The cluster growth stops at the front face of the aggregation tube where the mixture of carrier gases and target material clusters and atoms undergoes a supersonic expansion from a pressure in the millibar range within the aggregation tube to medium vacuum (10^{-1} mbar to 10^{-2} mbar) through an iris (f). The iris is adjustable in diameter from 1 mm to 15 mm. It is the diameter of the iris that determines the pressure that establishes within the aggregation tube under the applied carrier gas flow. The interplay of carrier gas flow, He/Ar ratio, source temperature, sputter power, gas pressure inside the aggregation tube, and aggregation length determines the size distribution of clusters leaving the cluster source. Typically, the size distribution of particles created in an inert gas condensation process follows a log-normal distribution [114].

The size distributions for different sets of source parameters can be measured by scanning the magnetic field of the sector magnet while recording the current of cluster ions passing through the sector magnet. Three mass spectra belonging to different sets of parameters are plotted in Figure 3-4(a). The kinetic energy of a cluster is about 5 eV after aggregation and gas expansion [5,7]. The aggregation tube is settled on ground potential because of technical reasons.

3.2 Cluster Ion Beam Optics

After their formation in the aggregation tube the clusters pass through the iris and stream into a continuously pumped cavity. Starting from here, the cluster ions are guided through the CIBD system all the way to the deposition stage. For this purpose, an ion-optical setup, consisting of several electrostatic lens sets and cage-like shielding tubes, is installed inside the CIBD system. The ion-optical setup is described in this section. A sketch focusing on the ion optics and the subsequent co-deposition is given in Figure 3-3. There, the aggregation tube discussed in the previous section is referred to as element (a). The beam of cluster ions is illustrated in cyan.

To manipulate and size-select a cluster, i.e., to change its state of motion, a cluster has to carry a net charge when leaving the aggregation tube. In the present work, the cluster ion beam is formed of negatively charged clusters. These are dragged into the 1st skimmer (b) by the applied small, positive electric potential, while the positively charged clusters are repelled. The 1st skimmer, with a circular opening of 8 mm in diameter, is located at a distance of about 35 mm behind the iris of the aggregation tube. Subsequently, a 2nd skimmer and a series of cylindrical electrostatic lenses (c) complete the acceleration lens set. This lens set is used to collimate the cluster ion beam while the cluster ions are accelerated to the beam potential U_{beam}. In general, U_{beam} is set to a voltage between 200 V and 800 V. The cluster ions are accelerated and collimated within 36 cm measured from the iris.

The two-stage skimmer section is also used as a two-stage pumping section in which most of the carrier gas and leftover clusters are removed from the system. Behind the pumping stages the vacuum is better than 10^{-5} mbar. The largest amount of gas load coming from the source is removed by a turbomolecular pump with a pumping speed of 1900 l/s installed on top of the source chamber between iris and 1st skimmer.

From the 2nd acceleration lens set on, the cluster ions propagate inside a cylindrical electrostatic cage-like tube coaxial to the ideal beam path. It shields the cluster ions from ground potential and maintains their enhanced kinetic energy (not included in the sketch).

Mass selection of the cluster ions is implemented with a sector magnet (f) (Danfysik, custom design), which can apply a magnetic field of up to 1.4 T normal to the beam plane. The magnetic field needs to point out of the drawing plane in order to bend the beam of negatively charged cluster ions towards the right side of the drawing. The sector magnet has a nominal bending angle of 90° and a nominal radius of 500 mm. At a maximum kinetic energy of 1 keV and with maximum magnetic field applied Fe clusters need to consist of 423 Fe atoms to pass through the sector magnet. This is the smallest Fe cluster size that can technically be selected by the system.
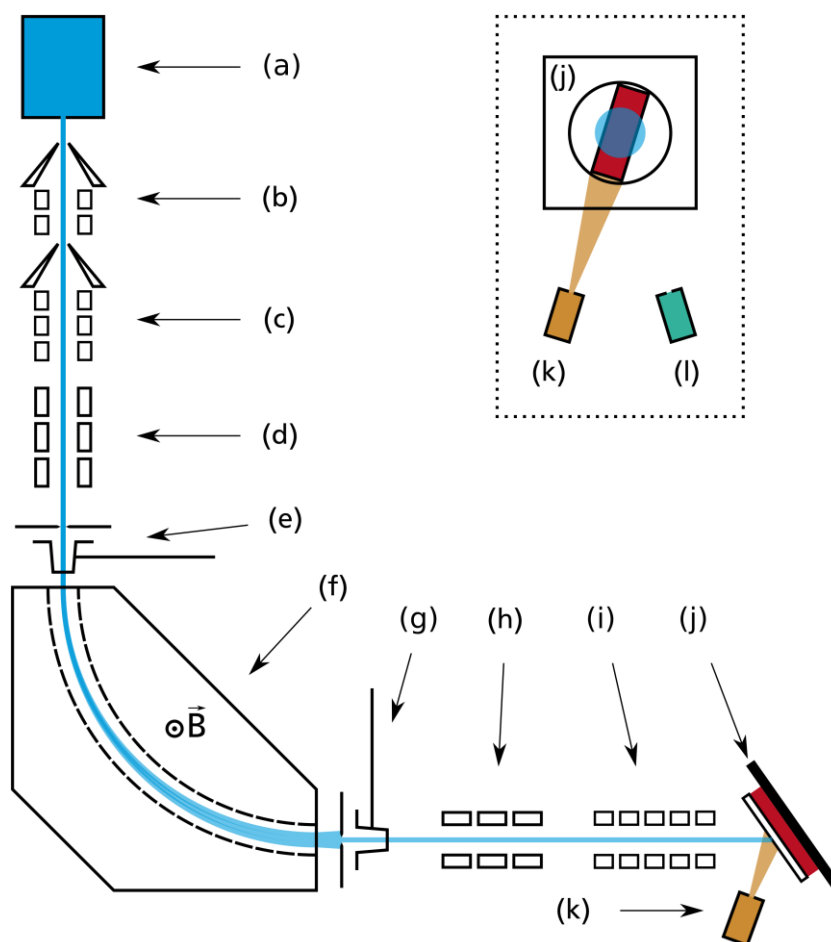
Figure 3-3: Sketch of the CIBD System with the Focus on Ion Optics and Co-deposition

(a) Haberland-type inert gas condensation cluster ion beam source, (b) 1st skimmer and 1st acceleration lens set, (c) 2nd skimmer and 2nd acceleration lens set, (d) 1st quadrupole triplet, (e) 1st slit and 1st Faraday cup, (f) 90° sector magnet, (g) 2nd slit and 2nd Faraday cup, (h) 2nd quadrupole triplet, (i) deceleration lens set, (j) co-deposition sample (simplified), (k) effusion cell, and (l) triple electron beam evaporator. Another Faraday cup can be moved into the beam at the position of the sample (not shown). The effusion cell and the triple electron beam evaporator are discussed separately in Section 3.3 in the context of Figure 3-6. The magnetic field in the sector magnet points out of the drawing plane in order to bend the beam of negatively charged cluster ions (cyan) into the direction illustrated in the sketch.

At each side of the sector magnet a quadrupole electrostatic lens triplet (d) and (h) is used to align the beam of cluster ions to the magnet. The one in front optimizes the beam for optimal transmission, while the exit side one collimates the size-selected beam behind the sector magnet. Two adjustable vertical slits, one in front of the sector magnet (e) and one at its back side (g), assure only cluster ions following the nominal path and some with minor deviations from it can pass through the selection unit. The slits are formed by two stainless steel plates with sharp and straight edges pointing towards each other. The opening of the front side slit was 9.1 mm, that of the back side one was 10.0 mm.

The cluster ion beam potential U_{beam} is chosen to have the highest possible value so that the sector magnet transmits the desired cluster ion size at maximum magnetic field. This way, the highest possible mass resolution is achieved, which results in an error of less than 10% of the nominal cluster size [5,7]. Two size distributions of samples prepared with the CIBD system are shown in Figure 4-2(c).

Finally, the cluster ion beam is decelerated by another set of lenses (i) to the desired deposition energy. This way, the cluster ions can be deposited in a soft-landing regime or with high impact energy. The deceleration lens set also offers the option to deflect and to (de-)focus the ion beam. The sample (j), here sketched in a simplified way, and the co-deposition sources (k) and (l) are discussed in Sections 3.3 and 4.2.2 in the contexts of Figures 3-6 and 4-5, respectively. The total propagation length of the cluster ions from cluster source to sample deposition is about 4 m.

The flux of the cluster ions corresponds to a current ranging from a few picoamperes to tens of nanoamperes. To monitor this current, Faraday cups with integrated retarding grids can be moved into the beam path at three locations between cluster source and deposition chamber: behind the entrance slit of the magnet (e), right after the exit slit of the magnet (g), and at the sample position (j). While the 1st Faraday cup is only used for a rough tuning of the parameters of cluster source and ion optics, the 2nd and the 3rd Faraday cup can be used to analyze the cluster size distribution by recording the cluster ion current as a function of the magnetic field in the sector magnet. To record such mass spectra, the current driving the magnetic field is ramped from zero to maximum (150 A). From the set beam potential U_{beam} and the atomic mass of the installed target material the nominal number of atoms per cluster can be calculated as a function of the applied magnetic field. Since the intensity and size distribution of the ion beam depends on the entire set of parameters applied to components upstream of the recording Faraday cup, mass spectra are an indispensable tool for finding the best parameter set with which the yield of clusters of the desired size is maximized. Equipped with a retarding grid, the Faraday cups can also be used to analyze the distribution of kinetic energy of the cluster ions in the beam. The Faraday cup installed inside the pulsed laser – buffer gas condensation (PL-BGC) setup that is reviewed later in Chapter 6 is based on the layout of the ones used in the CIBD system.

Representative parameters of the cluster source as well as parameters important for the size selection by the sector magnet are summarized in Table 3-1 for Fe_{500}, Fe_{1000} and Fe_{1500} clusters together with typical cluster ion currents. The total current of the not size-selected cluster ion beam can be measured with the 1st Faraday cup and is roughly -2 nA. Corresponding mass spectra are plotted in Figure 3-4(a). The distributions of numbers of atoms per cluster follow log-normal distributions in good approximation, as expected for inert gas condensation processes [114]. A log-normal distribution fitted to the distribution optimized for Fe_{500} clusters (green) is added to the plot (dashed line). An exemplary energy scan of the tabulated Fe_{1000} cluster ion beam is presented in Figure 3-4(b).
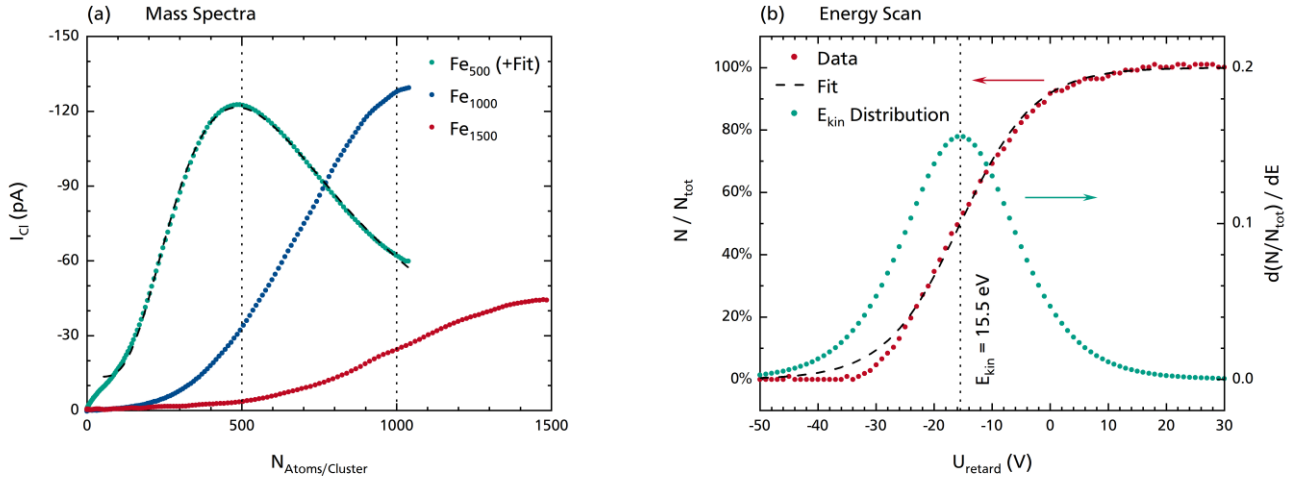
Figure 3-4: Example Mass Spectra and a Representative Cluster Ion Beam Energy Scan

(a) Mass spectra for an Fe_{500}, Fe_{1000} and Fe_{1500} parameter set. See Table 3-1 for used parameter sets.

(b) Energy scan of an Fe_{1000} size-selected cluster ion beam.

Table 3-1: Representative Parameter Sets for Fe_{500}, Fe_{1000}, and Fe_{1500} Clusters

Ar and He carrier gas flow, pressure in the aggregation tube, beam potential, sector magnet field, and total beam current and cluster ion current recorded on the sample.

Parameters Cluster	Ar / He (sccm)	p_{AT} (mbar)	$P_{Sputter}$ (W)	U_{beam} (V)	B (T)	I_{TBC} (pA)	I_{Cl} (pA)
Fe_{500}	100/300	2.3	45	+400	0.97	−165	−120
Fe_{1000}	125/110	1.9	70	+400	1.36	−202	−130
Fe_{1500}	95/10	1.6	75	+280	1.40	−123	−45

There is a trade-off between the slit widths, the intensity of the size-selected cluster ion beam, and the size distribution of the cluster ions in the size-selected beam. When smaller slit widths are chosen, a larger part of the cluster ion beam is sorted out, and the intensity of the size-selected beam decreases.

In the following, the principle of size-selection is explained in the simplified way illustrated in Figure 3-5. The sketch shows the entrance opening of the sector magnet and the slit aperture located in front of it. Note that the sector magnet describes an arch of 90° in total and that another slit aperture is installed at its back side. For calculations, the slits are assumed to have equal opening widths. In case the openings of both slits are chosen infinitesimally small, only the nominal cluster trajectory, which is the dashed center line in the sketch, is the one that leads towards the infinitesimal opening of the back side slit and, hence, to transmission. The radius of this arc trajectory is equal to the nominal radius r_0 of the sector magnet. At a kinetic energy K_0 of these cluster ions, the nominal mass of the transmitted, i.e., selected, cluster ions is $m_0 = (eBr_0)^2/2K_0$.
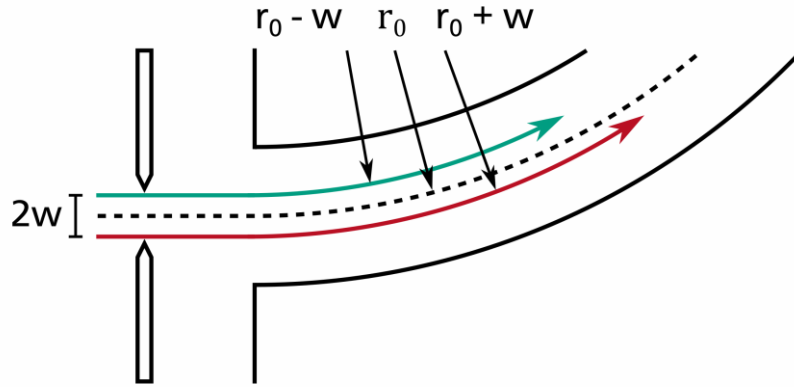
Figure 3-5: Sketch of Beam Trajectories with Maximum and Minimum Radius

The sketch depicts the entrance of the sector magnet and the slit located in front of it. Its opening is $2w$ wide and so is the one located at the back side of the sector magnet. When the slit width is infinitesimally small the nominal path is the only one that leads to a positive selection, i.e., only cluster ions following this path pass through the back side slit. When the slit is opened to a finite width, then, the inner (outer) edge allows for a trajectory with the smallest (largest) possible radius of bending. The corresponding trajectory is illustrated in green (red).

Now, assume the slits are opened to a finite width $2w$ and assume all cluster ions propagate with the same kinetic energy K_0. Further, the cluster ions are assumed to pass through the front side slit, towards and away from the sector magnet, and through the back side slit on paths parallel to the nominal trajectory. Then, the largest (smallest) radius that leads to transmission is $r_\pm = r_0 \pm w$, namely, when the arc trajectory is concentric to the nominal one. The corresponding trajectory is drawn in red (green) in the Figure 3-5. The corresponding cluster ion masses are $m_\pm^{slit} = \left(eB(r_0 \pm w)\right)^2/2K_0 \approx m_0(1 \pm \gamma_{slit})$ with $\gamma_{slit} = 2w/r_0$. Inserting $2w = 10$ mm and $r_0 = 500$ mm yields $\gamma_{slit} \approx 2\%$.

However, the kinetic energy K of the cluster ions is a quantity that obeys Gaussian statistics, as can be seen in Figure 3-4(b). This leads to a finite width of the distribution of cluster ion masses even when the slit openings are reduced to a minimum. The maximum (minimum) kinetic energy be $K_\pm = K_0 \pm \delta K$. They correspond to the following cluster ion masses to be selected: $m_\pm^{kin} = (eBr_0)^2/2(K_0 \pm \delta K)$. These can be approximated as $m_\pm^{kin} \approx m_0(1 \mp \gamma_{kin})$. With $K_0 = eU_{beam} + 15.5$ eV and $\delta K = 25$ eV, according to the kinetic energy scan plotted in Figure 3-4(b), one observes $\gamma_{kin} = 6\%$.

Both effects happen simultaneously during size selection, hence, the estimated maximum errors add: $\Delta m = m_0(\gamma_{slit} + \gamma_{kin})$. Furthermore, the cluster ions can also enter the sector magnet on inclined trajectories, i.e., on trajectories with arc angles slightly larger or smaller than 90°. The 2nd quadrupole triplet is installed for the very reason to again collimate the cluster ions transmitted following such inclined trajectories onto trajectories parallel to the nominal beam path.

3.3 Deposition Chamber

As can be seen in the CAD drawing of the CIBD system in Figure 3-1, the deposition chamber is of spherical shape. Let the center of the chamber be the origin of a coordinate system, let the beam plane of the cluster ions be the xy-plane, and let the beam enter the deposition chamber into the x-direction of this coordinate system. The directions of the coordinate axes resulting from this definition are visualized in Figures 3-6(a),(b). Sketch (a) of the figure shows a co-deposition sample (j) and the two sources (k), (l) located inside the deposition chamber, where the indices (j)–(l) correspond to those used in Figure 3-3. The view of sketch (a) is in direction of the cluster ion beam (cyan), i.e., the x-direction. Sketch (b) shows the same elements, now with the view directed towards the y-direction, and sketch (c) depicts a sample inserted into the sample pocket of the sample arm of the deposition chamber with the view directed towards the normal direction of the pocket shielding (green).

The two sources located inside the deposition chamber, an effusion cell (k) and a triple electron beam evaporator (l), can be used for simultaneous (co-)deposition with the cluster ion beam (cyan) on the one hand, but can also be used to deposit functional layers such as adhesion or capping layers on the other. Effusion cell and triple electron beam evaporator take an angle of 17° to the reverse direction of the z-axis in the yz-plane and of 20° in the xz-plane, as indicated in Figures 3-6(a),(b), respectively.

Inside the effusion cell (k) (CreaTec Fischer & Co. HTC), material is thermally evaporated via Ohmic heating of a coiled heating element. Since this technique provides a well-tunable and highly stable beam of atoms the effusion cell was used for the deposition of matrix materials in the present work. The output flux of matrix material is recorded by means of a quartz crystal balance. The layer thicknesses recorded by the crystal balance were calibrated via reference sample films, whose real thicknesses and densities were determined via X-ray reflectometry (XRR) measurements. The effusion cell may have also released charged particles, especially electrons. For this reason, a stainless steel sheet electrode installed half-way between the effusion cell and the sample arm, see Figure 3-6(b), was set to a constant potential of $-385\,\text{V}$. A cutout in the sheet allowed the uncharged output from the effusion cell to pass the electrode, while charged particles were deflected or absorbed by the sheet. This measure did not influence the deposition of the cluster ions.

The triple electron beam evaporator (Focus EFM 3T) provides three independent evaporation pockets. Besides a target rod, crucible or wire, each pocket is equipped with a filament and an ion flux meter. The ion flux meters each indicate the current of target ions impinging onto a cylindrical detector sheet mounted at the exit aperture of a pocket. This way, the output from a pocket can be related to a deposition rate. In the present work, the triple electron beam evaporator is used to deposit layers of
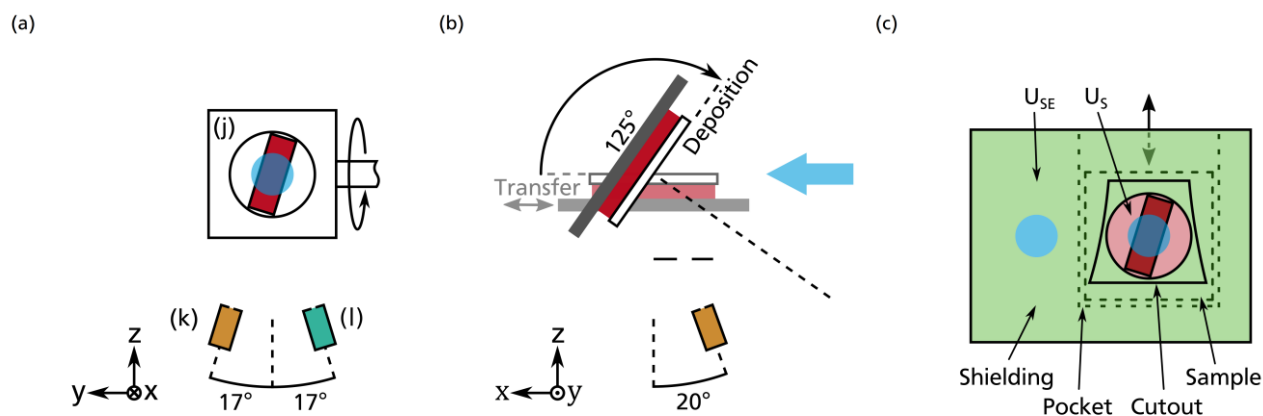
Figure 3-6: Sketches of the Sample in the Deposition Chamber

(a) Effusion cell (k) and triple electron beam evaporator (l) are each installed under an angle of 17° to the reverse direction of the z-axis in the yz-plane. The sample (j) can be translated into all directions (not shown) and rotated around the axis of the sample arm, which reaches into the chamber into positive y-direction. The cluster ion beam (cyan) is directed to the x-direction, i.e., into the drawing plane, where the beam plane of the CIBD system is the xy-plane of the shown coordinate system. The setup of the sample is discussed in Section 4.2.2.

(b) Seen from the side, the two sources take an angle of 20° to the reverse direction of the z-axis. For this reason, the sample was rotated by 125° after loading so that it is oriented half-way between the cluster ion beam and the flux of evaporated material from the effusion cell during deposition. A deflection electrode shields the sample from charged particles coming from the effusion cell.

(c) The sample pocket of the sample arm (outer dashed line) and the region around it are shielded by a stainless steel electrode. A cutout in this sheet allows to deposit clusters and materials from the two other sources onto the slid in sample. The shielding electrode and outer parts of the sample are insulated from ground potential and the rest of the sample (green area). The rest of the sample (red area) is also insulated from ground so that a potential can be applied. Since the shielding was used to monitor the cluster ion beam the beam had to be deflected fully onto the electrode to measure the total cluster beam (left cluster spot). During deposition only the current of cluster ions missing the red sample potential was measured.

different materials, namely, capping layers in case of Ge matrix samples and adhesion layers in case of Ag matrix samples. Before usage, the ion flux was calibrated via XRR measurements of reference films.

The sample arm of the deposition chamber reaches into the chamber along the y-direction. It can be translated along x-, y-, and z-direction and can be rotated about its axis in addition, as indicated in Figures 3-6(a),(b). The sample pocket installed on the sample arm comes with an integrated thermocouple for sample temperature monitoring, a heating element, and a coolant tubing that can be used for LN_2 cooling purposes. The heating element was not employed in the present thesis since neither deposition at temperatures above room temperature nor sample baking were performed.

As shown in Figure 3-1, a sample is transferred to the deposition chamber through the flange opposite to the cluster ion beam port. A sample needs to be oriented coplanar to the xy-plane in order to slide in or out of the sample pocket of the sample arm, as indicated in Figure 3-6(b). For co-deposition

a sample had to be rotated by 125°. At this orientation, a sample takes the same angle towards the cluster ion beam and the effusion cell, 35°, with respect to the xz-plane, i.e., a sample is then aligned half-way between them.

A sketch of the sample arm with a loaded co-deposition sample is presented in Figure 3-6(c). The bidirectional arrow corresponds to the one illustrating the sample transfer in sketch (b). The dashed lines indicate that a sample is slid under a shielding element, which covers most of the drawn region. A trapezoidal-like cutout in the shielding allows to deposit cluster ions and matrix material onto the inserted target. The shielding is made of stainless steel sheet and is insulated from ground potential. Therefore, it can be set to a potential U_{SE}, where 'SE' stands for 'sample electrode'. The shielding is insulated well enough to qualify it for being used for cluster ion beam current measurements during depositions. The 3rd Faraday cup is installed beside the sample arm region shown in sketch (c). However, it was not used for cluster ion current measurements in a running deposition in order to avoid too long interruptions of running depositions. As indicated by the green color used to represent the sample electrode potential, also a part of a sample is connected to U_{SE}. More precisely, the area of the sample beyond the circle is connected to the shielding in an electrically conducting way. The separation of the two electric potentials is a functional property of the deposition mask that is mounted on a co-deposition sample. As the co-deposition mask is specifically designed for the deposition of the present nanocomposites it is discussed in detail in Section 4.2.2.

The rest of the sample is insulated both from ground and sample electrode potential. It can be set to another independent potential U_S, with index 'S' for 'sample'. The corresponding area is colored red and occupies an area $A_S = 9.6$ mm² corresponding to a diameter of 3.5 mm. With these two potentials the impact energy of the cluster ions on the growing film can be controlled.

During the deposition of cluster ions the negative current collected by the sample electrode potential was measured by means of a picoampere meter (Keithley 6485). More precisely, the current I_{SE} of cluster ions missing the sample was measured. The sample electrode was chosen because the insulation of the sample potential, though better than 20 MΩ, was not good enough to measure currents in the picoampere range. To determine the real current I_{Cl} of clusters whose charge is absorbed by U_S the cluster ion beam had to be deflected fully onto the sample electrode shielding, as it is indicated by the left cyan cluster spot in sketch (c). Now that the total beam current I_{TBC} is known the current hitting the sample can be calculated via $I_{Cl} = I_{TBC} - I_{SE}$. This procedure was common practice to monitor the stability of the cluster ion beam during running depositions. Exemplary values are given in Table 3-1. U_{SE} and U_S are generated by battery packs rather than power supplies to avoid any noise that may have influenced the deposition of cluster ions or the measurement of the resulting current.

The base pressure of residual gas inside the deposition chamber with no gas load coming from the cluster source was better than 1×10^{-8} mbar in case of the Fe-Ge samples and in the 10^{-10} mbar range for the Fe-Ag samples. To maintain ultra-high vacuum (UHV) conditions in the deposition chamber also in a running experiment, turbomolecular pumps with a total pumping speed of 4200 l/s are attached to the system to remove remnant carrier gas. The largest part is removed by the pump located between the aggregation tube of the cluster source and the 1st skimmer, see Section 3.2.

Potential sources of oxygen contaminations in a growing film are impurities of the carrier gases (N6 purity) and oxygen stemming from a slow thermal decomposition of the alumina crucible inside the effusion cell. Oxygen contaminations coming from the sputter target are unlikely because the Fe target was sputtered for at least 30 min prior to every CIBD experiment.

4 Fe$_x$-Ge$_m$ Nanocomposite Films

Parts of this chapter have been published in MDPI Nanomaterials [115].

In this chapter, Fe-Ge nanocomposite films are prepared using the CIBD system presented in Chapter 3. Fe-Ge forms a partially miscible material system. The films are analyzed for their transport and magnetic properties. After an introduction to the Fe-Ge material system in Section 4.1, the fabrication process of Fe-Ge cluster-assembled nanocomposite films is presented in detail in Section 4.2. Nanocomposites containing either 500 ± 50 (Fe$_{500}$) or 1000 ± 100 atoms (Fe$_{1000}$) are synthesized by simultaneous deposition of cluster ions from a size-selected, low-energy cluster ion beam and Ge matrix material from an effusion cell. Ge is found to grow in an amorphous structure under the conditions present in the CIBD system during co-deposition. The nanocomposite samples studied in the present chapter are listed in Section 4.3. They vary between 17 nm and several 100 nm in thickness and were synthesized with Fe concentrations ≥ 15 at. %.

In the following Sections 4.4 and 4.5, transport and further characterization methods are discussed. Prior to the discussion of the Fe-Ge nanocomposite samples, the results observed from a reference sample of pure amorphous Ge (a-Ge) that was treated and measured similarly to the nanocomposites are presented in Section 4.6. Subsequently, in Section 4.7 the magnetotransport properties of the nanocomposites are investigated as a function of cluster size, cluster concentration in the matrix, and temperature. The magnetoresistance $\Delta\rho/\rho_0$ in the fabricated Fe-Ge nanocomposite samples is negative and on the order of 1%, and identified as a superposition of a saturating low-field component and a field-dependent component varying approximately linearly with the applied magnetic field. The former is identified as tunneling magnetoresistance and a correlation of its intensity with resistivity and average nanoparticle surface-to-surface distance is found. Potential field-dependent magnetoresistance effects are discussed as well.

Subsequently, the durability of the nanocomposites as well as the independence of the measured properties on the orientation of the magnetic field relative to the nanocomposite film, i.e., isotropy, and of the applied excitation currents are discussed in brief. Last, the changes observed from annealing experiments of some of the Fe-Ge nanocomposite samples are analyzed.

4.1 Material Properties: The Fe-Ge System and the Amorphous Germanium

4.1.1 The Fe-Ge System

In early works on granular materials, compounds were prepared via thermal annealing of films made of two immiscible constituents. To grow off-equilibrium films of partially miscible components, more sophisticated techniques have to be applied, e.g., such like these implemented in the used CIBD system, see Chapter 3. Fe-Ge is such a partially miscible material system.
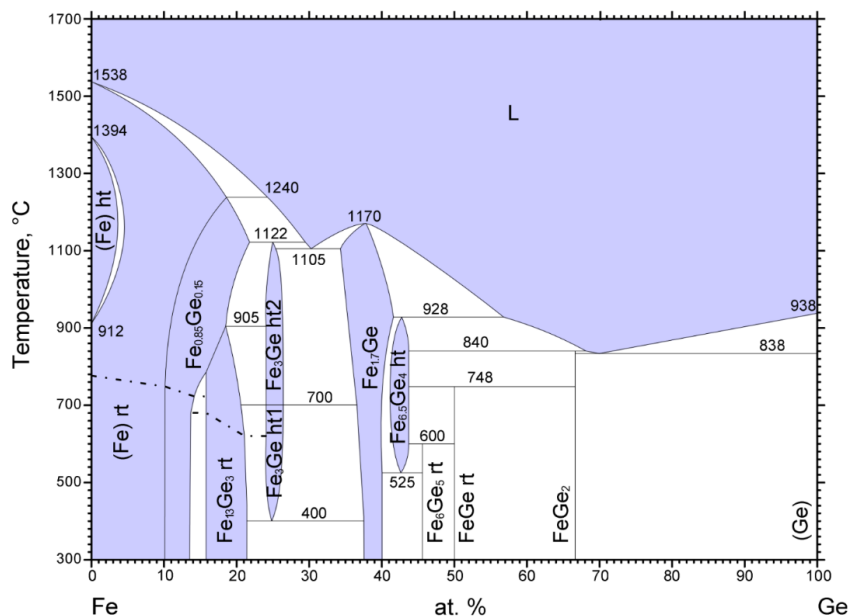
Figure 4-1: Fe-Ge Phase Diagram

The Fe-Ge phase diagram illustrates that Ge is soluble in Fe up until 17.5 at.%. Several stable alloys form at higher concentrations, all differing in their magnetic properties. For example, Fe_5Ge_3 (referred to as $Fe_{1.7}Ge$ in the phase diagram) is a ferromagnetic compound. Contrary to Ge in Fe, Fe atoms are not soluble in Ge at all. Phase diagram copied from Reference [116].

The Fe-Ge phase diagram depicted in Figure 4-1 [116] illustrates the existence of several stable Fe_xGe_y intermetallics at room temperature and solubility of Ge atoms in Fe of up to 17.5 at.%. On the contrary, Fe atoms are not soluble at all in crystalline Ge (c-Ge), which grows in a diamond crystal structure. Instead, $FeGe_2$ grains start to form in an elsewise pure Ge matrix. $FeGe_2$ exhibits a parasitic ferromagnetism (= imperfect antiferromagnetism) [117]. Increasing the Fe content, Fe_5Ge_3 (also referred to as $Fe_{1.7}Ge$ and $Fe_{1.67}Ge$) is worth to be mentioned since this compound is a true ferromagnet with a Curie temperature of 485 K [117].

Fe$_x$Ge$_y$ compounds can also exhibit polymorphism, i.e., there can exist several crystal structures, all with one and the same chemical composition but with different magnetic properties. Including high-temperature phases, e.g., both two Fe$_3$Ge polymorphic phases (hexagonal and cubic) are ferromagnetic [118] while the three polymorphic phases of FeGe (cubic, hexagonal, monoclinic) are helimagnetic, antiferromagnetic, and antiferromagnetic, respectively [119] (and various references therein). Fe$_x$:Ge$_{1-x}$ was also found to be a magnetic semiconductor that orders ferromagnetically below $T_C = 233$ K when $x = 5$ at. % [120]. Ge-based magnetic semiconductors can also be synthesized using, e.g., Cr [120] or (Co,Mn) [121].

To test the stability of the nonequilibrium Fe-Ge nanocomposites synthesized with the CIBD system, two transmission electron microscopy (TEM) samples were prepared on carbon-coated TEM grids prior to[†] the preparation of the Fe-Ge nanocomposite samples discussed in this chapter. While a 5 nm thin nanocomposite film (7 vol. %) was deposited onto one TEM grid, pure Fe$_{1000}$ clusters were deposited onto the other. An energy-filtered TEM micrograph of the first sample is shown in Figure 4-2(a), a standard TEM micrograph of the second one in Figure 4-2(b). Image processing software (ImageJ, [122]) was used on these two images in order to observe the particle size distributions plotted in Figure 4-2(c). The two fitted mean particle diameters are in good agreement (3.3 nm). However, this value is larger than the diameter that is calculated for a sphere of homogeneous density, i.e., with the density of bulk α-Fe (2.8 nm, see Table 4-2). The observation of a larger diameter is assigned to partially oxidized clusters as the structure of the clusters was found to be that of Fe$_3$O$_4$ in case of the TEM grid samples. Although transferred from deposition to TEM vacuum in Ar atmosphere, this measure could not prevent the unprotected films from getting oxidized. The difference in the widths of the observed distributions is assigned to the different modes of image formation used to record the shown images with the TEM and to the difference in the percentage of the areas occupied by the clusters. Nevertheless, from the micrographs it is evident that clusters do agglomerate to some extent and, hence, form chains of touching clusters. However, they do not fuse to drastically larger agglomerates.

4.1.2 Charge Transport and Magnetoresistance in Amorphous Germanium

In nonmagnetic materials, where charge transport happens in a conduction band, ordinary magnetoresistance is the dominating magnetoresistance effect. Amorphous Ge does not exhibit an energy gap like its crystalline counterpart but a mobility gap (see Section 2.4.1 for mobility). The gap is filled by the states of atomic orbitals and bonds that are localized because of bond distortions in the

---

[†]   The TEM grid samples were prepared by Dr. Thomas Reisinger, who also executed the size distribution analysis. The TEM was operated by Dr. Di Wang.
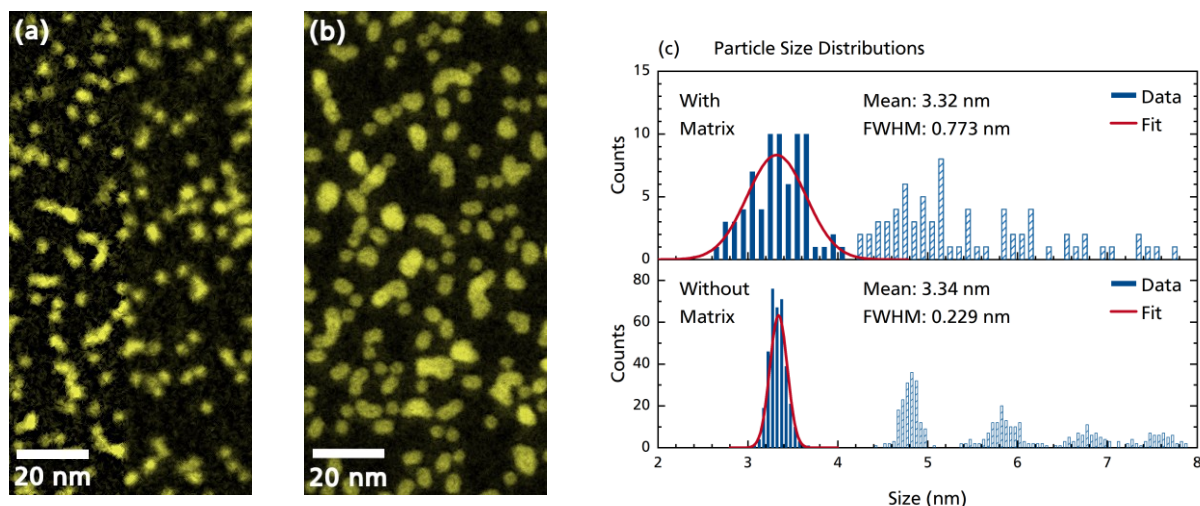
Figure 4-2: TEM Micrographs of Fe$_{1000}$ Monolayers and Corresponding Size Distributions

(a) Energy-filtered scanning TEM micrograph of a 5 nm thin film of Fe$_{1000}$ clusters in a-Ge matrix with a concentration of 7 vol. %. The film is thin enough to be treated as containing only one monolayer of Fe$_{1000}$ clusters. For TEM, see footnote on page 49.

(b) Standard TEM micrograph of a monolayer of Fe$_{1000}$ clusters deposited onto an 0.8 nm a-Ge buffer layer. The clusters occupy 14% of the available area.

(c) Corresponding particle size distributions[†]. The two fitted mean particle diameters, 3.3 nm, though not representative, are in good agreement. The diameter that is observed when a cluster is modeled as a sphere of homogeneous density, i.e., that of bulk α-Fe, is 2.8 nm. (see Table 4-2).

Both films were deposited onto carbon-coated TEM grids. Graphs (a),(b) each only show about half of the image that was used for particle size analysis. The difference in the widths of the observed distributions is assigned to the different modes of image formation used to record the shown images with the TEM and to the difference in the percentage of the areas occupied by the clusters.

amorphous structure. In this context, also unbound atomic orbitals with their energy close to the Fermi level are present in the amorphous semiconductor. At room temperature and below carriers are transported by variable-range hopping (VRH) across these states. This results in an anomalous negative magnetoresistance of the a-Ge at room temperature, which is due to the different changes in the rates of spin-flip hops and no-spin-flip hops.

In this section, the structure of a-Ge and properties related to its structure, i.e., its resistivity and its magnetoresistance, are reviewed. A discussion based on measurements using an a-Ge reference film will follow in Section 4.6.

4.1.2.1 The Structure of Amorphous Germanium

The resistivity ρ of an undoped crystalline semiconductor is determined by the density of charge carriers in its conduction band and the fact that the charge carriers propagate all with roughly the same mobility. The occupation probability of conduction band states with electrons scattered from the valence band assisted by phonons exponentially depends on the band gap E_g of a semiconductor and the inverse

of the temperature. Hence, the resistivity does: $\rho \propto \exp\left(E_g/2k_BT\right)$. In a $\log(R)$ vs. $1/T$ plot, the data of an undoped semiconductor form a straight line. The band gap of the semiconductor, which is the activation energy for intrinsic charge transport, can be calculated from the slope of this line.

In case of a doped semiconductor, there exists a second, much smaller activation energy, namely, the energy required to lift an electron from a donor state into the conduction band or an electron from the valence band into an acceptor state in order to leave a hole in the valence band. This leads to a kink in the elsewise straight $\log(R)$ vs. $1/T$ curve, which marks the onset of dominating intrinsic charge transport. At temperatures below the onset, charge transport via activated donor electrons or acceptor-state-induced holes dominates. In this case, the activation energy of the donor or acceptor states can be calculated from the slope.

Effects with no well-defined activation energy, however, lead to a continuous change of the slope rather than a kink. Clark [123] found a-Ge to show such a continuous change in the temperature range between 25 K and 325 K.

Walley [124] and Walley & Jonscher [125] observed $\log(R)$ vs. $1/T$ plots of continuous curvature with a slope of 0.05 eV at 60 K, 0.2 eV at 300 K and 0.65 eV at temperatures close to the crystallization temperature ($\sim$450 K) with no sign of saturation on either side; the (indirect) band gap of c-Ge is 0.67 eV at room temperature [126–128] and would give a slope of 0.34 eV. Thus, the authors concluded there is no well-defined activation energy for the conduction process in a-Ge. Also, the number of charge carriers is not well defined because electrons from deeper levels are activated to contribute to conductance with increasing temperature and, therefore, steadily change the slope of $\log(R)$ vs. $1/T$. The authors state that this implies a hopping type of transport process to be responsible for carrier transport.

Richter et al. [129] performed X-ray diffraction (XRD) measurements on evaporated a-Ge films with thicknesses on the order of 1 µm. In the observed radial distribution function the authors found a well-defined maximum that corresponds to the first nearest neighbor spheres. With an assumed mass density of 10% less than bulk density they found the corresponding coordination number to be 4 atoms. The second maximum, already overlapping with the third-nearest neighbor maximum, yielded a coordination number of 12 atoms. Beyond these maxima no well-defined other ones appeared in the radial distribution function. Therefore, they concluded that distorted tetrahedrons form the basic building blocks in a-Ge, similar to those forming c-Ge, which possesses a diamond-type crystal structure. The assumption made for mass density is justified since for bulk density a nonphysical coordination number of 4.4 atoms as first nearest neighbors would have been observed.

The experiments by Richter et al. [129] proved that a-Ge forms a network of covalently bound Ge atoms. In this context, the disorder in the network comes from distorted bond angles between tetrahedral

units and, hence, disorder of atomic positions at distances larger than the second-nearest neighbor distances. Since short-range order is preserved to good approximation and only long-range order is destroyed in amorphous semiconductors, they still have a band structure similar to their crystalline versions to some extent. However, additional delocalized band-like states are now included [128,130]. Consequently, the density of states adapts to the distortions. Valence band states in distorted bonds can raise in energy, i.e., above the valence band energy of the semiconductor E_V. Simultaneously, conduction band states can be lowered below the conduction band edge E_C because of the same argument. This leads to the formation of localized band tail states, forming Urbach edges [131], and localized states right below and above E_V and E_C, respectively. The states are localized because the energetic adaption of a state is due to the local distortions in the vicinity of the host atom.

The situation differing most from crystalline order that can happen to valence electrons is to be maneuvered out to positions from where no covalent bond can be formed because of the lack of close-by neighboring atoms with free valences. Such a valence state is called a dangling bond. Therefore, dangling bonds carry one very weakly bound electron on the one hand and provide an unoccupied state for another electron on the other. However, there is an energy penalty eU for double occupancy due to Coulomb repulsion. Their contribution to the density of states is to add localized states around (both above and below) the Fermi level of the semiconductor [128,130]. Moreover, distorted valence band states may even be higher in energy than distorted conduction band states. Therefore, electronic redistribution yields an appreciable amount of occupied states around the Fermi level, which is pinned close to the middle of the gap this way. Consequently, positively and negatively charged sites are left behind (compensated levels) [130]. Because of the dangling bonds a-Ge appears as p-type semiconductor when forming a junction with c-Ge and, hence, hopping processes must be the driving mechanisms besides regular conduction through the conduction band [123]. Another argument for a-Ge being a p-type semiconductor is given by Mott [132]. Mott states that "[it] is generally supposed that there are more [localized] states in the tail below the conduction band than above the valence band, so that the Fermi energy E_F lies nearer the valence than the conduction band … ."

According to Koc et al. [133], mass density and resistivity of a-Ge strongly depend on the deposition conditions when deposited at low deposition rates. The authors prepared a-Ge films via cathode sputtering at rates down to 0.45 μm/h = 0.125 nm/s and found a quick reduction of the observed mass densities and a strong decrease in conductivity when samples are deposited at rates below about 1.2 μm/h. Above, mass density and conductivity saturate at $\rho \approx 5.2$ g/cm^3, which is still below bulk value, and $\rho \approx 1$ Ωm. For a sample deposited at the lowest rate the authors determined a density of 4.13 g/cm^3. The lowest density stated in literature is 3.9 g/cm^3 [123].

Hauser & Staudinger [134] deposited a-Ge films with thicknesses between 2.5 nm and several 100 nm by sputtering arc-melted Ge both onto LN$_2$-cooled substrates (77 K) and onto substrates kept at room temperature. Subsequently, they examined the structure of their films. Characterizing their film deposited at 77 K at the temperature of LN$_2$ without letting it warm up, Hauser & Staudinger found the structure of that sample to be considerably more distorted compared to a sample deposited at room temperature. Moreover, the distorted structure of the sample deposited at 77 K anneals as soon as the sample is warmed up to room temperature. Arriving at room temperature, this film changed its structure into one that is similar to that of a film deposited at room temperature.

According to Hauser & Staudinger [134], Ge atoms are quite unlikely to diffuse at the temperature of LN$_2$. Therefore, two a-Ge islands cannot coalesce because adjacent atoms cannot satisfy tetrahedral bonding conditions when coming close together. Ad-atom diffusion would be required to form proper connections but this is barely happening at such a low temperature. Instead, improper bonds are formed leaving cracks in the sample when annealing sets in. In resistivity vs. temperature data Hauser & Staudinger found a shift in $\log(R)$ vs. $T^{-1/4}$ graphs at about 120 K when samples are warmed up for the first time after deposition, which marks the onset of annealing. After annealing, these samples became comparable with samples deposited at room temperature. The cracks were found to appear independent of the used substrate and to have no major influence on the electronic conductivity in case the sample was thicker than 10 nm.

4.1.2.2 Phenomenology of the Magnetoresistive Properties of the Amorphous Germanium

In amorphous semiconductors, unoccupied states around the Fermi level act as carrier traps (and donors) increasing the probability of the carriers to be scattered out of the conduction band. This shortens the mean scattering relaxation time of the carriers such way that ordinary magnetoresistance $\Delta\rho/\rho_0 \propto H^2$ (see Section 2.4.1) gets suppressed. Therefore, magnetoresistance phenomena in amorphous semiconductors must come from the discussed additional states not present in the crystalline counterpart. The existence of such localized states was discussed and found in several publications for pure, hydrogenated, and amorphous semiconductor alloys [125,135–137].

While c-Ge does show ordinary magnetoresistance $\Delta\rho/\rho_0 \propto H^2$ [138], a-Ge generally shows an anomalous negative magnetoresistance. It vanishes at about 450 ℃ and changes to a positive one at temperatures below 80 K. The magnetoresistance of a-Ge is independent of the applied current and the relative orientation of the magnetic field (isotropic), as was found by, e.g., Kubelík & Tříska [139,140], who prepared 3 μm to 6 μm thick a-Ge films via cathode sputtering. They found the magnetoresistance to be $\Delta\rho/\rho_0 \propto 1/T$ at temperatures above 250 K and to change into a positive one at 80 K. In between, it reaches a maximum in magnitude at 180 K. Apart from the intensity of the magnetoresistance, which

increases with increasing field, these characteristics are independent of the strength of the applied magnetic field, in particular, the maximum magnetoresistance and the change-over temperature to positive magnetoresistance. The authors suggest this to be the typical behavior of a-Ge.

Furthermore, Kubelík & Tříska [139,140] apply a model based on Zeeman splitting and energetic shifting of localized states to derive an expression capable of reproducing their observations. As the carrier levels are degenerate in zero field, both carrier concentration and mobility change because of energetic redistribution as soon as a magnetic field is applied. Hence, changing the hopping transfer rates for the spin-split levels yields a negative magnetoresistance.

Besides that type of magnetoresistive behavior, another one showing substantially different behavior was categorized by Kubelík & Tříska: That second type shows positive magnetoresistance at low magnetic fields and when below a certain temperature T_C, and changes to negative magnetoresistance at a certain high-enough field H_0 after going through a maximum in magnetoresistance at H_m. Both H_0 and H_m shift to higher fields with decreasing temperature and the magnitude of the magnetoresistance increases with decreasing temperature. Above T_C only negative magnetoresistance is observable.

Additional positive magnetoresistance arises from carrier transport through extended states, which quickly saturates already at low fields, adding a constant contribution for higher fields. The same behavior was found by Mell & Stuke [141] before, who observed the positive contribution to strongly depend on sample preparation.

4.1.2.3 Transport Mechanisms

As charge transport happens via localized states to an appreciable extent and as there is no well-defined energy gap between valence and conduction band edge anymore, covalently bound amorphous semiconductors are better explained by a mobility gap than by a band gap. This is because the mobility of carriers occupying states within the band gap between E_V and E_C is orders of magnitude lower than the mobility of classical valence and conduction band-like states [130].

Several transport models were developed in order to reproduce the magnetoresistive behavior observed and discussed above. Models that reproduce most of the explained features of a-Ge are based on Davis & Mott's VRH model [132,142], which is explained in brief as follows [130]. Three conduction processes contribute to carrier transport in different temperature regimes with different activation energies: conduction in extended states, conduction in band tails, and conduction in localized states near the Fermi level. Band tails reach into the band gap until an energy $E_{A,B}$ for conduction and valence band tail states, respectively.

Conduction in extended states is due to electrons thermally excited above E_C. The conductivity is given by

$$\sigma = \sigma_0 \, e^{-\frac{E_C - E_F}{k_B T}} = \sigma_0 \, e^{\frac{\gamma}{k_B}} \, e^{-\frac{\Delta E}{k_B T}}, \qquad [4\text{-}1]$$

where the energy difference $E_C - E_F$ is varies linearly with temperature as $E_C - E_F = \Delta E - \gamma T$ and where it is $\sigma_0 = e D(E_C) k_B T \mu_C$ with E_C and μ_C being average values at the conduction band edge. $D(E)$ and μ are the density of states and the carrier mobility, respectively.

Conduction via localized band tail states can only occur in terms of thermally activated hopping. In order to tunnel to another site an additional hopping energy ΔW_1 together with the energy difference of the sites has to be thermally overcome:

$$\sigma = \sigma_1 \, \exp\left(-\frac{E_A - E_F + \Delta W_1}{k_B T}\right). \qquad [4\text{-}2]$$

Either emission or absorption of a phonon is required to carry the difference in crystal momentum. For the energy of the final states the lowest possible one is chosen, namely, the lower edge of the conduction band extended states E_A. As $\sigma \propto \mu$ it is $\sigma_1 \ll \sigma_0$ because the mobility of carriers in band tail states is orders of magnitude lower than for carriers in extended states.

For hopping between states close to the Fermi level the activation energy is small so that a hopping energy ΔW_2 is sufficient:

$$\sigma = \sigma_2 \, \exp\left(-\frac{\Delta W_2}{k_B T}\right). \qquad [4\text{-}3]$$

Hopping is now due to thermally or phonon-assisted tunneling. At very low temperatures the number and energy of phonons is reduced to such an amount that carriers rather tunnel over larger distances to a site which is energetically closer than to a site closer in space but differing more in energy. Apsley & Hughes [143] explain this situation in terms of a 4D array of sites with a single 'range' parameter that combines and includes both spatial distance and energetic difference. These parameters are independent of each other in disordered systems. In this 4D array short-range hops are favored and as conduction is a result of successive hops it is the average distance in this array that determines the conductivity. After some intuitive assumptions Apsley & Hughes reproduce Mott's results for VRH, which exhibits a dominant $\log(\sigma) \propto T^{-1/4}$ temperature dependence for 3D systems

$$\sigma_{VRH} = \sigma_0(T) \exp\left(-\left(\frac{T_0}{T}\right)^{1/4}\right) \qquad\qquad [4\text{-}4]$$

with $T_0 = c_3{}^4 \alpha^3 / k_B D(E_F)$ [132,142], inverse localization length α of an Anderson-like localized state $\Psi \propto e^{-\alpha r}$ [144], which is set to $1/\alpha = 1\,\text{nm}$ [145], and a weak temperature dependence $\sigma_0 \propto 1/\sqrt{T}$ [146,147]. The numeric factor c_3 was determined by various authors from resistivity data, all within 15% deviation among each other (see Reference [145] and references therein), and is usually set to $c_3{}^4 = 2^4 = 16$. The most probable hopping distance is:

$$L_{VRH} = \left(\frac{8}{9}\pi\,\alpha\,D(E_F)\,k_B\,T\right)^{-1/4}. \qquad\qquad [4\text{-}5]$$

As an estimate of order, Movaghar & Schweitzer [148] state $T_0 = 7 \times 10^7$ K for a-Ge and mention that the corresponding density of states $D(E_F) \sim 10^{20} - 10^{21}\,\text{eV}^{-1}\,\text{cm}^{-3}$ [149] is much larger than the one proposed by Mott's theory, which is on the order $D(E_F) \sim 10^{18}\,\text{eV}^{-1}\,\text{cm}^{-3}$ [149,150]. This argument is supported by the fact that a spin density of states $\sim 10^{20}\,\text{cm}^{-3}$ would be very difficult to explain with the too low value from Mott's theory. Ortuno & Pollak [151] approximated the density of states of a-Ge around the Fermi level as an exponentially decaying function and found $D(E_F) = 2.6 \times 10^{18}\,\text{eV}^{-1}\,\text{cm}^{-3}$, which is not much more than what was found for a constant density of states $(D(E_F) = 2.0 \times 10^{18}\,\text{eV}^{-1}\,\text{cm}^{-3})$. Hauser & Staudinger [134] found $T_0 = 5.5 \times 10^8$ K for a 30 nm a-Ge film deposited at 300 K and $T_0 = 8.8 \times 10^7$ K for a 490 nm thick film measured after 48 h of annealing at 300 K. To summarize, values for T_0 are on the order of 1×10^8 K. The set of VRH parameters of a sample changes with its history of annealing [147]. The average hopping distance is $L_{VRH} \cong 8\,\text{nm} - 15\,\text{nm}$ at 77 K (see Reference [146] and references therein).

4.1.2.4 A Model for the Magnetoresistance of the Amorphous Germanium

Movaghar & Schweitzer [148] were the first authors who published a model that explains magnetoresistive phenomena in a-Ge (and a-Si) based on Davis & Mott's VRH in localized states around the Fermi level. Corrections due to some insufficient points of the model were added by Osaka [152]. The model is also well discussed by Mehra et al. [130].

Movaghar & Schweitzer divided dangling bond states around the Fermi level into singly, doubly and unoccupied states. Singly and doubly occupied states are separated by a uniform energy eU because of Coulomb repulsion in the doubly occupied case. There is a certain number of singly occupied states between $E_F - eU$ and E_F and the same number of states that can be doubly occupied lies between E_F and $E_F + eU$. Charge carriers can now hop upwards or downwards in terms of energy, where a spin-flip

is required to occupy a target state (anomalous hops) with a probability p_a and no spin-flip is involved (normal hop) with a probability $p_n = 1 - p_a$. A spin-flip may be required for a targeted double occupation to respect the Pauli principle. The relaxation time for normal hops is independent of energetic direction (up or down) and external field H_0:

$$\bar{\tau}_n = {\nu_0}^{-1} \exp\left(\left(\frac{T_0^{exp}}{T}\right)^{1/4}\right). \qquad \text{[4-6]}$$

Movaghar & Schweitzer distinguish between anomalous up and down hops $\bar{\tau}_a^{u,d}(H_0)$ [148]. An upward hop requires thermal activation while a downward hop does not. The attempt frequency is $\nu_0 = \bar{\nu} \exp\left(\left(T_0^{exp}/T\right)^{1/4}\right) \approx 10^{19} s^{-1}$, where $\bar{\nu}$ denotes the mean hopping frequency, and the constant T_0^{exp} in range of 7×10^7 K for a-Ge were observed from electron spin resonance (ESR) data of a-Ge samples [149].

They further take into account that a normal hop to a second nearest neighbor may happen more preferably than an anomalous hop to a first nearest neighbor. However, the authors found the anomalous hop to be the more probable one. This holds for temperatures between 50 K and 400 K. The differentiation between normal and anomalous hops is justified as long as the lattice spins appear to be frozen over time scales on the order of the hopping times. In other words, in the temperature range the model accounts for the mean hopping frequency must be higher than the inverse spin-lattice relaxation time $\bar{\nu} \geq {T_1}^{-1}$. Otherwise the spin system is already in equilibrium when the next hop appears. Magnetoresistance occurs as a consequence of spin rearrangements when the spin relaxation times are modified by an external magnetic field. From their ESR data [149], Movaghar & Schweitzer found hopping processes to make spin-lattice relaxation happen faster than spin-spin relaxation. Therefore, spins can be treated as only weakly interacting above 100 K and magnetoresistance is determined by the field and temperature dependence of the spin-lattice relaxation times. Below 100 K the hopping times become longer than the spin-spin relaxation time. Here, anomalous hops are the ones with highest hopping times and, hence, determine the spin-lattice relaxation time; by definition they turn into normal hops when relaxation time is exceeded. Then, spins are no longer weakly but strongly interacting. Differentiating between these two scenarios, Movaghar & Schweitzer [148] presented a formula for each temperature regime. Restricting themselves to weakly interacting spins and setting the averaged time for anomalous hops at zero field equal to the spin-lattice relaxation one $\bar{\tau}_a(0) = \bar{T}_1(0)$ the authors express the magnetoresistance as

$$\frac{\Delta R}{R} = \frac{R(H_0) - R(0)}{R(0)} = \frac{-p_a \, \bar{T}_1(0) \, \frac{1}{2} \, b^2 \, \gamma^{-2} \, (T/T_0^{exp})^{1/4} \ln\left(1 + H_0^2/\bar{v}^2\right)}{(1 - p_a) \, v_0^{-1} \exp\left((T/T_0^{exp})^{1/4}\right) \, + \, p_a \, \bar{T}_1(0)}, \quad [4\text{-}7]$$

where parameters $\bar{T}_1(0)$, b^2 and T_0^{exp}, and also $\gamma^{-2} = 10^2$ were determined from their ESR data. The maximum estimated magnetoresistance for a-Ge in their model is $\Delta R/R|_{H_0 \to \infty} \to b^2/\gamma^2 \approx 1\%$, which is of the correct order.

Both up and down hops possess a positive and a negative component of magnetoresistance. Positive magnetoresistance saturates quickly within 50 mT for both directions. Its magnitude decreases exponentially with temperature for $T \geq 150$ K and then saturates below about 0.3% until the lower limit of the model is reached at $T = 100$ K. Negative magnetoresistance is found to show a continuous flattening of the curvature without any sign of saturation at higher fields. Also, negative magnetoresistance becomes stronger with decreasing temperature. Because normal hops do not push the system out of spin equilibrium these hops have no influence on the magnetoresistance. Movaghar & Schweitzer find great similarity of their expression to the empirical fit used by Clark et al. [153] between 77 K and 300 K. Also, the model partially explains why the magnetoresistance increases with increasing temperature when a-Ge samples are annealed. Annealing increases the hopping time for normal hops $\bar{\tau}_n$ without significant changes in spin-lattice relaxation at zero field $\bar{T}_1(0)$. Therefore, anomalous hops happen more frequently, which results in a higher magnetoresistance.

Other effects come to play with increasing temperature. First, conduction via localized states in the band tails sets in. Negative magnetoresistance in this regime is explained by Hedgcock & Raudorf's [154] two-band model, in which a low-mobility band, i.e., a mobility gap, and a high-mobility band are modeled to act in parallel. Carriers are dumped from the high-mobility band into the low-mobility band, producing a negative magnetoresistance. Positive magnetoresistance is accounted for by the field dependence of the mobility of the carriers in the high-mobility band at high fields, where it decreases [155].

Beyond this regime, temperature-activated conduction via the conduction band of the amorphous semiconductor starts to contribute [147,155], which adds ordinary positive magnetoresistance. Pollak et al. [156] applied a simple parabolic band model for the localized states around the Fermi level to show that VRH does indeed account for hopping-only transport in a-Ge between the temperature of LN₂ and room temperature. They argue with a weighting factor that depends on the energy difference as $(E_m - E)^6$, where E is the energy of a state and E_m is an energy width around the Fermi level E_F. Transport via states energetically located beyond this energy range is entirely unimportant, while states

close to the Fermi level are greatly favored. The sample data provided by Pollak et al. [156] substantiate their arguments as it scales with the characteristic $T^{-1/4}$ dependence in the temperature range between the temperature of LN_2 and room temperature.

Mell & Stuke [141] proposed the negative magnetoresistance component to vary with the magnetic field as $\Delta R/R \propto -(\mu_0 H)^n$, where the exponent n changes with temperature from 0.7 to 0.4 at 500 K and 175 K, respectively [130]. This form has been generally agreed for negative magnetoresistance in a-Ge [138]. Moreover, it also supports the fact that the negative magnetoresistance of a-Ge does not saturate even in high fields of up to 10 T [148]. This is due to resonance of hop frequencies with the Zeeman splitting for downward hops. The required energetic activation for a hop is, in case of resonance, provided by the energy difference from the Zeeman split. Since the Zeeman splitting increases continuously with increasing magnetic field no saturation of magnetoresistance occurs even at a field of 10 T [148].

4.2 Fabrication of Fe-Ge Nanocomposite Films

The oxygen sensitivity of the Fe clusters made it necessary to protect the deposited nanocomposite films on the upper side against atmospheric influence. For this purpose, all samples were covered with protective material layers. As a consequence, the electric contact to the deposited nanocomposite films had to be made from the lower side, i.e., the films were deposited onto a pattern of contact lines that was evaporated onto each sample chip in advance. The layout of the sample chip that resulted from these requirements is explained in Section 4.2.1.

To fabricate a nanocomposite sample with the CIBD system reviewed in Chapter 3 the sample chip was mounted on a sample holder with a specialized shadow deposition mask that fulfilled the requirements pointed out in the context of Figure 3-6. In particular, the mask was designed in such a way that the area open to deposition is divided into two regions belonging to two different electric potentials. Also, it considers the orientation of the effusion cell inside the deposition chamber in terms of sample chip alignment. The complete sample layout used for co-depositions with the CIBD system is presented in Section 4.2.2 and the deposition process itself is discussed in Section 4.2.3. First characterization steps executed right after the deposition of a nanocomposite sample are summarized in Section 4.2.4.

4.2.1 Sample Chip Layout

Each sample was deposited onto a 5 mm × 5 mm wafer piece, which was cleaved off from a 4″ Si wafer with a thermal oxide coating[†]. A picosecond infrared laser (Trumpf TruMicro 5000) was used to score the wafers and to label each wafer piece with a unique identification number on its back side. After this step, the wafer pieces were cleaved by hand. The top surface of the substrate was protected by dicing tape during the whole dicing procedure.

The top surface of each chip was cleaned in a two-step process after removal of the dicing tape. The first step was CO_2-snow-jet (Applied Surface Technologies Carbon Dioxide Snow Cleaning) cleaning to get rid of both particles (from visible down to few nanometers in size) and hydrocarbon contaminations. The second one was oxygen plasma cleaning[††] (Oxford Instruments Plasmalab 80 Plus).

The next step was to deposit the contact line patterns used for resistivity measurements. To perform the deposition, a batch of up to 20 sample chips was mounted on a UHV-compatible stainless steel holder (Pink GmbH). The wafer pieces were fixed laterally in the pockets of a stack of four stainless steel frames and then covered and clamped by a shadow deposition mask. Both the frames and the deposition mask were cut out of 100 μm thick stainless steel sheets by means of the infrared laser mentioned above. Four sheets had to be used to counter the thicknesses of the loaded wafer pieces.

A drawing that combines both the frames and the shadow deposition mask is shown in Figure 4-3(a). The cyan square marks the outer edge of both the frames and the mask and has a side length of 44 mm. The green squares, 20 in number, are the pockets for the wafer pieces and have a side length of 5.4 mm. The shadow deposition mask carries the patterns to be deposited at the very same positions. These are drawn in red.

The magnification of a single sample chip site is presented in Figure 4-3(b). The sample films that were deposited with the CIBD system had a rectangular shape with dimensions 1.0 mm × 3.5 mm. For this reason, a pattern of ten parallel lines was chosen as contact pattern. This way, the pattern allowed to choose between seven possible quadruplets of neighboring lines to connect to a deposited film by means of the four-wire technique. The red lines have a width of 40 μm, a length of ~1.5 mm, and a gap of 160 μm between them. The width of the gap was chosen as a compromise between the diameter of the cluster ion beam and the length over which the cluster ion concentration in the deposited spot will be approximately homogeneous. The profile of the cluster ion beam was known from earlier experiments, e.g., by Dr. Fischer [5,7]. Also, the very high resistivity of the semiconducting Ge matrix to

---

[†]   The substrate used for the nanocomposite samples was 525 μm thick Si ({100}, P-doped, 10 Ωcm to 20 Ωcm) with a 200 nm insulating SiO_2 thermal oxide layer on each side.

[††]   The oxygen plasma was run at a pressure of 100 mTorr, with a flow of 15 sccm, at a power of 30 W, and for 120 s.
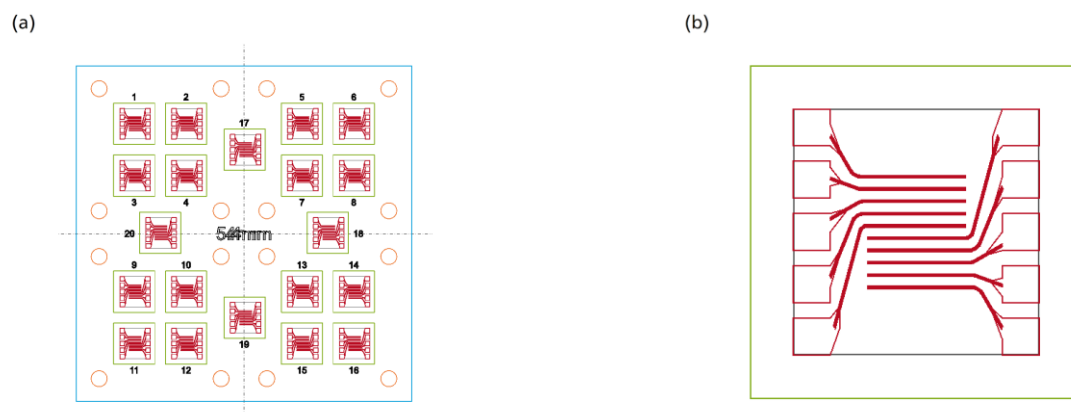
(a)

(b)

Figure 4-3: Laser Cutting Profile for the Shadow Deposition Mask and the Corresponding Sample Frames

(a) Sketch of the full structure. The cyan square is the outer edge of the pieces to be cut from the stainless steel sheets. The repeating square patterns are the deposition sites.

(b) Magnification of a single sample chip site. The green square is part of the sample frames and forms the edge of the pocket for a mounted chip. The red structure is part of the deposition mask. It is the pattern that is deposited onto a chip.

The total side length (cyan square) is 44 mm, that of a sample pocket (green squares) is 5.4 mm. The red structure consists of ten parallel contact lines that each end up in a bonding pad (0.6 mm $\times 0.6$ mm). The lines each have a width of 40 μm, the gaps in between are 160 μm wide.

be deposited was taken into consideration. As shown in Figure 4-3(b), one side of each contact line was extended to end up in a bonding pad. These 0.6 mm $\times 0.6$ mm bonding pads, in turn, were connected using a semiautomatic wire bonder equipped with 25 μm Al wire. For quick measurements at ambient atmosphere electrical contact could also be made with the help of micromanipulator controlled contact needles.

The contact pattern was made of a 5 nm Ti adhesion layer and a 20 nm Pt conducting film, both deposited via UHV electron beam evaporation. The pattern was deposited at a rate of about 0.12 Å/s. The resistance between a pad and a contact line at its end was measured to be about 300 Ω. A quality check using an optical microscope was made for each chip after the deposition to decide whether to use it for the deposition of a nanocomposite sample or not. An example optical micrograph of a chip carrying the deposited contact line pattern is presented in Figure 4-4.

As can be seen in the micrograph, the lower edge of each contact line turned out to be straight while the upper one appears corrugated. This systematic feature is an artifact stemming from the laser-cut mask and the electron beam evaporation process and is caused as follows.

On the one hand, the deposition mask was structured into a 100 μm thick stainless steel sheet while the cut out line width was only 40 μm. For this reason, only the upside edge of the cut out line structure came out with well-defined and straight shape. While cutting, the quality of the laser beam became
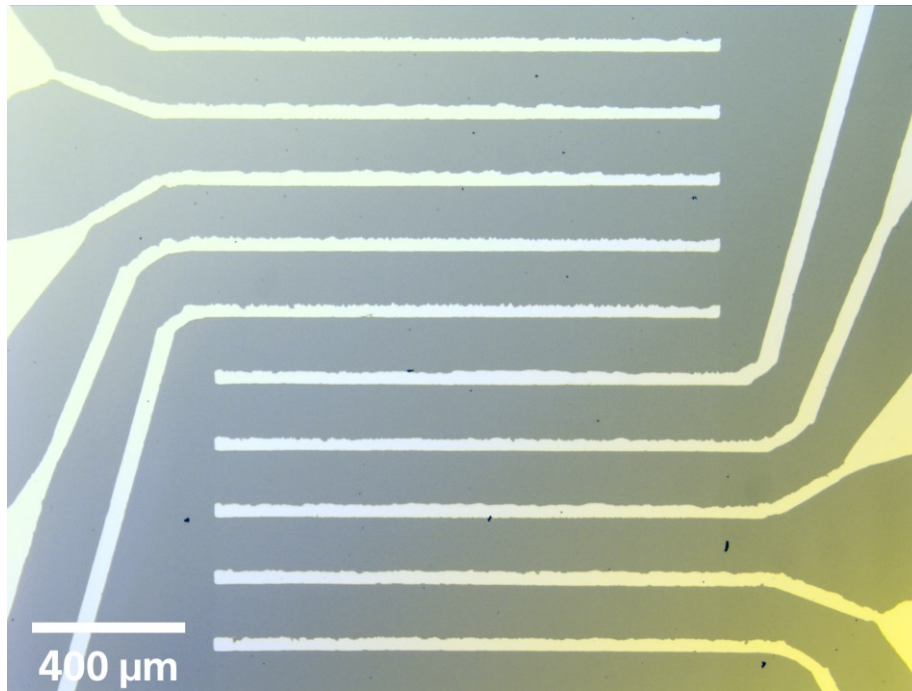
Figure 4-4: Optical Micrograph of a Contact Pattern Deposited onto a Si Chip by Means of UHV Electron Beam Evaporation

The ten parallel lines each have a width of $40\,\mu m$ and a gap of $160\,\mu m$ between them. The pattern is made of a $5\,nm$ Ti adhesion layer and a $20\,nm$ Pt conduction layer.

worse the deeper it cut into the stainless steel sheet. This resulted in a not-so-well defined cutout when breaching through the back side of the stainless steel sheet. On the other hand, the used UHV electron beam evaporator system provided three sources in total. Because the evaporator is built in a way that allows to deposit material simultaneously from all three sources, none of the evaporation sources was located exactly vertically below the loaded sample. For this reason, the atomic vapor coming from a heated crucible never arrived oriented perpendicular to the shadow deposition mask. Consequently, the sample chip was shielded by the upper side edge of the mask in case that side pointed towards the electron beam evaporation source. In turn, the side pointing away from it was shielded by the corrugated back side edge. This circumstance caused the artifact visible in Figure 4-4.

The corrugated edges are not considered to affect the transport measurements of the nanocomposite films. Even when a deposited film does not nestle against a corrugated Pt line along its full width there are still plenty of areas where the film and the contact line do form close-fitting contact. In case of a current-feeding line and a high-resistivity film the current paths entering the film through the contact areas are assumed to quickly expand right after entering the film in order to spread out across its entire cross section. In case of a voltage-sensing line the Pt line defines an area of equal electric potential, whether the contact to this line is partially interrupted or not. The situation is similar in case a metallic

film is deposited. Then, most of the current can be assumed to enter the nanocomposite film from a small part of the line right behind the point where it starts to be covered by the film. Also, the voltage is then sensed from a small area close to the edge of a nanocomposite film. This will be discussed in more detail in Section 5.1.3.3.

For consistency, the 'upper' edge of a sample chip was defined to be the one where the corrugated sides of the contact lines point towards. According to this definition the up-direction of the chip shown in Figure 4-4 points to the upper side of the image.

4.2.2 Cluster Ion Beam Deposition Sample

The layout of a sample to be loaded into the CIBD for co-deposition had to fulfill several prerequisites. On the one hand, the sample chip with its contact pattern (see Section 4.2.1) had to be connected to the potential of the sample pocket U_S. For this reason the upper side of a sample chip had to be electrically connected to the sample holder. On the other hand, it was the sample electrode potential U_{SE} that was used to monitor the current of cluster ions. Therefore, in order to have enough feedback via the change of the cluster ion current occurring when a co-deposition sample is translated with the sample arm, the area belonging to U_{SE} had to be continued towards the area of deposition as wide as possible. Otherwise, it would have been difficult to center the co-deposition sample to the cluster ion beam.

Another prerequisite was the ability to remove deposited material from the co-deposition mask, e.g., by grinding it off with sandpaper. This was of particular interest in case of the Ge matrix samples. Too much of deposited Ge would have worsened the conductivity of the surface of the mask. This would have led to undesired charging effects that, in turn, would have influenced the deposition of cluster ions. Since grinding off deposited matrix material with sandpaper is a quite rough way of handling the mask, it was of great desire to construct it of as little and as uncomplicated parts as possible. The resulting CIBD sample layout is presented in steps of assembly in the upper row of Figure 4-5.

Starting at the left-hand side of the figure's upper row, every CIBD sample was built on a standard Omicron Labs sample holder (anthracite) with a threaded hole at each corner. The sample chip with the deposited contact pattern is colored red (the pattern itself is not shown). In order to avoid charging of the sample and, hence, deflection of the cluster ions during deposition, the Pt contact pads of each row were electrically joined with the help of a thin strip of carbon tape (green), like it is used in electron microscopy sample preparation.
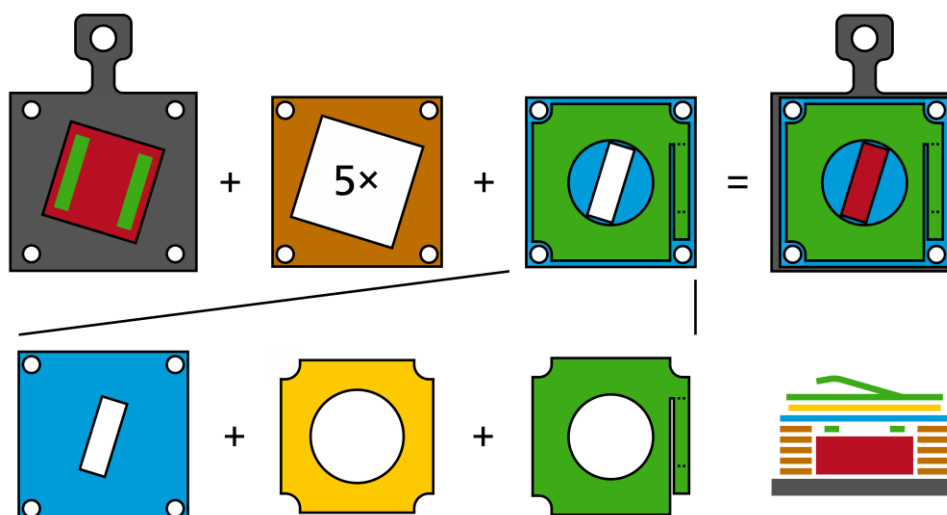
Figure 4-5: Sketch of the CIBD Sample Assembly

The first row shows the assembly of the full sample divided into three steps. Starting with the upper row and at the left-hand side, a sample chip (red) is put onto a standard Omicron Labs sample holder (anthracite). Its Pt contact pads are joined with two strips of carbon tape (green). Next, a set of five stainless steel frames is added in order to keep the sample chip in position. The inner frames are tilted by $17°$ to align the chip to the effusion cell when loaded into the deposition chamber. The co-deposition mask (green + cyan) completes the assembly. Finally, the assembly is tightened with a screw in each corner. The result is shown in the rightmost column. The upper sketch shows the assembly as seen from the top, the lower one as seen from the right-hand side.

The co-deposition mask consists of three elements, which are depicted in the second row. The lower one (cyan) is a slit mask, with the slit being tilted by $17°$ to align it to the tilted sample chip. This slit defines the film stripe to be deposited onto the chip. The upper element (green) is glued to the lower one with a piece of double-faced adhesive Kapton® tape (yellow), which also electrically insulates the upper and lower mask elements from each other. The upper mask carries a circular hole and is connected to the sample electrode potential U_{SE} when the sample is slid into the sample pocket of the sample arm. This functionality is provided by the pantograph-like antenna, which is seen best in the side view sketch. The rest of the sample is connected to the sample potential U_S.

A set of five stainless steel frames (brown), each with a thickness of 100 µm and a cut out square that fits the dimensions of a sample chip, were added to the holder to counter the height of the CIBD sample chip of 525 µm on the one hand and to keep it in position on the other. In order to align the sample chip to the direction of the output flux of the effusion cell the positioning frames are tilted by $17°$.

Finally, the co-deposition mask (green + cyan), which itself consists of three parts as depicted in the lower row, is added on top. Its lower element (cyan) is a slit mask (slit: 3.5 mm × 1 mm), which defines the shape of the film to be deposited onto the sample chip. It is also tilted by $17°$ in order to be aligned with the tilted sample chip. The upper element (green) is a hole mask with its diameter equal to the length of the slit. A piece of double-faced adhesive Kapton® tape (yellow) is used to glue the two Mo-made sheets to each other and to insulate them from each other at the same time. The area inside

the circle belongs to the sample potential U_S for this reason, while the area outside the circle belongs to the sample electrode potential U_{SE}, as it is illustrated in Figure 3-6(c).

Consequently, the lower side connects to the carbon strips on the sample chip. This way, the contact pattern of the chip is electrically connected to the potential of the sample holder U_S. The carbon tape strips also prevented the co-deposition mask from damaging the fine Pt contact line pattern by keeping the co-deposition mask at a safe distance.

The rightmost column in Figure 4-5 illustrates the fully assembled deposition sample. In the upper row the view from the top is presented, in the lower row the sample is sketched as it is seen from its right side. Last, frames and deposition were tightened to the holder with a screw in each corner (not shown).

In order to not form a continuous surface that could easily have been covered by deposited material and, in turn, would have led to a short-circuiting of the co-deposition mask, the circle in the Kapton® tape was cut slightly bigger than that of the hole mask. This resulted in a gap between the upper and the lower Mo-made sheet rather than a continuous surface.

Mo sheet was chosen as mask material in order to reduce the risk for the chip to get contaminated with Fe. The two sheets were insulated by a resistance of more than $200\,\mathrm{M\Omega}$. However, the use of Kapton® tape prohibited the baking of a sample for cleaning reasons at the beginning of a co-deposition experiment.

Electrical contact between the upper mask part and the sample electrode sheet above the sample pocket is made with the pantograph-like antenna of the hole mask. The antenna is seen best in the side view in Figure 4-5. When the sample is slid into the sample pocket of the sample arm the antenna touches the sample electrode sheet. The antenna was formed by bending the cut out stripe of metal on the right side of the hole mask to the illustrated shape.

One disadvantage that arose from the used co-deposition mask layout was the gap between the upper and lower mask sheet. A growing layer of deposited material could have short-circuited the two sheets, especially in case Ag is used as matrix material. This was partially prevented by orienting the slit of the slit mask towards the effusion cell (17° angle). However, matrix material was still deposited under an angle of 35°, and, hence, partially into the gap between the upper and the lower element of a co-deposition mask. Also, Ag tended to form flakes on the mask sheets during deposition. Although such flakes would have fallen down onto the bottom of the deposition chamber in case they got loose, there was a risk that such a flake could have short-circuited the co-deposition mask. Fe-Ag nanocomposites will be discussed in Chapter 5.

4.2.3 Nanocomposite Deposition Process

Fe-Ge nanocomposites were synthesized containing either Fe_{500} or Fe_{1000} clusters (Fe sputter target by Lesker, N4 purity). The clusters were embedded into matrices of porous, semiconducting, amorphous Ge (evaporation material: MaTeck, N5 purity, from alumina crucible) at base pressures of 9×10^{-9} mbar and lower.

A loaded sample was cooled by a constant flow of LN_2 through the coolant tubing of the sample arm, which resulted in a substrate temperature of $-135\,°C \pm 5\,°C$ during film growth. The cooling to low temperatures in combination with covering of clusters by the constant flux of matrix material from the effusion cell reduced the amount of diffusion along the surface of the film. This way, potential cluster agglomeration was reduced to a minimum [7]. Also, Ge grows as an amorphous (a-Ge) solid when the substrate temperature is lower than $450\,°C$ [125].

The effusion cell was run between $1100\,°C$ and $1300\,°C$ in order to achieve deposition rates of up to $0.3\,Å/s$ of Ge. The temperature point of operation had to be increased from deposition to deposition in order to adapt to the decreasing amount of material in the crucible and the narrowing of the exit aperture of the effusion cell.

As explained in Section 3.3, a relative deposition azimuth angle of 35° between sample normal and axis of the cluster ion beam was chosen in all deposition experiments. Deposition under this angle is also the reason why a-Ge grew in a porous way here.

A symbolic cross section through an Fe-Ge CIBD sample is shown in Figure 4-6, an optical micrograph in Figure 4-7. The deposition of every Fe-Ge nanocomposite sample started with a 1 nm buffer layer of matrix material. The deposition of this little amount prior to the co-deposition was done to achieve a better inclusion of the first clusters in the matrix. When the buffer layer was finished, the deposition rate, more precisely, the temperature, of the effusion cell was adjusted to the rate required to obtain the desired ratio of clusters and matrix material. Then, after a short time span, the film deposition was continued.

Amorphous Ge was found to form a continuous layer when grown thicker than 2 nm in Reference [145]. There, Ge is deposited onto sapphire substrates at $50\,°C$ that carry interdigital Cr arrays. In the present thesis, potential gaps in the a-Ge buffer layer are considered to be filled after continuation of film deposition.

While the effusion cell was adjusted to the desired deposition rate, which took several minutes, the intensity of the cluster ion beam was measured with the third Faraday cup installed on the sample arm (see Section 3.2). Also, the position of the co-deposition sample was fine-tuned in order to allow a
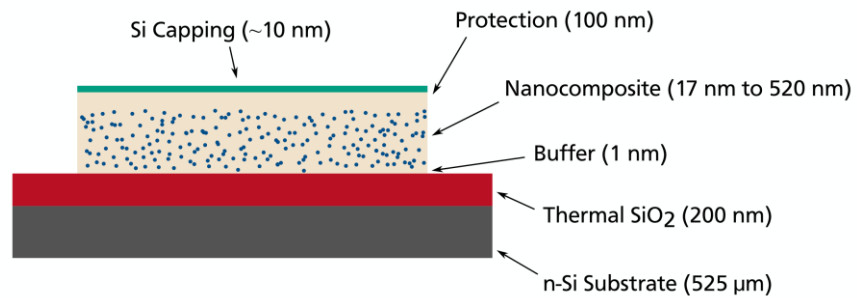
Figure 4-6: Cross Section Through the Layers of an Fe-Ge Nanocomposite Sample

Prior to the deposition of the nanocomposite layer, a buffer layer of matrix material was deposited. After deposition, the nanocomposite layer was covered with a protection layer of matrix material and a capping layer of self-passivating Si.

maximum of cluster ions to reached the sample. As explained in Section 4.2.2, fine-tuning was done by minimizing the cluster ion current recorded by the sample electrode.

For samples used in this work U_{SE} and U_S were set to voltages between +56 V and +57 V by two separate battery packs, which allowed to apply electric potentials free of noise to the sample electrode and the sample area. With the voltage range given above, the kinetic energy per atom in a cluster at impact was 0.12 eV, 0.06 eV and 0.04 eV in Fe_{500}, Fe_{1000} and Fe_{1500} clusters, respectively. Therefore, clusters were deposited close to or within the soft-landing regime [157,158]. Representative cluster ion currents are listed in Table 3-1.

After up to 6.5 h of co-deposition the cluster ion beam was blanked by turning off the magnetic field in the sector magnet. Meanwhile, deposition from the effusion cell was continued to cover the nanocomposite layer with a protecting layer of matrix material. The amorphous and porous structure of the Ge made it necessary to deposit a thick protection layer. Therefore, 100 nm of pure a-Ge were added. Additionally, a Si capping layer was deposited on top of the protection layer using the triple electron beam evaporator. This step was necessary since a-Ge is prone to oxidation because of its porous structure. Si forms a self-passivating oxide layer as soon as it is exposed to oxygen, i.e., to ambient atmosphere.

During the deposition of protection and capping layer a mass spectrum and an energy scan were recorded for every sample in order to keep track of long-term beam parameter changes. See Figure 3-4 for exemplary ones.

4.2.4 Characterization Steps Executed Right After the Deposition

After a CIBD sample was unloaded from the UHV system it was immediately disassembled (see Section 4.2.2 for assembly) and remnant pieces of carbon tape were peeled off from the sample chip.

Leftovers of the tape were carefully wiped off with a piece of crumbled tissue soaked with isopropanol that was clamped between a pair of tweezers, without contaminating the deposited film.

Immediately after the disassembly a first visual check with an optical microscope was performed, and the two-wire resistance between all pairs of neighboring lines were measured and documented. An optical micrograph of the film deposited onto the sample chip shown in Figure 4-4 is presented in Figure 4-7. The deposited film appears blue in the shown image and exhibits a vertical stripe on its right-hand side that is slightly darker in color. Moreover, a pale, brown vertical stripe of same width is visible on the left-hand side of the film. This artifact is caused by a lateral shift of the deposited matrix material and the later deposited Si capping layer. These were deposited under different angles of incidence (see Section 3.3), which led to different areas of deposition in conjunction with the spacing between the slit mask and the sample surface (see Section 4.2.2). The same effect caused a lateral shift of the matrix and the cluster deposition area as well. However, the effect is smaller because of the smaller difference between the directions of incidence. The result is an accumulation of clusters at the Pt lines on the left-hand film edge, where matrix material is lacking. Theses clusters immediately got oxidized when the sample was unloaded from the UHV system. The accumulations appear colored dark brown in the micrograph. Last, 'I±/U±' denote the contacts chosen for four-wire transport measurements of this particular sample.

The measured two-wire-resistance were dominated by the nanocomposite film deposited between the two neighboring lines. For some samples a color gradient, sometimes even visible to the naked eye, could be seen on the deposited films. The gradient is related to the Fe cluster concentration in the film, i.e., the cluster spot.

The measured two-wire resistances at room temperature varied in a range from above $200\,M\Omega$ for the pure a-Ge film down to $1.7\,k\Omega$ for several samples close to the percolation threshold (see Section 4.7.2.1). Since the resistance of a Pt line is on the order of $100\,\Omega$ the two-wire resistance 'mapping' was a useful tool to detect the pair of lines between which the Fe concentration was highest. Exemplary two-wire resistance data are shown in Figure 4-13(a) as blue bars. In that figure the two-wire resistance data are shown in combination with preliminary Fe concentration data. Preliminary EDX point measurements of the concentration on top of the Pt lines were used to decide where to perform transport measurements on each sample and were executed soon after deposition. These measurements will be discussed in more detail in Section 4.5.1.1.

As a precautionary measure the nanocomposite samples were stored under UHV conditions in the load lock of the CIBD system between measurements. As will be discussed in Section 4.7.5.3, the taken measures—protection layer, capping layer, UHV storage—successfully protected the nanocomposite from chemical and mechanical damaging.
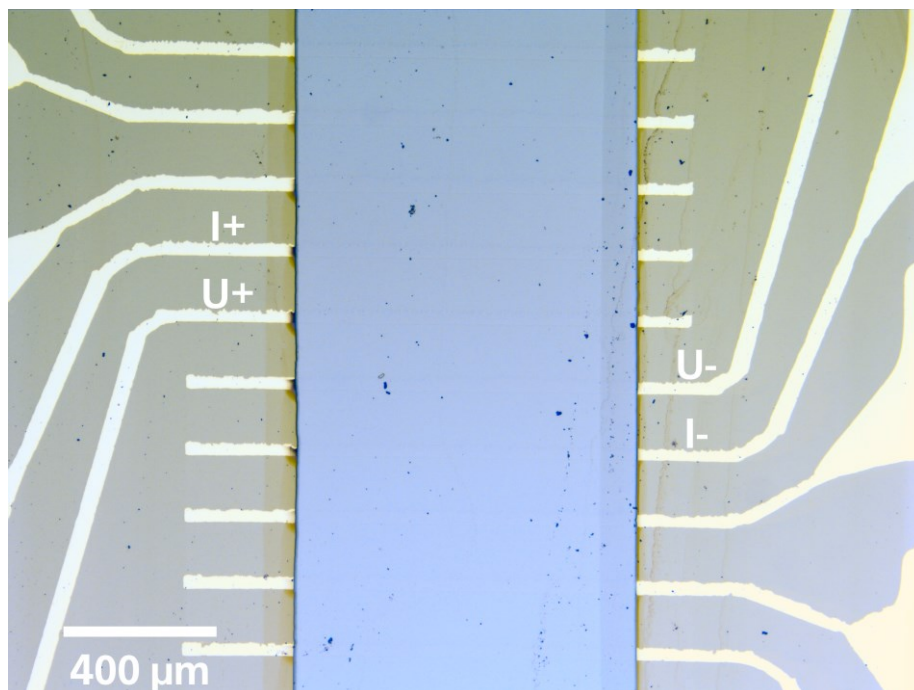
Figure 4-7: Optical Micrograph of Fe-Ge Nanocomposite Sample G157

The shown film was deposited onto the CIBD sample chip that is shown in Figure 4-4. On the left-hand side of the film a brownish stripe of deposited material from the electron beam evaporator (Si) and on the right-hand side the lack of the same is visible. The lateral shift of the deposited stripes of material, i.e., the difference in the shadowing by the mask, is caused by the different angles of incidence, see Section 3.3, in conjunction with the spacing between surface of the sample and bottom of the mask. The contacts chosen for four-wire transport measurements for this particular sample are labeled according to their function.

4.3 List of Used Fe-Ge Nanocomposite Samples

Starting deposition experiments at high cluster concentration and moving to lower concentrations, sample G136 was the first one to exhibit magnetoresistive properties. A bunch of Fe-Ge nanocomposite films were deposited, out of which a set of 11 samples could be used to analyze the magnetoresistive properties of the Fe-Ge nanocomposite system. Their deposition-related properties are listed in Table 4-1. There, samples are listed by increasing Fe concentration c_{Fe}. Besides the Fe concentration, the thickness of the nanocomposite layer t and the average distance between the surfaces of two neighboring clusters *MPS* (abbreviation of mean particle separation) are given. How these quantities were calculated from EDX data will be explained in Section 4.5.1.2. Together with samples that do show magnetoresistive behavior, samples that are too high (G128, G131, G158, G161, G163) or too low (G149) in concentration but that are, nevertheless, shown for comparison reasons in several figures, are added to the sample set.

To differentiate them from those samples showing magnetoresistive behavior their IDs are written in parentheses. Samples too high in concentration consist of clusters percolating to large extents. The samples are marked with a dagger symbol † in Table 4-1.

Table 4-1: List of Used Fe-Ge Nanocomposite Samples

Summary of Fe-Ge nanocomposite samples listed up with their deposition determined properties. Samples in parentheses did not show magnetoresistive behavior because of a too high or a too low cluster concentration.

Sample ID Fe_{500}-Ge	c_{Fe} (at. %)	t (nm)	MPS (nm)	Sample ID Fe_{1000}-Ge	c_{Fe} (at. %)	t (nm)	MPS (nm)
G160	16	232	1.9	(G149)	15	197	2.5
G159	24	120	1.3	G144	18	523	2.1
G164	28	130	1.1	G146	18	340	2.1
G165	28	121	1.1	G152	19	148	2.0
G136	28	17	1.1	G148	21	255	1.9
(G161)	35	102	$0.8^{†}$	G140	22	167	1.7
(G158)	41	52	$0.6^{†}$	G157	27	234	1.4
(G163)	42	68	$0.6^{†}$	(G131)	76	69.7	$0^{†}$
				(G128)	83	35.8	$0^{†}$

† Sample is above percolation threshold. See Section 4.7.2.1 and Figure 4-22.

Table 4-1 is meant to only give an overview over the sample IDs and the corresponding concentrations at this point. Data shown and discussed in the further course of this chapter will refer to these IDs and concentration values repeatedly. Samples containing Fe_{500} clusters will be represented by green triangles ▼, those containing the Fe_{1000} ones will be represented by blue circles ●. Data points representing samples that exhibited no magnetoresistance are represented by open symbols that are crossed in addition ✖ ▣. In graphs that show data plotted as curves a unique color is assigned to each sample, where also different symbols may be used to help differentiate between the sample. When the data of both Fe_{500}-Ge and Fe_{1000}-Ge samples are plotted within the same graph the data are represented by dashed and solid lines, respectively.

It is noteworthy that the nanocomposites for which magnetoresistive behavior was found possess an Fe concentration roughly between 15 at. % and 30 at. %. Moreover, all samples but one were thicker than 100 nm. These samples can all be treated as 3D films. The thinnest sample, G136, has a film thickness of only 17 nm. At this thickness and with the given concentration it can be estimated that only 1.9 clusters are stacked on top of each other on average across the whole film thickness. Therefore, G136 cannot be safely assumed to be a 3D film, however, it will be treated as one.

4.4 Measurement of Transport and Magnetoresistive Properties

After a first two-wire resistance check (Section 4.2.4) and a preliminary EDX Fe concentration analysis (Section 4.5.1.1) each sample underwent detailed transport measurements as a function of temperature, magnetic field, and electric current. In particular, the magnetoresistive behavior was examined.

The transport properties of all samples were measured with a Physical Properties Measurement System by Quantum Design (PPMS) equipped with a 'Resistivity Option'. The system provides a LHe cryostat with an accessible temperature range of 2 K to 400 K. Furthermore, it is equipped with a superconducting magnet located inside the PPMS's LHe dewar, with which magnetic fields of up to 7 T can be generated. The PPMS and, in particular, the execution of measurements, was controlled by the Quantum Design MultiVu software. Example sequences used for the measurements explained below are given in Appendix A.

Electric contact to a sample chip was made by wire bonding the selected contact pads, see Section 4.5.1.1, to a PPMS transport measurements sample holder, henceforth called 'puck'. The sample resistances were measured by the four-wire technique.

4.4.1 Measurement of Transport and Magnetoresistive Properties

For transport measurements each sample was installed in such a way that the four-wire excitation current was applied parallel to the direction of the magnetic field inside the PPMS (longitudinal orientation), i.e., in such a way so that the longitudinal direction of a sample film was oriented collinear to the magnetic field. The longitudinal orientation was chosen for the first series of measurements in order to avoid the appearance of Hall voltages.

The PPMS sample puck used for longitudinal sample orientation measurements allowed to simultaneously install and measure up to two CIBD sample chips. By installing the samples rotated by 90° the samples could also be measured in the transverse orientation. To orient the samples with the film plane perpendicular to the magnetic field another sample puck had to be used. Some transport measurements were also performed in these orientations in order to check if the measured response to the magnetic field is isotropic, see Section 4.7.5.1. The samples were fixed on the puck with cryogenic-temperature- and vacuum-compatible resin. The puck and a samples, more precisely, the corresponding pads available on both the puck and a sample, were electrically connected by means of wire bonding, see Section 4.2.1.

A series of transport measurements always started with the software-controlled recording of a $R(T)$ curve in zero magnetic field. Starting at 300 K, four excitation currents I_{exc} were set for resistance measurements: 200 nA, 150 nA, 100 nA, and 50 nA in case of Ge matrix samples. The strong increase in resistance inherent to semiconducting materials in general, i.e., inherent also to the Ge matrix, led to the situation that the set excitation currents could no longer be delivered by the current supply of the PPMS's resistivity option one after another. Consequently, excitation currents smaller than the ones given above had to be applied at lower temperatures. Also in this case, four excitation currents were used. The measurement of $R(T)$ data points was partially repeated with the new set excitation currents in this context. In order to make full use of the PPMS's capabilities of precise resistivity measurements, the limit for this is at about 4 MΩ, excitation currents as low as 10 nA were applied. The PPMS's maximum voltage limit to apply a set excitation current was 10 V.

In case resistance data could be collected with more than one of the set excitation currents the differences between the measured resistances turned out to be negligibly small. For that reason, all resistance measurements took place within the linear I–V regime. This is underpinned by the I–V characteristics of a-Ge shown in Reference [125], where non-Ohmic behavior of a-Ge films was observed to set in only when electric fields higher than 5×10^3 V/cm = 50 V/100 µm are applied, and by the I–V data of two Fe-Ge samples presented in Figures 4-24(c),(d). As an estimation, assume that the PPMS's maximum possible voltage drops, in accordance with the four-wire measurements, over a distance of three neighboring lines corresponding to about 600 µm. The resulting maximum electric field is about 1.7×10^4 V/m. This is well below the threshold mentioned above.

$R(T)$ data sometimes were even recorded in a ZFC/FC sequence. In brief, a ZFC/FC sequence is a measurement of a quantity as a function of temperature. First the quantity is measured from an upper to a lower temperature limit in zero magnetic field. Then, a magnetic field is applied and a second curve, now from the lower to the upper temperature limit, is recorded. Subsequently, the above procedure is repeated, however, under constant presence of the magnetic field. The ZFC/FC procedure is an important method used to detect superparamagnetic behavior. The physical background is explained in Section 2.3.

Now, knowing the proper excitation currents to be applied at certain temperatures, examination of the magnetic field dependence of the resistance of a sample measured at various constant temperatures followed the $R(T)$ measurements. Henceforth, these measurements will be called 'magnetoresistance curves'. To record a magnetoresistance curve the magnetic field was ramped in a loop: from zero to maximum magnetic field, to the maximum at reverse field direction, and again to maximum magnetic field. The set maximum magnetic field was 6 T within these sequences. Magnetoresistance curves were recorded starting at 300 K, and were performed down to 40 K, or lower if possible. After the recording

of the magnetoresistance curves, optional measurements, like detailed magnetoresistance curves at low fields and temperatures, were performed for some samples, too. The maximum recorded change in resistance due to the application of a magnetic field was about -0.5%. This magnetoresistive change is small compared to the change of the resistivity due to temperature variation.

All the transport measurements were performed with the PPMS in the alternating current mode. That means, a direct current is subsequently applied to the specimen in both directions and the mean value of the two observed voltages is taken to calculate the resistance of a specimen. For the present samples, 25 of such alternating current readings were executed and averaged for each resistance data point. After the 25 readings the measured resistance was automatically calibrated to the value observed from the measurement of an internal reference resistor (PPMS Standard calibration mode). The variances of these measurements were used to calculate the variances of the sample resistivities and of deduced quantities.

Last, it is argued by a model calculation that the transport measurement of the Fe-Ge samples took place in the low-field regime. In the low-field regime, processes, e.g., tunneling or activation of charge carriers, are thermally activated. When the average distance between the centers of two neighboring clusters, henceforth referred to as mean particle distance, is assumed to be 4 nm and the above maximum electric field is applied, the electrostatic energy a charge carrier gains on average when transferred to the next cluster, corresponds to a temperature of less than 1 K. Therefore, all samples are measured within the low-field regime $eV_{Cl \to Cl} < k_B T$. In case of Fe_{1000} clusters, a mean particle distance of 4 nm corresponds to a mean particle separation of 1.6 nm. In the opposite case, the high-field regime, processes are field induced [159,160].

To estimate the case where chains of touching clusters with large gaps in between are formed, assume ten Fe_{1000} that form a straight chain parallel to the direction of the electric field. Since the mean particle separation is still 1.6 nm the applied voltage effectively drops over a smaller distance. In the assumed scenario the electric field is larger by a factor of about 2.1 compared to the case of stepwise potential drops between isolated single clusters as assumed above. Also, the distance to the next chain is seven times larger than before. The temperature corresponding to the electrostatic energy is 11.5 K in this scenario. Therefore, even in this extreme scenario transport happens in the low-field regime.

From two-wire-resistance measurements, see Section 4.2.4, it can be concluded that the contact resistance between the Pt lines and the Ge matrix is on the same order as that of the Pt contact lines. For all Fe-Ge samples the two-wire resistance was dominated by the resistance of the nanocomposite. However, samples are compared by their resistivity and not by their absolute resistance R_{meas}. From a generalized film geometry for Fe-Ge samples it can be estimated by calculations that an applied excitation current equally spreads over the complete cross section of a film. Therefore, the resistivity ρ

of an Fe-Ge sample can be calculated from the dimensions of the cuboid spanned by the width w of the film, the thickness of the nanocomposite layer t, and the distance between the two contact lines used for voltage sensing d. The resistivity is then $\rho = wtR_{meas}/d$.

4.4.2 Magnetoresistance Data

Magnetoresistance curves are recordings of resistance data at a fixed temperature over one magnetic field cycle from maximum magnetic field to reverse maximum field and back. In principle, magnetoresistance curves could be recorded from room temperature down to the temperature of LHe. Because a magnetic sample memorizes its past measurement procedures its memory had to be erased by fully magnetizing it prior to each new recording. Therefore, for most samples the initial curve, recorded when the field was ramped to the first maximum, did not match with the henceforth reversible rest of the magnetoresistance curve. Also, magnetoresistance curves up to a lower maximum field in range of 1 T to 2 T and finer data point spacings were recorded. This way, a more detailed view on the low-field magnetoresistive behavior was observed.

Because for most samples the measured resistance continuously decreased over time at 300 K, and sometimes even at 250 K, the highest temperature for which magnetoresistance data are presented is 200 K. The continuous change in resistance is assigned to the annealing process happening in a-Ge, which is discussed in Section 4.6.2. Additional stress that affects the amorphous structure may be caused by the first alignment of clusters by an external field after a nanocomposite film was settled at a new temperature. The individual low-temperature limit of a sample was determined by its strong increase of resistance and the technical limitations of the PPMS. Data at 40 K were observed for every sample, therefore, 40 K is the lowest temperature where magnetoresistance data of samples used in the present chapter are compared at. In between these two temperatures, 100 K was chosen as a third temperature for comparison.

Various magnetoresistance curves of samples G152 and G164 are shown in Figures 4-8(a),(c), respectively. The data of these two samples are representative for all discussed Fe-Ge nanocomposite samples and, hence, serve as examples here.

The most prominent feature visible in all plots is the always negative magnetoresistance that quickly develops within the range of 1 T, i.e., in the low-field range. This feature is henceforth referred to as 'low-field magnetoresistance' $(\Delta\rho/\Delta\rho_0)_{\text{Low-Field}}$. Furthermore, the low-field magnetoresistance is obviously superimposed by at least one field-dependent magnetoresistance effect, which is linear to good approximation for most magnetoresistance curves. By extrapolating an approximating line to zero field, the magnitude of the low-field magnetoresistance is separated from a magnetoresistance curve. This is
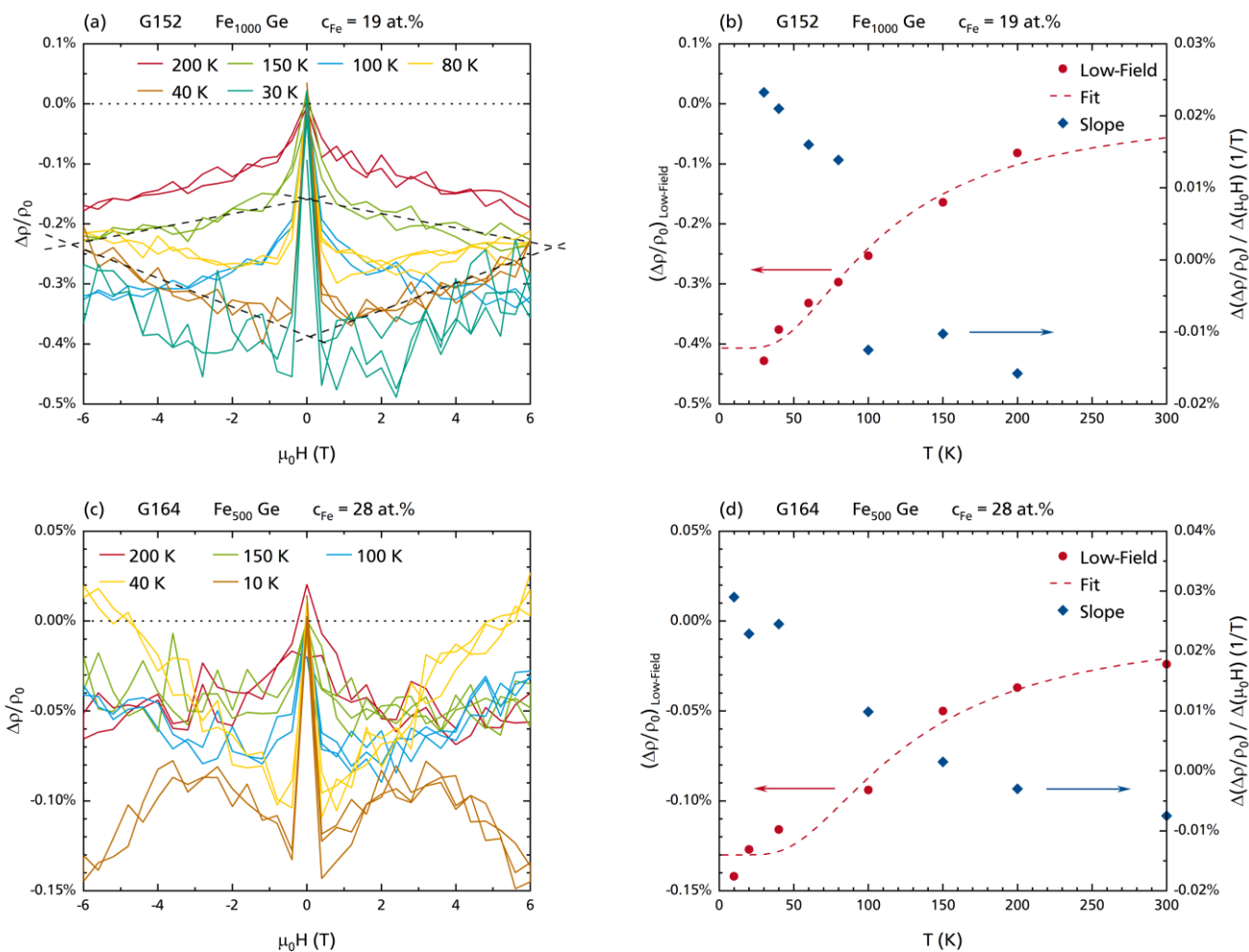
Figure 4-8: Magnetoresistance Curves and Magnetoresistance vs. Temperature plots of Samples G152 and G164

(a) & (c) Magnetoresistance curves recorded at several temperatures of samples G152 and G164, respectively.

(b) & (d) Low-field magnetoresistance (red circles) and slope of linear-in-field change approximations (blue diamonds) for samples G152 and G164, respectively.

The resistance of a sample first drops down to a temperature-dependent maximum magnetoresistance, which increases with decreasing temperature within an applied magnetic field range of $\mu_0 H = 500$ mT as can be estimated from graphs (a),(c). Secondly, when the magnetic field is increased further, the resistance usually follows an almost-linear dependence, except at low temperatures for some samples. The approximate slopes of these estimations are again temperature dependent and even change sign.

exemplarily shown in Figure 4-8(a) for the curves at 150 K and 40 K. Henceforth, the field-dependent component is referred to as 'field-dependent magnetoresistance' and is discussed by means of the slopes of the linear approximations $\Delta(\Delta\rho/\Delta\rho_0)/\Delta(\mu H_0)$. The slope is a good value for comparison since it reflects both sign and strength of the field dependence of the approximated-as-linear effect. The low-field and field-dependent magnetoresistance values resulting from this separation are discussed separately in Sections 4.4.2.1 and 4.4.2.2, respectively.

In Figures 4-8(b),(d) the respective magnitudes of the two effects are shown as a function of temperature. The low-field magnetoresistance is represented by red circles (left scale) while the slopes of the approximating lines are represented by blue diamonds (right scale). For the added fit curves (red, dashed lines) see Section 4.7.3.4. As can be seen, both effects are temperature dependent. The low-field magnetoresistance, on the one hand, is always negative and increases with decreasing temperature. The field-dependent magnetoresistance is characterized by a negative slope at 200 K and above but continuously changes to a positive slope with decreasing temperature. This holds for all samples listed in Table 4-1 (provided they show magnetoresistive behavior). At temperatures below 20 K, for some samples the field-dependent magnetoresistance becomes strongly nonlinear, e.g., for G164, as depicted in Figure 4-8(c). However, the low-field magnetoresistance could still be estimated with the method explained above. Also, at low temperatures the low-field magnetoresistance of some samples decreased again.

In Figure 4-9, a comparison of magnetoresistance curves recorded at 200 K, 100 K, and 40 K is presented, where the data belonging to Fe_{500}-Ge and Fe_{1000}-Ge samples are plotted in separate graphs. For series, three selected samples are shown. Similar plots comparing the magnetoresistance curves of all measured samples are given in Appendix B.

The following statements can be deduced from the data shown in Figure 4-9. First, the low-field magnetoresistance is larger for the larger cluster species and increases with decreasing cluster concentration. Secondly, for both cluster species the low-field magnetoresistance increases with temperature and at the same time saturates at smaller magnetic fields, while the field at which saturation is achieved seemingly does not depend on the Fe concentration. Third, the slopes of the flanks are a function of cluster size and cluster concentration. At high temperatures the slope is negative, reduces in steepness with decreasing temperature, and changes to a positive one at a sample-specific temperature. From G136, which carries by far the thinnest nanocomposite layer (17 nm, see Table 4-1 for comparison) almost no low-field magnetoresistance is observed, although the sample possesses a concentration similar to that of G164. Regarding the VRH hopping length, which is in the range of 10 nm, buffer and protection layer of sample G136 may have contributed to carrier transport to a reasonable amount for this specific sample. As discussed in Section 4.3, also to treat the nanocomposite layer of G136 as a 3D film is not justified because only about two clusters are stacked above each other between buffer and protection layer on average.
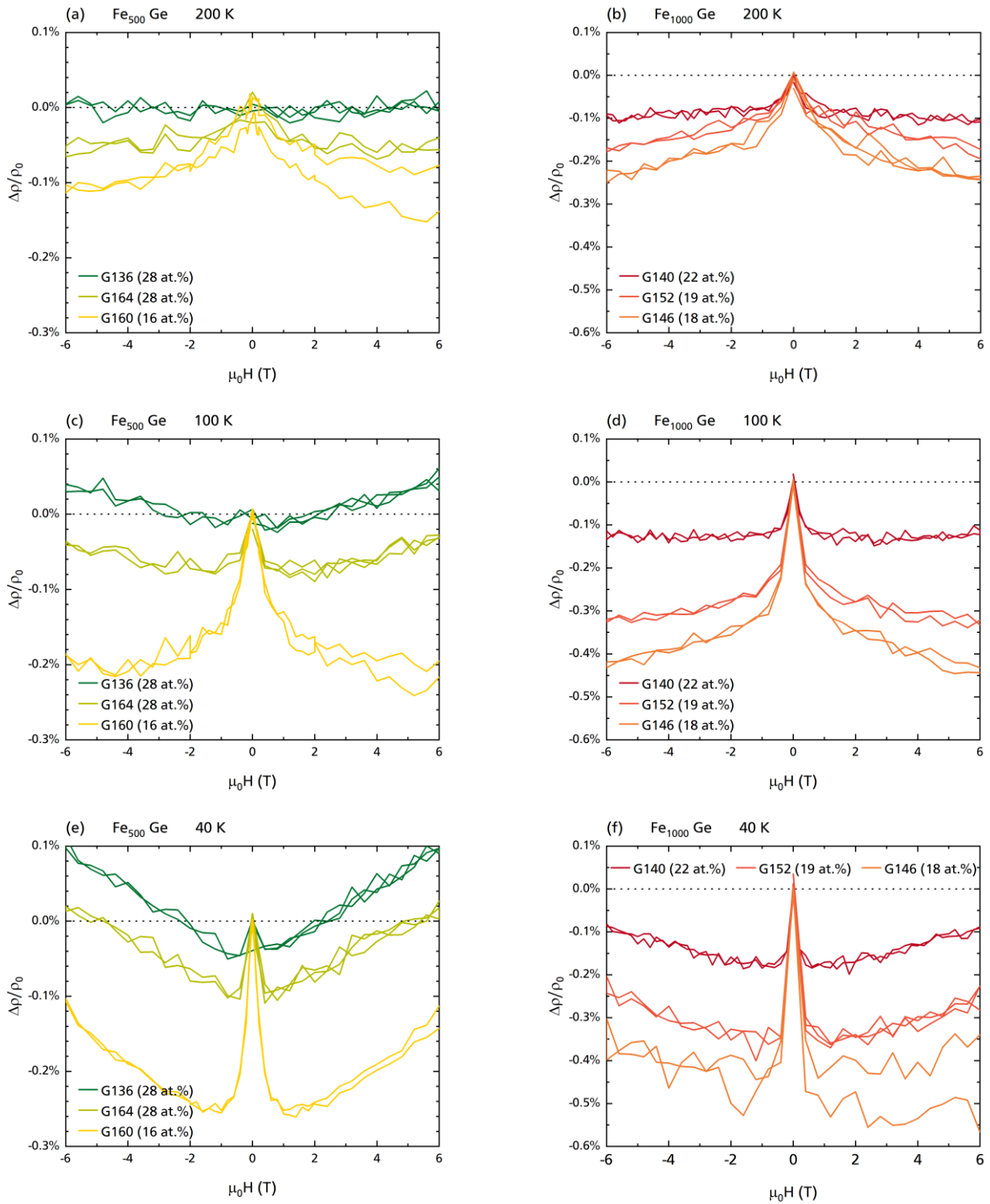
Figure 4-9: Comparison of Magnetoresistance Curves at $200\,\mathrm{K}$, $100\,\mathrm{K}$, and $40\,\mathrm{K}$ of Selected Fe_{500}-Ge and Fe_{1000}-Ge Nanocomposite Films

Sample G160 is represented by data of repeated measurements instead of original data. See Section 4.7.3.3. Similar graphs containing the curves of all samples are shown in Appendix B.
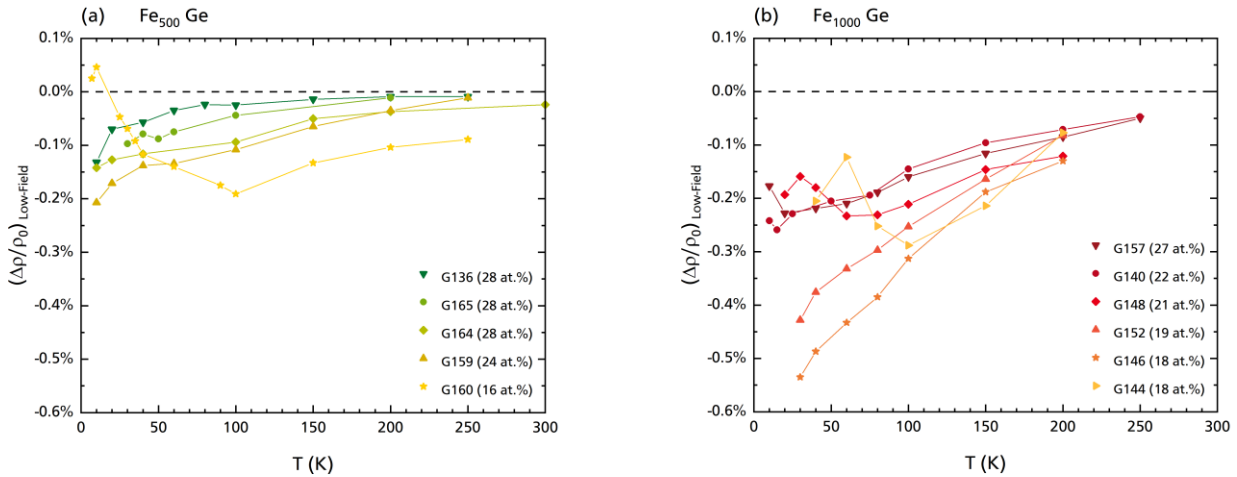
Figure 4-10: Low-Field Magnetoresistance vs. Temperature of all Fe-Ge Samples

  (a) Fe$_{500}$-Ge samples.

  (b) Fe$_{1000}$-Ge samples.

  Data for samples G144, G146 and G160 show a decrease in magnetoresistance magnitude for lower temperatures, intersecting the lines of the other samples. Arguments for this behavior are given later in Section 4.7.3.3.

4.4.2.1 Low-Field Magnetoresistance

The low-field magnetoresistance values of all samples are plotted in Figure 4-10 as a function of temperature. Generally, the magnitude of the low-field magnetoresistance increases with decreasing temperature and is larger for the larger cluster species. The effect remains well below 1% in magnitude. For samples G160, G144, and G148 a reduction in low-field magnetoresistance was observed at low temperatures, approximately from 100 K on. The reduction in magnetoresistance of these samples is associated with shunt currents because it is these three samples that exhibit a much flatter increase in resistivity with decreasing temperature compared to the other samples, as can be seen in Figure 4-12. The flatter resistivity curves will be discussed in Sections 4.7.3.3 and 4.7.3.4. Intersecting magnetoresistance data lines, or some which show the trend to do so, can also be found in literature [161,162], unfortunately lacking any discussion.

4.4.2.2 Field-Dependent Magnetoresistance

Sample G160 has a much lower concentration of clusters compared to the other Fe$_{500}$-Ge samples. Its magnetoresistance curve may have taken a different shape compared to the other samples for the shunt current reason that will be given in Section 4.7.3.3. This may explain why sample G160 diverges from the elsewise quite unambiguous trend given by the slopes of the approximated-as-linear field-dependence curves in Figure 4-11. Separated into Fe$_{500}$-Ge and Fe$_{1000}$-Ge films, Figure 4-11 presents
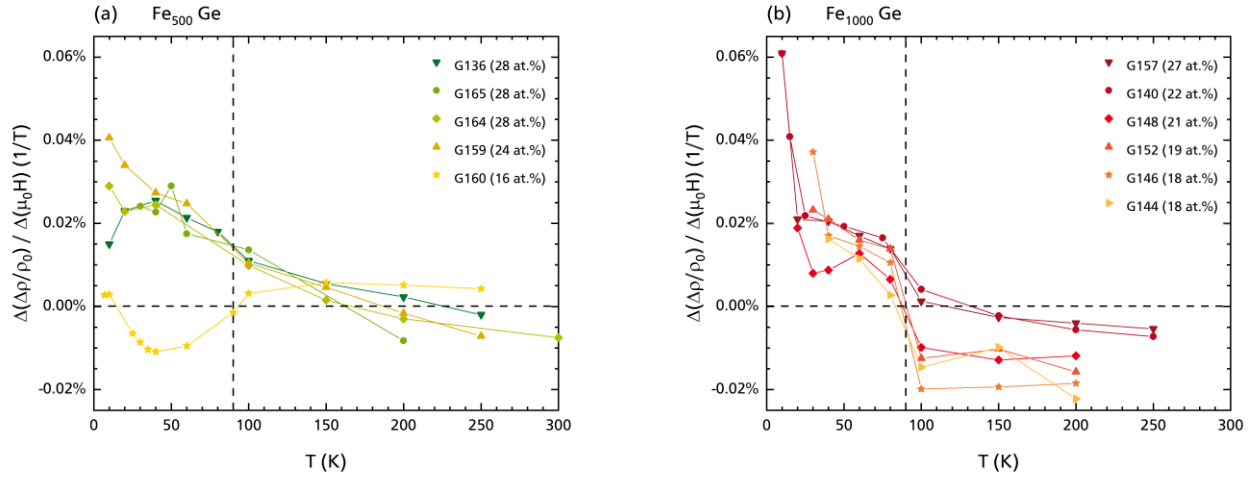
Figure 4-11: Magnetoresistance slope vs. Temperature of all Fe-Ge Samples

    (a) Fe_{500}-Ge samples.

    (b) Fe_{1000}-Ge samples.

       Fe_{500}-Ge curves smoothly increase from an almost-zero slope to a more and more positive one with decreasing temperature. Fe_{1000}-Ge curves follow this trend as well but remain smaller in magnitude compared to the Fe_{500}-Ge curves. Fe_{1000}-Ge curves exhibit a jump from negative to positive values around 90 K in their slope data.

the temperature dependence of all field-dependent magnetoresistance slopes as defined earlier in Section 4.4.2. Slope data points are added to Figures 4-8(b),(d) and 4-28(b) as blue diamonds.

Disregarding sample G160, the variations of the slopes $\Delta(\Delta\rho/\Delta\rho_0)/\Delta(\mu H_0)$ as a function of temperature can be described as follows. Nanocomposite films containing the smaller Fe_{500} cluster species, see Figure 4-11(a), have a slope close but not equal to zero at temperatures above 200 K. Some are negative, some are positive. With decreasing temperature, also the negative ones change to positive ones latest until a temperature of 150 K is reached. From this temperature on, the slopes continue to increase, i.e., the flanks of the magnetoresistance curves become steeper, with further decreasing temperature. Regarding the films containing the larger Fe_{1000} cluster species, Figure 4-11(b), the slopes are negative at high temperature for all samples. For Fe_{500}-Ge samples no systematic dependences on c_{Fe} and MPS are obvious at this point, which is assigned to the only small differences in the Fe concentrations of samples G136 to G159.

In contrast to Fe_{500}-Ge data, differences in the slopes can easily be identified and clearly assigned to different Fe concentrations in the Fe_{1000}-Ge series. The slope vs. temperature curves of samples G157 and G140, which are the samples with the highest Fe concentration, are well separated from the curves of the samples lower in Fe concentration and, at a first view, seem to follow the trend given by the Fe_{500}-Ge samples in graph (a). Samples G152 to G144, both possessing lower Fe concentrations, more or less show a similar slope that is constant to good approximation down until 100 K. Then, the slope

quickly changes over to a positive one within the temperature range limited by 80 K and 100 K. This quick increase also appears in the data of sample G157 and G140, though their slopes did already change to positive ones at 100 K.

4.4.3 Resistivity vs. Temperature Data

A summary of the ρ vs. T curves of all Fe-Ge samples is given in Figure 4-12. Starting at the low ρ side, samples with an Fe concentration too high to show magnetoresistance are represented by dotted lines: green ones represent Fe_{500}-Ge data and blue ones represent Fe_{1000}-Ge data. These samples, with room temperature resistivities between 10^{-5} Ωm and 10^{-4} Ωm in accordance with the minimum metallic conductivity [160], showed only little variation with temperature. As a consequence of their granular metallic structure, the resistivities of these samples decreased with decreasing temperature starting from room temperature and, after arriving at a minimum value, increased again with further lowered temperature. The second feature is assigned to not only the fraction of a-Ge in between the network of mostly touching clusters but also to the a-Ge buffer layer, which separates the nanocomposite film from the contact lines and the substrate in every sample. The decrease of resistivity with temperature dominates over the increase at lower temperature in case of the sample with the highest Fe concentration, (G128). However, the increase of resistivity at lower temperature overcomes and outnumbers the preceding decrease to an extent that increases with decreasing Fe concentration.

When the amount of Fe clusters is reduced further, the Fe-Ge nanocomposite samples start to show magnetoresistive behavior, the first one is G136 with 28 at. %. The room temperature resistivity of these samples vary over four orders of magnitude, i.e., up to the order of 10^0 Ωm, see sample G144. Since sample films with Fe concentrations lower than that of G144 could hardly be measured because of the very high resistivity and, hence, absolute sample resistance, the Fe concentration of G144, 18 at. %, represents the lower limit of the Fe concentration range accessible with the systems and techniques employed in this thesis. The sample with the lowest Fe concentration, (G149) with 15 at. %, does not show magnetoresistive behavior anymore and, therefore, is also drawn as dotted blue line, confirming 10^0 Ωm as the upper limit in room temperature resistivity for magnetoresistance to be observed. The resistivity curve of an a-Ge reference sample, see Section 4.6.1, is added to the graph as well.

The three color-coded, dotted lines are data from original measurements (samples G144, G148, and G160) which are, later in the analysis part, Section 4.7, argued to were measured incorrectly. However, they are shown for consistency reasons. The dashed and solid lines, accordingly belonging to one of the lines as indicated by the arrows, are data recorded in a repetition measurement performed months after the original data sets had been recorded. Arguments and explanations are given in Section 4.7.3.3.
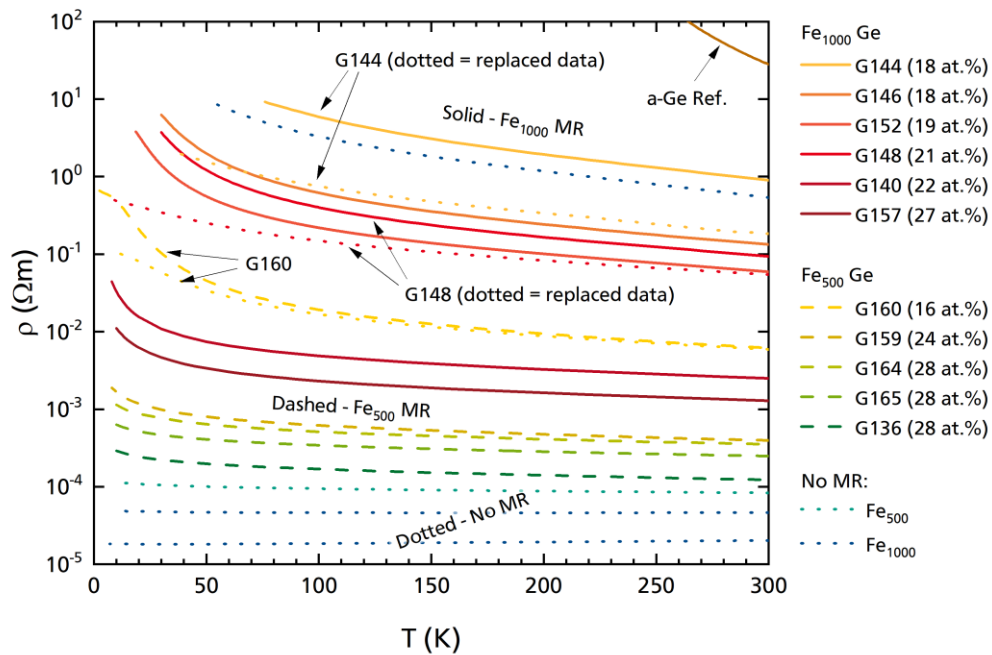
Figure 4-12: Resistivity of all Fe-Ge Samples vs. Temperature

Dashed and solid lines represent Fe_{500}-Ge and Fe_{1000}-Ge samples, respectively, that showed magnetoresistance. Dotted lines represent those which did not: green for Fe_{500} and blue for Fe_{1000} samples. For elsewise colored, dotted lines see text. The curve of an a-Ge reference sample is added as brown, solid line. Resistivity increases with decreasing Fe content and is higher for films containing the larger cluster species (Fe_{1000}).

As a last point, a systematically stronger increase in resistivity with decreasing temperature can be concluded from the plotted data. This feature will be discussed in the context of Figure 4-24(a) in Section 4.7.2.2.

To summarize, the resistivity systematically increases with decreasing Fe concentration and is higher at a fix Fe concentration when clusters of the larger species are embedded in the film. With the exception of samples G148 and G152, the samples of each series are well ordered by their Fe concentration determined via EDX analysis, see Table 4-1.

4.5 Further Characterization Techniques

4.5.1 Scanning Electron Microscopy and Energy-Dispersive X-Ray Spectroscopy

Energy-dispersive X-ray (EDX) spectroscopy performed with a scanning electron microscope (SEM) is a quick and easy method to spatially and quantitatively analyze the elemental composition of a specimen. This way, elemental composition information can be collected in addition to the electron microscopy imaging. The following brief review is based on References [163,164].

The electron beam of the SEM is used to transfer (kinetic) energy to the electrons of the specimen with the aim to remove inner shell electrons from the atoms of the specimen. The resulting vacancy is then occupied by an outer electron of the atom under simultaneous emission of an X-ray photon that carries the difference in binding energy. The binding energies are on the order1 keV. Disregarding very light elements, there are several inner electrons bound in different shells and, hence, with different energies. Consequently, X-ray photons with different energies can be emitted by a specific element with different probabilities, depending on the removed and the filling-up electron. The superposition of elemental-specific transitions is unique for each chemical element. Hence, by reconstructing a recorded spectrum from elemental-specific spectra the elemental composition of a specimen can be determined. The composition is then expressed in terms of concentrations, measured in atom, weight, or mass percent, where the sum of all contributions is 100% in every case. Since the electron beam can be scanned across a specimen this method can also be applied to record maps of elemental composition.

The electrons interact with the specimen via scattering processes and transfer their initial kinetic energy in a sequence of scattering events. This leads to a pear-like interaction volume since the scattering angle is generally nonzero. The penetration depth, i.e., the distance from the sample surface to the bottom of the interaction volume, can exceed 1 µm. The penetration of a 20 keV electron beam into a representative Fe-Ge film is illustrated in Figure D-1 in Appendix D. However, the volume in which the emission of X-ray photons happens is different from the interaction volume of the electrons. On the one hand, photons can be absorbed by the material located between the origin of the photon and the surface of the sample. On the other hand, additional photons can be created by backscattered beam electrons or secondary electrons from preceding scattering events. Therefore, the measured composition is a weighted average of the 'radiating volume'.

For the present work, a Zeiss Leo 1530 SEM equipped with an Oxford Instruments X-Max N50 EDX detector was used. The system was used to obtain high-resolution micrographs, EDX point spectra, and EDX maps of the nanocomposite films. Because the energy deposited by the electron beam could have
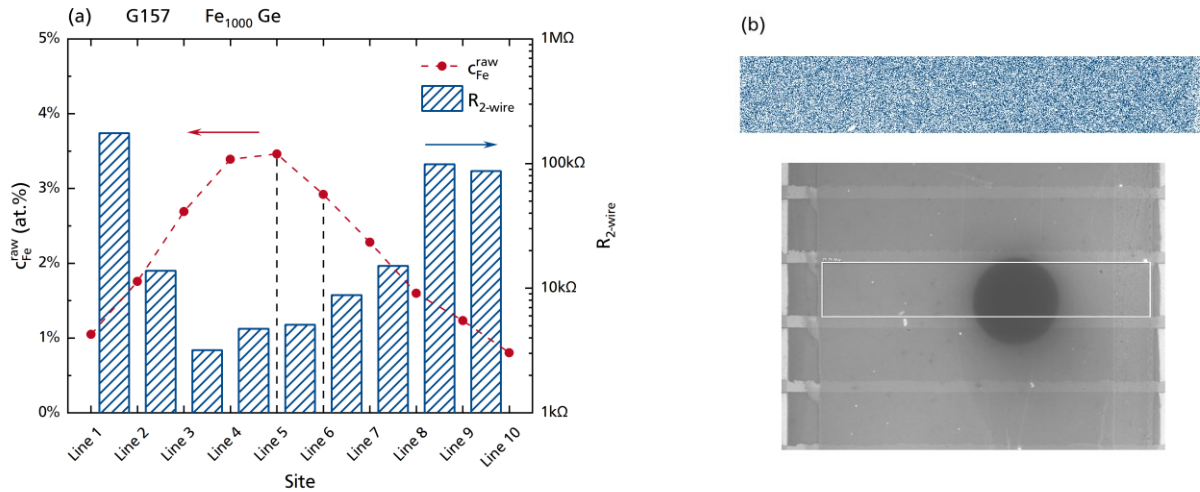
Figure 4-13: Preliminary and Ultimate Characterization of the Fe Concentration for Fe-Ge Sample G157

(a) Preliminary raw Fe concentration in weight percent (red) and corresponding two-wire-resistances (blue columns) of sample G157. The corresponding optical micrograph is presented in Figure 4-7. A Gaussian-like profile can be deduced from the plot as well as a correlation of the Fe concentration and the two-wire resistance. The dashed lines represent the two contact lines of a ten-lines-contact-pattern between which the voltage was sensed during transport measurements and between which the EDX map presented in graph (b) was recorded.

(b) The blue rectangle is the Fe concentration map of the area chosen for transport measurements. It was recorded from the white rectangle shown in the SEM image below the map. The SEM image shows the four contact lines used for four-wire transport measurements. The black circle in the SEM image is an imaging artifact originating from the use of the in-lens detector and did not affect the EDX measurements.

led to annealing due to irradiation of the as-deposited samples the SEM-based steps of characterization were always performed after transport measurements. However, a preliminary determination was performed for each sample as will be explained in the following section. In the present case, the composition of the nanocomposite layers are assumed to not vary along the direction of film growth, i.e., perpendicular to the film plane. Moreover, both nanocomposite and protection layers are assumed to contribute with equal portions, i.e., proportional to their layer thicknesses.

4.5.1.1 Preliminary Determination of the Distribution and the Concentration of Iron

The Fe concentration varies significantly across each sample film. For this reason, the results observed from the nanocomposite samples cannot be compare by the Fe concentrations that can be calculated from the sample-specific CIBD process parameters, i.e., the cluster ion. To estimate the concentration of clusters in a film and, in particular, to locate the region of highest cluster concentration, the elemental composition was analyzed by means of several EDX point spectra prior to transport measurements. The spectra were recorded at the middle of each of the ten Pt contact lines of a sample chip (see Figures 4-4 and 4-7). Potential alteration of the film at these positions is expected to only have minor effects on the subsequent transport measurements, whichever set of lines will be used.

The raw concentrations of Fe, given in atomic percent (at.%), measured for the example sample G157 are plotted in Figure 4-13(a) together with the measured two-wire resistances. A Gaussian-like Fe cluster distribution can be deduced from this plot. The tags 'Line 1' to 'Line 10'on the x-axis refer to the ten Pt contact lines on a sample chip, where 'Line 1' is the uppermost one. Usually, a sample was measured across that pair of lines between which the Fe concentration was highest. The pair of lines chosen for voltage sensing in terms of four-wire resistance measurements is marked by two vertical, dashed lines in graph (a). The presented sample was measured between lines 5 and 6. It can be seen that the measured two-wire resistivity (blue bars, right scale, see Section 4.2.4) and the preliminarily determined Fe concentration are correlated. Note the logarithmic resistance scale. The raw concentration of Fe in sample G157 measured at Line 5 is 3.5 at%. The raw concentrations of C, O, Si, Ti, Ge, and Pt are 18.9 at.%, 24.4 at.%, 39.9 at.%, 0.2 at.%, 11.5 at.%, and 1.6 at.%, respectively. A plot containing the full set of raw concentration data observed for sample G157 is given in Appendix D in Figure D-2.

4.5.1.2 Ultimate EDX-Assisted Determination of the Concentration of Iron

More precise determinations of the concentrations of Fe in the films at the areas chosen for transport measurements were performed following the transport and magnetic properties measurements. After these measurements, changes of the sample films due to enduring 20 keV electron bombardment were deemed acceptable. Therefore, EDX elemental maps between the voltage sensing Pt lines were recorded for each film. An example map, i.e., that of sample G157, together with the corresponding SEM micrograph are shown in Figure 4-13(b). There, four lines of the Pt contact line pattern, more precisely, lines 4 to 7, are visible in the SEM image.

As stated in the introduction, one problem was the weighting of signals coming from the protection layers and the nanocomposite layers. For simplicity, it is assumed that both layers contribute to amounts proportional to their thicknesses. This is justified because both the Pt and even the Ti of the contact lines (see Section 4.2) could easily be resolved even for the thickest sample G144 ($\sim$600 nm from sample surface to contact lines). The result of a Monte Carlo simulation of the trajectories of electrons penetrating into an Fe-Ge CIBD sample are attached in Appendix D in Figure D-1. The simulation shows that 20 keV electrons propagate deeper than 1 μm into the sample, i.e., deep down into the Si substrate.

The atomic concentration of Fe in a nanocomposite layer was calculated from the EDX data as follows. Let N_{meas} be the number of all atoms in the sample that contribute to the measured elemental concentrations. The raw atomic concentrations are defined as $c_i^{raw} = N_i/N_{meas}$, where i denotes the different elements present in the sample. In particular, the concentration of the cluster-type atoms is $c_{Cl}^{raw} = N_{Cl}/N_{meas}$ and that of the matrix-type atoms is $c_M^{raw} = (N_B + N_M + N_P)/N_{meas}$. Note, that matrix-type atoms occur in three different layers. They form the Buffer and the Protection layer, as well

as the <u>M</u>atrix in the nanocomposite layer. Further, let $c = c_{Cl}^{raw}/(c_{Cl}^{raw} + c_M^{raw}) = N_{Cl}/N_{tot}$ be the fraction of cluster-type to the sum of cluster- and matrix-type atoms, where $N_{tot} = N_B+N_M+N_{Cl}+N_P$ is the total number of these. The same ratio restricted to the nanocomposite layer, i.e., the concentration of cluster-type atoms in the nanocomposite, is $c_{Cl} = N_{Cl}/(N_{Cl} + N_M)$. Then it is

$$N_{Cl} = c\, N_{tot} = c\, (N_B + N_M + N_{Cl} + N_P) = c\, \left(N_B + N_M + \frac{c_{Cl}}{1 - c_{Cl}} N_M + N_P \right) \stackrel{!}{=} \frac{c_{Cl}}{1 - c_{Cl}} N_M. \qquad [4\text{-}8]$$

As the number of matrix-type atoms in a layer is proportional to the amount of material counted by the quartz crystal balance and because the output film thickness was calibrated with the help of an XRR reference sample, the numbers of atoms can be replaced by the thicknesses of the layers that were deposited onto a sample $N_i \rightarrow t_i$. Then, solving for the cluster-type atomic concentration within the nanocomposite c_{Cl} yields

$$c_{Cl} = \left(1 - \frac{(1 - c)\, t_M}{c\, (t_B + t_P) + t_M} \right). \qquad [4\text{-}9]$$

From this result, volume concentration c_{vol}, mean particle distance MPD, mean particle separation $MPS = MPD - d_{Cl}$, and nanocomposite layer thickness t can be calculated.

$$c_{vol} = 100\% \left(1 + \frac{1 - c_{Cl}}{c_{Cl}} \times \frac{m_{at}^M}{m_{at}^{Cl}} \times \frac{\rho_{bulk}^{Cl}}{\rho_{ref}^M} \right)^{-1}, \qquad [4\text{-}10]$$

$$t = t_M \left(1 + \frac{c_{Cl}}{1 - c_{Cl}} \times \frac{m_{at}^{Cl}}{m_{at}^M} \times \frac{\rho_{ref}^M}{\rho_{bulk}^{Cl}} \right), \qquad [4\text{-}11]$$

$$MPD = \left(\frac{V_{Cl}}{c_{vol}} \right)^{1/3} = \left(\frac{N_{at/Cl}\, m_{at}^{Cl}}{\rho_{bulk}^{Cl}\, c_{vol}} \right)^{1/3}, \qquad [4\text{-}12]$$

$$MPS = MPD - d_{Cl} = \left(\left(\frac{\pi}{6\, c_{vol}} \right)^{1/3} - 1 \right) d_{Cl}, \qquad [4\text{-}13]$$

where

$$V_{Cl} = \frac{\pi}{6} d_{Cl}^3 = \frac{N_{at/Cl}\, m_{at}^{Cl}}{\rho_{bulk}^{Cl}} \qquad [4\text{-}14]$$

was used to express the volume of a cluster V_{Cl} and its diameter d_{Cl}. The clusters are assumed to be spheres with a homogeneous distributions of mass.

The following mass densities of Fe, Ge, and Ag were used for calculations throughout this thesis:

$\rho_{Fe} = 7.87 \text{ g/cm}^3$ bulk density of Fe [58],

$\rho_{Ge} = 5.1 \text{ g/cm}^3$ for a-Ge, determined via XRR from a reference sample, and

$\rho_{Ag} = 10.0 \text{ g/cm}^3$ for Ag determined from reference sample films via XRR.

For comparison, the densities of c-Ge and Ag as listed in literature are 5.32 g/cm^3 and 10.50 g/cm^3, respectively [58]. In case of Ge the lower density is because Ge grew amorphous under the conditions present during deposition. The density of Ag differs by 5% from the literature value. With the mass densities given above, the cluster diameters and volumes given in Table 4-2 can be calculated. Fe_{1500} clusters are only used in Fe-Ag nanocomposites, see Chapter 5.

Table 4-2: Calculated Diameters and Volumes of Fe_{500}, Fe_{1000}, and Fe_{1500} Clusters

	Fe_{500}	Fe_{1000}	Fe_{1500}
d_{Cl} (nm)	2.2	2.8	3.2
V_{Cl} (nm^3)	5.9	11.8	17.7

Table 4-3 compares the Fe concentrations calculated from deposition data c_{dep} with those determined with the explained EDX-based method c_{Cl}. I_{Cl} is the average current of clusters absorbed by the sample potential U_S. The cluster ion current I_{Cl} multiplied with the time of deposition T_{dep} divided by the elemental charge e yields the number of clusters deposited into the red circle illustrated in Figure 3-6(c). Meanwhile, matrix material with a thickness t_M was grown during T_{dep}. The EDX-based value given on the right-hand side was calculated from the ratio c explained above. As can be seen, the values determined by means of EDX are more than twice as large as the values calculated from deposition data.

Table 4-3: Comparison of Fe Concentrations Calculated from Deposition and EDX Data

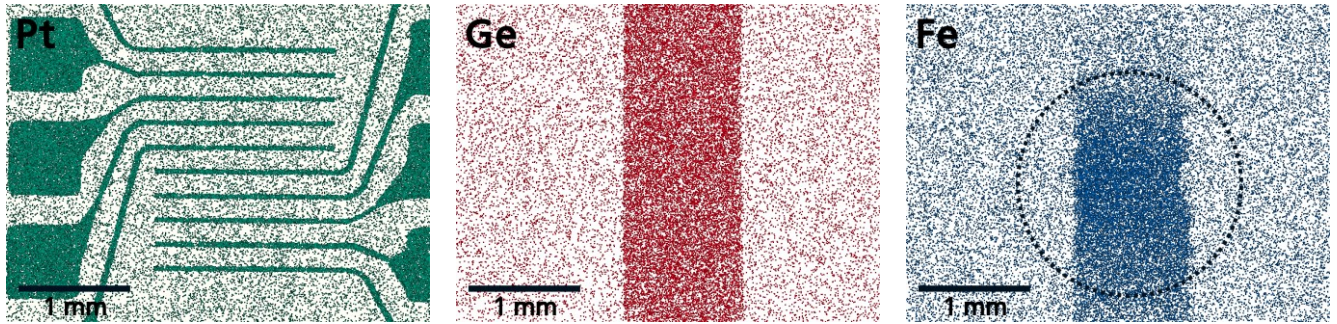| Sample ID	Clusters-Matrix	$I_{Cl} \times T_{dep}$	t_M (nm)	c_{dep} (at. %)	c	c_{Cl} (at. %)
G144	Fe_{1000}-Ge	$-97 \text{ pA} \times 6 \text{ h}$	473	6.4	0.155	17.6
A184	Fe_{500}-Ag	$-111 \text{ pA} \times 3 \text{ h}$	163	4.1	0.095	10.1

Figure 4-14: EDX Maps of Fe_{1000}-Ge Sample (G128)

From left to right the Pt, Ge, and Fe EDX signals are shown. The Pt contact pattern and the Ge stripe are clearly resolved. The Fe signal reveals the Fe cluster spot, i.e., the intensity profile of the cluster ion beam. A circle with a diameter of 2 mm is added as reference.

4.5.1.3 Full Sample EDX Elemental Mapping

EDX elemental maps were acquired for some of the samples to examine the total distribution of Fe cluster on the sample. This was done at the largest possible scan field of the SEM (~4 mm) at the working distance optimal for EDX measurements (8.5 mm). As an example, the EDX maps observed from sample (G128) are shown in Figure 4-14. Besides a clear signal from the Ge stripe, both the Pt contact lines and the spot of Fe clusters are clearly resolved. Ideally, the concentration of Fe should follow a top-hat distribution since it is an image of the 1st skimmer of the CIBD system, see Section 3.2. However, since the cluster source is most likely not optimally aligned with the 1st skimmer, the resulting image, i.e., the distribution of Fe clusters on the deposition sample, deviates from a top-hat profile. Moreover, the beam of cluster ions can be defocused during deceleration of the cluster ions or because of charging effects due to the badly conducting sample surface. This leads to a more Gaussian-like concentration profile. However, the distribution of Fe in the region of maximum concentration is approximately uniform.

Charging effects on the sample surface may have also led to cluster accumulations along the edges of the nanocomposite films, especially where the Pt contact lines meet the film. Such accumulations appear as dark spots at the left-hand edge of the film presented in the optical micrograph in Figure 4-7. Charging effects can be also identified in Figure 4-14 by comparing the straight edges of the Ge film (red signal) with the fringed edges of the Fe spot (blue signal).

The diameter of the cluster ion beam can be estimated to be within 1 mm to 2 mm from the observed Fe concentration distribution. A circle with a diameter of 2 mm is added to the Fe signal image as reference.

4.5.2 Magnetic Properties

4.5.2.1 Measurement of Magnetic Properties

Nanometer-sized magnetic clusters tend to be in a single-domain state below the Curie temperature. Behaving as giant paramagnetic moments, such particles possess superparamagnetic properties across a temperature range that is limited by the blocking temperature to the lower side and by the Curie temperature to the upper side. At temperatures below the blocking temperature the particles behave like ferromagnets. The superparamagnetism of nanoparticles is explained in Section 2.3.

To identify superparamagnetism in the present nanocomposites the magnetic properties were examined using SQUID magnetometers (Quantum Design MPMS XL and VSM). Each sample was inserted into the respective sample chamber using a plastic straw, which is a common-practice way of mounting, and with the long side of the sample film pointing in direction of the magnetic field.

For each sample a ZFC/FC sequence at $\mu_0 H = 20$ mT between 300 K and 5 K was used to prove the existence of superparamagnetic nanoparticles by the existence of a blocking temperature and paramagnetic behavior well above this temperature. For ZFC and FC measurements and superparamagnetism see Section 2.3.

After the ZFC/FC sequence the magnetization of each sample was recorded at 300 K and 5 K while the magnetic field was ramped in a loop similarly to the recording of magnetoresistance curves (see Section 4.4). The maximum applied magnetic field was $\mu_0 H_{max} = 4.5$ T. Again, the MultiVu software by Quantum Design was used to control the instruments and the measurements. The sequence codes are similar to those used for transport measurements printed in Appendix A, i.e., follow the same logic.

Diamagnetic contributions from the Si substrate to the recorded magnetization vs. magnetic field curves are eliminated by subtracting the average linear contributions observed at high fields.

Also, in contrast to transport measurements, the response of the entire volume of a nanocomposite film is recorded in magnetization measurements. Besides the eliminated contributions of the substrate, the region with the highest amount of Fe will, of course, provide the largest contribution to the measured magnetization. However, the results of the magnetic measurements do not directly correspond to the results observed from transport measurements. The latter only contain information from the region a sample was measured at, nevertheless, this usually was the region of highest Fe concentration.
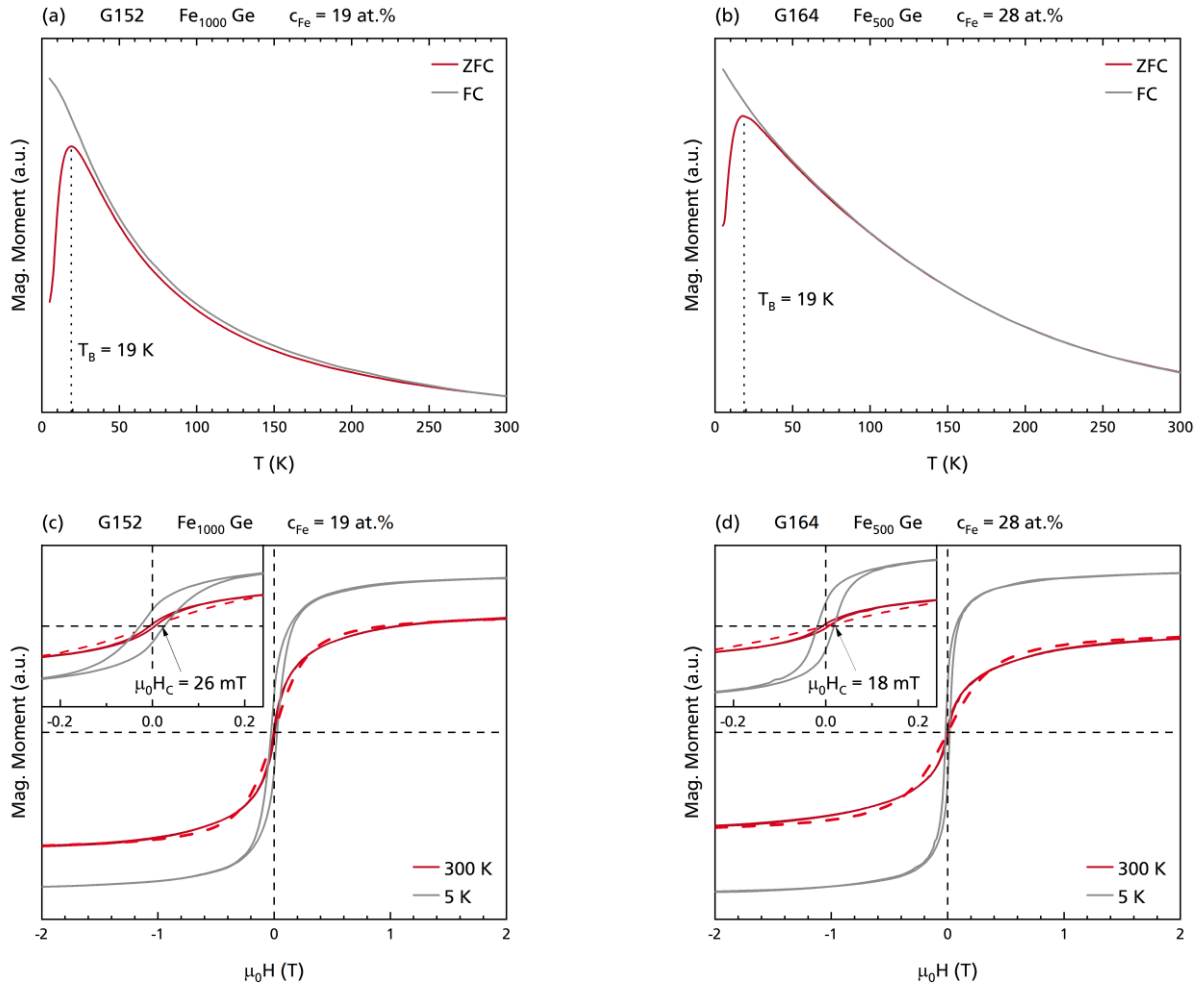
Figure 4-15: Magnetization vs. Temperature and Magnetic Field of Fe_{500} and Fe_{1000} Clusters Embedded into a-Ge Matrix

    (a) & (b): Example zero-field and field-cooled curves of samples G152 and G164, respectively.

    (c) & (d): Corresponding magnetization curves at 300 K. and 5 K. The dashed lines are approximating Langevin functions.

4.5.2.2 Results of Magnetic Properties Measurements

SQUID measurements were used to provide evidence for the presence of clusters in the samples used for magnetoresistance experiments. Except for samples (G149) and (G161), SQUID measurements were performed for all samples listed in Table 4-1. For this purpose, each sample underwent ZFC/FC measurements as explained above. Two of such measurements are shown in Figures 4-15(a),(b). The blocking temperature, more precisely, the temperature for maximum magnetization of the ZFC curve (red), is 19 K for both samples. The ZFC and the FC curves (gray) coincide to good approximation at larger temperatures, which means the measured magnetic moments are caused by the external magnetic field rather than remnant collective magnetization.

Owing to the deposition process (Section 4.2), in particular, to the Gaussian-like cluster ion beam profile, the slit deposition mask and a fix orientation of the sample under deposition to the cluster ion beam, each sample was grown with an Fe concentration distribution changing across both its film width and length, see Sections 4.5.1.1 and 4.5.1.3. Because magnetic dipole-dipole interaction between clusters depends on their distance and, therefore, the local Fe concentration, blocking of clusters is not an abrupt effect but a fluent change in the deposited nanocomposite films. Definitely, the area of a sample highest in concentration dominates its magnetic properties.

The magnetization curves corresponding to the ZFC/FC curves shown in Figures 4-15(a),(b) are plotted in Figures 4-15(c),(d), respectively. The gray curves correspond to data recorded at 5 K. Here, below the respective blocking temperature, clusters are blocked and reveal a ferromagnetic nature. Accordingly, hysteresis in magnetization was observed at 5 K for both samples. The coercive fields are 26 mT and 18 mT, respectively, as written in the insets. The insets show the same data, however, reduced to a range within which the hysteresis is clearly visibly. A third magnetic hysteresis plot is presented in Figure 4-28(d).

As expected, the samples exhibit larger magnetic moments at lower temperatures. At 300 K, well above the blocking temperatures, anhysteretic magnetization behavior caused by the continuous alignment of superparamagnetic moments was observed. To be precisely, the magnetization curves have the shape of an initial magnetization curve, however, the magnetization curves remain fully reversible. The samples behave like ferromagnets, however, without being subject to magnetic hysteresis.

The effective magnetizations of the samples are average values over one SQUID measurement period and, thus, reduce with increasing temperature because of the decreasing relaxation time of the clusters. Therefore, the red anhysteretic magnetization curves, which are each approximated by a Langevin function (Equation [2-9]) in the plots, represented by the dashed, red lines, are less prominent than the gray hysteretic ones. Both the effect of blocking and a magnetic hysteresis at 5 K were observed for all measured nanocomposite samples.

Generally, for nanocomposite samples showing magnetoresistive behavior blocking temperatures between 10 K and 40 K were observed, as shown in Figures 4-16(a),(b). There, the blocking temperatures of all samples are plotted vs. the concentration of Fe, graph (a), and vs. the sample resistivity, graph (b).

When the data point belonging to sample G136, highlighted in Figure 4-16, is disregarded because of the sample's small thickness (see Section 4.3), it can be concluded that the blocking temperature increases with increasing cluster concentration and is generally larger for the larger clusters. Fe_{1000}-Ge samples that do show magnetoresistance exhibit an average blocking temperature of 25 K, the average
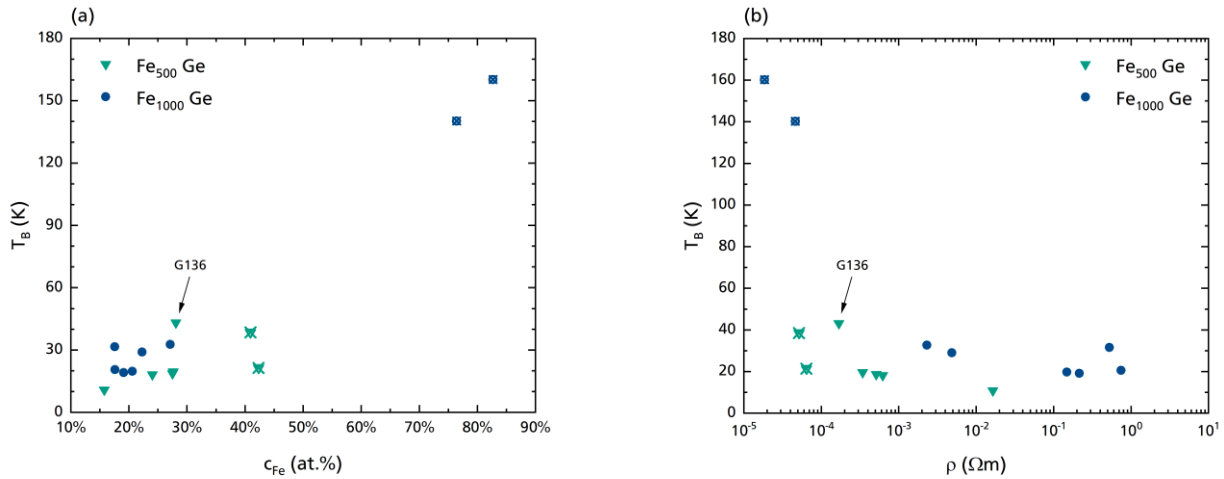
Figure 4-16: Blocking Temperature vs. Fe Concentration and Resistivity

> Above an Fe concentration of $30\,\mathrm{at.\%}$, see graph (a), and a corresponding resistivity lower than $10^{-4}\,\Omega\mathrm{m}$, see graph (b), Fe clusters are percolating in the nanocomposite samples. This causes the blocking temperature to increase as there are effectively larger particles in the layers due to accumulations of touching clusters. Data points of samples that do not show magnetoresistive behavior are represented by crossed symbols.

of Fe_{500}-Ge ones is 17 K. Samples with an Fe concentration too high to show magnetoresistive behavior, as discussed in Sections 4.3 and 4.4.3, are represented by crossed symbols in the plots. These samples possess larger blocking temperatures than those samples that do show magnetoresistive behavior. Obviously, for these samples the blocking temperature increases with increasing Fe concentration. This is assigned to both stronger magnetic interaction between the clusters and to the formation of larger Fe compounds.

Also, no cooperative ferromagnetic phase of blocked Fe clusters was found from FC curves at low temperatures [165]. With the definition of the blocking temperature, Equation [2-16], the bulk magnetocrystalline anisotropy constant of Fe at the temperature of LHe $K_1 \approx 53.1 \times 10^3$ J/m^3 [166] and the cluster volume according to Table 4-2 for Fe_{1000} clusters a blocking temperature of about 2 K can be estimated. All samples were found to exhibit a blocking temperature well above that single-particle blocking temperature. This is related to collective blocking of cluster aggregates due to exchange coupling between touching clusters and dominating dipolar interaction between isolated compounds [25,167].

In the nanocomposite samples discussed in the present chapter clusters are only separated by distances in the range of their diameter, i.e., of 1 nm to 2 nm. Since they are expected to magnetically interact, the Langevin functions approximating the magnetization curves shown in Figures 4-15(c),(d) as dashed lines are expected to need the magnetic moment appearing in the argument to be set to values exceeding the moment of a single cluster. The approximations require $4200\,\mu_B$ and $3000\,\mu_B$,

respectively, to follow the shape of the magnetization curves at 300 K. These moments correspond to superparamagnetic base units of 1.9 Fe_{1000} and 2.7 Fe_{500} clusters, respectively, assuming every atom provides the moment of an α-Fe atom, which is 2.2 μ_B. The reason is agglomeration: The observed moments are the apparent moments of agglomerating coupled clusters [25]. With increasing Fe concentration the average amount of coupled clusters increases, which is the reason for the blocking temperature to increase.

4.5.3 Thermal Annealing, Hydrogenation, and Crystallization of Fe-Ge Nanocomposite Films

The deposited Fe-Ge nanocomposite films represent a nonequilibrium state of the Fe-Ge system. In general, several alloys can form in the Fe-Ge system, see Section 4.1, and up to 17.5 at.% of Ge can dissolve in bcc α-Fe. Also, transport in a-Ge is sensitive to thermal annealing. Moreover, disabling the dangling bonds of an amorphous semiconductor by hydrogenation is known to change the transport properties of the amorphous semiconductor. From the observed changes in transport and magnetometric measurements further conclusions on the as-deposited nonequilibrium nanocomposite phase may be drawn. For this purpose, both the a-Ge reference twin sample G2-45A&B (see Section 4.6.3) and five nanocomposite films (G144, G146, G148, G152 and G160) were annealed under the presence of hydrogen gas, more precisely, in 5×10^{-5} mbar ARCAL 15 atmosphere (Air Liquide ARCAL™ 15 is a mixture of Ar gas and (5 ± 0.5) vol.% of H_2) at 220 °C (Section 4.7.6). Both the reference samples and one nanocomposite sample, G152, were also annealed at 700 °C, where a-Ge is expected to crystallize and the constituents of the nanocomposite film are expected to intermix (Section 4.7.7). The samples underwent a different number of annealing steps under different conditions. Each sample was characterized by magnetotransport measurements prior to the annealing procedure and after each annealing step.

The annealing temperatures were determined with a thermocouple attached to a dummy sample holder installed such way that the temperature was sensed right at the position where the sample chips were installed during the annealing experiments.

As will be explained in more detail in Section 4.6.3, a-Ge starts to crystallize when annealed in the temperature range from 300 °C to 450 °C. Therefore, equilibrium phases according to the Fe-Ge phase diagram should form at 700 °C, see Figure 4-1. On the high Fe concentration side, i.e., in the vicinity of Fe clusters, neighboring clusters may merge and segregate as Fe inclusions. At an equilibrium concentration of ~20 at.%, which is a good estimate for the average concentration of Fe in all samples of Table 4-1 that show magnetoresistive behavior, the parasitic ferromagnetic phase $FeGe_2$ in

conjunction with a phase of pure c-Ge would be present. In between the local-concentration-limit (locally high Fe concentration) and the homogeneous-intermixing-limit, another ferromagnetic phase, Fe_5Ge_3, with a Curie temperature well above room temperature ($T_C = 485$ K [117]) exists according to the phase diagram. Therefore, annealed Fe-Ge nanocomposites may form good magnetic semiconductors.

4.6   Amorphous Germanium Reference Film

In this section, an a-Ge reference film that is deposited across two contact line patterns similar to those used for the transport measurements of nanocomposite samples is presented. The a-Ge contact patterns consist of only four lines, are smaller in line width, and come with a much narrower gap in between them compared to the pattern deposited onto CIBD sample chips. The two contact patterns are sufficiently apart from each other to be treated as independent from each other. For that reason, the term 'twin samples' will also be used. Their sample IDs are G2-45A and -B. Transport processes and the magnetoresistance of a-Ge are discussed in detail in Section 4.1.2.

4.6.1   Resistivity of the Amorphous Germanium Reference Sample

To examine the dependence of the matrix material properties upon variation of temperature and magnetic field, the reference twin sample G2-45A&B was prepared under conditions similar to those of the nanocomposite samples (see Sections 4.2): Sputter gas flow (without sputtering) for similar ambient pressure, LN_2 cooled sample in the deposition chamber, similar deposition rate of Ge, use of Si substrate with a 200 nm SiO_2 surface layer, and contact lines consisting of 5 nm Ti + 20 nm Pt.

One property that had to be taken into consideration was the enormous total resistance of a-Ge of more than 200 MΩ that was measured across Fe-Ge samples between pairs of contact lines away from the cluster spot. To achieve the lowest possible resistance of a reference sample film the gaps between the contact lines had to be reduced to a minimum, while simultaneously the cross-sectional area to be penetrated by the excitation current, i.e., the film width, had to be maximized.

Because the film width did not have to be restricted to the diameter of the cluster ion beam by a slit deposition mask, see lower row in Figure 4-5, maximizing the film width was one measure to increase the cross-sectional area. For this reason, a larger 10 mm × 10 mm Si chip was used for the a-Ge reference film. Making full use of the maximum possible width of a sample, a 5.6 mm wide film of a-Ge was deposited and contacted along its full width.

As a second measure, another contact line pattern with a narrower spacing was deposited onto the chip used for the reference film. For this reason, an alternative contact line pattern was structured into a positive resist using electron beam lithography[†]. After lithography, the resist was developed, then Ti and Pt were deposited in the same way as for the regular CIBD sample chips, and a lift-off process yielded the final contact line pattern shown in Figure 4-17(a). There, the structure is already covered by the a-Ge film, which appears blue in the micrograph. The bonding pads on the left-hand side are covered with the leftover Al from wire bonding connection. The inset shows the four parallel contact lines with their narrow spacing.

With this more complicated process, two patterns of four equally sized 10 μm wide contact lines with a spacing of only 2.0 μm could be deposited onto the 10 mm × 10 mm chip. Amorphous Ge was deposited onto this sample chip. With a spacing of several millimeters between the two contact patterns the two contacted areas could be treated as insulated from each other and, therefore, as individual samples. The individual thicknesses of the deposited a-Ge were determined via AFM profilometry to be 490 nm (G2-45A) and 450 nm (-B), respectively.

It was observed that the resistance of the a-Ge film at first strongly depended on ambient parameters after the sample was loaded into the PPMS. Even purging the sample annulus of the PPMS and sealing it containing a thin atmosphere of several millibars of He gas had large influence on the measured resistance. Waiting for the film to stabilize, the sample was left inside the annulus under constant conditions, including constant excitation current load, for about two days. Then, the measurement routines were started.

These efforts allowed to measure the reference twin sample down to temperatures as low as 220 K. In the corresponding plot, see Figure 4-17(b), a kink in the resistance appears at about 250 K as can be seen best from the data of sample B. This kink translates to peaks in the plots of the derived parameters E_{Act} and T_0, where E_{Act} is the pro-forma calculated activation energy of a potential thermally activated process in graphs (c),(d), respectively. A constant activation energy E_{Act} is the identifying feature of thermally activated transport and comes from the Arrhenius law used to empirically model such processes (rate $\propto \exp(-E_{Act}/k_B T)$). For the VRH parameter T_0 see Equations [4-4] and [4-16].

Since this kink artifact is reproducible it can be caused either extrinsically by thermal elongation due to the different thermal expansion coefficients of Pt, a-Ge, etc., or intrinsically by activation of other transport processes in addition to VRH through states close to the Fermi level. These may be hopping processes in band tail states or even thermally activated transport via conduction band states above the

---

[†]   Because access to the required equipment was restricted to well-trained coworkers only, the electron-beam lithography process was performed by Dr. Thomas Reisinger.
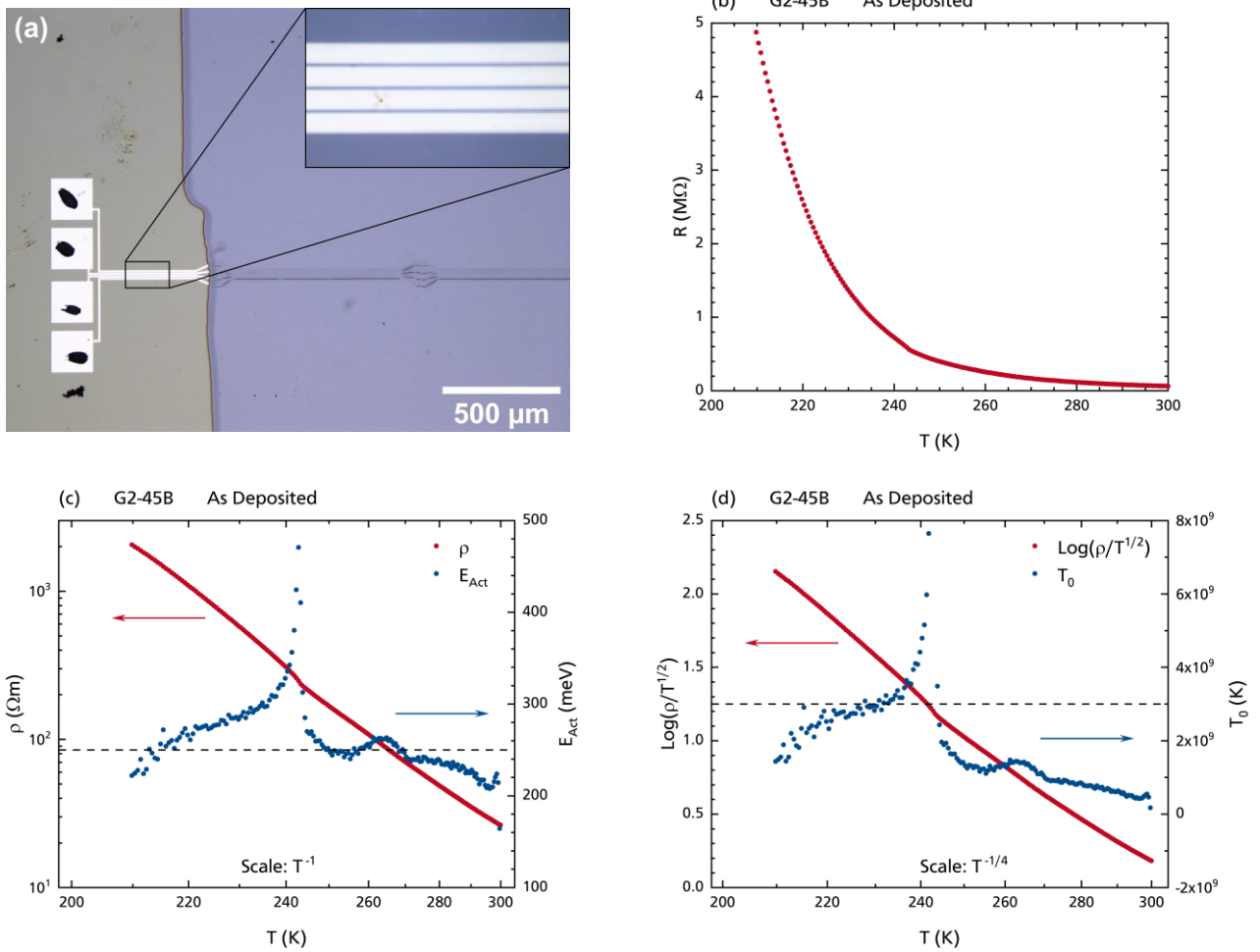
Figure 4-17: Optical Micrograph and Various Resistance / Resistivity vs. Temperature Plots of the a-Ge Reference Sample

(a) Optical micrograph of one of the two contact line patterns of sample G2-45. On the left side, four bonding pads with remnant Al wire are visible. The blue part is the a-Ge film. The contact lines each have a width of 10 μm and gaps of 2.0 μm between them. Because of the required electron-beam lithography process the contact pattern was performed by another person[†].

(b)–(d) Resistance of sample G2-45B plotted vs. temperature in three differently scaled graphs:
(b) ρ vs. T, (c) $\log(\rho)$ vs. T^{-1}, and (d) $\log(\rho/T^{1/2})$ vs. $T^{-1/4}$ ('VRH scaling').

Blue data points in graphs (c),(d) represent the slope in the according scaling, see Section 4.7.2.3 for an explanation. The dashed lines represent the suggested literature value $E_{Act} = 250\,\mathrm{meV}$ for activated transport according to Pollak et al. [156] and an estimated value for the VRH parameter $T_0 = 3 \times 10^9\,\mathrm{K}$, respectively, for the shown data.

mobility edge. From Figures 4-17(c),(d) no clear conclusion can be drawn. An activated transport process happening with an activation energy of $E_{Act} = 250\,\mathrm{meV}$, indicated by the horizontal, dashed line in Figure 4-17(c), is supported by data from Pollak et al. [156]. They found conductivity in an a-Ge sample to be activated with a similar activation energy above room temperature while below VRH is responsible for charge carrier transport. At temperatures lower than the temperature corresponding to the kink the VRH parameter tends to $T_0 \approx 3 \times 10^9\,\mathrm{K}$ as indicated by the horizontal, dashed line in

Figure 4-17(d). This value is one order of magnitude larger than the values stated in literature (see Section 4.1.2.3) and yields a density of states of $D(E_F) \approx 5 \times 10^{16} \text{ cm}^{-3} \text{ eV}^{-1}$.

Because of the kink and the narrow examined temperature range, resistance data are not as robust as for the as-deposited reference sample. Below 220 K the PPMS's range of precise resistance measurement was exceeded. However, data of the annealed Ge reference sample (Section 4.6.3) support the given interpretation.

Also, co-deposited Fe clusters distort and interrupt the a-Ge matrix during deposition. This strategy of growth leads to a discontinuous structure of the a-Ge matrix in which temperature-dependent strain can easily occur and influence the sample properties. Therefore, the a-Ge reference samples may not represent the properties of the a-Ge forming the matrix between the clusters of the co-deposited nanocomposite samples.

4.6.2 Magnetoresistance of the Amorphous Germanium Reference Sample

Magnetoresistive properties of the a-Ge reference sample were measured down to as low as 240 K and are presented in Figure 4-18. During the recording of the magnetoresistance curves, the measured resistances still decreased continuously in about the same order as the applied magnetic field affected the resistance. This is depicted in Figure 4-18(a), where the resistance of G2-45A is plotted over the time lapse of a complete field loop sequence. The dashed line indicates a linear-in-time change of the zero-field resistance of the film from the first reversal of the direction of field ramping at 6 T until the end of the hysteresis cycle (again at 6 T) so that $R(H,t) \approx R_0 + \alpha(t - t_0) + \Delta R(H)$ was a good approximation to cancel out the continuous reduction of the sample resistance. The data point (t_0, R_0) was chosen to be the first zero-field pass after applying maximum field. The slope α was calculated using the second zero-field pass at (t_1, R_1). The assumed linear decrease is justified by the resulting curve which is shown in Figure 4-18(b) (yellow data, the green data are the raw data from graph (a)). In the shown case the change in resistance within the time span from maximum field ($t \approx 1.5$ h) to maximum field ($t \approx 6.5$ h) is about two times larger than the change caused by the maximum applied magnetic field of 6 T. The initial curve misleadingly features a strong field dependence. However, the steeper slope is due to a finer spacing of the magnetic field used for data acquisition in this field range. Independence from the change in field ramping is evidenced by the linear change in time from the start until the maximum field is reached for the first time at $t \approx 1.5$ h. In Figures 4-18(c),(d), only data without the initial curves are shown. Except at 240 K, all curves were recorded with an excitation current of 100 nA.

Although the data remain vague, especially for positive field polarity, nonetheless, the change of the magnetoresistance both as a function of the magnetic field and of the temperature could be
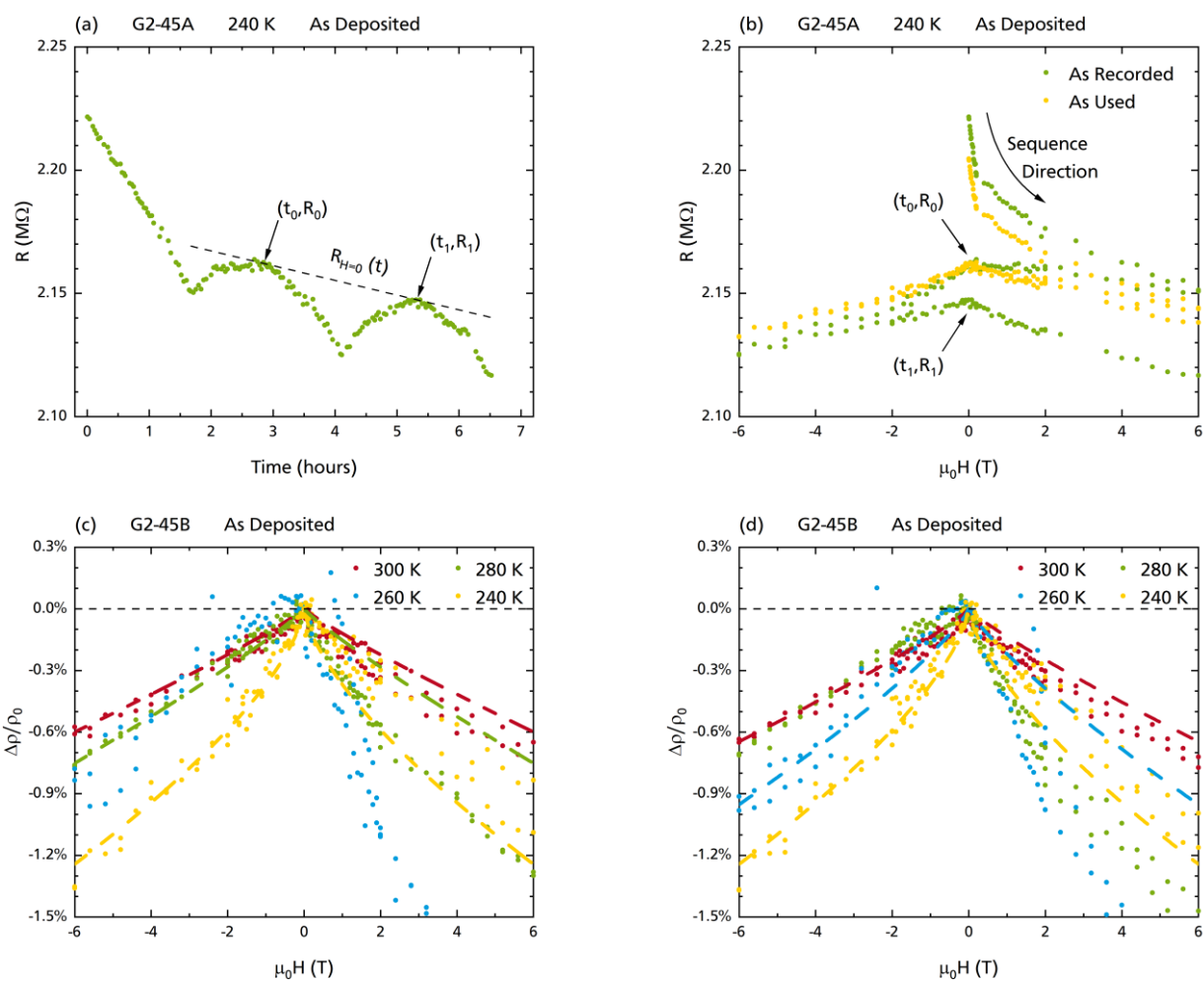
Figure 4-18: Magnetoresistance of the a-Ge Twin Reference Sample G2-45

    (a) Resistance vs. time, recorded over a full magnetic field sequence.

    (b) Resistance vs. magnetic field, as measured (green) and with subtracted time-dependent decrease (yellow).

(c) & (d) Magnetoresistance vs. magnetic field for samples G2-45A and -B, respectively.

           The magnetoresistance is negative and increases in magnitude with increasing magnetic field and decreasing temperature.

roughly revealed and approximated by an exponential dependence $\rho/\rho_0 = -C(\mu_0 H)^n$ with a temperature-dependent exponent n that stresses the negative magnetic field dependence of the magnetoresistance [130,138,141]. Magnetoresistance curves at several temperatures for both twin samples G2-45A and -B are plotted in graphs (c),(d), respectively, each with approximating curves of the exponential form mentioned above. The exponents are summarized in Table 4-4. They are within the range $0.5 < n < 1.0$ as specified in References [130,138]. For temperatures lower than 175 K a positive component adds to the so far purely negative magnetoresistance. However, this temperature range remained inaccessible with the used sample layout and measurement equipment because of strong increase of the sample resistances.

Table 4-4: Exponent of a-Ge Negative Magnetoresistance

Sample ID	300 K	280 K	260 K	240 K
G2-45A	0.90	0.89	—	0.68
G2-45B	0.87	—	0.82	0.68

Both short- and long-term changes in resistance over time of a-Ge samples are reported in the literature. Walley & Jonscher [125] report an increase in resistivity by a factor of up to 3 several weeks after film deposition. In the present thesis, a decrease in resistance was observed during the measurements. However, this decrease followed a slow increase in resistance by several 10% prior to the resistivity and magnetoresistance recordings within the two days in which the a-Ge reference film stabilized. Because this property was also observed both after the reference sample had been annealed at 220 °C and 700 °C in ARCAL 15 atmosphere (see Section 4.6.3) the change is assigned to the adaption of the deposited Ge to the topology of the sample chip. The topology is dominated by the deposited contact line pattern on the one hand and adaption happens via rearrangements within the anyway porous structure of a-Ge on the other. Both effects lead to a better connectivity between potential Ge grains or islands, that is, to a lower resistivity of the film. Because of its amorphous structure and the related distortion of tetrahedral base units a-Ge is thought to be very sensitive to temperature changes.

Kubelík & Tříska's phenomenological $\rho/\rho_0 \propto 1/T$ dependence [139,140] could not be deduced from the recorded $\rho/\rho_0\ (T,H)$ data.

4.6.3 Annealing of the Amorphous Germanium Reference Sample

Transport in a-Ge at room temperature and below is dominated by VRH via dangling bond states located close to the Fermi level of the a-Ge, which is a direct consequence of the atomic bond structure. See Section 4.1.2.3 for VRH. This structure is irreversibly changed when an atomic misalignment gets straightened as soon as a sufficiently high temperature is reached [125,155]. The structure of a-Ge deposited at the temperature of LN_2, as in this thesis, starts to anneal as soon as the deposited film is warmed up to room temperature. Annealing happens within the limit set by the thermal energy available at room temperature [134]. The degree of disorder in a-Ge determines the concentration of dangling bonds in its atomic structure and, hence, its resistivity. A higher deposition rate causes more disorder and results in a lower resistivity [133]. Therefore, the transport properties of a-Ge depend on the annealing history of a sample [125].
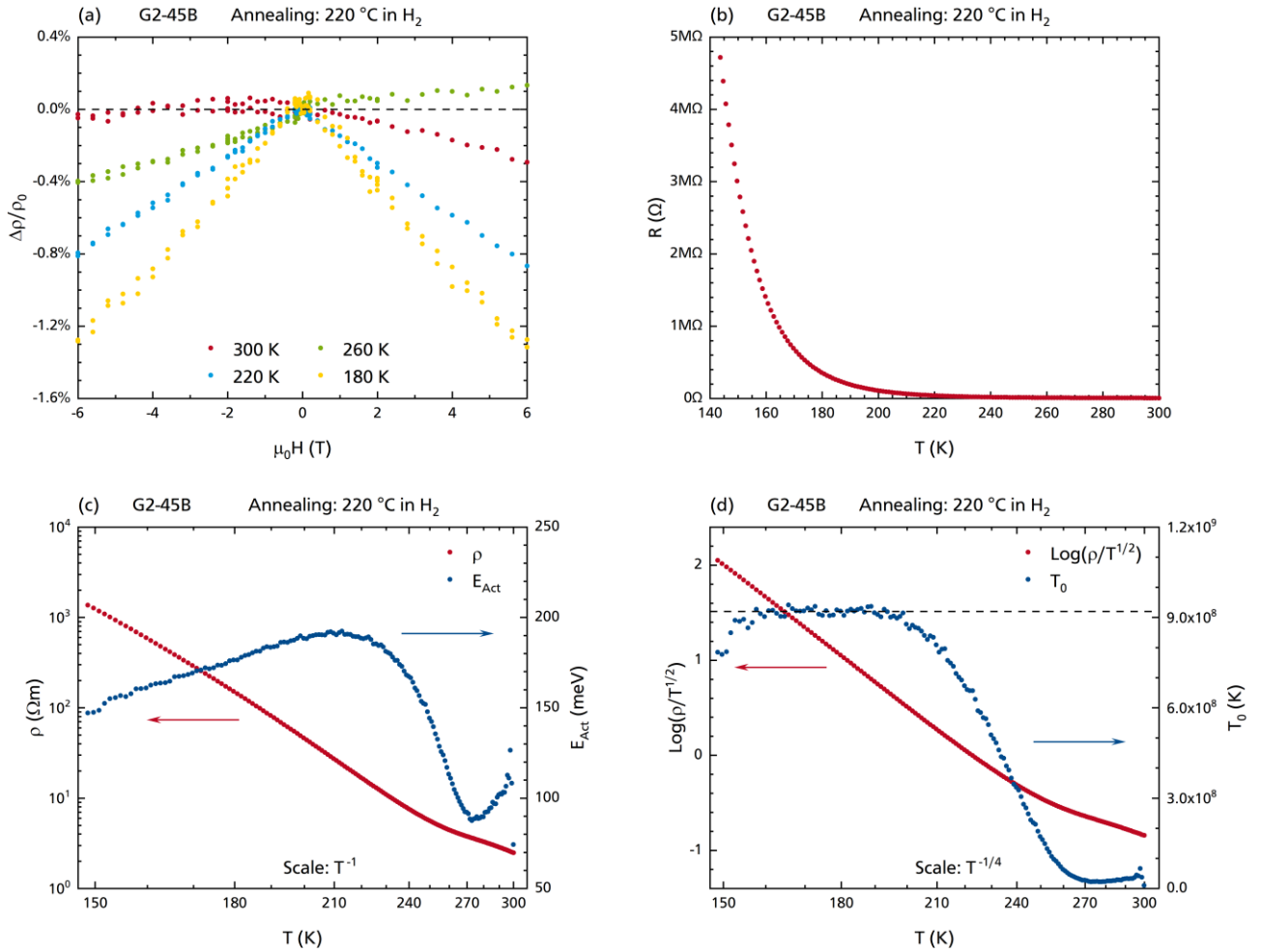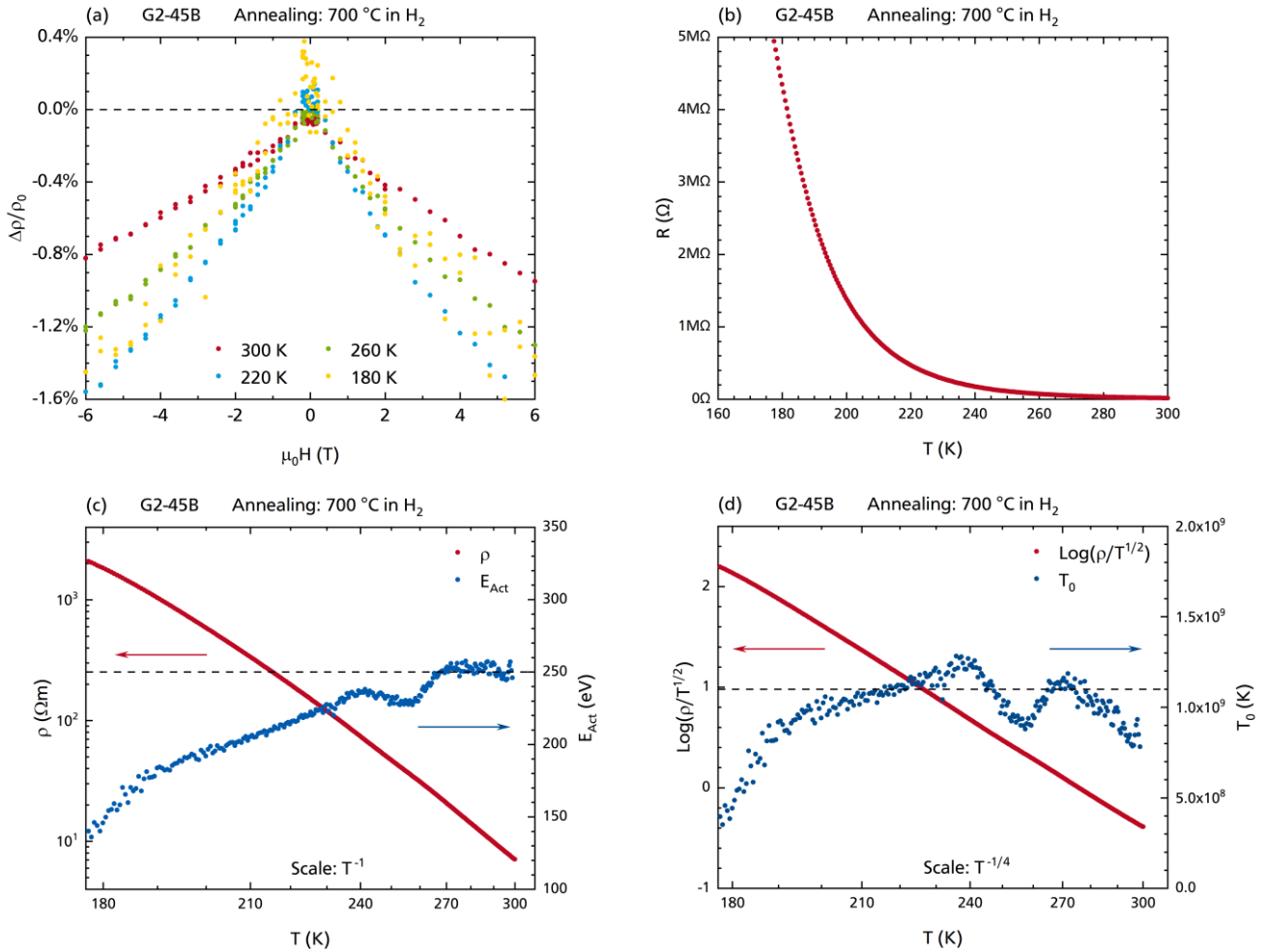
Figure 4-19: Resistivity and Magnetoresistance of a-Ge Reference Sample G2-45B After Annealing at 220 °C

    (a) Magnetoresistance vs. magnetic field at various temperatures.
    (b) Absolute sample resistance.
    (c) Resistivity in 'activated transport scaling'.
    (d) Resistivity in 'VRH scaling'.

Also, disabling the dangling bonds of an amorphous semiconductor via hydrogenation is a way to alter its transport properties. Dangling bonds saturated with a H atom have bonding and antibonding states outside the mobility gap of the amorphous semiconductor. This way, the density of states around the Fermi level is reduced [128].

For that reason, the reference twin sample G2-45 was annealed in ARCAL 15 atmosphere in the same way some of the Fe-Ge samples were. First, at 220 °C for 1 h in vacuum and another hour in ARCAL 15 atmosphere and, in a third step, at 700 °C for 1 h in ARCAL 15 atmosphere. Since a-Ge tends to crystallize when annealed above 300 °C to 450 °C [130,168], crystallization is expected to happen in the latter annealing step. The respective magnetoresistance and resistivity data are plotted in Figures 4-19 and 4-20, and are compared in Figure 4-21.

Figure 4-20: Resistivity and Magnetoresistance of a-Ge Reference Sample G2-45B After Annealing at 700 °C

(a) Magnetoresistance vs. magnetic field at various temperatures.
(b) Absolute sample resistance.
(c) Resistivity in 'activated transport scaling'.
(d) Resistivity in 'VRH scaling'.

4.6.3.1 Resistivity of the Annealed Germanium Reference Film

Compared to the as-deposited film, whose resistivity data are plotted in red in Figures 4-21(a),(b), the resistivity of a-Ge decreases by a factor of 10 when annealed at 220 °C, see data plotted in green. Below 200 K, VRH with $T_0 \approx 9.2 \times 10^8$ K is clearly present (see Section 4.1.2.3 and Equations [4-4] and [4-5] for VRH). At 160 K, the absolute resistance exceeded the upper limit of the PPMS for precise resistance measurement. The lower $T_0 \propto 1/D(E_F)$ indicates a higher density of states at the Fermi level and, according to Equation [4-5], a shorter VRH hopping distance. Because the annealing in ARCAL 15 atmosphere even improved transport via VRH only the thermal component is assumed to affect the film, in particular, its structure. It is noteworthy that the kink in resistivity found at 250 K in the resistance of the as-deposited film (red) disappeared. The inefficiency of post-deposition hydrogen annealing was
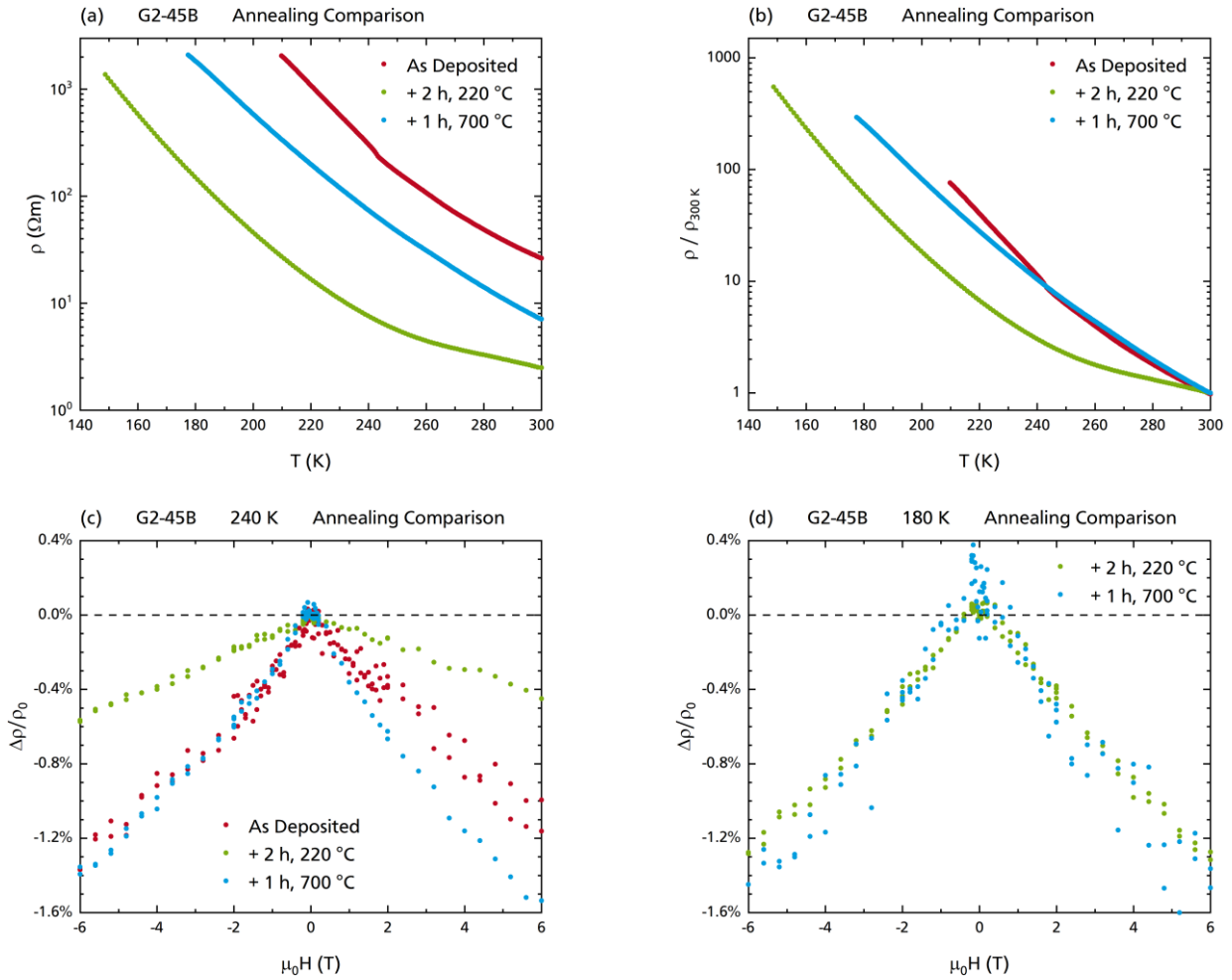
Figure 4-21: Comparison of Data from the As-Deposited and Annealed Ge Sample G2-45B

  (a) Comparison of absolute resistivity vs. temperature curves.
  (b) Comparison of relative resistivity vs. temperature curves.
  (c) Comparison of magnetoresistance curves recorded at 240 K.
  (d) Comparison of magnetoresistance curves recorded at 180 K.

explicitly confirmed by annealing an Fe-Ge nanocomposite film first in vacuum and secondly in ARCAL 15 atmosphere, both at 220 °C, see Section 4.7.6. Usually, amorphous semiconductors are hydrogenated right during deposition [169].

When annealed at 700 °C for one hour in a third annealing step, the resistivity of the Ge reference film increases again, see cyan data in Figures 4-21(a),(b), but stays below that of the as-deposited film. Analyzing its resistivity data for activated and VRH transport, which is illustrated in Figures 4-20(c),(d), respectively, yields a constant activation energy $E_{Act} \approx 250$ meV above 270 K. Below, the resistivity is approximately linear in 'VRH scaling' with $T_0 \approx 1.1 \times 10^9$ K. As stated in Section 4.6.1, an activation energy of 250 meV can be related to carrier activation above the mobility gap of a-Ge. Also, because the resistivity of a Ge sample should decrease when becoming crystalline [168], nucleation may have

happened in the film. However, the film cannot be assumed to be fully crystallized. For a crystallized semiconductor, activated transport with its band gap as activation energy would have been observed. The bandgap of c-Ge is about 700 meV.

4.6.3.2 Magnetoresistance of the Annealed Germanium Reference Film

Because of the lower absolute resistance of the annealed Ge film magnetoresistance curves could be recorded down to 180 K. Both after annealing at 220 °C and 700 °C the magnetoresistance is negative and of the same shape observed for the as-deposited film. When annealed at 220 °C magnetoresistance at room temperature and below is smaller compared to that of the as-deposited film in the accessible temperature range.

According to the transport model by Movaghar & Schweitzer, see Section 4.1.2.4, an increase in magnetoresistance must be due to a change to a higher discrepancy of the hopping times for spin-preserving 'normal' hops and spin-lattice and spin-spin relaxation times. Therefore, the observed reduced magnetoresistance can be related to a smaller hopping time. This is in agreement with the observed lower resistivity because a smaller hopping time causes quicker carrier transport, higher throughput and, hence, current conducted through the film.

Consequently, magnetoresistance increases again when the Ge reference film is annealed at 700 °C. The magnetoresistance curves of the annealed Ge film are quite similar to these of the as-deposited ones as is exemplarily shown in Figure 4-21(c) for 240 K. The magnetoresistance of the film annealed at 220 °C continuously approaches the one the very same film exhibits after being annealed at 700 °C in terms of magnitude. At the lowest possible temperature, 180 K, presented in Figure 4-21(d), the magnetoresistance curves seem to overlap. However, the resistance of the film annealed at 700 °C was slightly above 4 MΩ at that temperature and, therefore, at the PPMS's upper limit for precise resistance measurement.

4.7 Analysis

4.7.1 Uncertainties for Fe-Ge Nanocomposite Samples

The uncertainties of the characteristic quantities are governed by the mass density of a-Ge determined via XRR, the crystal balance calibration performed by means of XRR reference samples, and the tampering of the EDX signal by the layers covering the nanocomposite layer. Here, absolute errors are estimated for a representative Fe_{1000}-Ge sample consisting of a $t_B^{raw} = 1$ nm Ge buffer layer and a

$t_P^{raw} = 100$ nm protection layer. For the nanocomposite layer, $t_M^{raw} = 150$ nm of Ge are assumed to be co-deposited with the clusters, and the raw Fe concentration determined by EDX is assumed to be $c_{Fe}^{raw} = 15$ at. %.

For the raw crystal balance output an error of $\Delta t_i^{raw} = 0.5$ nm is assumed since the deposition was stopped either manually or by a LabVIEW program as soon as a set limit of deposited layer thickness was overcome. The largest standard deviation in EDX data was 0.37 at. %, therefore, an error $\Delta c_{Fe}^{raw} = 0.5$ at. % is assumed. The XRR correction factor is 0.775, an error of 0.080 is assumed.

This yields $t_B = (0.8 \pm 0.5)$ nm, $t_M = (116.3 \pm 12.4)$ nm and $t_P = (77.5 \pm 8.4)$ nm. The XRR-calibration-corrected concentration is then $c_{Fe} = (22.8 \pm 2.2)$ at. %.

For Fe, the mass density of α-Fe is assumed and deviations from a perfect crystal structure are respected by variations in it: $\rho_{Fe} = (7.9 \pm 0.4)$ g/cm^3. For a-Ge, the mass density was determined via XRR and is $\rho_{Ge} = 5.1$ g/cm^3. This value is respected with an error of $\Delta\rho_{Ge} = 0.2$ g/cm^3. This results in a calculated nanocomposite thickness of $t = (133.3 \pm 17.8)$ nm.

With the distribution width of the sector magnet of 10% an error of 0.15 nm of the cluster diameter can be deduced for the nominal 2.82 nm. The corresponding volume concentration of the calculation example sample is then $c_{Fe}^{vol} = (12.8 \pm 2.5)$ vol. %.

Finally, the mean particle separation is $MPS = 1.69$ nm with an absolute error $\Delta MPS = 0.38$ nm.

The relative error of the resistivity is the sum of the relative errors of the dimensions of the nanocomposite film volume under measurement, i.e., width, thickness, and length. The relative error is dominated by the relative error of the thickness, which is 13.4% in this representative example.

4.7.2 Transport Properties

4.7.2.1 Percolation Threshold and Tunneling between Clusters

Embedding Fe clusters into a-Ge allowed for tuning the resistivity of the nanocomposite films over five orders of magnitude by varying the amount of Fe in the film. In Figure 4-22(a) film resistivities at 100 K are plotted as a function of the concentration of Fe in the samples, where the gray, dashed lines in graph (a) are guides to the eye. As a first point, the data reveal a percolation threshold of 30 at. % as indicated by the vertical lines in graphs (a),(b). At concentrations below this threshold the resistivity quickly increases over several orders of magnitude with decreasing Fe concentration. However, at concentrations above the percolation threshold the resistivity decreases only slowly with increasing Fe concentration. In particular, the resistivity stays in the 10^{-5} Ωm range on this side. Samples above the percolation threshold did not show any magnetoresistive behavior (crossed symbols ✖ ▩).
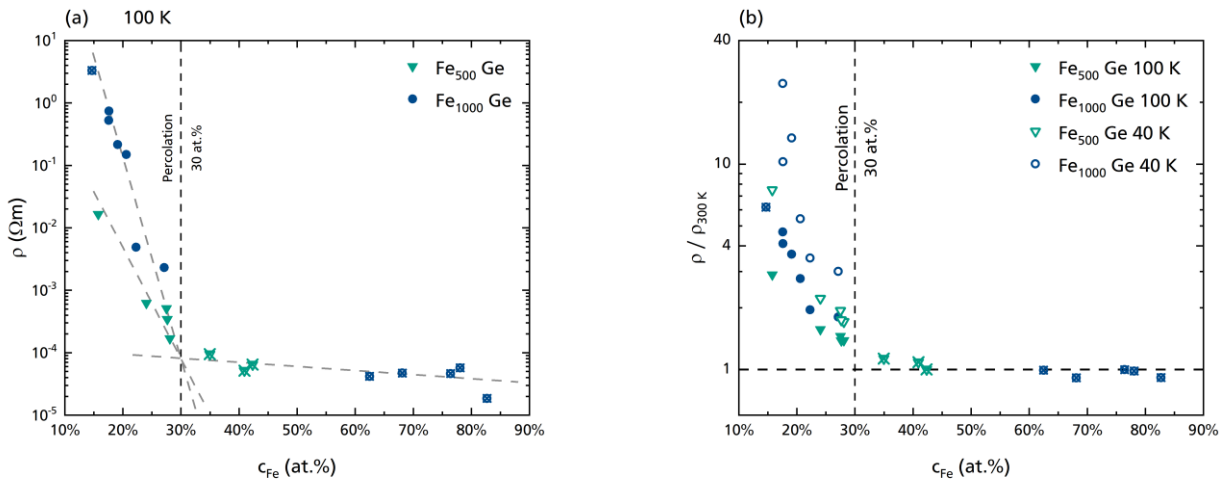
Figure 4-22: Resistivity vs. Fe Concentration Data of the Fe-Ge Films Reveal a Percolation Threshold

(a) Resistivity of Fe-Ge films at $100\,\mathrm{K}$ vs. Fe concentration.

(b) Relative resistivity at $100\,\mathrm{K}$ and $40\,\mathrm{K}$ vs. Fe concentration.

The percolation effect appears as a kink in the graphs at $30\,\mathrm{at.\%}$. Both absolute and relative resistivity increases rapidly with decreasing temperature when the Fe concentration falls below the percolation threshold. To better visualize the trends data points of samples not listed in Table 4-1 are added to both plots.

Figure 4-22(b) shows relative resistivity data at $100\,\mathrm{K}$ and $40\,\mathrm{K}$ (solid and open symbols, respectively) defined as $\rho/\rho_{300\,\mathrm{K}}$. As expected, samples above percolation threshold only show minor changes in relative resistivity. To better visualize the percolation effect the data of some Fe_{1000}-Ge samples not listed in Table 4-1 are added to the plots in Figure 4-22.

Below the percolation threshold, clusters are on average isolated within the a-Ge matrix, while aggregation of clusters still occurs. As a consequence of the poor resistivity of a-Ge, especially at lower temperatures, the resistivity of the nanocomposites increases rapidly across several orders of magnitude with decreasing Fe concentration. This effect appears as a kink in Figure 4-22(a). Moreover, it is worth noting that samples containing the larger cluster species (Fe_{1000}, ●) exhibit a stronger increase of the resistivity with decreasing Fe concentration compared to the Fe_{500} series ▼. This conclusion can also be drawn from Figure 4-22(b), which depicts the relative resistivity $\rho/\rho_{300\,\mathrm{K}}$ at $100\,\mathrm{K}$ (solid symbols) and $40\,\mathrm{K}$ (open symbols). Below the percolation threshold the ratio increases both with decreasing Fe concentration and increasing Fe cluster size. As a scaling effect, MPS varies as $N_{at/Cl}^{1/3}$ with the cluster size in case the volume concentration remains constant. However, as shown in Figure 4-23, the resistivity increases exponentially with increasing MPS independent of cluster size. This suggests that charge transport must be dominated by effects that depend on this average nearest neighbor surface-to-surface distance.
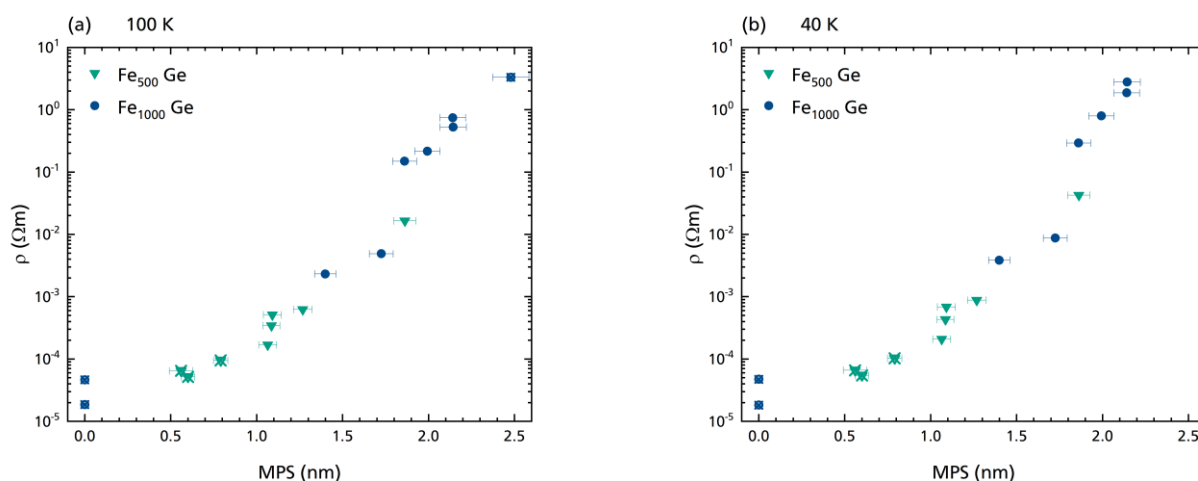
Figure 4-23: Resistivity vs. Mean Particle Separation at 100 K and 40 K

The resistivity of the Fe-Ge nanocomposite films is a function of *MPS* independent of cluster size.

Scher & Zallen [170] simulated finite basic 3D lattices (sc, bcc, fcc, hcp and diamond) by randomly placing hard spheres on the sites of these lattices. Since the spheres are assumed 'hard', only pairs of nearest neighbor spheres form close contact, i.e., touch each other. When only few spheres are placed, the spheres remain isolated on their sites. But, with further increased number of placed spheres, a network of touching spheres starts to form. Finally, a first closed path through the finite lattice forms at a critical occupation density. The occupation density is the product of the occupation probability (number of placed spheres divided by the total number of lattice sites) and a lattice-specific filling factor. As one result, Scher & Zallen [170] found that the critical occupation densities are quite similar for the tested lattices, i.e., on average a volume fraction of only 15.4 vol. % of hard spheres is sufficient for closed paths to appear. Arguing that a disordered system can be described as a system of local superpositions of standard lattices, Scher & Zallen conclude that 15.4 vol. % holds for any 3D system [171]. Transformed to the atomic concentration of Fe within the Fe-Ge cluster-assembled nanocomposite films, this threshold calculates to approximately 27 at. %, which is in good agreement with the graphically estimated 30 at. %.

When metallic grains are embedded in an insulating matrix, tunneling is the only possible process of electron transport [171]. With its high resistivity and the temperature dependence characteristic for a semiconductor, a-Ge can, as a first approximation, be treated as an insulating matrix material. The major difference between successive tunneling from metallic grain to metallic grain along a conduction path and classic tunneling between two metallic bulk electrodes across a thin tunneling barrier is that charge neutrality is broken in the first case because the tunneling of an electron turns a pair of neutral grains into a pair of oppositely, singly charged grains [172].

Sheng, Abeles and coworkers [159,160] were the first authors who published a model that explains the detected $\log(\rho) \propto T^{-1/2}$ resistivity dependence that had been found for disordered materials like granular metals and some disordered semiconductors (see Reference [160] and references therein) based on the data the authors extracted from Ni-SiO$_2$ and other granular films with an intrinsic grain size distribution of 1 nm to 5 nm and between 1.3 K and 300 K. They prepared sample films, about 100 nm thick, by co-sputtering the two constituents and leaving it to diffusion processes to form segregated Ni grains within a SiO$_2$ insulating matrix. This statistical process leads to a distribution in grain size d, particle separation s, and a charging energy E_C^0 required to create a fully dissociated pair of singly and oppositely charged grains. However, these three parameters have to be correlated since the ratio of deposited metal and insulator is a sample constant. For this reason, the volume fraction x of metal embedded in the form of grains within the film is constant when averaged over a volume larger than a few surface diffusion lengths (several 10 nm). Spectating a small region in which the grain size is roughly uniform, then, grain size d and separation s are directly proportional for a constant volume fraction x: $s = \left((\pi/6x)^{1/3} - 1\right) d$. As the charging energy of a grain within a granular metal is $E_C^0 = (e^2/d)\, F(s/d)$, where $F(s/d)$ is a function that accounts for the shape and the arrangement of the grains and the interaction between the pair of grains getting charged, the quantity sE_C^0 is a constant for a given x. In the low-field regime ($e\,\Delta V_{Cl\to Cl} < k_B T$, which generally holds for the samples of this work as discussed in Section 4.4.1) thermal activation is the main mechanism for carrier generation and the number density of activated charge carriers obeys a Boltzmann law $\exp(-E_C^0/2k_B T)$. The generated carriers drift along paths of largest mobility and, so, the optimal path becomes an optimization problem because carriers are neither likely to tunnel to smaller grains because of the higher charging energy nor to smaller grains with smaller charging energies that in turn come with larger tunneling distances because $sE_C^0 = $ const. Therefore, the carriers follow paths via grains with similar charging energies. The sum of such percolation paths finally yields a conductivity that varies as

$$\sigma_T = \sigma_0 \exp\left(-2\left(\frac{C}{k_B T}\right)^{1/2}\right) \qquad [4\text{-}15]$$

with temperature-independent σ_0 and $C = \chi s E_C^0$, where $\chi = \sqrt{2m^*\phi/\hbar^2}$ is the constant of decay in the tunneling probability $\exp(-2\chi s)$ with effective carrier mass m^* and effective tunneling barrier height ϕ.

In the random network of Fe clusters the charging energy is estimated from the energy of a singly charged cluster surrounded by neutral clusters (= isolated sphere) to one of which the electron will tunnel next: $E_C^0 = e^2/2C_{sph}$. Here, $C_{sph} = 2\pi\varepsilon_0\varepsilon_r d_{Cl}$ is the capacity of an isolated sphere, with the cluster diameter d_{Cl} and the dielectric constant of c-Ge [127,146]. The use of the dielectric constant of c-Ge is justified by the quite similar refraction indices of c-Ge and a-Ge, 4.0 and 4.3, respectively [173].

Abeles et al. [160] point out the similarities and differences between Mott's VRH and their own model as follows. On the one side, the differences in charging energies between clusters can be seen as analog to the energies of the localized states in Mott's VRH. However, tunneling does not only depend on the difference in energy between the initial and final state but also on the absolute charging energy. Also, in Mott's VRH model the density of charge carriers is assumed to be constant, while in case of low-field regime tunneling charge carriers are temperature-activated and, hence, the density is not constant but always in thermal equilibrium.

From general considerations tunneling conductance through a sample of randomly distributed spheres is also a percolation problem. Balberg & Binenbaum [174] found that in a hard-sphere model each sphere needs 2.8 neighbors on average when a globally connected 3D network of spheres is supposed to form [171]. Following that result, the problem of 'percolating' spheres connected by tunneling barriers is treated by Balberg [171] by introducing a critical radius r_C. This radius spans a sphere in which there are 2.8 neighbors included on average. Usually, there are enough spheres close-by offering various options to tunnel to within r_C forming subnetworks of tunneling 'resistors' in which connections between spheres with distances larger than r_C are ignored. However, there are also connections that only offer one tunneling option, and that one is across the limiting distance r_C. It is these links that dominate the resistance of the whole system: Tunneling conduction is dominated by bottlenecks.

Sheng & Abeles et al. [159,160] found good agreement of the Ni-SiO$_2$, Pt-SiO$_2$ and Au-Al$_2$O$_3$ data with the derived $\log(\rho) \propto T^{-1/2}$ dependence. Nonetheless, there is a large number of publications that deal with metallic granules embedded in insulating materials using different techniques of preparation. Hattink et al. [175] produced Co-ZrO$_2$ granular films via pulsed laser deposition at room temperature from rotating composite targets. Fujimori et al. [13] used radio frequency sputtering of Co-Al alloy targets with Ar + O$_2$ gas mixture to create granular films of Co granules separated by insulating Al$_2$O$_3$ grains serving as tunneling barrier. Lukashevich et al. [176] ion-implanted Fe into a polymer (polyethylene terephthalate, PET). Probably the most exotic films were prepared by Holdenried et al. [24] who used well-defined prefabricated Co clusters from an inert-gas aggregation source with diameters between 2 nm and 12 nm with a narrow distribution of only 20%. Cooling a substrate with the cold finger of a He cryostat the authors were able to embed their clusters into matrices of frozen, completely inert Kr and Xe noble gas. This way, they produced samples with no leftover magnetic impurities, which allowed them to study pure tunneling transport up to a temperature of 40 K.

All authors observed, with more or less accuracy, Sheng & Abeles et al.'s $\log(\rho) \propto T^{-1/2}$ temperature dependence of tunneling transport between isolated granules. Holdenried et al. [24] argue that for their samples of equally sized and equally separated Co clusters a $\log(\rho) \propto T^{-1}$ dependence, which was found

for CoO-coated Co clusters by Peng et al. [177], would have been expected. Neugebauer & Webb [178] derive such a behavior for a network of metallic islands with voids in between that need to be overcome by tunneling to transport charge from one island to the next. Assuming charge transfer between islands is a thermally activated process the number of charged islands is proportional to $\exp(-E_{Act}/k_B T)$. Considering the net rate of electrons tunneling in or opposite to the direction of an applied electric field yields the mentioned exponential inverse temperature dependence.

Holdenried et al. [24] suppose that size-variable aggregates of percolating clusters effectively form a cluster size and separation distribution that reproduces the broad cluster size distribution the $\log(\rho) \propto T^{-1/2}$ temperature dependence by Sheng & Abeles et al. is based on. This argument may also hold for the present Fe-Ge cluster-assembled nanocomposite films because the growth process essentially yields the same structure.

4.7.2.2 Tunneling between Coulomb-Blocked Clusters

Another effect that can change the ratio of carrier transport via VRH and direct tunneling is related to the fact that a cluster gains a net charge when an electron tunnels onto it, increasing the (Coulomb) energy barrier for a second one within tunneling range to tunnel onto the cluster as well and, for this reason, is isolated from tunneling transport. Therefore, the major difference compared to tunneling barriers sandwiched between two electrodes is that charge neutrality is abrogated [172].

Schelp et al. [179] examined tunneling conduction between Co electrodes across an insulating Al_2O_3 barrier intersected by a monolayer of equally sized (2 nm to 4 nm mean diameter) and separated Co clusters within the tunneling barrier. The authors kept a constant distance of 2.7 nm between the monolayer of Co clusters and the second electrode while they varied the distance between the first electrode and the monolayer of clusters between 0.5 nm and 2.5 nm in order to tune the tunneling properties of the samples. In the low-voltage range, meaning the tunneling barrier is much higher than the electrostatic energy because of the voltage applied across the tunneling barrier, only little temperature dependence is expected in the I–V characteristics. For their sample possessing the shortest distance between Co cluster monolayer and first electrode (0.5 nm, referred to as sample A) Schelp et al. [179] find an increase in resistance only by a factor 2 when cooled from room temperature down to the temperature of LHe, while the resistance increases by a factor 200 for their sample with the largest distance (2.5 nm, referred to as sample B). In contrary to sample A, sample B does show a strong variation of the I–V curves with temperature. While the authors were able to fit sample A to Simmons's theory of tunneling [50], [51], which yields I–V relations for generalized tunneling barriers, with a reasonable set of parameters (barrier height $\phi = 1.4$ eV and width $s = 1.7$ nm) they conclude to have observed simple tunneling conductance for sample A. However, the authors state they were not able to
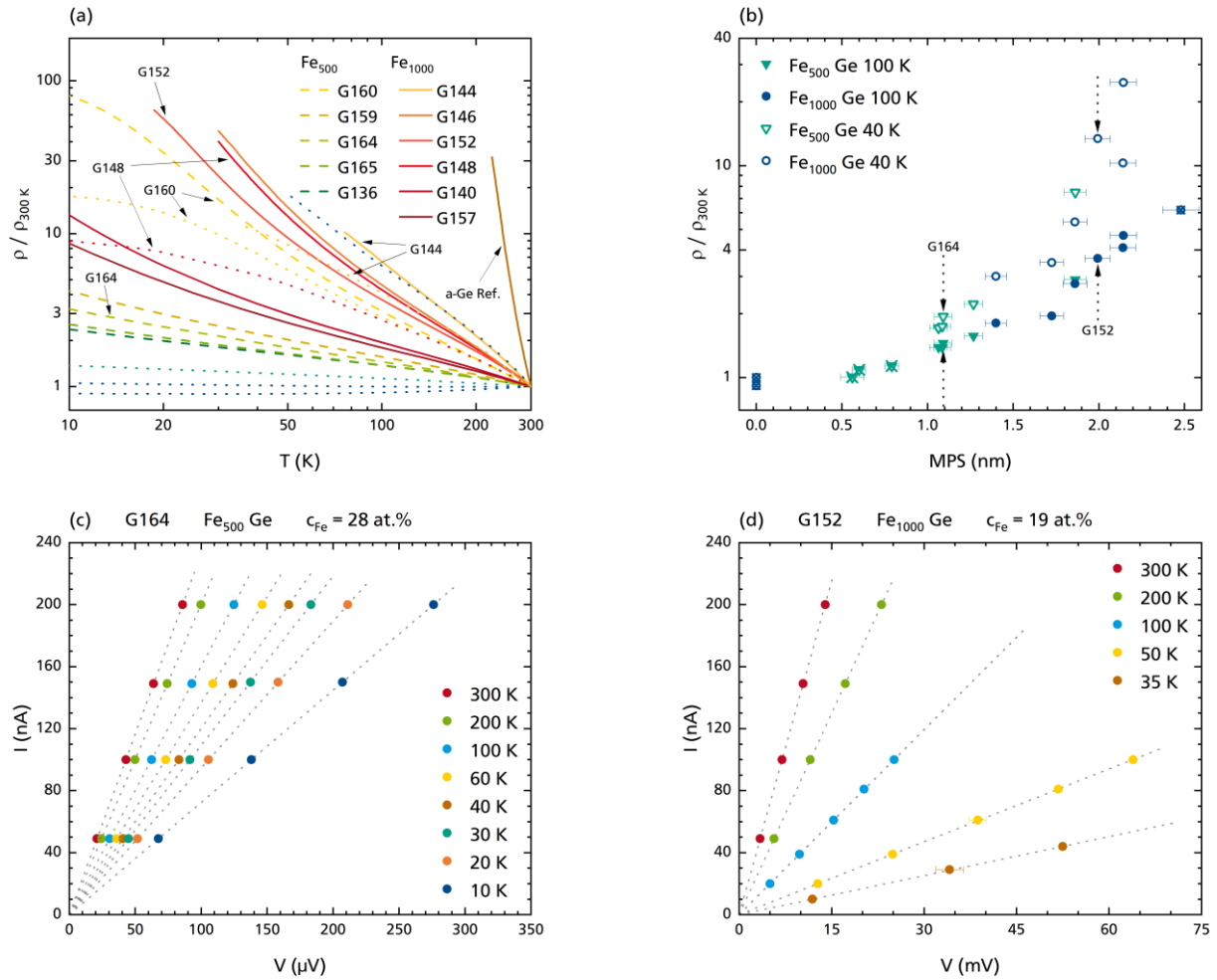
Figure 4-24: Resistance Ratio and I–V Characteristics Plots to Support Arguments for Coulomb Blocking

    (a) Resistance ratio vs. $\log(T)$, including the slope of reference sample G2-45A. For dashed and dotted lines see caption of Figure 4-12.

    (b) Resistance ratio vs. MPS. Samples G164 and G152 are highlighted. Solid symbols show data at $100\,\text{K}$, open symbols represent data at $40\,\text{K}$.

(c) & (d) I–V characteristics for samples G164 (Fe_{500}, $MPS = 1.1\,\text{nm}$) and G152 (Fe_{1000}, $MPS = 2.0\,\text{nm}$). Note the difference in voltage-scaling: microvolts in graph (c) and millivolts in graph (d).

fit sample B by any reasonable set of parameters. Moreover, Schelp et al. [179] observed that a minimum voltage needs to be applied across the tunneling barrier to even generate some tunneling current at all. They assert that Coulomb blocking of clusters causes the explained deviations from pure tunneling transport.

As the Fe-Ge samples in the present work are comparable to the samples of Schelp et al. [179] both in cluster size and cluster separation (roughly 1.0 nm to 2.2 nm) and, moreover, also in barrier height when compared with the energy gap found by Gibson & Meservey (20 meV) [146] and the band gap of c-Ge (~700 meV [126–128]), Coulomb blocking may also be a driving effect for the resistivity behavior of the present samples that is found when the temperature is varied. Figure 4-24(a) summarizes the

relative resistivity $\rho/\rho_{300\,K}$ vs. temperature curves of all Fe-Ge samples exhibiting magnetoresistance plotted in a double-logarithmic diagram (dashed and solid lines). The data of the samples are colored and ordered according to Section 4.3. For comparison, also the slope of a-Ge reference sample G2-45A is added (brown line close to the right y-axis). Except of the curve close to the one of G144, the dotted blue and green lines represent samples with concentrations above the percolation threshold. For this reason, these samples only show minor changes in resistivity with temperature variation. Even a decrease in resistivity is possible here, as indicated by one curve that ends below $\rho/\rho_{300\,K} = 1$ at 10 K.

It is evident that the volume fraction of cluster material defines the tendency of the relative resistivity to increase with decreasing temperature. Moreover, it can be seen that also Fe-Ge samples can show both small (factor 3) and strong (factor 100) increases in resistivity when the temperature is decreased from room temperature down to 10 K, depending both on the Fe concentration in the film and the size of the embedded clusters. Graph (b) shows relative resistivity data at 100 K and 40 K plotted vs. MPS. It can be seen that the relative increase in resistivity is a function of MPS, independent of cluster size as it was already found earlier for the absolute resistivity (Section 4.7.2.1).

The two I–V characteristics plotted in graphs (c),(d) belong to samples G164 and G152, respectively, which are highlighted in plot (b) by arrows. As can be seen in graph (a), sample G164 shows the lowest resistivity ratio out of all samples below the percolation threshold with $\rho/\rho_{300\,K} \approx 3$ at 10 K. Sample G152 on the low-concentration side shows a ratio that can safely be extrapolated to $\rho/\rho_{300\,K} \approx 100$ at 10 K. However, the resistance of this sample exceeded the PPMS's range of reliable resistance measurement (4 MΩ). Nevertheless, resistance data of G152 could be recorded beyond this limit.

The decent and strong temperature dependence of I–V characteristics in graphs (c),(d) for small and larger MPS, respectively, is in accordance with the I–V characteristics shown by Schelp et al. [179], which were discussed earlier. However, the I–V characteristics of presented Fe-Ge films are linear although a nonlinear dependence can be expected for tunneling conduction. Moreover, a minimum voltage necessary to generate a finite current at low temperatures was not found. On the contrary, all I–V guidance lines (dotted, gray) intersect in the origin of each plot. This linearity can be explained by the major difference that, in case of Fe-Ge films, MPS is a value averaged across a 3D random distribution of clusters rather than a strictly defined distance, as it is in case of the Co monolayer assisted tunneling by Schelp et al. [179] Also, Schelp et al. applied voltages of up to several 100 mV to their Co cluster monolayer tunneling samples.

4.7.2.3 Conduction Processes in Fe-Ge Nanocomposite Films

The final step towards 'badly' insulating tunneling barriers, namely, the explicit use of a-Ge as matrix material, brings Mott's VRH back into play (see Section 4.1.2.3) as transport through the matrix now

represents an alternative way to direct tunneling between clusters and, thus, charge transport through Fe-Ge nanocomposite films in general.

The average hopping length defined as a compromise of closeness in space and energy within Mott's VRH model increases with decreasing temperature [146] and, hence, becomes comparable to any mean particle separation when the temperature is low enough. Gibson & Meservey [146] examined a-Ge tunneling barriers between Al/Al, Fe/Al, and Ni/Al electrode pairs and found a change of the transport mechanism, resulting in a kink in the resistance vs. tunneling barrier thickness plot at about 10 nm, when measuring their samples at 77 K, the temperature of LN_2. Below, the resistivity strongly depends on barrier thickness, while above, it approaches a value independent of thickness when transport via VRH is the dominating process.

To summarize, as a first step to seek for the transport processes happening in the fabricated Fe-Ge nanocomposite films, it is inevitable to analyze the recorded $R(T)$ data. To do so, the data are plotted into different graphs that are scaled in accordance with the different R–T characteristics of the various transport processes that are possible. In case a linear dependence is observed across a certain temperature range in any of the plots, the transport process corresponding to the graph is the dominating one in the identified temperature range [172]. Exemplary analyses of this kind are presented in Figures 4-25 and 4-26 for samples G152 and G164, respectively.

Linear behavior above a $T^{-1/2}$ and $T^{-1/4}$ temperature scale were motivated earlier. Because Fe clusters can also be seen as magnetic impurities, a $\log(T)$ scale was also tested (not shown). As a check for temperature activated processes the resistivity of each sample was also plotted into a $\log(\rho)$ vs. T^{-1} scaled graph (also not shown). No such processes were detected.

Samples below the percolation threshold showed a slow increase of resistance below room temperature followed by a strong increase below roughly 100 K as is exemplarily shown in graphs (a) of Figures 4-25 and 4-26. The $\rho(T)$ data of each sample were plotted into correspondingly scaled diagrams (red data in plots (b),(c)).

In case of the presented samples, linear behavior is already adumbrated both in tunneling and VRH scaling. To get a more meaningful graphical indication the slope for each scaling interpreted as a simple x-y-coordinate system was calculated approximating it for each data point i with the difference between the neighboring data points $i + 1$ and $i - 1$, which yields the following formula in case of 'VRH scaling' (see Figure 4-25(c)):

$$\frac{d \log(\rho/T^{1/2})}{d\, T^{-1/4}}\bigg|_i = \log(e)\, T_0^{1/4}\big|_i \approx \frac{\log\big(\rho_{i+1}/T_{i+1}^{1/2}\big) - \log\big(\rho_{i-1}/T_{i-1}^{1/2}\big)}{T_{i+1}^{-1/4} - T_{i-1}^{-1/4}}. \qquad [4\text{-}16]$$
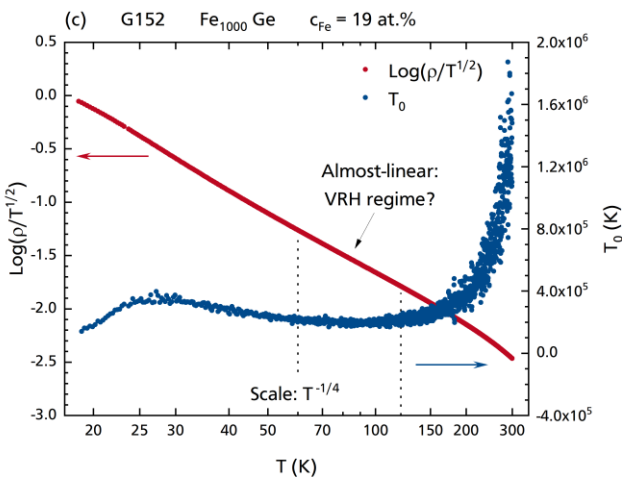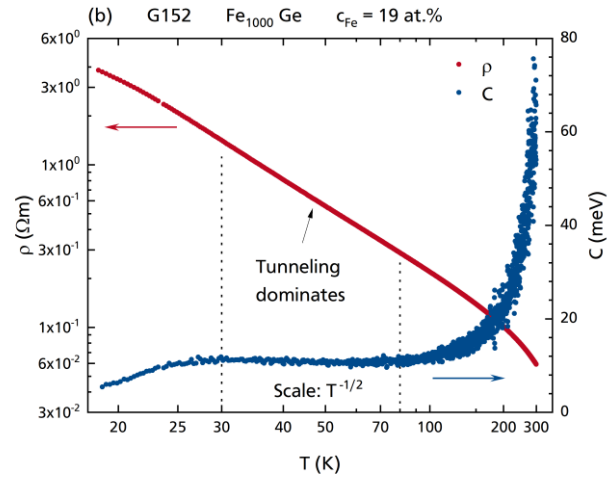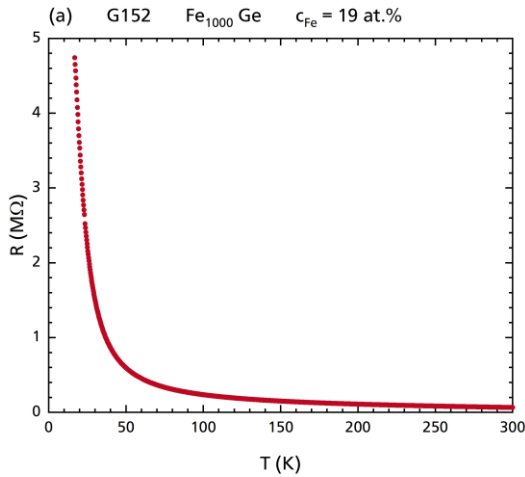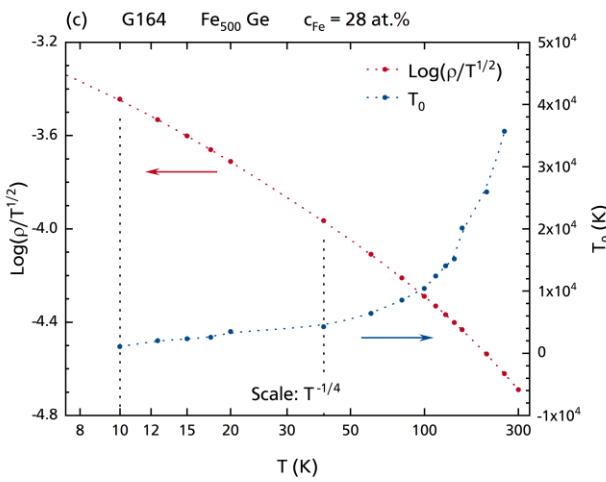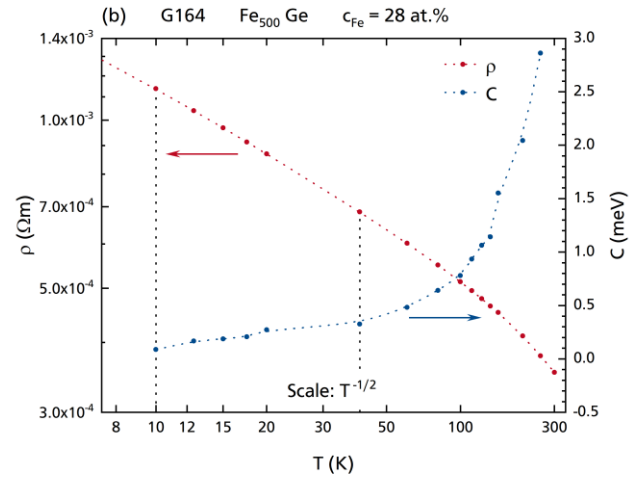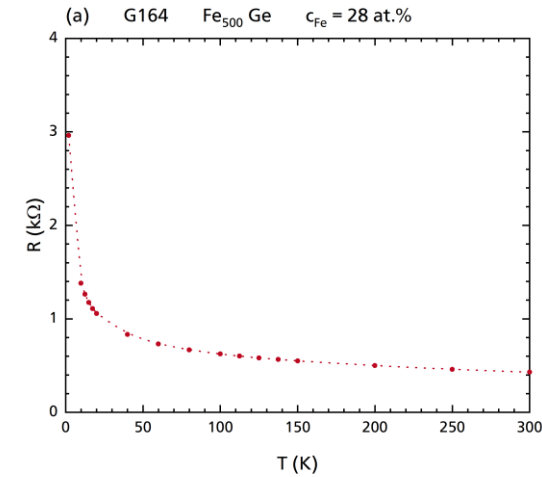
Figure 4-25: Resistance vs. Temperature Graphs of Sample G152

(a) Absolute sample resistance.
(b) $\log(\rho)$ vs. $T^{-1/2}$ ('tunneling scaling').
(c) $\log(\rho/T^{1/2})$ vs. $T^{-1/4}$ ('VRH scaling').

The characteristic quantity T_0 can be deduced from the slope of the plot. T_0 is the only parameter relating theory and experiment in case of VRH and is plotted in blue and to the right scale in each graph (c). T_0 takes a constant value when VRH is the dominating process of transport.

Similar operations were performed for 'tunneling scaling' and double-logarithmic scaling, yielding tunneling parameter C and exponent k, respectively. The result of the former is added to each graph (b), the latter is not presented.

4.7.2.4 Tunneling Transport

A random spatial distribution of partially agglomerating clusters can be interpreted as a random network of tunnel junctions that are connected by conducting pathways. Within such a network the parameters characterizing the tunnel junctions are distributed quantities. However, the conductivity of the network follows the behavior of a single tunneling junction [182].

Figure 4-26: Resistance vs. Temperature Graphs of Sample G164

(a) Absolute sample resistance.
(b) $\log(\rho)$ vs. $T^{-1/2}$ ('tunneling scaling').
(c) $\log(\rho/T^{1/2})$ vs. $T^{-1/4}$ ('VRH scaling').

Fe_{1000}-Ge sample G152, with an EDX-determined 19 at.% of Fe, provides a *MPS* of 2.0 nm, which is well below the calculated cluster diameter of 2.8 nm (see Table 4-2). Obviously, tunneling transport is the dominating effect between 80 K and 30 K with $C = 11$ meV see Figure 4-25(b). With an estimated charging energy $E_C = e^2/4\pi\varepsilon_0\varepsilon_r d_{Cl} = 32$ meV for isolated Fe_{1000} clusters and by taking *MPS* as barrier width, following the model explained in Section 4.7.2.1, a tunneling barrier height as low as $\phi = 1.2$ meV can be estimated. This value is unphysically small.

Besides sample G152 only one other (G146, Fe_{1000}, 18 at.%, $MPS = 2.1$ nm, $C = 17$ meV, yielding $\phi = 2.5$ meV) features a 'plateau' in C from which the plot deviates again at lower temperatures, see Figure 4-26(b). However, this artifact originates from a less steep increase in resistivity setting in and is thought to be caused by leakage currents bypassing the sample region under measurement. The unprotected pattern of Pt lines eases the formation of short-circuits; this is a clear disadvantage of the chosen method of how to electrically connect a sample film. In case of the two mentioned samples, also the very high resistance at low temperatures (> 1 MΩ) may have been already too high for accurate voltage sensing with the used PPMS. Sample G164 (Fe_{500}, with $E_C = 40$ meV, 28 at.% Fe, $MPS = 1.1$ nm,

$C = 0.21$ meV), presented in Figure 4-26, only shows a slowly varying C for low temperatures below 40 K. This behavior is typical for all other samples as well. In the specific case of G164, a barrier height of less than 1 µeV is observed. As a rule of thumb, the height of a tunneling barrier can be expected to be about half the band gap of the material [24], which is about 350 meV in case of Ge. This value is two orders of magnitude larger than the calculated barrier height values. The inapplicability stresses the importance of hopping transport through the a-Ge. Moreover, it is noteworthy that carrier mass and barrier height appear as a product in Equation [4-15]. That is, an effective electron mass $m^*/m_e = 0.1$ would shift the two barrier heights at least to the order found by Gibson & Meservey [146]. In fact, from $\sigma \propto 1/m^*$ and $\sigma_{tot} = \sum \sigma_i$ for conduction through parallel channels σ_i the conductivity effective mass for c-Ge is

$$m_c^* = \frac{3}{\dfrac{1}{m_{long}^*} + \dfrac{2}{m_{trans}^*}} = 0.12 \, m_e \qquad \text{[4-17]}$$

with longitudinal and transvers relative effective mass $1.64 \, m_e$ and $0.082 \, m_e$, respectively [127]. However, in a-Ge conduction takes place via localized states close to the Fermi level. The effective mass of the electrons may differ noticeably from the value given above. In contrary to the above effective mass, Gibson & Meservey found the most compatible value to be $m^*/m_e = 2.8$ for their data. Regarding the effective electron mass of Fe, abnormally large $8.0 \, m_e$ were derived from heat capacity measurements [183]. Last, alloying of Fe clusters with Ge atoms, i.e., a continuous change from cluster to matrix, may lead to a reduction in barrier height.

Also, values for C from almost-linear low-temperature data were even lower than the presented values and, therefore, cannot serve as pertinent values either. A value as low as $C = 7$ meV was also found by Mitani et al. [172] for closely packed nonspherical Co grains (2 nm to 4 nm in diameter, 0.5 nm to 1.0 nm in separation) in an Al_2O_3 matrix samples (whereas also Co-oxides may have surrounded the actual Co inclusions). The sample discussed by Mitani et al. [172] shows linear dependence in 'tunneling scaling' all between 4 K and 400 K since tunneling is the only transport process possible when an insulating matrix material is used. From structural considerations and an assumed barrier height of 1 eV the authors find C to also be about 1 eV. Although an assumed tunneling barrier height of 1 eV may be reduced by structural defects, stress, or impurities within the insulating matrix Mitani et al. [172] conclude that approximating grains as isolated spheres is not appropriate for the structure of their samples. The same argument holds for the present Fe-Ge samples. Since it is the largest gaps within a network of connected or close-by clusters and agglomerates that form the bottlenecks for transport and that should in consequence dominate the resistivity of a sample, also using *MPS* as barrier width is not a good approximation. Holdenried et al. [24], who lacked of the ability to use microscopy techniques
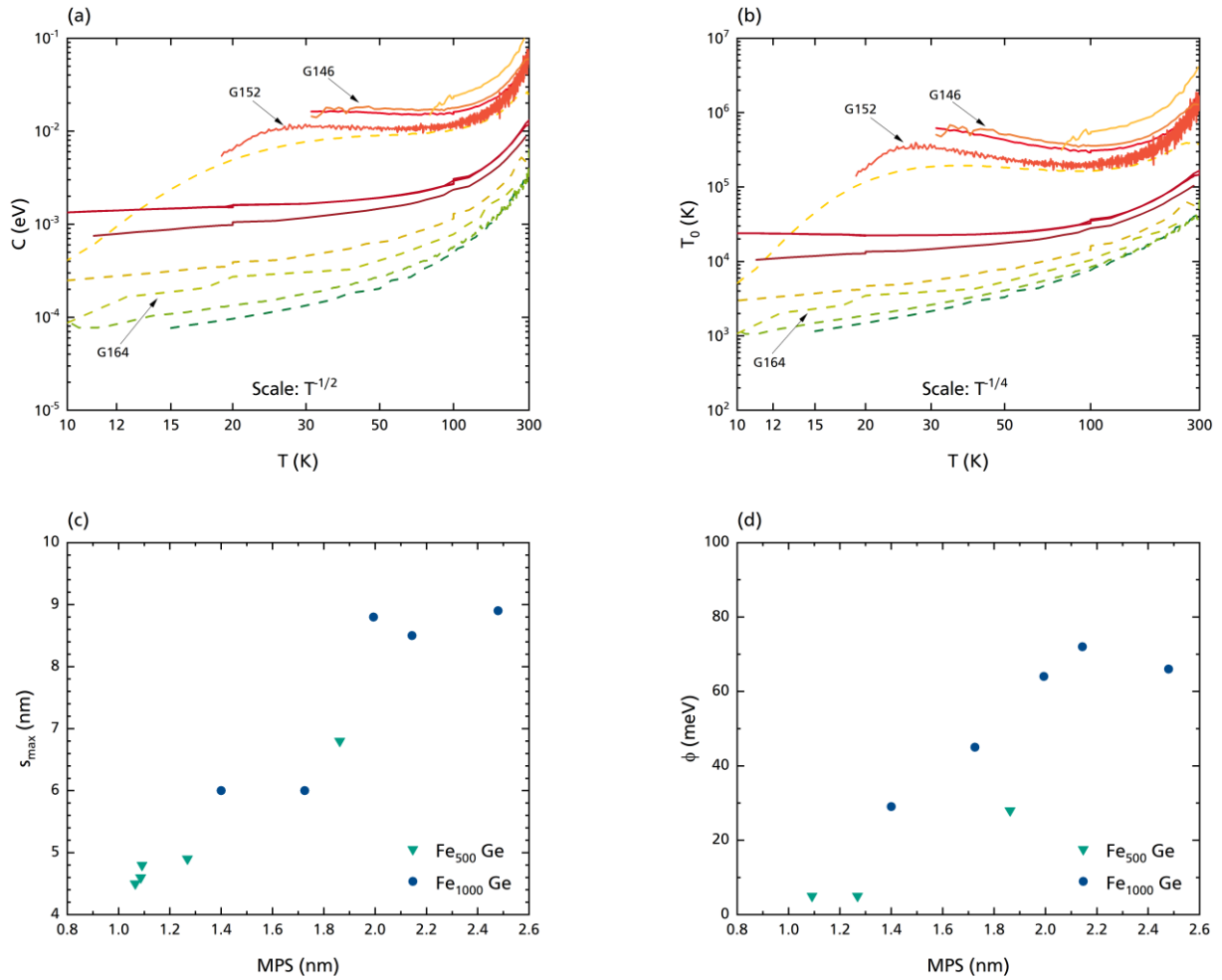
Figure 4-27: Tunneling and VRH Parameters C and T_0 vs. T and Barrier Parameters s_{max} and ϕ from Simmons's Theory vs. MPS

(a) Set of 'tunneling scaling' slopes, calculated with Equation [4-16]. When constant, tunneling is the dominant transport process.

(b) Set of 'VRH scaling' slopes, calculated with Equation [4-16]. When constant, VRH is the dominant transport process.

(c) Estimated 'bottleneck' maximum barrier width s_{max} using Gibson & Meservey's tunneling barrier height of 20 meV.

(d) Average barrier heights ϕ calculated after Simmons's theory using Equation [4-18].

since their Co-Kr and Co-Xe samples had to be kept in LHe temperature range without cease, had to estimate the tunneling barrier width s from their data and found values as low as 0.1 nm to 0.2 nm, which is in range of atomic diameters and, therefore, unphysically low.

In Figure 4-27(a), parameter C, which represents the temperature derivatives of resistivity in 'tunneling scaling', is plotted as a function of temperature for all samples. Samples containing the larger cluster species (Fe$_{1000}$, solid lines) show a higher tendency to approach a constant C. This means, tunneling tends to become the dominating process here. The curves belonging to the series of samples

containing the smaller cluster species (Fe$_{500}$, dashed lines) possess smaller *MPS* values in general since the clusters are more close to each other because of their smaller size. For this reason, the corresponding curves are below those belonging to the Fe$_{1000}$ series. This means, both a minimum *MPS* and a certain cluster size is required in order to achieve transport to happen mainly via tunneling.

The widths of the 'bottlenecks' s_{max} of the presented Fe-Ge nanocomposite samples can be estimated using the tunneling barrier height of a-Ge of about $\phi = 20$ meV, as found by Gibson & Meservey [146], and the cluster-specific charging energies E_C calculated in the text above. The results for samples G146 and G152 are 0.3 nm and 0.2 nm, respectively. Gibson & Meservey calculated the given value from I–V data of 4 nm to 15 nm thick a-Ge barriers applying Simmons's theory [180,181,184]. In addition, they calculated a second value, $\phi = 57$ meV, from fitting $R(s)$ data (s is the thickness of the tunneling barrier). Also using the second tunneling barrier height, the calculated distances are not reasonable. Therefore, the model by Sheng & Abeles et al., which explains transport via Coulomb charging, is not applicable to Fe-Ge nanocomposite samples. As tunneling needs not to be the only transport process happening there may even be no such temperature regime where it is the dominant effect giving the expected linear dependence and, thus, no realistic values for C could be deduced from $R(T)$ data.

Estimating bottleneck barrier widths s_{max} and average barrier heights ϕ from I–V data can also be done for Fe-Ge samples using the low-voltage limit of Simmons's equation [180,181] with a Stratton-like [185] temperature dependence [184]. Because of the linear I–V characteristics of the samples, see Section 4.7.2.2, here, the linear approximation is used. A rearranged version is as follows:

$$R(T) = (\alpha\,\gamma(T)\,S)^{-1} \tag{4-18}$$

$$\text{with} \quad \alpha = e^2 A\sqrt{\phi}/4\pi h s^2 \exp\left(-A\sqrt{\phi}\right), \quad \gamma(T) = \pi B k_B T/\sin(\pi B k_B T),$$

$$A = (4\pi s/h)\sqrt{2m^*}, \qquad\qquad B = A/2\sqrt{\phi},$$

where $R(T)$ is the resistance of a sample at a temperature within the linear regime in 'tunneling scaling' and $S = \lambda \times t \times 1000\ \mu m$ is its cross-sectional area reduced to the fraction that is taken by the cross sections of clusters (the fraction of cluster-occupied vs. total area is $\lambda = \left(\pi d_{Cl}^2/4\right)/(MPS + d_{Cl})^2$). ϕ and s represent the height and width of a barrier, respectively. e is the elementary charge, h the Planck and k_B the Boltzmann constant. According to Gibson & Meservey's finding [146] the electron effective mass is set to $m^* = 2.8\,m_e$. When a sample is assumed to be dominated by one bottleneck barrier per conduction path the complete voltage is assumed to drop across the bottleneck's width s_{max}. In case an average height is estimated, the voltage drops in equal steps. Results for both 'bottleneck' cluster

separations (using Gibson & Meservey's 20 meV) and barrier height (using MPS as barrier width) are listed up in Table 4-5 for representative samples and are summarized in Figures 4-27(c),(d), respectively.

Table 4-5: Estimation of Tunneling Barrier Heights from Absolute Resistance Data
See text above for formulas and quantities. ϕ was estimated setting $s = MPS$, then s_{max} was estimated using Gibson & Meservey's 20 meV. s_{max} and ϕ are representative for all samples.

Sample ID	c_{Fe} (at. %)	MPS (nm)	T (K)	R (kΩ)	t (nm)	$\alpha\gamma$ ($\Omega^{-1}m^{-2}$)	s_{max} (nm)	ϕ (meV)
G152	19	2.0	50	597	148	4.2×10^4	8.9	64
G146	18	2.1	50	905	340	1.3×10^4	8.5	72
G164	28	1.1	20	1.06	130	2.0×10^7	4.8	5

The maximum tunneling distances s_{max} found for an assumed tunneling height of 20 meV are very reasonable since they are a multiple of the mean particle separation of each sample. As expected, the estimated maximum separation increases with mean particle separation. A maximum of up to 10 nm is reasonable, since this is the tunneling barrier width from which on transport through the tunneling barrier by VRH dominates over passing the barrier by tunneling, as found by Gibson & Meservey [146].

The estimated tunneling barrier heights ϕ are on the order of those observed by Gibson & Meservey [146], i.e., several 10 meV, and, therefore, are quite reasonable. In general, values ranging from the discussed 10 meV up to the range of 1 eV may be expected since the latter is on the order of the band gap of c-Ge and the tunneling barrier height of other materials. As an example, 1 eV to 3 eV were found for 1 nm to 2 nm of Al_2O_3 between Al/Au, -Ag and -Cu electrodes at 77 K [186]. The estimated average barrier height also increases with increasing MPS. This is assigned to the continuous change from cluster to matrix phase because of interface roughness or even alloying effects.

Because both approaches yield reasonable values, i.e., none of them is dominating. An intermediate state, where conduction happens across isolated islands and chains of agglomerating and percolating clusters must be present.

4.7.2.5 Variable-Range Hopping

Applying Equation [4-16] to 'VRH scaling' produces the set of slopes shown in Figure 4-27(b). As a first difference compared to tunneling transport it is to be mentioned that with increasing T_0 (VRH parameter, see Equation [4-6]) the slope changes over from a monotonously positive one to a slope that shows a minimum when plotted over T and around which the slope can be approximated as being constant.

Again, data from these minima or points within an almost-straight temperature regime can be taken to calculate the VRH parameter T_0. The results for representative samples are given in Table 4-6. An Anderson localization length $1/\alpha = 1\,\text{nm}$, which is close to the value of $1/\alpha = 1.3\,\text{nm}$ stated by Ortuño & Pollak [151] for a-Ge and a good value in general to reasonably estimate a density of states [145]. The calculated densities of states are about two orders of magnitude higher than those of the a-Ge reference samples G2-45A&B and also than those mentioned in literature on a-Ge ($\sim 10^{18}\,\text{eV}^{-1}\,\text{cm}^{-3}$, see Section 4.1.2.3). This can be interpreted in the following way: Fe clusters add a mentionable amount of carriers to the amorphous semiconductor system, which increases the amount of carriers that are transported through the matrix.

Table 4-6: Estimated VRH Temperature Coefficients and Calculated Density of States at the Fermi Level

Sample ID	c_{Fe} (at. %)	MPS (nm)	T (K)	T_0 (K)	$D(E_F)$ ($\text{eV}^{-1}\text{cm}^{-3}$)
G152	19	2.0	$60 - 120$	2.1×10^5	8.9×10^{20}
G146	18	2.1	$95 - 105$	3.6×10^5	5.2×10^{20}
G164	28	1.1	$10 - 40$	2.7×10^3	7.0×10^{22}

Moreover, for the highlighted samples G152 and G146 it is noteworthy that the minimum in 'VRH scaling' appears at the upper temperature limit of the (almost-)linear resistivity vs. temperature range in 'tunneling scaling'. This suggests tunneling is the only transport happening at low temperatures with VRH setting in at higher temperatures leading to a deviation from linear behavior in 'tunneling scaling'. However, this cannot be stated for all samples.

4.7.3 Low-Field Magnetoresistance

For samples with an Fe concentration below the percolation threshold, roughly between 15 at. % and 30 at. %, magnetoresistive behavior was observed. On the low-concentration side the limit is set by the exponential drop of tunneling probability with mean particle separation between neighboring clusters and the associated enormous increase in resistance. On the high-concentration side magnetic interaction restricts the random alignment of cluster magnetic moments. Magnetoresistance effects that depend on the relative orientations between superparamagnetic moments can only be observed between these two limits. In this range a set of optimum conditions for a maximum magnetoresistance effect should exist.

In Section 4.4.2, the evolution of the magnetoresistance curves with temperature was presented for two different samples, followed by a comparison by Fe concentration at three different temperatures.

From the findings, magnetoresistance was then intuitively separated into a saturating low-field magnetoresistance and a field-dependent contribution, where the latter was approximated as linear and compared by its approximated slope.

4.7.3.1 Hysteresis at Low Temperature

The physical processes responsible for the magnetic field dependence of the conduction of electrons through a tunneling connected random network of grains (tunneling magnetoresistance) are explained in Section 2.4.3.

As long as a network of clusters is in the superparamagnetic state its average magnetization obeys a Langevin function, Equation [2-9], and results in a reduction of resistance as soon as an external magnetic field starts to align the superparamagnetic moments. With increasing field the superparamagnetic moments are aligned over increasingly larger fractions of their relaxation time τ. This way, the probability that an electron needs to flip its spin in order to tunnel onto a neighboring cluster is reduced. Since the relaxation time τ increases with decreasing temperature, the magnitude of the magnetoresistance effect also increases. The effect seemingly saturates and was treated as such, however, without ever doing so, when the time span is long enough so that the clusters appear to be blocked in terms of alignment of their moment to the magnetic field.

This continuous enforcement of magnetoresistance is displayed in the series of magnetoresistance curves plotted in Figure 4-28(a) (and also in those shown in Figures 4-8(a),(c)). When at low-enough temperature the moments of the clusters remain blocked and start to show ferromagnetic properties, i.e., a magnetic field hysteresis. A sample containing superparamagnetic moments exhibits maximum resistivity when the moments are totally disordered, i.e., when the magnetic moments of all clusters add up to zero. In the superparamagnetic regime, this is only the case when no magnetic field is applied. In the blocked regime, the coercive field has to be applied in order to reduce the magnetization of the ensemble back to zero after it was magnetized. Therefore, the maximum of a magnetoresistance curve is shifted to the coercive field [24]. In particular, the coercive field observed from magnetoresistance data is equal to the coercive field observed from magnetization hysteresis.

In Figure 4-28(c), the resistance of the presented sample is largest at $\mu_0 H_C = \pm 31$ mT (here, it is $T = 7$ K). This shift from zero field matches with the coercive field observed from magnetization hysteresis measurements of the same sample at 5 K, which are plotted in Figure 4-28(d). The arrows in graph (c) as well as the use of two different colors indicate the direction of ramping of the magnetic field. Note, that the maximum in resistance is observed after the field is ramped through zero-field.

Although the low-temperature magnetoresistance curve was recorded at a slightly larger temperature than the magnetization hysteresis, the data are comparable because at both temperatures
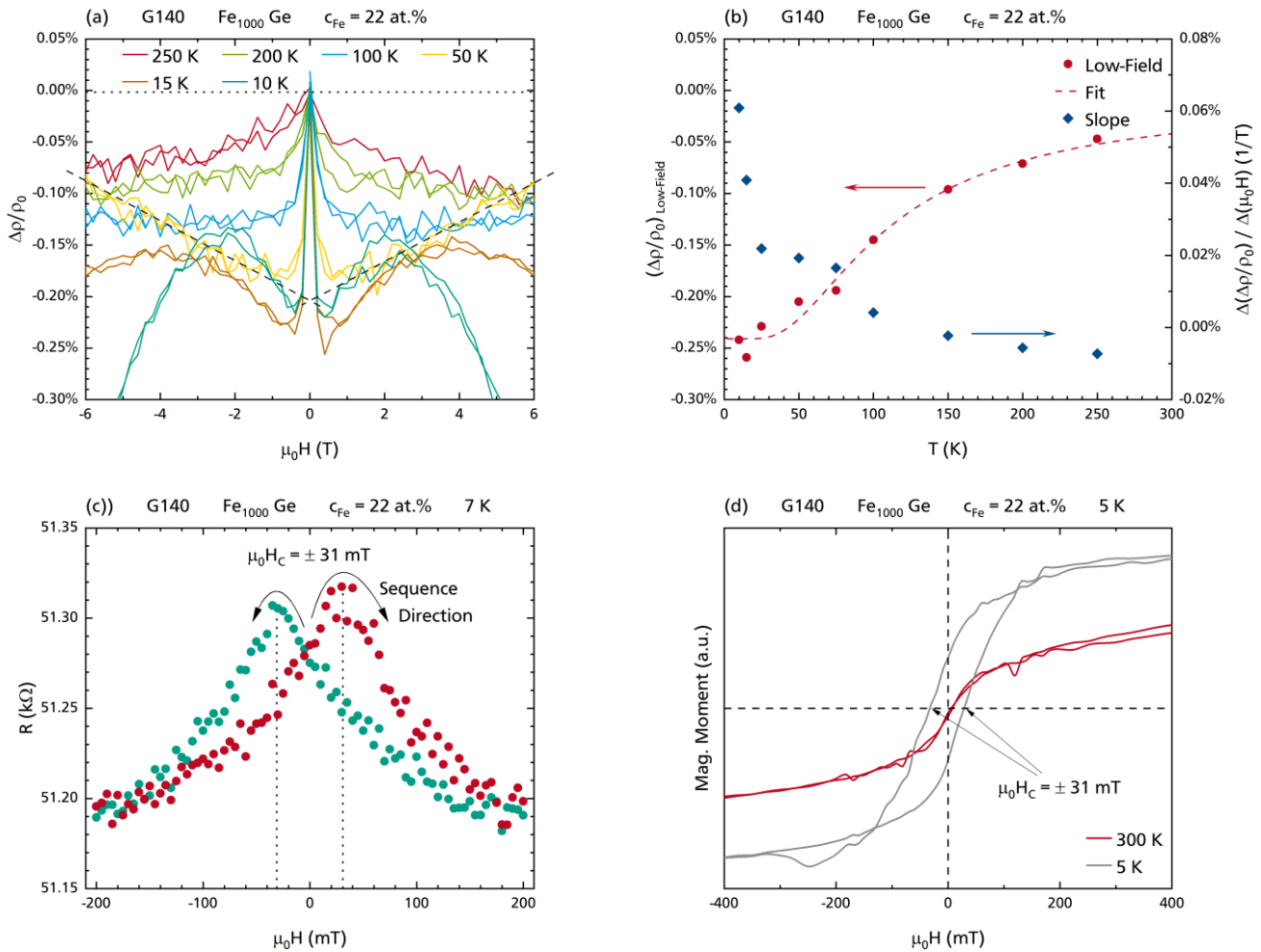
Figure 4-28: Key Signature of Tunneling Magnetoresistance of Sample G140 Below the Blocking Temperature

(a) Magnetoresistance curves of sample G140 at various temperatures.
(b) Low-field magnetoresistance (red circles) and slope (blue diamonds) with a fitted curve (red dashed line).
(c) Magnetoresistance curve at 7 K shows that resistance peaks are shifted from zero field to ± 31 mT. The arrows and the use of different colors indicate the direction of magnetic field ramping. In particular, maximum resistance is observed after the magnetic field passed through zero-field.
(d) Magnetization curves reveal an anhysteretic shape at 300 K but a hysteresic one at 5 K.

Maximum resistance appears at the coercive field of a sample, which is where clusters are totally randomized in orientation after the sample had been completely magnetized. This proves that the relative magnetic moment orientations among clusters determine the tunneling probability and, in this way, the observed magnetoresistance.

sample G140 is in the blocked (ferromagnetic) state well below the sample-specific blocking temperature of $T_B = 29$ K. Together with the dependence of the nanocomposite resistivity on mean particle separation (see Section 4.7.2.1) the following conclusion is drawn:

The artifact at first referred to as 'low-field magnetoresistance' is identified as tunneling magnetoresistance (TMR) caused by spin-dependent direct tunneling between surface atoms of neighboring clusters.
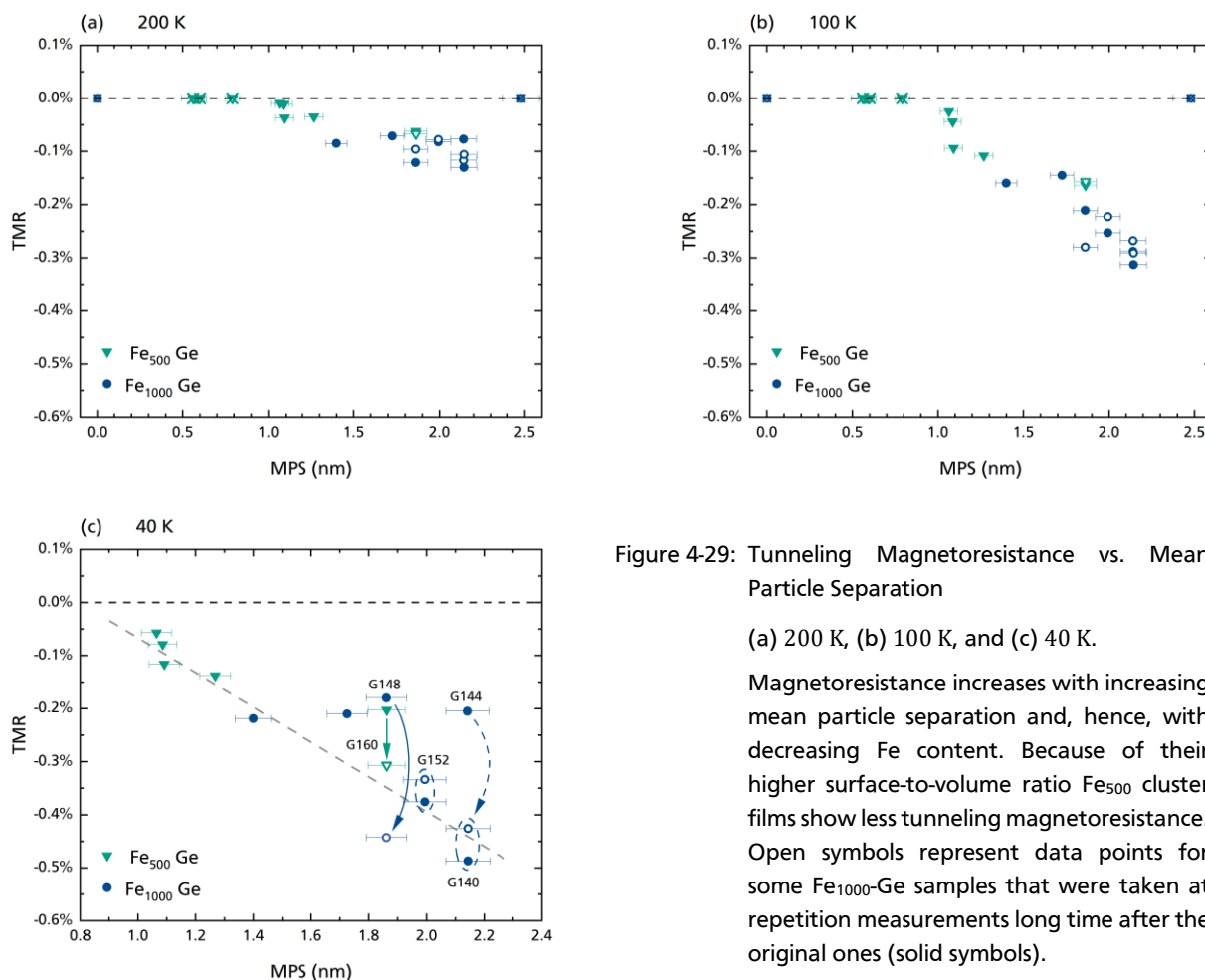
Figure 4-29: Tunneling Magnetoresistance vs. Mean Particle Separation

(a) 200 K, (b) 100 K, and (c) 40 K.

Magnetoresistance increases with increasing mean particle separation and, hence, with decreasing Fe content. Because of their higher surface-to-volume ratio Fe_{500} cluster films show less tunneling magnetoresistance. Open symbols represent data points for some Fe_{1000}-Ge samples that were taken at repetition measurements long time after the original ones (solid symbols).

4.7.3.2 Dependence on Mean Particle Separation

The dependence of the nanocomposite resistivity on mean particle separation, see Figure 4-23, suggests that only cluster surface states participate in tunneling processes. The dependence of the tunneling magnetoresistance on mean particle separation is presented in Figure 4-29 at 200 K, 100 K, and 40 K. Because the clusters consist of a few hundred atoms only, it is misleading to assume that the surfaces of the clusters are of exact spherical shape. Instead, the interface between a cluster and the amorphous matrix is most likely an irregular pattern of Fe and Ge atoms. Therefore, the local magnetic and electronic situation in the vicinity of a surface Fe atom may restrict the magnitude in which its magnetic moment can be oriented by an external magnetic field. Moreover, the atoms at the surface of a cluster do not necessarily have their magnetic moments aligned parallel to the easy axis of the clusters. However, the magnetic moments of the inner atoms do (see Section 2.2.3.4 for magnetic anisotropy). Instead, involving all atoms at the surface of a cluster, a collective misalignment of magnetic moments may be energetically more favorable. Therefore, the alignment of tunneling-active atoms can deviate from the status of total alignment to mentionable extents. Consequently, the discrimination of electrons
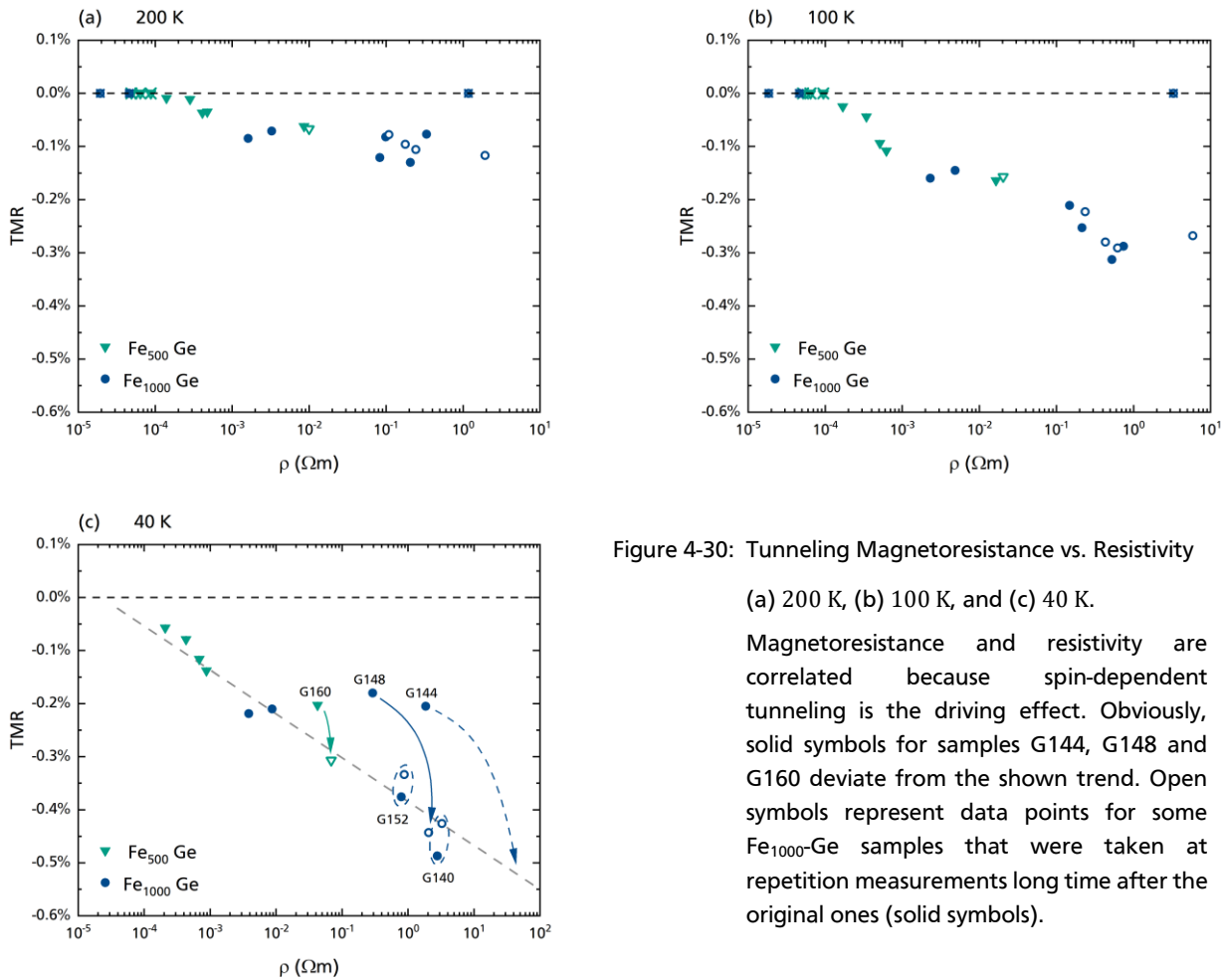
Figure 4-30: Tunneling Magnetoresistance vs. Resistivity

(a) 200 K, (b) 100 K, and (c) 40 K.

Magnetoresistance and resistivity are correlated because spin-dependent tunneling is the driving effect. Obviously, solid symbols for samples G144, G148 and G160 deviate from the shown trend. Open symbols represent data points for some Fe_{1000}-Ge samples that were taken at repetition measurements long time after the original ones (solid symbols).

with antiparallel spin is reduced. Therefore, these electrons can still participate in tunneling conduction to an appreciable amount. Holdenried et al. [24], who embedded well-defined Co clusters into completely inert matrices of frozen noble gas in order to observe pure tunneling transport, found the fraction f of moments on the surface of a cluster being misaligned because of the competition of magnetocrystalline and surface anisotropy to be a linear function of the surface curvature of the clusters. That is, smaller clusters possess a greater fraction of misaligned moments, which yields a smaller magnetoresistance. Moreover, this competition may be one reason why magnetoresistance values of always less than 1% were observed. An analysis similar to that performed by Holdenried et al. [24] is presented in Section 4.7.3.4.

A summary of all tunneling magnetoresistance values $\Delta\rho/\rho_0$, graphically determined from plotted magnetoresistance curves as explained in Section 4.4.2, vs. separation *MPS* and resistivity $\rho(T)$ is given in Figures 4-29 and 4-30, repsectively. As was already discussed in Section 4.7.2.1, a minimum cluster separation is needed for magnetoresistance to appear. According to Figure 4-29 the percolation threshold of 30 at. % corresponds to a minimum mean particle separation of 0.8 nm. This agrees well with

the trend indicated by the data plotted in Figure 4-23. There, a similar mean particle separation is observed when the resistivities of the nanocomposites are extrapolated towards the dirty metal limit ($\rho = 10^{-4} - 10^{-5}$ Ωm). This can be interpreted as follows: At smaller mean particle separations there exist enough chains of agglomerated clusters to make any tunneling gratuitous. Above that threshold magnetoresistance increases linearly with increasing mean particle separation to good approximation and also increases in magnitude with decreasing temperatures. When deposited closer to another, magnetic interaction between clusters becomes stronger and the moments of the clusters are correlated to a higher degree. Consequently, less change in orientation is achieved when getting aligned by an external field compared to when clusters with larger MPS get aligned. For that reason, magnetoresistance does not increase infinitely but should have a maximum between these two limits. For example, Fujimori et al. [13] observed a maximum of tunneling magnetoresistance in their $(Co_{0.75}Al_{0.25})_{1-x}O_x$, $x = 30$ at. %, samples already at a resistivity of $\rho = 10^{-3}$ Ωm, i.e., already when the resistivity of their samples was one order of magnitude above the granular metal limit.

Here, the limit where magnetic interaction between Fe clusters in a-Ge becomes negligible is at several nanometers [26]. This is already in a range where VRH through the a-Ge matrix becomes dominant [146].

4.7.3.3 Tunneling Magnetoresistance vs. Resistivity

In both tunneling magnetoresistance vs. mean particle separation, Figure 4-29, and vs. resistivity plot, Figure 4-30, each at 40 K (graph (c)), three data points obviously deviate from the general trend as is already indicated by their data at higher temperature: these of samples G144, G148, and G160. Despite the low-temperature behavior of these three samples a clear correlation between resistivity, magnetoresistance, and mean particle separation is evident. The trend is indicated by the gray, dashed lines as a guide for the eye in each graph (c). Note, that it is these three samples that start to decrease in tunneling magnetoresistance when the temperature is reduced below 100 K, compare Section 4.4.2.1 and Figure 4-10. The deviations from the 'standard' behavior can have several reasons, which may originate from both the measurement setup and the sample itself. Arguments are given bellow.

(1) In case of samples G144 and G148 the flanks approximated as linear are already superimposed by a nonlinear component. Thus, the flank steepnesses are underestimated, therefore, their points of intersection yield underestimated low-field magnetoresistance values.

(2) None of the three samples under discussion surpasses a resistance of 1 MΩ and each of the three samples also remains much flatter in terms of increase of resistivity at low temperatures compared to the other samples in the ρ vs. T plot given in Figure 4-12. The less steep increase may be a hint for shunt currents. These are negligible when the resistance of a sample is low at higher

temperature. However, when the sample has a similarly high resistance at lower temperatures a shunt lowers the observed voltage drop across the pair of contact lines used for sensing to a reasonable amount. Then, the voltage dropping across the actual 'resistor' under measurement, the nanocomposite, is lower than it would be without a shunt resistor connected in parallel. This way, the resistance of a sample is underestimated and, supposed the case the shunt does not show magnetoresistive behavior, also the magnetoresistance is. Shunts can be formed by dust particles, remnant carbon tape, and metallic particles that merge and form chains because of adhesion when a sample was cleaned with a tissue soaked with ethanol or isopropanol. Sample-intrinsic shunts may come from conduction via the doped Si substrate or cluster accumulations that may have appeared because of the following reason.

The cluster ion beam, matrix material from the effusion cell, and capping layer material from the triple electron beam evaporator were deposited each under a different angle of incidence with respect to the surface of an installed sample chip. Therefore, there always remained an uncapped stripe of protecting Ge on each sample because of the shadowing effect of the slit deposition mask. The uncapped stripe is the slightly darker stripe on the right-hand side of the sample film shown in Figure 4-7.

In the same sense, an accumulation of clusters along one side, or because of electrostatic reasons along the Pt lines, is thinkable. The dark spots on the Pt lines on the left-hand side film edge of the sample shown in Figure 4-7 is assigned to such accumulations of clusters. However, EDX analysis always clearly revealed the position of the cluster spot and never gave any sign for strong accumulation within a nanocomposite film. Also, no sign of dependence on whether a film was connected by the contact lines from the protected or unprotected side was observed. Moreover, unprotected Fe clusters oxidize immediately when a sample is unloaded from vacuum.

(3) For sample G144 probably a too low excitation current was applied, generating a too weak voltage drop for accurate measurements. Usually, a current of 200 nA could be applied down until 100 K, then it had to be continuously reduced with further decreasing temperatures. Depending on the sample, reasonable data could be recorded with currents as low as 20 nA. For the original recordings of sample G144 these low currents in fact were needed to observe a resistance value from the sample, in contrary to the quite low resistance that intuitively suggests that higher excitation currents may have been used.

(4) Several months after first 'original' sample recordings the measurement of some samples was repeated before annealing experiments were started, see Section 4.5.3, to check whether a sample has changed in the meantime. Samples G146 and G152 did not change in absolute resistance to a mentionable degree, however, samples G144, G148, and G160 did. Henceforth, the latter ones are

referred to as 'off-trend samples'. For sample G144 the magnetoresistance curves were reproducible to good approximation, for samples G148 and G160 the magnetoresistance even increased in magnitude compared to the original measurements, see Figure 4-12.

The according data points for the five samples are added as open symbols in Figures 4-29 and 4-30. The minor changes of samples G140 and G152 are symbolized by the two ellipses drawn into the graphs, each enclosing the pair of data points that belong to one and the same sample. Simultaneously, the data points belonging to the off-trend samples are each linked by an arrow that indicates the observed change. A data point for sample G144 at 40 K can only be estimated because of the sample's too high resistance; this arrow is drawn with a dashed line for that reason. The open data point of each sample, i.e., also these of the off-trend samples, follows the depicted trend.

For this reason, it is justified to use data from the repeated measurements instead of the originally recorded data of these samples. Original data of the three samples under discussion are added as dotted lines in Figures 4-12 and 4-24(a) and their curves are highlighted by sample ID labeled arrows. In Figure 4-24(a), later recorded data are again added with open symbols. Tunneling magnetoresistance and resistivity data at 100 K are summarized in Table 4-7.

Table 4-7: Tunneling Magnetoresistance Data at 100 K

Relation between cluster size, Fe concentration, the nanocomposite film resistivity, mean particle separation, and magnitude of tunneling magnetoresistance.

Fe_{500}-Ge Sample ID	c_{Fe} (at. %)	t (nm)	ρ at 100 K (Ωm)	MPS (nm)	TMR at 100 K
G160	16	232	1.6×10^{-2}	1.9	-0.16%
G159	24	120	6.2×10^{-4}	1.3	-0.11%
G164	28	130	5.1×10^{-4}	1.1	-0.09%
G165	28	121	3.4×10^{-4}	1.1	-0.04%
G136	28	17.4	1.7×10^{-4}	1.1	-0.03%
Fe_{1000}-Ge					
G144	18	523	7.4×10^{-1}	2.1	-0.29%
G146	18	340	5.3×10^{-1}	2.1	-0.31%
G152	19.	148	2.2×10^{-1}	2.0	-0.25%
G148	21	255	1.5×10^{-1}	1.9	-0.21%
G140	22	167	4.9×10^{-3}	1.7	-0.15%
G157	27	234	2.3×10^{-3}	1.4	-0.16%

4.7.3.4 Fraction of Misaligned Surface Moments and Shunt Current Model

Holdenried et al. [24] examined pure tunneling transport between well-defined Co clusters embedded into completely inert noble gas matrices. In analogy to their analysis, the fraction $f(E,T)$ of misaligned moments on the surface of a cluster compared to the total number of surface moments is calculated for the presently observed tunneling magnetoresistance data. It obeys the thermodynamic function

$$f(E,T) = \frac{A\, e^{-\frac{E}{k_B T}}}{1 + A\, e^{-\frac{E}{k_B T}}}$$

[4-19]

with E the energy needed to misalign one surface moment and A the fraction of misaligned to well-aligned surface moments. In the high-temperature limit $k_B T \gg E$ it is $f_{T\to\infty} = A/(1+A)$, therefore, $A/(1+A)$ is the fraction of misaligned surface moments in the high-temperature limit. Ignoring spin flip processes, the temperature dependence of the tunneling magnetoresistance is then given by

$$TMR = -\frac{\left(1 - 4f(1-f)\right) TMR_{T=0\mathrm{K}}}{1 - 4f(1-f)\, TMR_{T=0\mathrm{K}}}.$$

[4-20]

From its zero temperature value $TMR_{T=0\mathrm{K}}$ the spin polarization of the tunnel current, which is connected to the spin polarization of the tunneling current via $TMR_0 = P^2/(1+P^2)$, can be calculated.

The magnetoresistance vs. temperature data of the Fe-Ge nanocomposites could mostly be fit to an extent so that the increase in tunneling magnetoresistance with decreasing temperature was reproduced. The low-temperature decrease in magnitude, see Figure 4-10, was excluded from the data to be approximated. The obtained fit curves are added as dashed lines in the corresponding example sample graphs Figures 4-8(b),(d) and 4-28(b). All tunneling magnetoresistance vs. temperature data together with five representative fit curves are summarized in Figure 4-31.

Table 4-8 summarizes the obtained fit parameters and deduced quantities. Good agreement is achieved for Fe_{1000} clusters where, according to the fits, about 45% of the surface moments are misaligned. To estimate the number of atoms at the surface of a cluster surface, the number of these atoms is approximated to fill the outermost shell of a cluster with a thickness of one atomic diameter $2r_{at}$. Expressed in terms of atoms per cluster $N_{at/Cl}$ the ratio is given by

$$N_{surf} \,/\, N_{tot} = 1 - \left(1 - 2/\sqrt[3]{N_{at/Cl}}\right)^3.$$

[4-21]
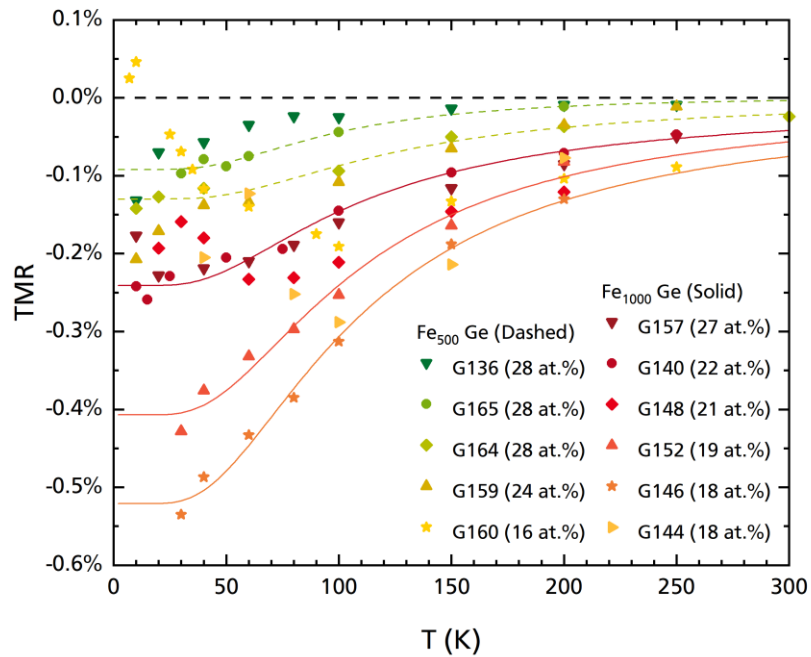
Figure 4-31: Summary of Tunneling Magnetoresistance vs. Temperature Curves and According Fits

Most tunneling magnetoresistance data could be fitted so that the increase with decreasing temperature could be reproduced.

Table 4-8: Fit Parameters and Results After Holdenried et al.

The tunneling magnetoresistance is determined by the fraction $A/(1 + A)$ of atoms with their moment misaligned to the total moment of the corresponding cluster. For Fe_{1000} it turns out that almost half of the surface atoms are misaligned.

Fe_{500}-Ge Sample ID	c_{Fe} (at. %)	MPS (nm)	A	E/k_B (K)	TMR_0	$\frac{A}{1 + A}$	P
G160	16	1.9	0.65	270	0.21%	40%	4.6%
G159	24	1.3	0.74	142	0.18%	42%	4.2%
G164	28	1.1	0.89	219	0.13%	47%	3.6%
G165	28	1.1	1.29	196	0.09%	56%	3.0%
G136	28	1.1	0.59	25.2	0.16%	37%	4.0%
Fe_{1000}-Ge							
G144	18	2.1	—	—	—	—	—
G146	18	2.1	0.83	184	0.52%	45%	7.2%
G152	19.	2.0	0.86	188	0.41%	46%	6.4%
G148	21	1.9	0.82	298	0.24%	45%	4.9%
G140	22	1.7	0.75	179	0.24%	43%	4.9%
G157	27	1.4	0.85	239	0.22%	46%	4.7%

Therefore, in case of Fe_{1000} clusters about 490 atoms participate in forming the surface of a cluster and the ratio obtained above by fitting $TMR(T)$ data represents about 220 misaligned atomic moments. For Fe_{500} clusters, it is 58% or 290 out of all atoms that form the cluster's outermost shell. The deviating fraction of misaligned moments of sample G136 is assigned to its low thickness (17 nm), see Section 4.3. Disregarding sample G136 for this reason, the fraction of misaligned surface moments increases with decreasing mean particle separation, is 46% on average, and represents 130 misaligned atoms on average.

For Fe_{1000} clusters, the fraction of misaligned moments is constant to good approximation, however, for both cluster species the spin polarization decreases with decreasing mean particle separation. This is because the tunneling magnetoresistance also does.

The energy parameter of the fit, which represents the energy penalty E/k_B of a misaligned atom, is found to be in the range of 100 K and, therefore, one order of magnitude larger than those found by Holdenried et al. [24]. The lower tunneling magnetoresistances and spin polarizations of the Fe_{500}-Ge nanocomposites are attributed to their shorter mean particle separation. When clusters are closer, i.e., separated by distances smaller than their diameters, they cannot be approximated as dipole moments anymore. Instead, surface atoms experience the individual moments of the surface atoms of neighboring clusters. This effect is larger for Fe_{500} nanocomposites because these films exhibit lower mean particle separations in general. Another reason may be found in the higher sensitivity to agglomeration and oxidation of the Fe_{500} clusters due to their higher surface-to-volume ratio.

The spin polarizations P observed from the fitting procedure are way below values observed from tunneling experiments at Fe/superconductor interfaces [187]. There, a spin polarization of 43% was observed. According to Reference [187], for Fe it is the itinerant d-like electrons that predominate the tunneling. From Fe/superconductor point contact spectroscopy experiments similar spin polarizations were observed [188]. Nevertheless, the following trend can be seen from the data when sample G136 is again disregarded for the reason given above: The spin polarization decreases with increasing mean particle separation. One reason for that may be the transport via matrix states which becomes more probable compared to direct tunneling with increasing mean particle separation.

From the above spin polarization a maximum possible tunneling magnetoresistance of -15.6% can be derived. Assuming a shunt resistor parallel to the sample 'resistor' under measurement the diminished magnetoresistance to be observed is

$$\left(\frac{\Delta\rho}{\rho_0}\right)_{\text{shunted}} = \frac{1}{1 + \frac{\rho_0'}{\rho_S}\left(1 + \left(\frac{\Delta\rho'}{\rho_0'}\right)_{\text{no shunt}}\right)}\left(\frac{\Delta\rho'}{\rho_0'}\right)_{\text{no shunt}}. \qquad [4\text{-}22]$$

Here, ρ_s is the resistivity of the shunt, ρ_0 and $\Delta\rho$ are the resistivity of the shunted nanocomposite at zero field and its apparent change due to an applied magnetic field, respectively. The dashed quantities ρ'_0 and $\Delta\rho'$ are the corresponding quantities for the pure nanocomposite. In particular, the undiminished magnetoresistance is $(\Delta\rho'/\rho'_0)_{\text{no shunt}}$. At high-enough temperature or large shunt resistivity it is $\rho_s \gg \rho'_0$ and according to Equation [4-22] the pure magnetoresistance of the nanocomposite is observed. In the limit $\rho_s \ll \rho'_0$ the observed magnetoresistance approaches zero. Inserting an observed low-temperature magnetoresistance of -0.5% and setting the no-shunt magnetoresistance to the maximum value given above a relative shunt resistivity $\rho_s/\rho'_0 \approx 0.028$ can be deduced. This would mean that only 3% of the excitation current pass through the nanocomposite while 97% pass through the shunt.

Inoue & Maekawa [82] apply the model of tunneling conductivity in granular materials by Sheng, Abeles, and coworkers [159,160] to magnetic grains. They recalculate their results with a transmission coefficient $|T|^2 \propto \left(1 + P^2\cos(\theta)\right)e^{-2\chi s}$ for tunneling between two neighboring grains that now depends on both the joint density of states spin polarization P of the two clusters and the angle θ between their magnetization directions. Averaging $\cos(\theta)$ over the whole sample the authors express the average value in terms of the relative magnetization: $\langle\cos(\theta)\rangle = m^2$. They formally arrive at the same result like Sheng, Abeles and coworkers, Equation [4-15], but now with a spin-polarization and relative-magnetization-dependent prefactor $\sigma_0 \rightarrow \sigma_0(1 + P^2m^2)$ through which a weak temperature dependence is added in the superparamagnetic state since m obeys the Langevin function.

However, this model is not thought to be suitable for describing tunneling magnetoresistance in the prepared Fe-Ge nanocomposites for two reasons. As the surface-to-surface distance MPS was found to be the parameter determining the resistivity and the tunneling magnetoresistance of a film, tunneling does happen between cluster surface states, which is why the approach of Holdenried et al. [24] of misaligned moments represents a more realistic scenario. The other reason is that the model Inoue & Maekawa's one is based on, yielded unreasonable values though data of the presented example sample followed the expected $\log(\rho) \propto T^{-1/2}$ dependence (see Section 4.7.2.4).

4.7.3.5 Granular Giant Magnetoresistance and Geometrically Enhanced Magnetoresistance

Venugopal et al. [189,190] used an ion implanter to inject Fe ions into a c-Ge (110) wafer at an energy of 60 keV. Though the implantation process caused damage in the crystalline structure of the used Ge substrate the energy deposited by the ion beam also stimulated annealing process, which led to the formation of ferromagnetic Fe_3Ge grains (size of 13 nm to 25 nm) in their sample with a lower implantation rate $(2 \times 10^{16}\ \text{ions/cm}^2)$ and to Fe precipitates (average diameter of 4 nm from magnetization vs. magnetic field and 3.5 nm from ZFC/FC data) in their sample with a higher

implantation rate $(2 \times 10^{17}$ ions/cm$^2)$. In both samples the matrix remained partially amorphous because of the ion implantation damaging. The higher-rate sample had a maximum Fe concentration of about 23 at. % in the implanted layer and only this sample exhibited superparamagnetic behavior in terms of a blocking temperature below 300 K. Venugopal et al. [189,190] attribute the observed negative magnetoresistance to spin-dependent scattering of charge carriers by magnetic Fe clusters, i.e., the granular giant magnetoresistance effect, to cause the observed magnetoresistance with a tremendous magnitude of −19% at 180 K.

Because resistivity was observed to strongly depend on the mean particle separation of a film and because transport via carriers thermally excited into a conduction band is suppressed by the energetically favored VRH for the present samples, the granular giant magnetoresistance effect can be excluded from happening in the present Fe-Ge nanocomposites. Unfortunately, from Venugopal et al. [189,190] magnetoresistance data are available down to 180 K and to fields of 800 mT only, therefore, no low-temperature or high-field behavior can be deduced from their data for comparison purposes.

The magnitude of the granular giant magnetoresistance effect can be enhanced from geometry aspects [191–193]. When a metallic grain is embedded in a semiconducting matrix, the interface of that metallic inclusions is of equal electric potential, i.e., the electric field is oriented perpendicular to its surface. Generally, electric current density and electric field are related by a conductivity tensor: $\vec{j} = \hat{\sigma}\vec{E}$. Because of the off-diagonal components of the conductivity tensor, which are functions of the applied magnetic field, a component oriented perpendicular to the electric field is added to the electric current. This causes a fraction of the electric current to circumvent the metallic inclusion rather than to pass through it, and this effect increases with increasing magnetic field. The fraction of the electric current flowing through the semiconductor experiences a much higher resistance than the fraction passing through the metallic inclusion. For this reason, the resistivity of a nanocomposite sample with a similar structure—metallic grains embedded in a semiconducting matrix—can increase drastically when a magnetic field is applied. In this case, a saturating, large, positive magnetoresistance is observed.

Preparing films with well-defined metallic inclusions is a crucial condition for magnetic field sensors based on this geometric effect. Because a-Ge is not a suitable matrix to microscopically define a current density vector because of the intrinsic VRH process and because transport mainly happens via direct tunneling, the geometric enhancement of resistivity is excluded from happening in the present nanocomposite films.

4.7.4 Field-Dependent Magnetoresistance

Because the nanocomposite films do not show any magnetoresistance above the percolation threshold when in the granular metal regime, the field-dependent magnetoresistance must originate from the cluster-assembled structure.

4.7.4.1 Approximated-As-Linear Field Dependence

The approximated-as-linear magnetoresistance defined in Section 4.4.2.2 was found to exhibit the following features, see Figure 4-11. At room temperature the field-dependent component is negative, i.e., the slope of the curve is negative. The slope becomes flatter and turns positive with decreasing temperature. In case of Fe_{1000}-Ge samples the change of sign of the slope was found to happen in a jumping way, i.e., to happen within a small temperature range around 90 K in which the change of the slope is significantly larger than at temperatures above and below. Because a-Ge changes its sign of magnetoresistance at a similar temperature it may be responsible for the approximated-as-linear magnetoresistance. As discussed in Section 4.1.2.2 a-Ge shows anomalous negative magnetoresistance at room temperature, which first increases with decreasing temperature, then starts to decrease again down until 80 K where it becomes zero, and changes to positive magnetoresistance at even lower temperatures.

Below 80 K Fe_{1000}-Ge data follow the trend of Fe_{500}-Ge but remain below the slope values found for the latter ones. The fact that higher tunneling magnetoresistances were found for Fe_{1000}-Ge samples implies that, compared to the samples containing the smaller cluster species, more current is transported by direct tunneling between clusters. Vice versa, more current is transported through the a-Ge matrix when it comes to Fe_{500}-Ge samples and, thus, the contribution of the a-Ge matrix to the total magnetoresistance is higher. This argument holds for all Fe_{500}-Ge samples. High values of samples G157 and G140 at 10 K are assigned to another, nonlinear component and are, thus, not representative.

When plotted vs. mean particle separation, which is done in Figure 4-32, the flanks are less steep and even change over to a positive slope at a certain temperature-dependent *MPS* with decreasing temperature. As the magnetoresistance of pure a-Ge is negative at 200 K and 100 K, bringing clusters closer together has to be the origin of a more and more positive contribution. At 100 K, where the magnetoresistance of a-Ge is small yet close to its zero point, the data at 200 K (graph (a)) seem to be shifted upwards with decreasing temperature (graph (b), at 100 K). Finally, at 40 K (graph (c)) the slopes are all positive.
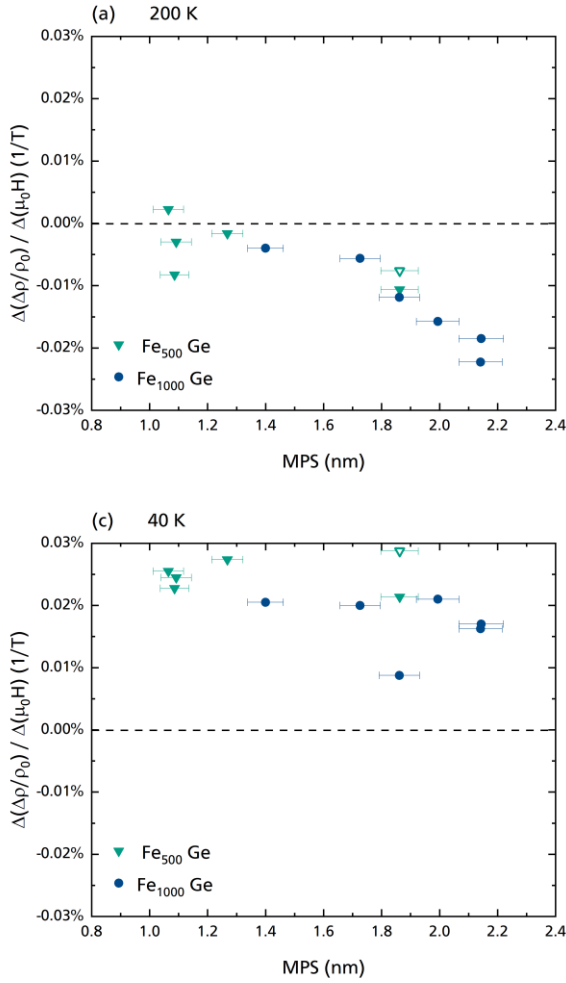
Figure 4-32: Slope vs. Mean Particle Separation at 200 K, 100 K, and 40 K

(a) 200 K, (b) 100 K, and (c) 40 K.

The slope decreases with increasing MPS. At 200 K it is negative for almost all samples. With decreasing temperature it progressively turns to positive values.

4.7.4.2 Nonlinear Magnetoresistance at Low Temperatures

As mentioned earlier in Section 4.4.2, a strongly nonlinear, negative magnetoresistance adds at low temperatures in case of some samples. The magnetoresistance curves recorded at 10 K of the five samples for which nonlinear low-temperature magnetoresistance was observed are plotted in Figure 4-33(a). The nonlinear magnetoresistance can be separated from the data by subtracting the approximated linear field dependence and shifting it by the observed tunneling magnetoresistance value. For the sample shown in Figure 4-33(b), G164, a tunneling magnetoresistance shift of -0.14% and a slope of 0.03% T^{-1} were subtracted from the as-recorded data to arrive at the depicted curve. As indicated in the graph, the nonlinear component of each sample can be approximated by an exponential function of the form $(\rho/\rho_0)_{NL} = -C(\mu_0 H)^k$, with $\mu_0 H$ in tesla, to great accordance. The parameters corresponding to the presented sample are $C = 1.85 \times 10^{-5}$ and $k = 2.6$.

All prefactors and exponents observed this way are plotted in Figures 4-33(c),(d), respectively. Obviously, the strength of the field dependence of the nonlinear magnetoresistance, represented by
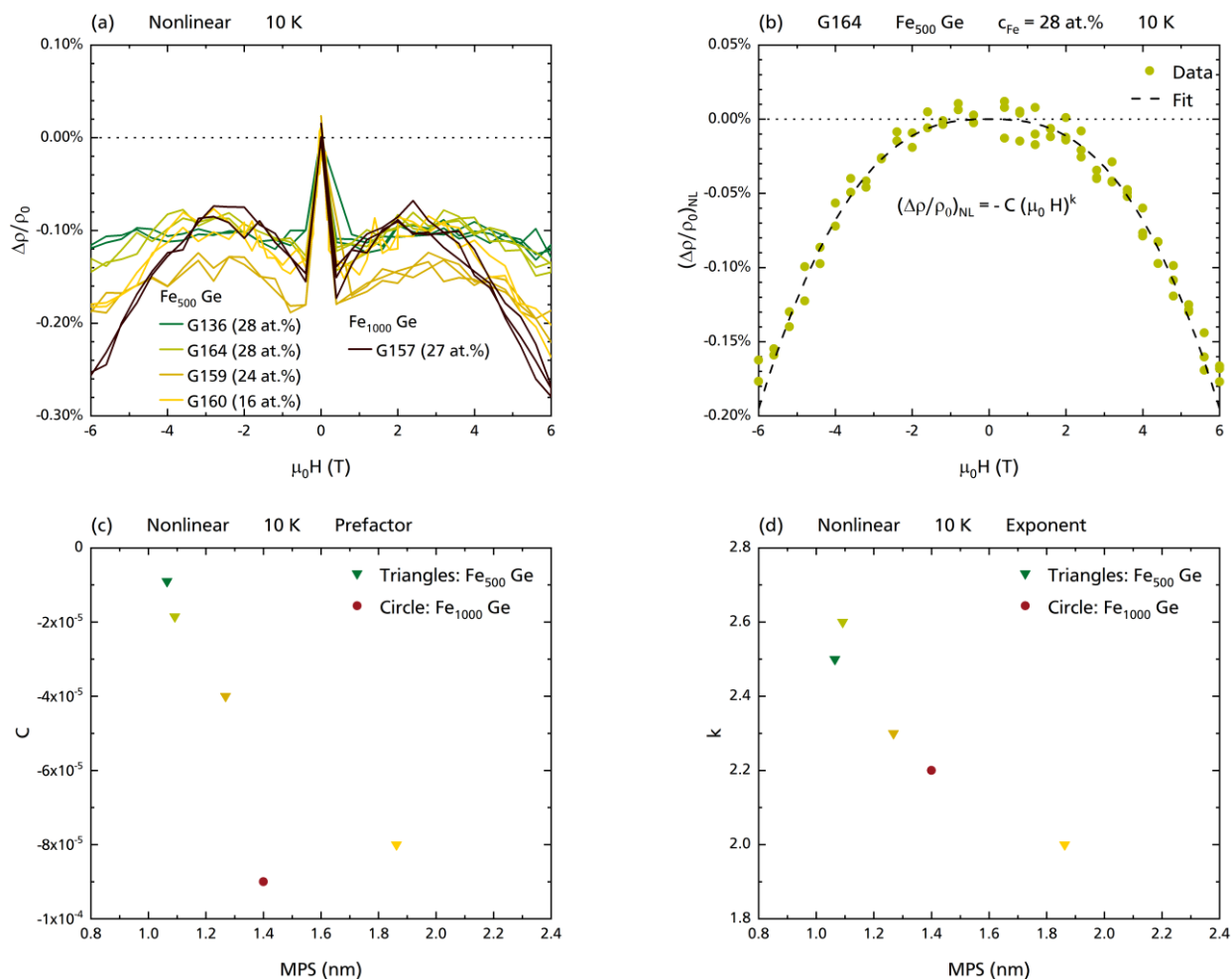
Figure 4-33: Magnetoresistance vs. Mean Particle Separation at 200 K, 100 K, and 40 K

(a) Magnetoresistance curves of five samples showing strong nonlinear magnetoresistance. As before, G160 is represented by the data of repeated measurements.
(b) Nonlinear component of a magnetoresistance curve extracted from sample G164, see text.
(c) Prefactors of the nonlinear fit curves vs. MPS.
(d) Exponents of the nonlinear fit curves vs. MPS.

exponent k, decreases with increasing mean particle separation. This means, the effect adds with more sensitivity to field changes when clusters are packed closer together. On the other hand, the prefactor C is larger in magnitude for samples with larger cluster separation but tends to zero as expected when approaching the percolation threshold.

Because the nonlinear component was only observed at temperatures of about 10 K, i.e., at or below the blocking temperatures of the samples, the effect may be related to blocked, i.e., apparently ferromagnetic Fe clusters. The higher intensity of the nonlinear magnetoresistance is assigned to stronger interaction taking place when clusters are packed closer on average.

4.7.4.3 Discussion of Field-Dependent Magnetoresistance Effects

Ordinary positive Lorentzian magnetoresistance can also occur in granular films, leading to a field-dependent increase in resistivity, which is best visible when low-field effects have saturated [8]. However, this is thought to happen in clusters much larger in size compared to the clusters of only 1000 atoms that were used in the present case, and where also metallic conduction can be assumed to happen inside. In semiconductors a positive magnetoresistance that increases linearly with an applied field can arise from microscopic local fluctuations of the conductivity at grain boundaries [43]. Because of the amorphous structure and, hence, the lack of grain boundaries the effect cannot occur in the present Fe-Ge nanocomposite samples.

In a nanocomposite material with ferromagnetic inclusions domain walls can form even below the physical percolation threshold when the superparamagnetic moments of an ensemble are blocked [165]. Carriers are scattered by these [194], which results in an isotropic negative magnetoresistance. Scattering at these domain walls can have an out-of-plane and an in-plane component. The ratio of perpendicular anisotropy and magnetostatic energy defines whether a bubble or a striped domain structure forms [165,195]. A characteristic feature of this effect is the bimodal behavior of the magnetoresistance: An inner maximum appears because of irreversible processes, e.g., domain wall motion and demagnetization. Therefore, the maximum in magnetoresistance not necessarily appears at the coercive field as was observed and assigned to domain wall scattering, e.g., by Lukashevich et al. [176]. However, for the present Fe-Ge nanocomposites the maxima positions match, as was proven in Section 4.7.3.1. Additionally, secondary outer maxima appear when the out-of-plane alignment of magnetic domains progressively rotates towards the (here in-plane oriented) field axis. Since the appearance of side maxima is a low-temperature feature and seemingly an effect that occurs when superparamagnetic moments are blocked, the ferromagnetic nature, i.e., the existence of magnetic domains, may be the origin of the side maxima observed in Fe-Ge nanocomposites at low temperatures.

Another explanation apart from the a-Ge matrix can be the following: High magnetic field behavior from room temperature down to 4.2 K of mainly Ni and Fe thin films between 3 nm and 300 nm in thickness was examined with the use of a pulsed magnet capable of up to 60 T by Gerber et al. [196]. Both in their Ni and Fe films—and also explicitly in granular ferromagnet-semiconductor systems—the authors observed an isotropic and positive magnetoresistance that increases linearly with the field at temperatures below 100 K. Gerber et al. relate this observation to electron-electron interactions. In their opinion, this is the only effect that "… seems to provide an adequate description of the [observed] LPMR [LPMR— abbreviation of linear positive magnetoresistance, authors remark]." [196]

However, Gerber et al. only present data of their metallic thin films. From the observed resistivity vs. temperature and magnetic field data Gerber et al. conclude that the mentioned electron-electron

interaction is the driving mechanism because of the following feature: A minimum in resistivity occurs at a certain temperature independent of the applied magnetic field and increases with decreasing film thickness (~10 K for 10 nm of Ni, ~30 K for 4 nm of Fe and 92 K for a 3 nm Ni film). Below this temperature, the resistivity obeys a logarithmic temperature dependence (in 2D, which holds for their samples under discussion). Above 100 K, other effects like spin-wave scattering add a temperature dependence to the resistivity that can turn the overall magnetoresistance into a negative one.

For the ferromagnetic metals Fe, Ni, and Co, Gerber et al. explain the detected LPMR as follows. The 4s electron sub-bands are spin-split because of the net magnetic field caused by the fully spin-polarized 3d electrons. This field causes the 4s sub-bands to be separated by an energy gap $\Delta(0) > 0.1$ eV [197]. This gap is further increased by an applied magnetic field so that it becomes $\Delta(H) = \Delta(0) + g\mu_B H$, where $g\mu_B H \ll \Delta(0)$ and $k_B T \ll \Delta(H)$. This mechanism adds a contribution $\delta\rho$ to the resistivity of a film that is linear in H both in 2D and 3D films.

First, as the high-field magnetoresistance curve of Fe-Ge nanocomposites are approximately linear above 40 K and change sign at about 90 K at least in case of the larger cluster species, and secondly, because the slopes of the magnetoresistance curves of the Fe-Ge samples (~10^{-2}% T^{-1}, see Figure 4-11) are within the range pointed out by Gerber et al. (~10^{-3}% T^{-1} for low-, ~10^{-1}% T^{-1} for high-resistivity materials), the phenomenology of the observations discussed by Gerber et al. suggests that the high-field magnetoresistance of the Fe-Ge nanocomposites of this thesis occurs for the same reason. Here, the electron-electron interactions suggested by Gerber et al. may occur within chains of agglomerated clusters that form metallic compounds of comparable expansions in the nanometer range. In samples below the percolation threshold the characteristic minimum in resistivity of the effect may be overdrawn by the strong temperature dependence of the tunneling conductance. In fact, for Fe-Ge samples above the percolation threshold a field-independent but Fe-concentration-dependent minimum in resistivity was observed.

However, this minimum in resistivity is a common feature of granular metallic films and is an effect of electron multiple scattering and localization at low temperatures [198,199]. In contrary to the diffusion of classical particles, the coherent backscattering effect appears when the electron is treated as a quantum mechanical wave rather than a particle: Scattering by an angle of 180° is always coherent and, therefore, can diminish the diffusion constant by a reasonable amount. This is because of the strong scattering by impurities, e.g., by the clusters in a cluster-assembled material in the present case. A sufficiently strong backscattering contribution can lead to electron localization. To be precisely, when the number of backscattered electrons is on the same order as the number of electrons diffusing in the classical way. Furthermore, negative magnetoresistance in granular metals is generally believed to be caused by a reduced backscattering effect due to an applied magnetic field [198,199]. However, Fe-Ge

samples above the percolation threshold did not show any magnetoresistance within measurement accuracy.

Owing to the random deposition of clusters an effective size distribution of clusters due to agglomeration and coupling of Fe clusters is present in the nanocomposite films. Therefore, both blocked (ferromagnetic) and superparamagnetic regions coexist within the temperature range defined by the following two limits. Small and well-isolated clusters experience negligible interaction and possess a low blocking temperature. On the other hand, regions with a high local cluster concentration exhibit higher blocking temperatures because of stronger interaction. Besides the individual blocking temperature of a single cluster, it is the tendency of the surface moments of a cluster to become aligned and the effective surface-to-volume ratio of aggregates of clusters that determine at what temperature a compound of clusters becomes collectively blocked. This is respected by a disorder temperature that is added to the temperature dependence of the Langevin function. The resulting magnetoresistance is field dependent and negative [200–204]. Since this effect happens in range of the blocking temperature of a sample it is a good candidate for the negative field-dependent component adding at temperatures below 40 K.

4.7.4.4 Competition of Cluster and Matrix Magnetoresistance

Tunneling magnetoresistance between ferromagnetic clusters depends on the relative orientation between the surface moments of the clusters and the relative orientation between their net moments in general. The more the majority carriers are favored by a best possible parallel alignment of moments, the lower the resistance of a tunneling contact becomes. However, conduction is expected to also happen within and through the nonmagnetic a-Ge matrix. A carrier hopping from a cluster surface state into a matrix dangling bond state also obeys VRH conditions (see Section 4.1.2.3) because its original state is close to the Fermi level (the Fe clusters are of metallic kind) and seeks for a state that anyway belongs to the a-Ge matrix. In VRH, hops that require a spin flip in order to occupy a close-by state are favored above hops to states that are further apart, but for the occupation of which no spin flip is required. As non-spin-preserving tunneling, e.g., over distances longer than the spin diffusion length [13], reduces the magnetoresistance, these spin flip processes counter the tunneling magnetoresistance by turning majority spin carriers into minority spin carriers as well. Then, transport happens in the sense of multistep tunneling just like as the moments of the target cluster would have been reversed [205]. Spin flips can also be caused by impurities within the matrix or by surface states [24,205]. In contrary to tunneling magnetoresistance between ferromagnetic particles, a-Ge does not gain its magnetoresistance from the degree of alignment of charge carriers but from the change in the spin relaxation times that determine the ratio of hops including a spin-flip and hops that do not. Gibson & Meservey's [146] result that tunneling currents through a-Ge tunneling barriers do not show any spin polarization suggests the following explanation. A surplus of majority spin carriers on the superparamagnetic clusters that can, as

an alternative to direct tunneling, hop into the matrix represents an off-equilibrium situation of the matrix. Accordingly, the fraction of majority spin carriers performing spin-preserving normal hops increases because the number of preferred anomalous hops is limited and best possibly utilized already under equilibrium spin conditions. Impeding minority carriers from anomalous hops by occupying their preferred target states to a higher degree, transport of majority carriers effectively decreases the degree of spin polarization of charge carriers that are transported via matrix states. Turning majority carriers into minority carriers by spin-flip hops, therefore, is also a mechanism which reduces the magnitude of tunneling magnetoresistance and, hence, the magnetoresistance observed from Fe-Ge nanocomposites.

4.7.5 Isotropy of Magnetoresistive Properties, Influence of the Excitation Current, and Durability of the Nanocomposite Samples

Though soft-landing conditions were met during co-deposition of the nanocomposites, see Section 4.2.3, the Fe clusters may still have carried enough thermal energy from the aggregation and formation processes to permit mixing and alloying of cluster and matrix material. Especially, since the Ge matrix material is also deposited 'hot' from the effusion cell. Storing samples at room temperature for weeks and months may have also lead to the formation of Fe-Ge alloys. Besides the formation of larger species out of agglomerated clusters, Ge atoms slowly diffusing into the Fe clusters would have been the most probable process of aging in the deposited films.

Even after long exposure times to air that inevitably came with successive sample handling no T^{-1} dependence was observed, although, clusters may have got oxidized resulting in oxide shell samples as used in Reference [177]. Some samples even did not change in resistance after more than 200 days from first measurement in which they could have developed Fe_xO_y inclusions or shells around Fe inclusions or even Fe_xGe_y alloy phases. This is counted as a great effectiveness of the protecting Si and Ge layers that were deposited onto each co-deposited film (see Section 4.2.3) and film stability, motivating for annealing experiments, as discussed in Sections 4.5.3, 4.7.6, and 4.7.7.

4.7.5.1 Isotropy of Magnetoresistive Properties

The transport measurements of all samples were performed in a longitudinal orientation in order to avoid any Hall effect influence. To do so, a sample was mounted onto the PPMS sample puck with the long side of the sample film pointing into the direction of the magnetic field inside the PPMS, see Section 4.2.2 and Figure 4-7. Because some magnetoresistive effects depend on the relative orientation between magnetic field and excitation current (anisotropy of magnetoresistance) some samples were measured in all three orientations,
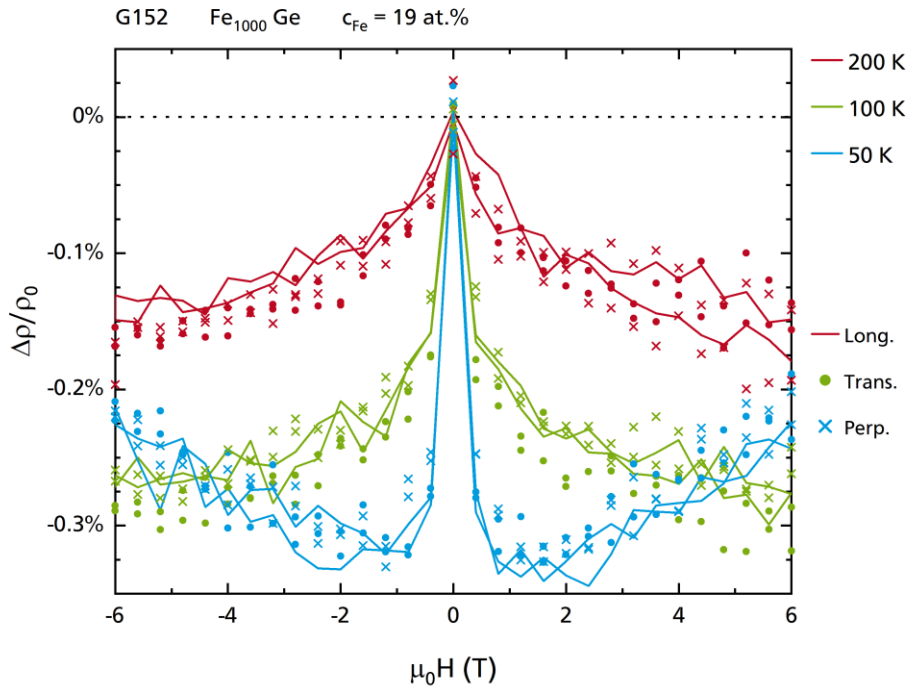
Figure 4-34: Magnetoresistance Curves of G152 for all Three Orientations and at Three Different Temperatures

Data recorded in longitudinal alignment are plotted as lines, these recorded in transverse and perpendicular orientation are added as circles and crosses, respectively. No anisotropic behavior is observed within data accuracy.

(1)   Longitudinal: Current parallel to magnetic field (standard),

(2)   Transverse: Current perpendicular to magnetic field with field still parallel to sample plane,

(3)   Perpendicular: Magnetic field perpendicular to sample film plane,

to exclude orientation-dependent effects. Both tunneling magnetoresistance between clusters and the intrinsic magnetoresistance of a-Ge are expected to be isotropic. In Figure 4-34, magnetoresistance curves recorded in longitudinal orientation are drawn with lines, data recorded in transverse and perpendicular orientation are added as circles and crosses, respectively. Same colors represent data recorded at the same temperature. In fact, no anisotropic behavior was observed within data accuracy.

4.7.5.2 Influence of the Excitation Current

Like shown for samples G152 and G164 in Figures 4-24(c),(d), the excitation current applied to a sample and the voltage measured are of linear dependence. For this reason, also magnetoresistance curves should be independent of the applied current. As magnetoresistance curves were usually recorded using up to four excitation currents this could be counterchecked for most of the samples, like it is shown for sample G146 and G164 in Figures 4-35(a),(b), respectively. Variations were found to be within data
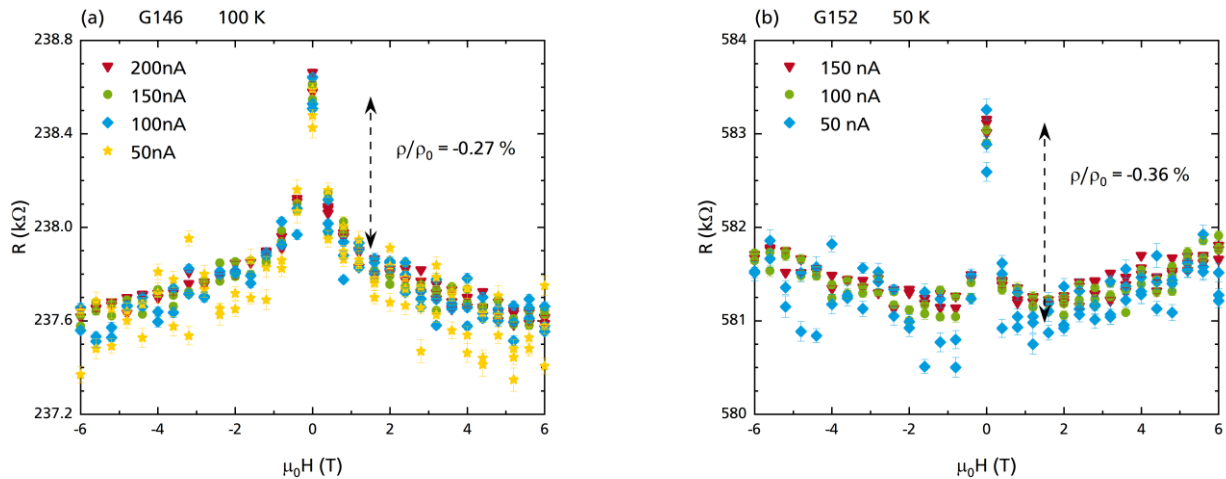
Figure 4-35: Magnetoresistance Curves of Samples G146 and G152 Recorded with Different Excitation Currents

The observed magnetoresistance curves are independent of excitation current within data accuracy.

accuracy. Only at low temperatures and high resistances, where excitation currents of 20 nA and less had to be applied, deviations were found. However, accounting these nonlinearities to the samples is vague because the PPMS was run at its limit of resolution to record these data.

4.7.5.3 Durability of Fe-Ge Nanocomposite Samples

Bare Fe clusters are prone to oxidation. Because the a-Ge grew as a porous structure, 100 nm of additional a-Ge and a Si capping layer were deposited on top of the nanocomposite films in order to protect them from chemical and mechanical damaging. Some samples were again measured several months after their first measurement prior to annealing experiments, see Section 4.5.3. Although samples were stored in vacuum most of the time, each sample was exposed to ambient atmosphere many hours or even days until this next measurement because of the unloading and loading of other samples and also during sample handling (transfer, wire bonding, etc.). It turned out that the taken measures successfully protected the nanocomposite layers of the samples from chemical and mechanical damaging. As can be seen exemplarily in Figures 4-36(a),(b) and 4-39(b) from resistivity and magnetoresistance data, respectively, only little deviations between the original data and the data recorded prior to annealing were observed.

4.7.6 Annealing and Hydrogenation at 220 °C

Thermal annealing is one strategy to irreversibly change the properties of a nonequilibrium film. Another, more specific way is to saturate the dangling bonds of the a-Ge matrices with hydrogen atoms, briefly referred to as hydrogenation. Both measures were performed with some of the present Fe-Ge
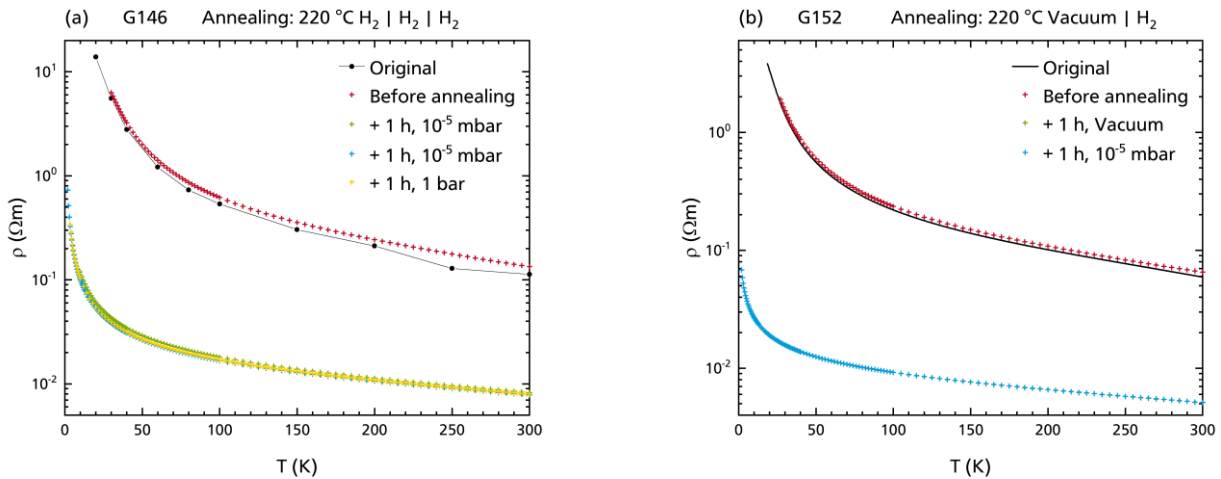
Figure 4-36: Resistivity vs. Temperature as Measured Before and After Different Annealing Steps Performed at 220 ℃

Data taken in the original measurement are plotted in black. Data recorded right before annealing procedures are colored in red. Data recorded after annealing steps are drawn in green, cyan, and yellow.

nanocomposites, as explained in Section 4.5.3. In this section, the results of thermal annealing at 220 °C and hydrogenation are discussed.

4.7.6.1 Influence of Annealing Time and Gas Pressure

To test the dependence of the Fe-Ge nanocomposite properties on annealing time sample G146 was annealed twice for one hour at 220 °C and 5×10^{-5} mbar ARCAL 15 atmosphere each, and for one hour at 1000 mbar in a third step. As shown in Figure 4-36(a) the resistivity data recorded after each step, colored green, cyan, and yellow, respectively, coincide over the entire temperature range. Therefore, one hour of annealing is sufficient to irreversibly transform a nonequilibrium Fe-Ge nanocomposite film into a film with equilibrium composition.

Also, the presence of hydrogen does not affect the nanocomposites. This was tested by annealing sample G152, first, in UHV, and secondly, in ARCAL 15 atmosphere. As it was observed for sample G146, again, no further annealing happened after the first annealing step. The resistivity data overlap almost perfectly as it is depicted in Figure 4-36(b). This implicates that the presence of hydrogen does not influence the annealing of the nanocomposite films. Since it is the a-Ge matrix that is changed by hydrogenation it can be concluded that hydrogen cannot permeate the nanocomposite or that transport is not mediated by matrix dangling bond states to reasonable extents. The independence is further confirmed by the third annealing step performed with sample G146. Though continuously venting the process chamber with ARCAL 15 at 1000 mbar, no changes were observed in the transport measurements following this step.
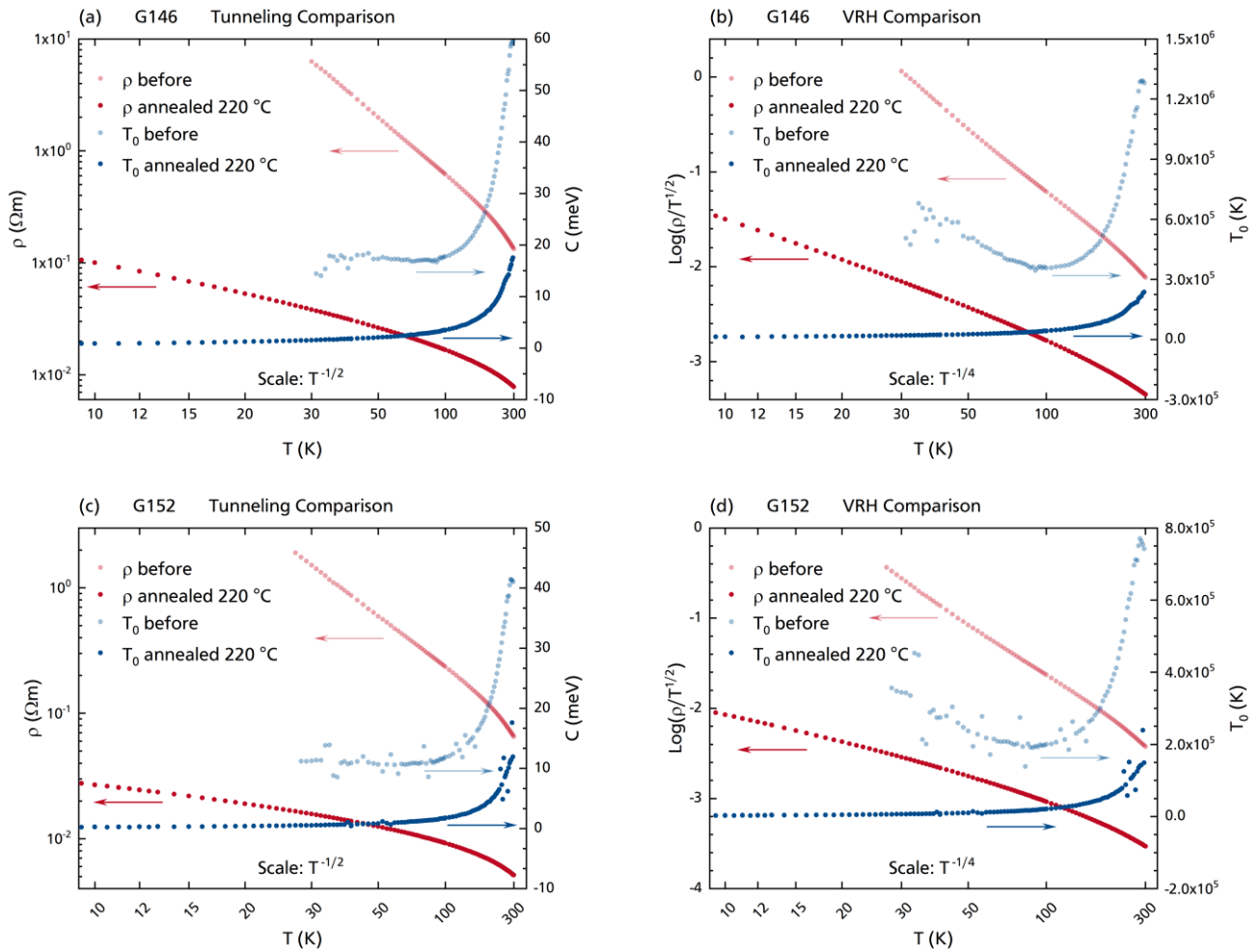
Figure 4-37: Comparison of Resistivity vs. Temperature Data Taken Before and After Annealing at 220 °C

The upper row shows data of sample G146, the lower row shows data of sample G152. The plots in the left column are scaled according to 'tunneling scaling', those of the right column are scaled according to 'VRH scaling'. None of the effects is dominating in any temperature range.

Moreover, it is noteworthy that the two shown samples experienced no mentionable ageing due to oxidation or long-term annealing at room temperature during storage and sample handling. The resistivity data recorded in the original measurement (black) and these taken right before the annealing procedures (red) overlap in very good agreement.

4.7.6.2 Transport Properties

The resistivities of the five samples at 300 K decreased by a factor of 4 (G160, Fe_{500}-Ge), 5 (G144, Fe_{1000}-Ge), and 13 (G146, G148, and G152, all Fe_{1000}-Ge) during annealing at 220 °C. As it is shown exemplarily for samples G146 and G152 in Figure 4-37, analyzing resistivity data according to Section 4.7.2.3 reveals that neither tunneling nor VRH is dominating at any temperature range. Both in 'tunneling scaling', plots (a),(c), and 'VRH scaling', plots (b),(d), parameters C and T_0 reduce to much

lower approximate values at low temperature compared to the original values. The minima in 'VRH scaling' observed for the as-deposited samples disappear or shift to a much lower temperature (~30 K). However, the shape of resistivity vs. temperature curves (summarized in Figure 4-12) stays very much the same, i.e., of the kind typical for semiconductors.

If it was only the a-Ge matrix that undergoes a structural annealing in terms of reorganizing its tetrahedral base units, tunneling should still be the transport process dominating at lower temperatures, even when the amount and width of 'bottleneck' gaps along paths of high conductivity are reduced. This implicates that a diffusion of Ge atoms into Fe clusters and a connection of separated Fe clusters by linking inter-cluster Fe precipitates or Fe impurity atoms in the a-Ge matrix may have happened during annealing. In this manner, the structural change induced a rebalancing of transport processes and this rebalancing is reflected by the resistivity curves of the annealed samples.

4.7.6.3 Magnetic Properties

Further details about the effects of annealing on the nanocomposite films may be revealed by investigating the magnetic properties of the films, first, in the as-deposited and, subsequently, in the annealed state. ZFC/FC data (red/gray) of sample G144 recorded (a) prior to and (b) after annealing are compared in Figure 4-38. Sample G144 was annealed three times for one hour under the conditions specified above (220 °C, 5×10^{-5} mbar ARCAL 15) before the magnetization data shown in graph (b) were recorded.

Prior to annealing, a blocking temperature of 21 K was found for G144. Well above this temperature, the magnetization was fully reversible, as expected for an ensemble of superparamagnetic particles. After annealing, blocking occurs already at 8 K, where the ZFC maximum also became more defined in shape. Moreover, the magnetization curve of the annealed sample is no longer reversible. Figure 4-38(b) clearly shows that the FC curve is always above the ZFC curve. Also, no hysteresis in magnetization vs. applied magnetic field measurements was observed at 5 K within data accuracy. Instead, anhysteretic behavior with a saturation magnetization of only 40% of the one of the as-deposited sample was observed.

The shift to a lower temperature and the reduced width of the maximum in the ZFC curve implicate that the size distribution of superparamagnetic particles in the film became sharper and its mean value shifted towards smaller particles. For the first view, this is the opposite of what is expected when a cluster-assembled nonequilibrium nanocomposite film is annealed. However, it can be interpreted as follows. The magnetization signal is dominated by small single clusters that remain isolated after the annealing procedure. Clusters that are closer together merged to larger particles that do not exhibit superparamagnetic properties anymore but seem to be of ferromagnetic kind instead. Also, Fe impurity
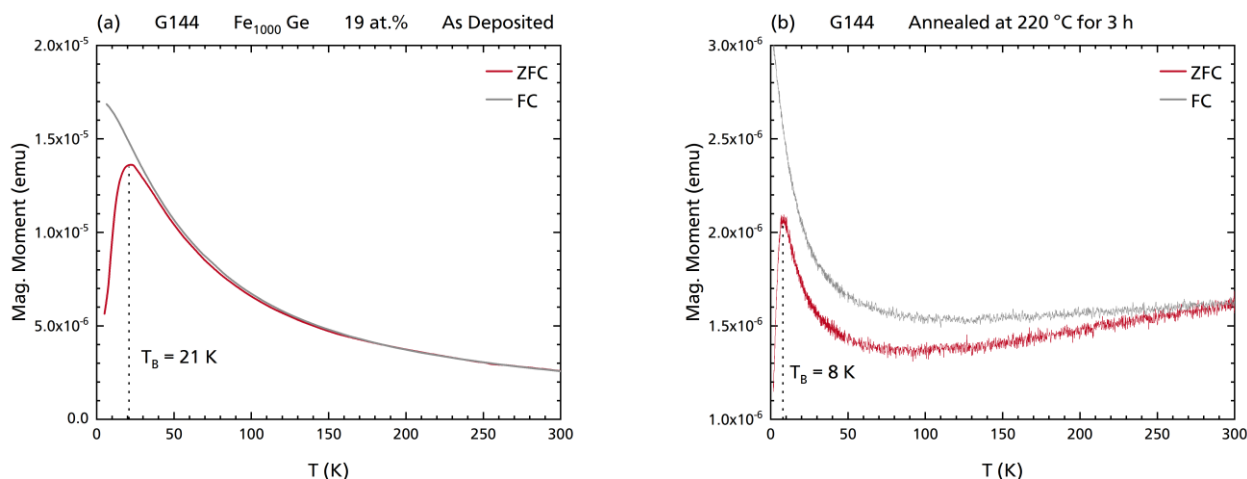
Figure 4-38: Comparison of ZFC/FC Magnetization Curves Before and After Annealing at 220 ℃

ZFC/FC magnetization curves of sample G144 (a) before and (b) after annealing at 220 ℃. The maximum of the ZFC curve shifts from 21 K to 8 K. Also, the curves are irreversible above the blocking temperature. This indicates the presence of a ferromagnetic phase.

atoms may have entered the a-Ge matrix via atom diffusion while simultaneously Ge atoms may have been incorporated into the Fe granules.

It is difficult to assign the irreversibility of the magnetization in the ZFC/FC measurements up until room temperature to the formation of ferromagnetic moments during annealing since neither at 5 K nor at 300 K hysteretic behavior was observed in the magnetization vs. magnetic field curve of the sample under discussion. However, larger superparamagnetic compounds with a blocking temperature above 300 K that may have formed during annealing may explain the observed behavior instead. The superparamagnetic moments of the magnetically active component progressively become blocked with decreasing temperature. Consequently, a progressively larger and irreversible contribution adds to the magnetization recorded during a ZFC/FC cycle.

The reduction of saturation magnetization is also mirrored by the observed total magnetization in ZFC/FC magnetization measurements, which reduces by about one order of magnitude. Obviously, the number of magnetic moments that can be aligned decreases. This may be because of larger surface-to-volume ratios of Fe inclusions, the formation of nonmagnetic Fe_xGe_y alloys, or Ge atoms that now intersperse the outer shells of the clusters because of reorganization of Fe/Ge interfaces. In the latter case, the magnetically active core of a cluster is effectively shrunken, thus, providing a lower total cluster moment.

The lack of hysteresis even at low temperatures means there are neither blocked superparamagnetic particles with a blocking temperature above 5 K nor was the applied magnetic field strong enough to reverse potentially existing ferromagnetic domains in the film.

4.7.6.4 Magnetoresistive Properties

Annealing Fe-Ge nanocomposites at 220 °C strongly changes the observed magnetoresistive behavior. In Figure 4-39(a) several magnetoresistance curves of the annealed sample G146 are shown. Down to at least 40 K the total magnetoresistance of the sample remains even lower in effect compared to the curves recorded from the as-deposited sample. At lower temperatures, a strong negative magnetoresistance occurs that, judged by its characteristic field dependence, was not observed in the as-deposited nanocomposites. It increases approximately linearly with the applied magnetic field and reaches several percent of effect at a maximum magnetic field of 6 T when measured at temperatures of less than 10 K.

Showing decent tunneling magnetoresistance of about −0.3% and a total magnetoresistance of −0.4% at 100 K and 6 T, the repeated magnetotransport measurements performed right before the annealing procedure replicates the original magnetoresistance curves to very good agreement as can be seen in Figure 4-39(b). However, annealing reduced the magnetoresistance of the shown nanocomposite sample to approximately zero. Again, the data implicate there is neither a dependence on annealing duration, i.e., number of repetitions, nor on the amount of ARCAL 15 fed to the vacuum chamber during annealing experiments.

Also, a clear and distinct increase at low fields like it was observed from the as-deposited nanocomposites now occurs only at low temperatures. In Figures 4-39(a),(d) the low-field magnetoresistance can only be clearly identified in the curve recorded at 2 K. At temperatures above 2 K, the field-dependent component veils the characteristic shape of the low-field drop, which makes it hard to identify and separate it from the data. Above 10 K the magnetoresistance becomes comparably small in effect.

For annealed sample G146 hysteretic behavior was observed in the magnetoresistance curve at 2 K, and 2 K only, as presented in Figure 4-39(c). This is in accordance with the lack of hysteresis in the magnetization curve of annealed sample G144 at 5 K. In contrast to G146, no hysteretic behavior at temperatures as low as 2 K was observed from annealed sample G160, whose low-temperature magnetoresistance evolution is shown in Figure 4-39(d). This can be assigned to the smaller clusters embedded in this nanocomposite film since these also exhibit smaller blocking temperatures. The single-particle blocking temperature of Fe_{1000} clusters is about 2 K (see Section 4.5.2.2). At 2 K also a weak shoulder-like feature develops between 2 T and 3 T. It appears in the magnetoresistance data of both sample G146 and G160, see graphs (a),(d), respectively.
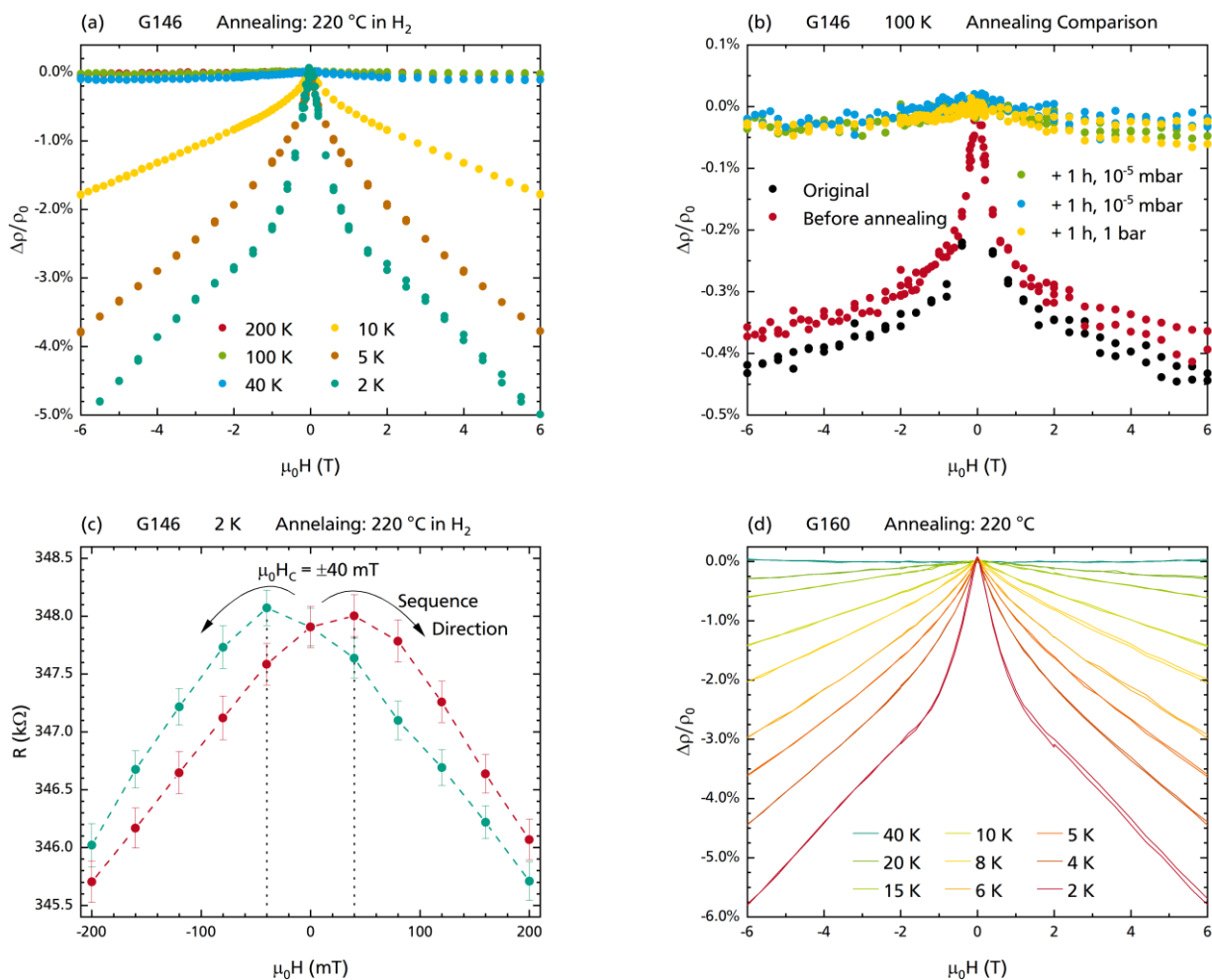
Figure 4-39: Example Magnetoresistance Data of Fe-Ge Nanocomposite Samples Annealed at $220\,°C$

(a) Magnetoresistance curves of annealed sample G146 at various temperatures. The data recorded at $200\,K$ are hidden behind the data recorded at $100\,K$ and $40\,K$.
(b) Magnetoresistance curves of annealed sample G146 at five different stages of annealing, see legend in plot.
(c) Center of the low-field range in the magnetoresistance curve of annealed sample G146 at $2\,K$. Hysteretic behavior is evident.
(d) Magnetoresistance curves of annealed sample G160 at various low temperatures.

4.7.6.5 Conclusions

For the samples annealed at $220\,°C$, no correlations between resistivity, magnetoresistance, and mean particle separation were found. This is in contrast to the as-deposited samples. Regarding the discussed transport, magnetization, and magnetoresistive properties, the following conclusions about the changes of the nanocomposite films upon annealing at $220\,°C$ can be drawn.

The reduction of resistivity by one order of magnitude implicates that transport is simplified in general. As the maximum in the ZFC curve of sample G144 became sharper and shifted towards a lower temperature during annealing, the average size of superparamagnetic clusters must have reduced.

Because of the random deposition during synthesis, clusters can both remain isolated from and be deposited in immediate vicinity of other clusters. This affects the superparamagnetic properties of the clusters and causes a size distribution of aggregates of effectively embedded clusters. The lower and narrower maximum in ZFC magnetization data indicates that well-isolated clusters are still present in the annealed nanocomposite. Therefore, tunneling still occurs but is of less dominance. The reduction in tunneling magnetoresistance and the fact that the annealed sample G146 shows hysteresis in resistivity only at 2 K, at about the single-particle blocking temperature of Fe_{1000} clusters, supports the assumption that small clusters are still present in the annealed nanocomposites.

The decrease in resistivity suggests that transport through the Ge matrix becomes more important. Its structure definitively must have changed during annealing. Charge transport favors paths of high mobility. The decrease in resistivity implicates that the conductivity of 'links' between well-conducting segments along these paths was improved and these links are not of bare tunneling junctions anymore. This can be explained by the intermixing of Fe and Ge atoms in regions of high local Fe concentration. Intermixing of atoms also gives an explanation for the observed reduced saturation magnetization.

Impurity states from Fe atoms within the a-Ge matrix may change the VRH conditions within the a-Ge matrix. In pure a-Ge there is no spin polarization of electrons. This changes when Fe atoms with a finite moment are added and this may lead to a different hopping behavior due to the induced imbalance. This effect may be amplified when the magnetic moments of the Fe atoms are aligned by an external magnetic field and the effect should be recognizable at all temperatures. In particular, the change from negative to positive magnetoresistance at 80 K should be observed. However, the magnetoresistance was found to be reduced in effect over most of the examined temperature range. A strong field-dependent magnetoresistance is only observed at low temperatures. Therefore, conduction through a matrix that exhibits better transport properties due to the annealing is not the dominating process of transport.

A better explanation can be given by the picture already drawn when discussing the magnetic properties. Regions locally high in Fe cluster concentration effectively merge into superparamagnetic particles with a high degree of misaligned moments due to an intermixing with Ge matrix atoms during annealing. This way, again an effective size distribution forms in the annealed nanocomposite films, providing an even wider distribution compared to the as-deposited films. Therefore, the condition that some clusters are blocked while others are still in their superparamagnetic state is fulfilled over an even wider temperature range, which leads to a negative field-dependent magnetoresistance as was discussed for the as-deposited nanocomposite samples. In this approach well-isolated clusters remain as such and only contribute to little extents. The weak shoulders present at 2 K may be related to the existence of magnetic domains.

4.7.7 Annealing at 700 °C

Annealing sample G152 at 700 °C, i.e., at a temperature largely above the range where crystallization of a-Ge was found to set in [130,168], see Section 4.6.3, completely changed its properties in terms of both charge transport and magnetic behavior. The results are the topic of the present section.

Magnetoresistance data were recorded in longitudinal, transverse, and perpendicular orientation and magnetization data were collected both with the magnetic field applied in-plane (parallel to the long side of the sample stripe) and perpendicular to the film plane.

4.7.7.1 Magnetotransport Properties

In Figure 4-40(a), the temperature evolution of the absolute resistance of G152 after crystallization is plotted (red, left y-axis) together with its approximate derivative (blue, right y-axis, according to Equation [4-16] for linear scaling). The three arrows highlight the data points at which magnetoresistance data are compared in graphs (b)–(d): 200 K, 70 K, and 30 K.

The room temperature resistance of 700 °C-annealed sample G152 is two orders of magnitude lower compared to its 220 °C-annealed state and by even three orders of magnitude compared to its as-deposited state. In contrast to both of its former states, the resistance now decreases with decreasing temperature, i.e., now exhibits a metal-like temperature dependence (red data in graph (a)). At 90 K the resistance reaches a minimum, at even lower temperature the resistance increases again by two orders of magnitude, and at 30 K the resistance has a maximum. The resistance decreases again when the temperature is reduced further. However, precise resistance measurements were not possible at temperatures lower than 24 K anymore, as indicated by the error bars. Low-temperature resistance data recorded down until 10 K are shown in Figure D-3(a) in Appendix D. Apart from the error bars that are explicitly shown for some low-temperature data points the error bars are smaller than the size of the symbols.

The cyan data points in graph (a) represent resistance values recorded at 6 T with the field applied perpendicular to the film plane. Obviously, the resistance peak is shifted to a slightly higher temperature. The shift is not present when the field is applied in-plane (yellow and green data points).

No dominating transport mechanism (activated, tunneling, or VRH) could be identified from resistance data at temperatures below about 90 K. However, within its metal-like conduction temperature-regime the resistance of the sample changes its slope between 250 K and 300 K (300 K is the highest temperature resistance data were recorded at). The change is seen best in the approximate derivative data. This feature may be connected to an intrinsic change within the nanocomposite as it coincides with the temperature at which magnetization data suggest that a reorientation of the
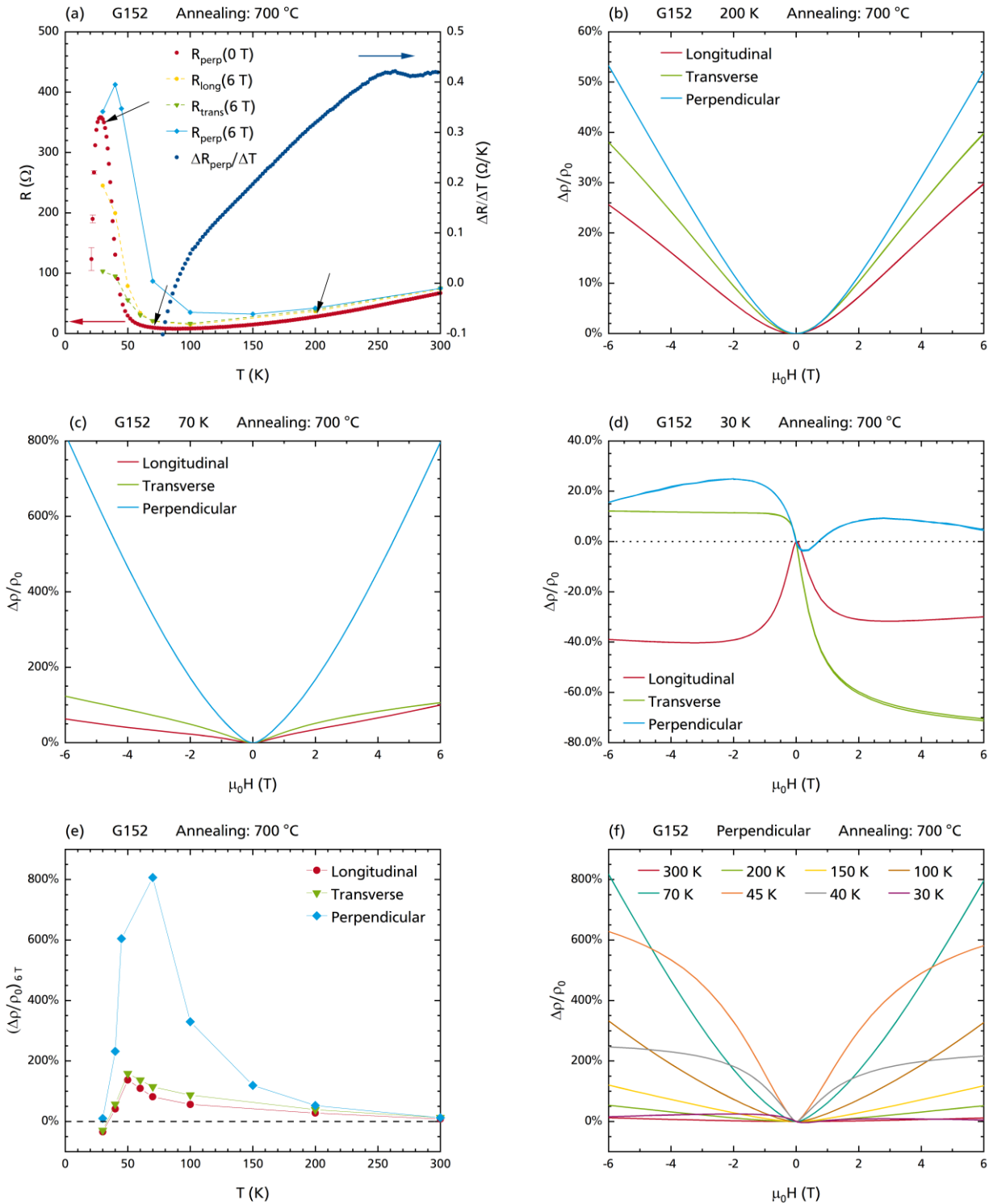
Figure 4-40: Resistance and Magnetoresistance Data of the $700\,°\mathrm{C}$ Annealed Fe-Ge Sample G152

   (a) Resistance in zero field, with the sample installed perpendicular to the direction of the applicable magnetic field (red), resistance at $6\,\mathrm{T}$ in longitudinal, transverse, and perpendicular orientation (yellow, green, and cyan), and approximate derivative (blue) vs. temperature.

(b)–(d) Magnetoresistance curves recorded with the magnetic field longitudinal (red), transverse (green), and perpendicular (cyan) to the sample film plane at (b) $200\,\mathrm{K}$, (c) $70\,\mathrm{K}$, and (d) $30\,\mathrm{K}$.

   (e) Summarized magnetoresistance vs. temperature data from longitudinal, transverse, and perpendicular alignment.

   (f) Magnetoresistance curves recorded in perpendicular alignment at various temperatures.

superparamagnetic moments to a collective in-plane orientation is happening. This will be discussed in the next section, Section 4.7.7.2. However, the two events may also be uncorrelated. Then, the artifact may be assigned to changes in the contact qualities between the co-deposited film and the Pt contact lines due to thermal expansion. Nevertheless, the artifact is reproducible and appears in all three sample orientations (longitudinal, transverse, perpendicular).

Assuming that activated transport is veiled by a superposition with other effects, the raw evolution of the resistance at low temperature (Figure D-3(a) in Appendix D) may be interpreted in terms of a doped semiconductor as follows. The initial decrease from 10 K to 20 K and the second decrease between 30 K and 90 K are assigned to the activation of charge carriers from doping levels. The increase in resistance following each decrease is due to the increasing rate of extrinsic charge carriers scattering with phonons. In this picture, a final decrease of the resistance caused by intrinsic charge carriers starting to dominate the transport is expected. This feature may occur at temperatures above 300 K.

As highlighted by the arrows in graph (a), magnetoresistance curves recorded at 200 K, 70 K, and 30 K are compared by the orientation of the sample film relative to the direction of the applied magnetic field in Figures 4-40(b)–(d), respectively. A dependence on the relative alignment is evident from the recorded curves at all three temperatures. The strongest effect is achieved when the magnetic field is applied perpendicular to the film plane (cyan), followed by transverse alignment (green, field in-plane but perpendicular to the direction of the excitation current). In longitudinal alignment (red, field parallel to the direction of the current) the magnetoresistance is smallest. Regarding Figure 4-40(c), it is noteworthy that the magnetoresistance at 70 K is one order of magnitude larger in the perpendicular alignment compared to the transverse and longitudinal case. The relative change of the resistance due to the maximum applied magnetic field $\Delta\rho(6\,\text{T})/\rho_0$ is largest at about 50 K. This is proven in Figure 4-40(e), which summarizes all magnetoresistance data in a temperature evolution plot.

In Figure 4-40(f) the magnetoresistance curves recorded in perpendicular alignment are plotted for various temperatures. The data create the cyan curve in graph (e). When the temperature is above 50 K the magnetoresistance increases approximately quadratically with the applied field with no indication of saturation. Below 50 K, a quadratic field dependence is only observed for magnetic fields ≤ 100 mT while for larger fields the magnetoresistance curves are of concave shape, i.e., they either tend to saturate at high fields or are superimposed by a negative magnetoresistance effect that progressively overcomes the positive one. When approaching 30 K the magnetoresistance is strongly reduced over the entire magnetic field range and even changes its sign from positive to negative. The asymmetry of the magnetoresistance curves with respect to the sign of the applied magnetic field is assigned to the sample layout, in particular, to the electric contact via four parallel Pt contact lines and variations of the Fe concentration across the region under transport measurement.

4.7.7.2 Magnetic Properties

In Figure 4-41, magnetization vs. temperature data of sample G152 annealed at 700 °C with (a) the magnetic field applied in-plane (parallel to the long side of the sample stripe) and (b) perpendicular to the film plane are shown. Besides the ZFC warming and FC cooling curves (red and gray, plotted against the left y-axes), magnetization data recorded during the initial warming to 400 K in zero field are added in green (plotted against the right y-axes). Before the initial warming the sample was exposed to a 10 mT field at room temperature for sample positioning reasons and, though this already happened several days before, to 6 T at 10 K in the preceding transport measurements. After the initial warming, the sample was demagnetized in an oscillating field at 400 K and cooled to 2 K in zero field right after. Again, magnetization is the sum of all contributions from the sample, i.e., from the entire cluster spot region. Therefore, features that appear in the magnetization vs. temperature curves need not represent the state of the annealed film at the very region chosen for transport measurements, which was the region with the highest Fe concentration.

Obviously, the 700 °C-annealed nanocomposite behaves differently depending on whether the field is applied parallel to the nanocomposite layer (in-plane) or perpendicular to it (out-of-plane). With the field applied in-plane a larger magnetization is recorded. This may be explained by the fact that the disk-shaped volume of embedded Fe (circular cluster ion beam spot × film thickness) is approximated as a magnetic dipole when the magnetic moment of the sample is measured. The plateaus of the FC curves below about 40 K are assigned to Fe atoms in not further defined ferromagnetic or blocked superparamagnetic states. The ZFC curve (red) shows a quick decrease when the field is applied in-plane (graph (a)) but a quick increase when it is applied perpendicular (graph (b)) at this temperature as highlighted by arrows. Because of the low temperature this is assigned to small superparamagnetic clusters far apart from the center of the cluster spot and to those that may still be present in the region of higher Fe concentration closer to the center of the disk. Nonetheless, this suggests that an out-of-plane alignment of these moments is favored.

When the magnetic field is applied in-plane the magnetization remains approximately constant up until about 250 K. Above, it starts to increase. This change is highlighted by another arrow in Figure 4-41(a). With the field perpendicular to the film plane, however, the magnetization increases continuously. In the latter case this means magnetic moments are progressively aligned, out from a blocked or favored orientation to that of the magnetic field. Hence, the data indicate that in-plane alignment is the favored orientation of the magnetic moments and that this orientation is present when no magnetic field is applied. A progressive alignment to an in-plane applied magnetic field starts at about 250 K. Because a ferromagnet would show a decrease in magnetization with increasing temperature it again must be superparamagnetic moments that become aligned.
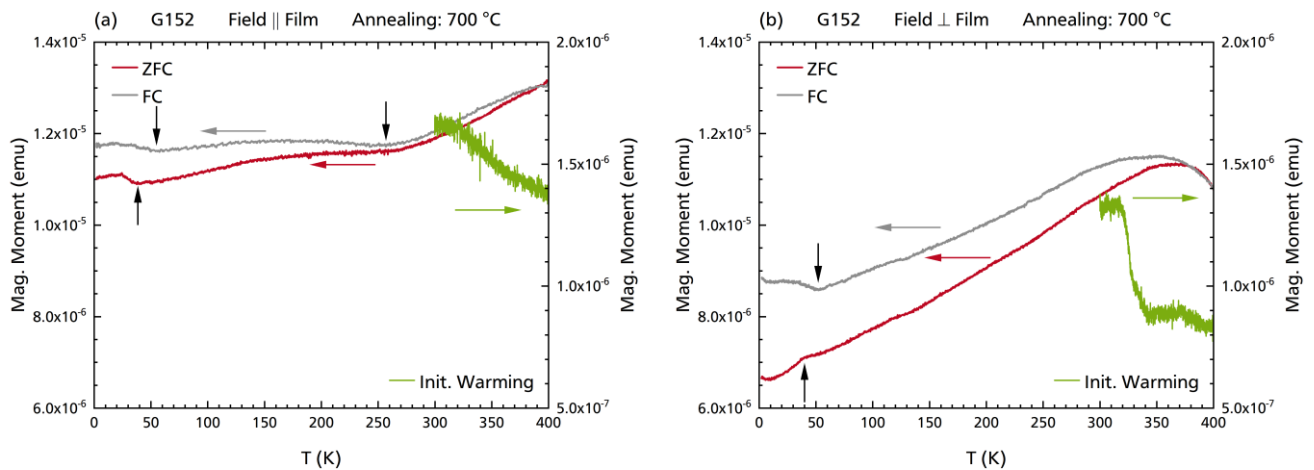
Figure 4-41: ZFC/FC Magnetization vs. Temperature Curves of 700 ℃ Annealed Sample G152

(a) With the magnetic field applied in-plane.
(b) With the magnetic field applied perpendicular to the film plane.

Magnetization varies differently depending on whether it is recorded with the magnetic field applied in-plane or perpendicular to the film plane. Besides ZFC (red) and FC curve (gray), initial warming in zero field is shown in green.

The superparamagnetic ensemble becomes fully unblocked, or the magnetic moments uncorrelated, at about 350 K when the magnetic field is applied out-of-plane. This event is indicated by the maximum in magnetization. Beyond this maximum the magnetization becomes reversible, i.e., the ZFC curve (red) and the FC curve (gray) start to overlap.

The unblocking or the loss of correlation of magnetic moments happens in a quite narrow temperature range as it is indicated by the abrupt decrease of the magnetization recorded during the initial warming (green curve). With the magnetic field applied in-plane, the magnetization decreases much slower and also the maximum in magnetization is shifted to a temperature above 400 K, i.e., beyond the temperature limitations of the used SQUIDs. This again indicates that an in-plane alignment of moments is favored by the annealed nanocomposite.

4.7.7.3 Discussion

Group-IV-based GeFe ferromagnetic semiconductor films prepared by low-temperature molecular beam epitaxy (MBE) were intensively investigated by a group of varying members around M. Tanaka; their results are published in a series of journal articles [206–214]. First, the authors varied the Fe concentration of the films and the substrate temperature set during deposition [206,207,210], and secondly, they investigated the annealing of the as-deposited films in N_2 atmosphere [211]. The maximum Fe concentration in their studies was 24 at. %, the films were deposited onto Si(001) or

Ge(001) substrates at temperatures between 100 °C and 400 °C, and exposed to temperatures from 400 °C to 600 °C for 30 min in case post-growth annealing was executed. Among all of their samples, the 60 nm thick GeFe layer deposited at 240 °C with a concentration of 10.5 at. % of Fe and which was post-growth annealed at 500 °C was the one exhibiting the largest Curie temperature, i.e., 210 K [211]. Moreover, the authors state that ferromagnetism is an intrinsic property of these GeFe films. In particular, the authors could not identify any precipitates of Fe or any known GeFe intermetallic phase in their ferromagnetic semiconductor films.

This single-phase state was no longer observed when GeFe was grown or annealed above a certain temperature threshold. The growth temperature evolutions of the properties of GeFe were examined with samples containing 6.5 at. % and 10.5 at. % of Fe [210]. Interpreting the magnetic circular dichroism (MCD) vs. magnetic field and Curie vs. growth temperature data, the authors of References [210,211] state that these "… [indicate] that there are two or more magnetic phases in the film." That is, "… the GeFe films were phase-separated magnetically …" when grown at 280 °C or above. Also, nanoparticles formed in their film grown at 240 °C and with an Fe concentration of 10.5 at. % during annealing at 600 °C [211].

However, already when the ferromagnetic semiconductor films grow as a single-phase diamond crystal lattice the Fe atoms are not equally distributed within these film. On the contrary, the films exhibit Fe-rich and Fe-poor regions. In the Fe-rich regions the increased amount of Fe atoms causes stacking faults within the diamond crystal lattice. Also, their results indicate that the nonuniformity of the Fe distribution increases with increasing post-growth annealing temperature. In particular, "… the increase in [the Curie temperature] is correlated with the enhancement of the nonuniformity of the Fe atoms." [211] Stacking faults are present in the Fe-rich regions already in the single-phase films as was revealed by transmission electron diffraction (TED) imaging. In case of a non-single-phase film obtained by annealing one sample at 600 °C (see text above), the nanoparticles are characterized by the occurrence of periodic twins and stacking faults while the diamond type crystal structure of c-Ge is preserved. In fact, no "… diffractions from precipitates with crystalline [GeFe] intermetallic compounds of other crystal structures" were found from TED images [211]. The TED micrographs of these nanoparticles indicate a size of ≤ 10 nm.

The sample by Tanaka and coworkers annealed at 600 °C is thought to be quite similar to the 700 °C annealed one of the present thesis because the Fe atoms that were formerly building the Fe clusters within the sample film under discussion must have diffused into the Ge matrix at least in parts during the annealing. However, no magnetotransport data were reported for comparison with the data of the present sample.

Nevertheless, the model of how magnetism in the films evolves with temperature given in Reference [211] is thought to be also applicable to the present sample since the model is mainly based on the nonuniform distribution of Fe atoms. Above an asymptotic Curie temperature (asymptotic since it was estimated from a Curie-Weiss plot), all Fe atoms are in a paramagnetic state. In case of the 600 °C annealed sample discussed above the asymptotic Curie temperature is approximately in the range of 260 K (as-grown) to 285 K (annealed at 500 °C) depending on the annealing temperature. Below this uppermost critical temperature, ferromagnetic coupling induced by short-range interaction appears between the Fe atoms within the Fe-rich regions. These local ferromagnetic domains increase in size with further decreasing temperature and the local domains are thought to show superparamagnetic behavior in this temperature range. At the Curie temperature (as-grown: 170 K; annealed at 500 °C: 210 K) the local domains did grow large enough to coalesce, and consequently, the film turns into a global ferromagnet. At a much lower temperature the magnetic state changes again, namely, into that of a spin-glass. In case of the as-grown sample discussed in Reference [211], this happens at about 26 K (in zero magnetic field, the temperature decreases with increasing field). After the film was annealed at 600 °C, i.e., when nanoparticles were present in the film as discussed above, these nanoparticles caused a second cusp to appear in the ZFC curve at 260 K besides the one related to the spin-glass transition. It is related to the occurrence of phase separation and superparamagnetism.

Finally, a model for the band profile present in the epitaxially grown GeFe ferromagnetic semiconductors that is based on the nonuniform distribution of Fe atoms is suggested in Reference [214]. In case of the 6.5 at. % GeFe film reported there, "… about 80% of the Fe atoms are located at … substitutional lattice sites of the diamond structure …" [214]. Also, the Fe atoms are in an Fe^{2+} state [213], hence, they act as acceptor levels [214]. In the Fe-rich regions the Fe atoms form an impurity band 0.35 eV above the valence band maximum [213]. The effective charge carriers in their GeFe films are holes and the dominating, i.e., limiting, component is the hopping transport of holes across the Fe-poor regions to other Fe-rich regions. On the one hand, the corresponding hopping probability is determined by the temperature rather than the hole concentration. On the other hand, most of the holes are located in the Fe-rich regions so that the hole concentration in the impurity band is large enough to mediate ferromagnetic coupling via double-exchange here. When the Fe concentration is low (corresponding to their one sample containing 2.3 at. % of Fe) the Fe-poor regions are depleted of carriers and the Fe-rich regions are small. When the Fe concentration is increased not only the Fe-rich regions grow but also the hole concentration in the Fe-poor regions increases. Consequently, above a certain concentration the formation of an Fe impurity band is no longer restricted to the localized Fe-rich regions but happens all over the ferromagnetic semiconductor. The present sample with a concentration of 19 at. % and a metal-like thermal evolution of resistivity is assumed to be beyond this threshold.

The authors present magnetoresistance data of two of their samples, containing 10.5 at.% and 14.0 at.% of Fe, respectively, in the supplementary material of Reference [214]. The magnetoresistance effect is negative and superimposed by a weaker positive component, and larger in effect for the sample with the higher concentration. However, the effect is quite small, i.e., about -0.5% at 20 K and 5 T applied perpendicular to the film plane in case of the 14.0 at.%-sample. Spin scattering at the boundaries of Fe-rich and Fe-poor regions is suggested as the origin of the negative magnetoresistance. This implies again that the present GeFe sample is beyond the concentration threshold where Fe-poor regions start to form an impurity band. Therefore, the present sample is not a DMS in the original sense, and other mechanisms have to be responsible for the presently observed magnetoresistive behavior.

Two magnetic phase transitions of one and the same ferromagnetic semiconductor were also observed by Li et al. [215], who examined MBE-grown GeMn ferromagnetic semiconductor films free of intermetallic precipitates. Maxima of the inhomogeneous dopant concentration are titled as spin-clusters in their publication. Spin-clusters are ensembles of closer-than-average dopant atoms whose magnetic moments are coupled for this very reason. In contrary to regular clusters, spin-clusters are not related to a formation of intermetallic precipitates or nanoparticles in the film.

In case of their 5 at.% Mn film, the spin-clusters start to exist from 112 K on, where global ferromagnetic ordering occurs only below a much lower temperature of 12 K. Li et al. suggest "… that the ferromagnetic interaction is mediated by thermally activated carriers moving in an impurity band." [215]

The change to global ordering is accompanied by a cusp in the resistivity curve around this temperature and a change of the magnetoresistance to negative values. Above the characteristic temperature for global ferromagnetic ordering the magnetoresistance is positive with a distinct peak located roughly between 30 K and 50 K. In case of their sample with 8.8 at.% of Mn, which is the one that shows the largest magnetoresistance, a maximum value of about 270% was observed, with the magnetic field applied perpendicular to the film plane.

Disregarding the metal-like evolution of the resistance with temperature because of the higher concentration of the different dopant (Mn instead of Fe), the sample of Li et al. [215] and the present sample do show some similarities in the data sets. Both exhibit a cusp in the resistivity vs. temperature data, which is assigned to global ferromagnetic ordering at low temperatures, and which is shifted when a magnetic field is applied perpendicular to the film plane. The peak maximum magnetoresistance is very large. However, the magnetoresistance tends to turn negative at temperatures below the peak maximum.

In general, several transport processes can dominate at different temperatures in one and the same film of a doped semiconductor, i.e., even the majority carriers can change type. In return, such changes are reflected by the magnetoresistive behavior of a film. For example, Tsui et al. [121] observed large positive magnetoresistance in ferromagnetic $Co_{0.7x}Mn_{0.3x}Ge_{1-x}$ nanocomposites which they associate with hole conduction. For their sample with $x = 8\%$ the authors observed a maximum positive magnetoresistance of up to 10% at about 50 K and a change to negative magnetoresistance at about 20 K. The sharp fall from positive to negative magnetoresistance is identified to be correlated with a sign change of the Hall coefficient, i.e., a change of the dominating type of charge carriers.

Besides exhibiting a maximum in the resistivity at about 180 K, in fact, both resistivity and magnetoresistance data are quite similar to the data observed from the present sample. The samples of Tsui et al. [121] show a valley in the resistivity at about 60 K, which is close to the temperature where maximum magnetoresistance values (defined as the magnitude of the effect at 5 T there) were observed. In this temperature range, the magnetoresistance is linear at low fields, concave in the intermediate range, and approaches a linear behavior, yet with a smaller slope, in the high-field range. The slope of the low-field magnetoresistance increases with further decreasing temperature, while that of the high-field slope decreases and may even become negative. At higher temperatures, the low-field magnetoresistance changes to a quadratic field dependence. The authors also find the magnetoresistance effect to be larger when the magnetic field is applied perpendicular to the film plane. All these aspects agree well with the findings presented in Figures 4-40(b)–(d),(f). The large magnetoresistance values and the corresponding evolution of resistivity with temperature are assigned to extrinsic hole transport. Therefore, similar transport mechanisms may be present in the Fe-Ge sample annealed at 700 °C of the present thesis.

Choi et al. [120] present ferromagnetic semiconductor diamond-type single crystal data of GeFe containing 5 at. % of Fe and of GeCr doped with only 1 at. % of Cr. Both single crystals were created by slowly cooling the material mix from the liquid phase to a temperature below the melting point in an evacuated ampoule. The single crystals are paramagnetic at room temperature and turn into ferromagnets at 233 K and 126 K, respectively. Despite the low concentration of dopant atoms, the authors observed positive slopes in the thermal evolutions of resistivity at temperatures above the Curie temperature for each sample.

Surprisingly, the 5 at. % Fe-doped Ge crystal keeps its metal-like transport properties even below it. The slope just takes a smaller value in the vicinity of the Curie temperature. On the other hand, the GeCr crystal exhibits a minimum in the resistivity at the Curie temperature and shows semiconductor-like behavior when the temperature is decreased further below the Curie temperature. Electrons are

stated to be the effective type of charge carriers in the former case, while holes were identified to be the dominant type in the latter case. Choi et al. [120] assign the change in resistivity to "... a phase transition ... due to the changes in spin-related scattering and conduction mechanisms between [ferromagnetic/paramagnetic] states."

This is very likely to be also the cause for the change in the slope of the resistivity curve of the present sample between 250 K and 300 K. However, the magnetization vs. magnetic field data observed for the present sample are too noisy to accordingly identify a magnetic phase transition. Also from ZFC/FC magnetization data, see Figure 4-41, no artifact that may be related to a magnetic phase transition at about 90 K can be identified.

Goswami et al. [216] prepared GeFe nanocomposites by MBE as well, however, the authors deposited their films onto GaAs(111) substrates. From their samples, which contain 4.0% to 9.4% of Fe, they found that single-domain precipitates of ferromagnetic Fe_3Ge_2 ($T_C = 433$ K) [217] start to form when the nanocomposites are grown on substrates heated to at least 150 °C. The superparamagnetic precipitates do not form immediately but nucleate from the supersaturated GeFe solid. The mean diameter of the precipitates is larger for higher substrate temperatures. For example, it is 3 nm at 150 °C and 15 nm at 400 °C for a nanocomposite containing 5.6 at. % of Fe. Therefore, precipitates of Fe_3Ge_2 are also candidates to appear in the present film. Finally, Goswami et al. [216] state that the diffusivity of Fe in Ge is $D \approx 10^{-8}$ cm^2/s at 400 °C and calculate a diffusion distance of 5 µm after 1 min [218]. Consequently, annealing the nanocomposites of the present work in steps of one hour of duration was definitively enough time to bring a sample into an equilibrium state. This is confirmed by the sample data presented in Figure 4-36 and should definitely hold for the sample annealed at 700 °C.

As a last point, the enormous magnitude of the magnetoresistance of the present sample remains to be discussed. The first out of two effects to be presented, called extraordinary magnetoresistance (EMR), is capable of producing positive, saturating magnetoresistance of hundreds and even thousands of percent [193,219–222]. The EMR effect is a consequence of the Hall effect and happens as follows [220,221]. When a magnetic field is applied to a body made of a homogeneous conductor the Lorentz force deflects the component of the current perpendicular to the applied magnetic field. The occurring imbalance of the charge carrier distribution causes an internal electric field, which adds to the externally applied one such that the current trajectories present without magnetic field are restored. For this reason, the current remains collinear to the externally applied electric field. However, the current is no longer collinear to the total electric field but is conducted under an angle to it, defined as the Hall

angle. Since the additional internal electric field increases in proportion to the applied magnetic field also the Hall angle increases with increasing magnetic field. This is the well-known Hall effect [223].

Now suppose, the body under examination is not of homogeneous kind but consists of a homogeneous semiconductor matrix in which a single homogeneous metallic inclusion is embedded. Furthermore, the metallic inclusion is assumed to be an ideal conductor, i.e., the semiconductor-metal interface is assumed to be an equipotential surface of the electric potential in this structure. In zero magnetic field the metallic inclusion short-circuits the structure. More precisely, charge transport through the semiconductor is reduced to a minimum, i.e., happens only between current source and the metallic inclusion, and current drain and the metallic inclusion. In particular, the direction of the total electric field and of the current are oriented perpendicular to the surface of the metallic inclusion at the metal/semiconductor interface.

However, the situation changes when a magnetic field is applied. With increasing magnetic field also the Hall angle increases. At sufficiently large fields it approaches 90°, i.e., the total electric field remains aligned perpendicular to the surface of the inclusion while the current direction is oriented tangential to the interface. This means, the current no longer penetrates the inclusion, but is fully conducted through the semiconductor. Simulations of the current distribution in disk-shaped and rectangular structures are discussed and plotted in References [219,220,222]. As the resistivity of the semiconductor is much higher than that of the metallic inclusion, large positive magnetoresistance is observed in such structures. Since the maximum possible Hall angle is 90°, the effect is of saturating kind. It is noteworthy that the effect occurs whether the structure possesses an intrinsic magnetoresistance or not. The direct influence of the magnetic field is of pure geometrical type. However, an indirect dependence may be caused by a magnetic-field-dependent carrier mobility [221,224].

EMR would require that Fe segregates into larger inclusions. Since the distribution of Fe appears homogeneous within the resolution of the used EDX elemental mapping, EMR can most likely not be accounted for the enormous magnitude of the positive magnetoresistance that was observed in parts.

The second effect is deduced from the inhomogeneity of a metallic dopant concentration. The effect is the reason for the large, positive, not saturating magnetoresistance discovered in nonstoichiometric, diamagnetic, narrow-gap, n-type silver chalcogenide semiconductors ($Ag_{2+\delta}Se$ and $Ag_{2+\delta}Te$) [225]. These materials exhibit a not saturating, quasi-linear magnetoresistance in magnetic fields of up to 60 T, despite the fact that these semiconductors possess no intrinsic magnetoresistance [225–227]. In experiments that used hydrostatic pressure to tune the band structure of both Ag-rich (n-type) and Ag-deficient (p-type) samples, the magnetoresistance was found to be linear, and largest right when the dominant type of charge carrier changes its type, i.e., when the Hall constant crosses through zero [228].

Parish & Littlewood [227,229] suggested a simple model of macroscopically disordered and strongly inhomogeneous semiconductors that exhibit a non-saturating magnetoresistance similar to that observed in the materials discussed above. The model is based on 2D square lattices of coupled four-terminal resistors with the magnetic field applied perpendicular to the plane of the array. Consequently, the model is restricted to the simulation of transverse magnetoresistance; a 3D model would be required to also simulate longitudinal magnetoresistance. To simulate real inhomogeneous conductors, Parish & Littlewood take both the carrier mobility μ and the resistivity ρ to be Gaussian distributed over the ensemble of four-terminal resistors. They find that current paths can be misaligned with the driving electric field; the current paths can even form loops [227]. The magnetoresistance becomes explicitly linearly dependent on the magnetic field $\Delta R/R \propto H$ when the width of the distribution of the mobility exceeds its average value $\Delta\mu/\langle\mu\rangle > 1$. This effect is, again, assigned to the contribution of the Hall resistance, which increases proportional to the magnetic field. The Hall resistance contributes with increasing amount to the magnetoresistance the longer the time the magnetic field distracts the charge carriers such that they propagate perpendicular to the applied voltage [227]. The model by Parish & Littlewood is refined in Reference [230] and, further, extended to 3D in Reference [231].

A certain degree of inhomogeneity can be safely assumed for the distribution of Fe in the present sample, because Fe was originally inserted into the sample in form of clusters. For this reason, the inhomogeneity-based magnetoresistance may contribute to the magnetoresistance observed from the crystallized GeFe sample. However, the effect cannot account for the maximum in the magnetoresistance occurring close to the minimum of the resistance vs. temperature curve.

Though different scenarios were discussed above, none of them may clearly explain the results observed from the Fe-Ge nanocomposite of the present thesis annealed at 700 °C. Nonetheless, it can be safely assumed that Fe atoms diffused into the Ge matrix, breaking up the Fe clusters and complexes of these. In this turn, different phases of Fe_xGe_y may have formed in the annealed nanocomposite film. There may still be Fe-rich particles that are surrounded by an Fe-poor Ge matrix, regions with different composition and different magnetic properties may have formed, and there may also exist Fe impurities within c-Ge regions. The observed transport and magnetoresistance properties are most likely a superposition of several effects. Moreover, the weightings of the contributions may change both when the temperature and the magnetic field are varied.

The formation of DMSs by annealing co-deposited nonequilibrium films may be an interesting way to fabricate materials with transport and magnetoresistance properties as shown above. However, knowledge about how Fe dissolves in the Ge matrix is crucial for further research. In order to study diffusion processes on the length scale of the clusters, i.e., on the nanometer scale, imaging and

measurement techniques that can resolve variations in the Fe concentration at this length scale have to be used. One technique, which was used to prove the stability of the Fe clusters in the Ge matrices in this thesis, is energy-filtered TEM.

4.8 Conclusions

In this chapter, Fe-Ge nanocomposites synthesized by the simultaneous deposition of Fe clusters from a size-selected cluster ion beam and of matrix material from an effusion cell were presented, analyzed, and discussed in detail. Nanocomposite samples containing clusters of either 500 ± 50 or 1000 ± 100 Fe atoms were prepared.

Starting from the purely deposited matrix material, it was proven by the magnetoresistive behavior of the deposited material that Ge grows as amorphous solid under the conditions present during the experiments. Furthermore, it was shown by (energy-filtered) scanning TEM that the Fe clusters remain stable in this nonequilibrium intermetallic system. From the revealed structure, that showed isolated single clusters but also chains and agglomerates of touching clusters, the average distance between the surfaces of two neighboring clusters was found to be a characteristic quantity of the Fe-Ge nanocomposites. Below a percolation threshold of about 30 at. % the resistivities of the nanocomposites were found to strongly depend on the Fe concentration and to be correlated with the average distance between the surfaces of two neighboring clusters independent of the size of the embedded clusters. Therefore, tunneling transport was suggested as dominating transport process.

Magnetometric measurements were executed to examine the superparamagnetic properties of the nanocomposites.

The magnetoresistive properties of the nanocomposites were analyzed between 300 K and 40 K, and in case of some samples to even lower temperatures. Besides a saturating low-field effect, both negative and positive field-dependent magnetoresistance were observed. From a hysteresis occurring both in the resistivity and the magnetization curve when an applied magnetic field was ramped in a loop sequence at low temperature, the low-field magnetoresistance was finally identified as tunneling magnetoresistance.

To bring the Fe-Ge nanocomposites into an equilibrium state some samples were annealed at 220 °C and one was additionally annealed at 700 °C. The former caused the resistivities of the nanocomposites to decrease by about one order of magnitude. Simultaneously, the tunneling magnetoresistance reduced while a strong negative field-dependent magnetoresistance appeared in the observed magnetoresistance

curves. Annealing one sample at 700 °C reduced its resistivity by another two orders of magnitude. Annealing the sample at such a high temperature caused a fundamental restructuring of the fixed chemical composition of the sample, i.e., the formation of GeFe intermetallics according to the phase diagram and depending on the local concentration of Fe in the film. The observed magnetoresistance is no longer isotropic but is largest when the magnetic field is applied perpendicular to the nanocomposite film. The restructuring led to a metal-like decrease in resistivity with decreasing temperature until a minimum is taken at 90 K. In the temperature range above the minimum the magnetoresistance is positive, field-dependent, and very large. Below, it reduces, while simultaneously the resistivity strongly increases when the temperature is lowered further. Then, at about 30 K the resistivity has a maximum. Here, the magnetoresistance turns negative.

Co-deposition of clusters and matrix material is an interesting way to install magnetic properties in a semiconducting matrix. However, for future Fe-Ge nanocomposite samples a new sample layout should be designed that also allows for Hall measurements. This would help to distinguish between magnetic-field-caused and magnetization-caused effects and would allow to determine the carrier mobilities and dominant carrier types at different temperatures.

The annealing of low-concentration co-deposition samples may be a way to turn highly resistive cluster-assembled nanocomposites into DMSs with precisely tunable transport and magnetoresistive properties. Since the samples exhibit larger magnetoresistive responses when annealed, systematic studies of the annealing of cluster-assembled nanocomposites would be of great interest in order to elucidate the temperature-activated changes.

5 Fe_x-Ag_m Nanocomposite Films

In addition to the Fe-Ge nanocomposite films discussed in the previous chapter, Fe clusters were co-deposited with Ag in order to synthesize three series of cluster-assembled nanocomposites with metallic matrices. Two series with the cluster species already used in the Fe-Ge nanocomposite films, Fe_{500} and Fe_{1000}, and third series with clusters consisting of 1500 Fe atoms were deposited. The main difference to Fe-Ge nanocomposites, i.e., nanocomposites with a semiconducting matrix, is the metallic nature of the Ag matrices. In particular, Ag is a better electrical conductor than Fe. Moreover, choosing Ag as a matrix for the Fe clusters has the advantage of complete immiscibility of the two constituents. For this reason, charge transport is no longer expected to depend on percolation of clusters. Granular giant magnetoresistance is expected to occur because of spin-dependent scattering at the ferromagnet/non-ferromagnet cluster/matrix interfaces (see Section 2.4.4). Along with the use of Ag as matrix material and the differing order of deposited layers of a nanocomposite sample, differences with respect to the Fe-Ge nanocomposite had to be faced s in fabrication and transport measurements. The differences are discussed in brief in Section 5.1. Magnetotransport and magnetization measurement results are presented in Section 5.2 and analyzed in Section 5.3.

Generally, in Fe-Ag nanocomposite films it is the Fe particles whose magnetic moments are influenced by an applied external magnetic field and that bring about the granular giant magnetoresistance effect by spin-dependent scattering. In principle, electrons can be scattered by atoms located at the interface as well as by atoms inside the Fe cluster.

Alof et al. [45] prepared Fe-Ag nanocomposite films by deposition of the two constituents onto heated Si/SiO_2 substrates using molecular beam epitaxy. There, the Fe particles formed because of the immiscibility of the two constituents. The highest effect Alof et al. found for their samples measured at room temperature was -2.8% (at a maximum field of 1.5 T), in a sample with an Fe concentration of 33.5 at. % in form of particles with radii of 1.0 nm, which corresponds to 540 Fe atoms per particle. Alof et al. were able to quantitatively distinguish between Fe atoms located at an interface between an Fe particle and the Ag matrix, and Fe atoms located in the inside of a particle by means of Mössbauer spectroscopy. From the number ratio of these two different atom states the authors were able to calculate the size of the (spherical) particles that formed in the film and, hence, the number ratio of atoms located

at the surfaces of the particles to atoms located inside the particles. For nanocomposites with concentrations ≥ 33.5 at. % the authors found the strength of the granular giant magnetoresistance to scale with this ratio, i.e., to reduce with increasing particle size according to the change of the number ratio of surface to core atoms. Alof et al. conclude that spin-dependent scattering at the interfaces between the Fe particles and the Ag matrix plays the dominant role for the magnitude of the granular giant magnetoresistance effect in Fe-Ag nanocomposite films.

How granular giant magnetoresistance varies with magnetic field and temperature depends on the magnetic properties of the ensemble of magnetic Fe nanoparticles in a nanocomposite film. The superparamagnetic moments of the clusters, more accurately, the sum of the correlated magnetic moments of a cluster, can interact with those of neighboring clusters by long-range dipolar interaction or short-range exchange interaction. Therefore, the equilibrium magnetic state of an ensemble is also a question of randomness.

Allia et al. [46] examined Fe-Ag nanocomposites grown by dc-magnetron co-sputtering containing between 10 vol. % and 30 vol. % of Fe in form of clusters with diameters of 3.0 nm (at 10 vol. %) and larger. Percolation in their samples appears at about 20 vol. %. In the examined concentration range the granular giant magnetoresistance takes a maximum, which is about -23% at "… very low temperatures [which most likely refers to their lower temperature limit of 4 K, author's remark] …" and appears at a concentration of 15 vol. %. At 270 K the effect is about -8% at 21 vol. % of Fe.

Also, Fischer et al. [5,7] tested the functionality of the CIBD system employed in the present thesis preparing Fe-Ag films containing Fe_{1000} clusters. They deposited four samples containing equal amounts of Fe while the amount of Ag was varied from sample to sample such that the four samples exhibited Fe concentrations of 2 vol. %, 10 vol. %, 50 vol. %, and 100 vol. %, respectively. 10 vol. % correspond to about 14 at. % in case of the Fe-Ag samples studied in the present work. Fischer et al. calculated the amount of deposited Fe directly from the picoampere cluster current and confirmed it later on by means of EDX. However, the authors only examined the magnetic properties of the Fe-Ag nanocomposites. As one important result, the authors found from Langevin fits to magnetization vs. magnetic field data recorded at 300 K that each Fe_{1000} cluster contributes to the magnetization of a sample with a dipole moment of 2.2 μ_B/atom in case of the 2 vol. % sample. The blocking temperature of that specific sample was less than 10 K, and the evolution of magnetization in ZFC/FC measurements of this samples followed a $1/T$ dependence in the fully unblocked, reversible regime of the superparamagnetic moments. This means, all atoms of an Fe_{1000} cluster preserve their full (bulk α-Fe) magnetic moment at this low concentration and neither do the clusters magnetically interact nor do they aggregate to mentionable amounts with neighboring clusters here.

Fischer et al. [7] had to set larger average cluster sizes in order to fit the data of the higher concentration samples, indicating "… aggregation or at least strong magnetic interaction of clusters in those samples." [7] This was also confirmed by the increase of the blocking temperatures (10 vol. %: 35 K; 50 vol. %: 120 K) and deviations from the $1/T$ behavior. Moreover, at 300 K the saturation magnetization was found to be about 110 emu/g for the 2 vol. % sample increasing to about 190 emu/g for 100 vol. % of Fe.

5.1 Differences between Silver and Germanium Matrix Samples

5.1.1 Fe-Ag Sample Films

The Fe-Ag nanocomposite samples differ in several points with respect to the Ge-matrix-based nanocomposite samples. The most important one is that now metallic conduction instead of hopping or activated transport is the intrinsic mechanism of transport of the matrix. To be precise, both components forming the nanocomposite are electric conductors of metallic kind. Moreover, the matrix material now is an even better conductor than the cluster material. As a consequence, the negative charges of the cluster ions are absorbed immediately by the 'sample potential' U_S (see Section 3.3) during co-deposition via the nanocomposite already deposited onto the sample. Furthermore, the magnetoresistance is expected to be caused by spin-dependent scattering at the interfaces of ferromagnetic and nonmagnetic metals, i.e., at the cluster/matrix interface [45,232]. In the same turn, no significant effect of percolation on charge transport is expected for the Fe-Ag nanocomposites.

Below 1184 K, which is the transition temperature of α-Fe and γ-Fe, see Section 2.2.2, Fe and Ag are only soluble to a vanishingly small amount. In α-Fe a maximum of 2 ppm of Ag atoms and in fcc Ag a maximum of 15 ppm of Fe atoms is soluble [233]. Therefore, no intermetallic compounds form in the nonequilibrium Fe-Ag nanocomposites synthesized by co-deposition of Fe cluster ions and Ag atoms. However, larger particles and chains of percolating clusters may still form. From percolation aspects, the same structure as was found for the a-Ge-matrix-based nanocomposites is to be expected, see Figure 4-2. As it was motivated in Section 4.7.2.1, closed paths of percolating clusters form already at a threshold of 15.4 vol. % for randomly deposited hard spheres. Using the mass densities given in Section 4.5.1.2, the percolation threshold corresponds to ~22 at. %. The Fe concentrations of all present Fe-Ag nanocomposites are all below this limit.
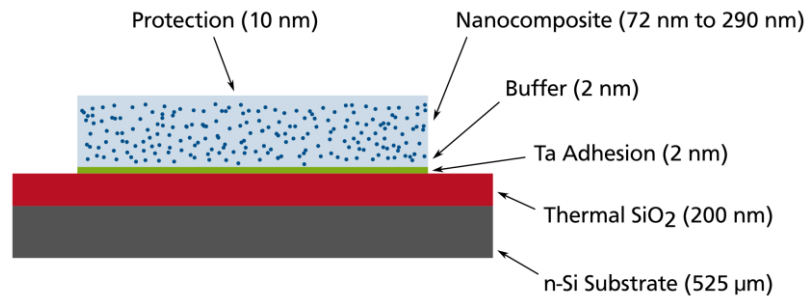
Figure 5-1: Cross Section Through the Layers of an Fe-Ag Nanocomposite Sample

In case of Ag matrix samples a Ta adhesion layer was deposited prior to the deposition of the buffer layer. Also, the nanocomposite layer was only covered with a protection layer of matrix material, i.e., without a Si capping layer.

5.1.2 Differences in the Fabrication Process of Fe-Ag Nanocomposite Films

Fe-Ag nanocomposite samples were fabricated in a way similar to the preparation of Fe-Ge nanocomposite samples (Section 4.2). In particular, Ag (Balzers, N4 purity, from alumina crucible) was deposited from the effusion cell. For this reason, only the differences with respect to the Fe-Ge samples are discussed. A symbolic cross section through the layers of an Fe-Ag sample is illustrated in Figure 5-1.

The direct deposition of Ag atoms onto the SiO_2 surface layer of a CIBD sample chip (see Section 4.2) results in the growth of a porous film with low adhesion to the SiO_2 surface as it is depicted in the SEM micrograph Figure 5-2(a). To obtain a film free of pores instead, a 1 nm to 2 nm thin adhesion layer of Ta was deposited from a Ta rod installed in one of the pockets of the triple electron beam evaporator (see (l) in the inset of Figure 3-3) prior to the deposition of Ag buffer layers, as proposed in Reference [5]. The result—a smooth film free of pores—is depicted in Figure 5-2(b) for comparison.

The two SEM micrographs Figures 5-2(a),(b) show the surface of one and the same 122 nm Ag reference film. Because Ta and Ag were deposited from different sources, i.e., under different angles of incidence (see inset of Figure 3-3), a mismatch of the respective deposition areas occurs. This circumstance was already discussed in Section 4.2.4. While Figure 5-2(b) depicts the main film, micrograph (a) was taken at the thin stripe at the right-hand side of the film where no Ta adhesion layer was deposited underneath.

Subsequently to the adhesion layer, a 2 nm Ag buffer layer was deposited. Then, the nanocomposite films with thicknesses between 72 nm and 290 nm were co-deposited. Besides Fe_{500} and Fe_{1000} clusters, also clusters consisting of nominally 1500 atoms per cluster (Fe_{1500}) were embedded into Ag matrices. Due to its excellent conductivity, only 10 nm of Ag were deposited onto Fe-Ag nanocomposite layers for
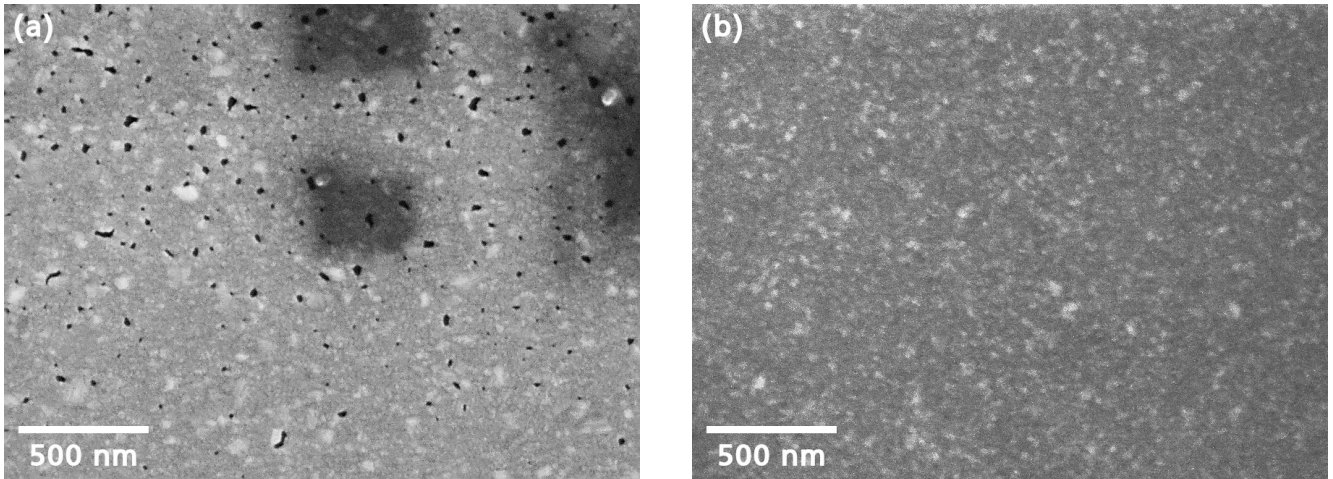
Figure 5-2: SEM Micrographs of the Surface of a 122 nm Thick Ag Film

  (a) The SEM micrograph shows the surface at the small film stripe where there is no Ta adhesion layer deposited underneath the Ag layer because of the mismatch between effusion cell and electron beam evaporator deposition areas.
  (b) The SEM micrograph shows the same film but now at a position with the 2 nm Ta adhesion layer deposited underneath. Without the Ta adhesion layer Ag grows as a porous film, however, with Ta underneath the Ag matrix grows as a film free of pores.

film protection purposes. Also, no Si capping layers were deposited. The base pressures during the depositions of Fe-Ag samples were lower than these during Fe-Ge depositions, i.e., always in the 10^{-10} mbar range.

5.1.3 Differences Related to Transport Measurements

The lowest temperature the PPMS was able to maintain for the full duration of a magnetoresistance curve recording was 10 K in case of Fe-Ag nanocomposite samples.

5.1.3.1 Four-Wire Excitation Currents

Again, four equally spaced excitation currents I_{exc} were set for resistance measurements. Because of the much lower two-wire resistances, which were on the order of $100\,\Omega$, these were set to $200\,\mu A$, $150\,\mu A$, $100\,\mu A$, and $50\,\mu A$ for Ag matrix samples. Moreover, there was no necessity to change the set excitation currents as the temperature was reduced. See Section 4.4.1 for more details about transport measurements with the PPMS.

5.1.3.2 Resistivity Calculation: Film Thicknesses

The thicknesses of the co-deposited Fe-Ag nanocomposite films range from 70 nm to 290 nm. Each nanocomposite layer was sandwiched between a 2 nm Ag buffer and a 10 nm Ag protection layer. In principle, each sample represents a trilayered structure for that reason, the total resistivity of which is the sum of three resistive materials with different resistivities in a parallel arrangement. However, subtracting the contributions of buffer and protection layer by means of a parallel resistor model remained unsuccessful for all samples.

Therefore, the two Ag-only layers are treated as being part of the nanocomposite layer by adding their contributions to the thicknesses of the nanocomposites. This is justified because the thickness of the buffer layer is in the range of one cluster diameter (see Table 4-2) on the one hand. On the other hand, the thickness of the protection layer is also in the range of expected cluster separations and, moreover, electrons first have to pass through the nanocomposite layer to be scattered into the thin topmost layer free of clusters. The contribution of the Ta adhesion layer is neglected because of its small thickness and because its resistivity is one order of magnitude larger than that of pure Ag [234,235].

5.1.3.3 Resistivity Calculation: Geometry Correction Factors

The four-wire resistances measured between two neighboring lines were always less than $1\,\Omega$. Therefore, the two-wire resistances measured in the course of a first sample characterization, see Section 4.2.4, were dominated by the integrated length of the Pt lines used for the two-wire resistance measurements. Hence, Ag matrix films were effectively connected via four point-like regions at the side edges rather than by four parallel, equidistantly spaced lines.

The resistivity of an Fe-Ge cuboid (cross-sectional area: $w \times t$, length: d) is given by

$$\rho_{cub} = \frac{w\,t\,R_{meas}}{d} = \lambda_{cub}\,t\,R_{meas}\,, \tag{5-1}$$

where $\lambda_{cub} = w/d$ is defined as the geometry correction factor corresponding to the cuboidal geometry and where R_{meas} is the measured resistance. In general, the functional form of the correction factor $\lambda(w,d)$ depends on the geometry chosen for the measurement. These corresponding to the four-point geometries used with the sample chip layout are calculated in the following. The calculations are motivated by Reference [236].

To calculate the resistivity of an Fe-Ag nanocomposite sample of thickness t the applied excitation current I_{exc} is assumed to spread in such way so that the corresponding equipotential planes are

half-cylinder planes (flat film approximation). Therefore, the electric current density in a generalized sample film is
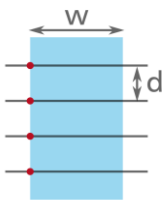
$$\vec{j}(\vec{r}) = \frac{I_{exc}}{\pi\, t}\left(\frac{\vec{r} - \vec{r}_{I+}}{|\vec{r} - \vec{r}_{I+}|^2} - \frac{\vec{r} - \vec{r}_{I-}}{|\vec{r} - \vec{r}_{I-}|^2}\right), \qquad [5\text{-}2]$$

where $\vec{r}_{I\pm}$ is the position the excitation current is fed into (conducted from) the film. With Ohm's law $\vec{E} = \rho\vec{j}$, the electric potential difference $V = -\int_{\vec{r}_{V-}}^{\vec{r}_{V+}} \vec{E}\, d\vec{s}$, and $R_{meas} = \frac{V}{I_{exc}}$ the resistivity can be expressed as

$$\rho(\vec{r}_{I+}, \vec{r}_{V+}, \vec{r}_{V-}, \vec{r}_{I-}) = \frac{\pi\, t\, R_{meas}}{\ln\left(\frac{|\vec{r}_{V-} - \vec{r}_{I+}|\, |\vec{r}_{V+} - \vec{r}_{I-}|}{|\vec{r}_{V-} - \vec{r}_{I-}|\, |\vec{r}_{V+} - \vec{r}_{I+}|}\right)}, \qquad [5\text{-}3]$$

where $\vec{r}_{V\pm}$ are the coordinates of the points between which the voltage V is sensed.

For the Fe-Ag samples the same CIBD sample chips as used for the Fe-Ge samples are employed, i.e., the sample films are connected by four parallel and equally spaced contact lines. Hence, there are three possible contact geometries for the Fe-Ag films: (i) all contacts are located at the same side ('40'), (ii) one current line is located on the other side ('31'), and (iii) both one current and one voltage line are located on each side ('22'). The corresponding correction factors are depicted below together with the corresponding geometry correction factors that are calculated from the general formula Equation [5-3].

$$\lambda_{40} = \frac{\pi}{\ln(4)}, \qquad \lambda_{31} = \frac{2\pi}{\ln\left(4 + \frac{12d^2}{d^2 + w^2}\right)}, \qquad \lambda_{22} = \frac{\pi}{\ln\left(4 + \frac{w^2}{d^2}\right)}. \qquad [5\text{-}4]$$

The distance d between two contact lines and the width of the deposited film w were determined from optical micrographs (see Figure 4-7) by transformation of pixel coordinates to spatial coordinates. The relation between spatial and pixel coordinates was determined with the help of a calibration sample.

5.2 Measurement Results

5.2.1 List of Used Fe-Ag Nanocomposite Samples

In addition to the two cluster species Fe_{500} and Fe_{1000} used in the Fe-Ge nanocomposites, Chapter 4, also Fe clusters containing 1500 ± 150 atoms (Fe_{1500}) were embedded into Ag matrices as a third series. Besides the green triangles ▼ and blue circles ● used to represent the data points of samples containing Fe_{500} and Fe_{1000} clusters, respectively, red diamonds ◆ are used to represent these containing the Fe_{1500} ones. In curve plots that present data of samples containing clusters of different sizes the curves of Fe_{1500}-Ag, Fe_{1000}-Ag, and Fe_{500}-Ag samples are plotted as solid, dashed, and dotted lines, respectively.

From EDX data, Fe concentrations between about $1\,\text{at.\%}$ and $12\,\text{at.\%}$ were calculated applying Equation [4-9]. For samples whose transport properties were measured in the '40' geometry, see Section 5.1.3.3, the Fe concentration was usually determined from an area close to the connected film side. The reason for this is that most of the excitation current is conducted through the region close to the edge of the connected film side. The area to be used for concentration determination was chosen to be limited by the two voltage sensing lines on the upper and lower side, and by the film edge on the left or the right sides. The width of the area was chosen so that about one quarter of a film was measured. For the other geometries '31' and '22', where the excitation currents cross the nanocomposite films from one edge to the other, the concentration was calculated from full film width data. However, c_{Fe} and the deduced MPS turned out to not be correlated with the transport properties of the samples. This is most likely because the excitation current follows the path of lowest resistivity, and along this way the Fe concentration may deviate from the one determined by means of EDX to a mentionable degree.

For that reason, the samples are tabulated by the relative resistivity $\rho_{100\,\text{K}}/\rho_{300\,\text{K}}$ in decreasing order in Table 5-1. This quantity is independent of film thicknesses and contact geometry correction factors (see Section 5.1.3.3) and, hence, well suited as an alternative point to start discussing the recorded sample transport properties. Besides the relative resistivity, the observed magnetoresistance $\Delta\rho/\rho_0$ at maximum magnetic field (6 T), the Fe concentration determined by EDX c_{Fe}, the calculated film thickness, and the used contact geometry are listed in Table 5-1.

The largest error of the relative resistivity deduced from measurement uncertainties in the data set is $\rho_{100\,\text{K}}/\rho_{300\,\text{K}} = 4 \times 10^{-4}$, which is smaller than the size of the data symbols used in the graphs. The uncertainties of the magnetoresistance values listed in Table 5-1 are calculated from the resistance data that were recorded in the courses of the corresponding measurements. The maximum errors of the magnetoresistance values are estimated from the data of a magnetoresistance curve as follows:

Table 5-1: List of Used Fe-Ag Nanocomposite Samples

The samples are listed by decreasing value of $\rho_{100\,K}/\rho_{300\,K}$. $\Delta\rho/\rho_0$ is the relative magnetoresistive change of resistivity at 6 T, c_{Fe} the Fe concentration determined via EDX, and t the film thickness. The used contact geometries are listed in the last column.

Sample ID Fe$_{500}$-Ag	$\dfrac{\rho_{100\,K}}{\rho_{300\,K}}$	$\Delta\rho/\rho_0$ (at 100 K)	c_{Fe} (at. %)	t (nm)	Contact Geometry
A184	0.89	$-2.0\% \pm 0.08\%$	10 ± 1.7	188	'40'
A185	0.82	$-3.8\% \pm 0.11\%$	5 ± 2.5	141	'40'
A181	0.79	$-4.3\% \pm 0.11\%$	9 ± 1.4	175	'40'
A182	0.52	$-0.8\% \pm 0.62\%$	2.0 ± 0.78	168	'40'
Fe$_{1000}$-Ag					
A178	0.89	$-1.0\% \pm 0.22\%$	9 ± 2.2	300	'31'
A175	0.85	$-1.8\% \pm 0.09\%$	10.3 ± 0.05	304	'22'
A173	0.84	$-0.3\% \pm 0.10\%$	4.6 ± 0.06	257	'22'
A177	0.84	$-2.2\% \pm 0.04\%$	11.4 ± 0.12	87	'22'
A179	0.55	$-0.4\% \pm 0.95\%$	1.2 ± 0.04	309	'40'
Fe$_{1500}$-Ag					
A187	0.88	$-0.1\% \pm 0.06\%$	9.2 ± 0.20	172	'40'
A186	0.87	$-1.5\% \pm 0.07\%$	$12 \pm$ n. a.	136	'40'
A191	0.81	$-0.9\% \pm 0.10\%$	6.2 ± 0.26	145	'40'
A189	0.81	$-1.3\% \pm 0.14\%$	4.8 ± 0.31	155	'40'
A188	0.81	$-1.0\% \pm 0.13\%$	7.8 ± 0.11	156	'40'

$$\Delta\left(\frac{\rho(H) - \rho_0}{\rho_0}\right) = \frac{\rho(H)}{\rho_0}\left(\frac{\Delta\rho(H)}{\rho(H)} + \frac{\Delta\rho_0}{\rho_0}\right) \approx 2\frac{\rho(H)}{\rho_0}\left\langle\frac{\Delta\rho}{\rho}\right\rangle \approx 2\frac{\rho(H)\,\Delta\rho_0}{\rho_0{}^2}, \qquad [5\text{-}5]$$

where it is assumed that the relative errors of all resistivity data points of one curve are similar and well represented by the value recorded at zero magnetic field. The errors given for c_{Fe} are the errors obtained from the EDX composition analyses. The thicknesses are assumed to have a maximum error of 10% due to the calibration factors determined via XRR measurements on reference sample films.

5.2.2 Transport and Magnetoresistive Measurements

Both resistance vs. temperature and resistance vs. magnetic field data were recorded using the PPMS. The results are presented and summarized in this section.

5.2.2.1 Resistivity Measurement Results

Figure 5-3(a) shows the raw data of resistance vs. temperature (red) of sample A175. As expected, the curve is of a shape characteristic for metallic conduction. Down to about 50 K it decreases linearly

with temperature to good approximation, as it is also indicated by the calculated temperature coefficient of resistivity α (blue data), and approaches a constant value at low temperatures. α is defined via $\rho(T) = \rho_0(1 + \alpha(T - T_0))$, where $T_0 = 300$ K was used as reference temperature here. The measured four-wire resistances of all Fe-Ag nanocomposite samples were found to be in the range of 20 mΩ to 1.0 Ω in the examined temperature range of 300 K to 10 K in general.

The absolute and relative resistivity vs. temperature curves of all Fe-Ag nanocomposite samples are plotted in Figures 5-3(b),(c), respectively. Within their series, the samples are ordered by decreasing relative resistivity according to their position in Table 5-1. A graph that summarizes all samples by their temperature coefficient of resistivity α is attached in Appendix D, Figure D-4.

An upper limit for the absolute resistivity is given by the (quasi-)granular Fe film (G128). (G128) is the Fe-Ge nanocomposite sample highest in Fe concentration, see Table 4-1. With its concentration $c_{Fe} = 83$ at. %, (G128) can be assumed to be a granular metal film of randomly distributed Fe_{1000} clusters to sufficient approximation. This sample exhibits resistivities of $\rho_{300\,K} = 2.03 \times 10^{-5}$ Ωm and $\rho_{100\,K} = 1.85 \times 10^{-5}$ Ωm. Accordingly, a relative resistivity of $\rho_{100\,K}/\rho_{300\,K} = 0.91$ can be calculated as the high-concentration limit of this quantity. The relative resistivity curve of (G128) is added to plot (c) as black double-line and, indeed, resides above the curves of all Fe-Ag nanocomposite samples. The absolute resistivity of sample (G128) is on the order of 10^{-5} Ωm. Since this exceeds the plot range of the resistivity plot it is not shown in graph (b). Instead, its resistivity data are plotted separately in Figure D-3(b) in Appendix D.

The low Fe concentration limit of the resistivity is represented by the value for pure Ag. Reference data curves of Ag from literature [234] are added to both graphs (b),(c) as gray double-lines. As expected, these reference curves limit the plots to the low-concentration side. Pure Ag possesses the lowest resistivity and the strongest change of relative resistivity with temperature, i.e., the smallest relative resistivity. With $\rho_{300\,K}^{Ag} = 1.6 \times 10^{-8}$ Ωm and $\rho_{100\,K}^{Ag} = 4.2 \times 10^{-9}$ Ωm the relative resistivity of Ag at 100 K calculates to $\rho_{100\,K}/\rho_{300\,K} = 0.26$. The low and high cluster concentration limit of temperature coefficient of resistivity can be deduced from Ag literature data from Reference [234] and the treated-as-granular sample (G128) as well. They are 3.7×10^{-3} K^{-1} and 4.3×10^{-4} K^{-1} (see Figure D-3(b) in Appendix D), respectively.

Figure 5-3(b) proves that, except samples A188 to A191, which are close-by in the relative resistivity plot, see graph (c), the data lines mostly do not intersect. The only line that crosses through other ones is the line belonging to sample A175. This is assigned to the different cluster species the concerning
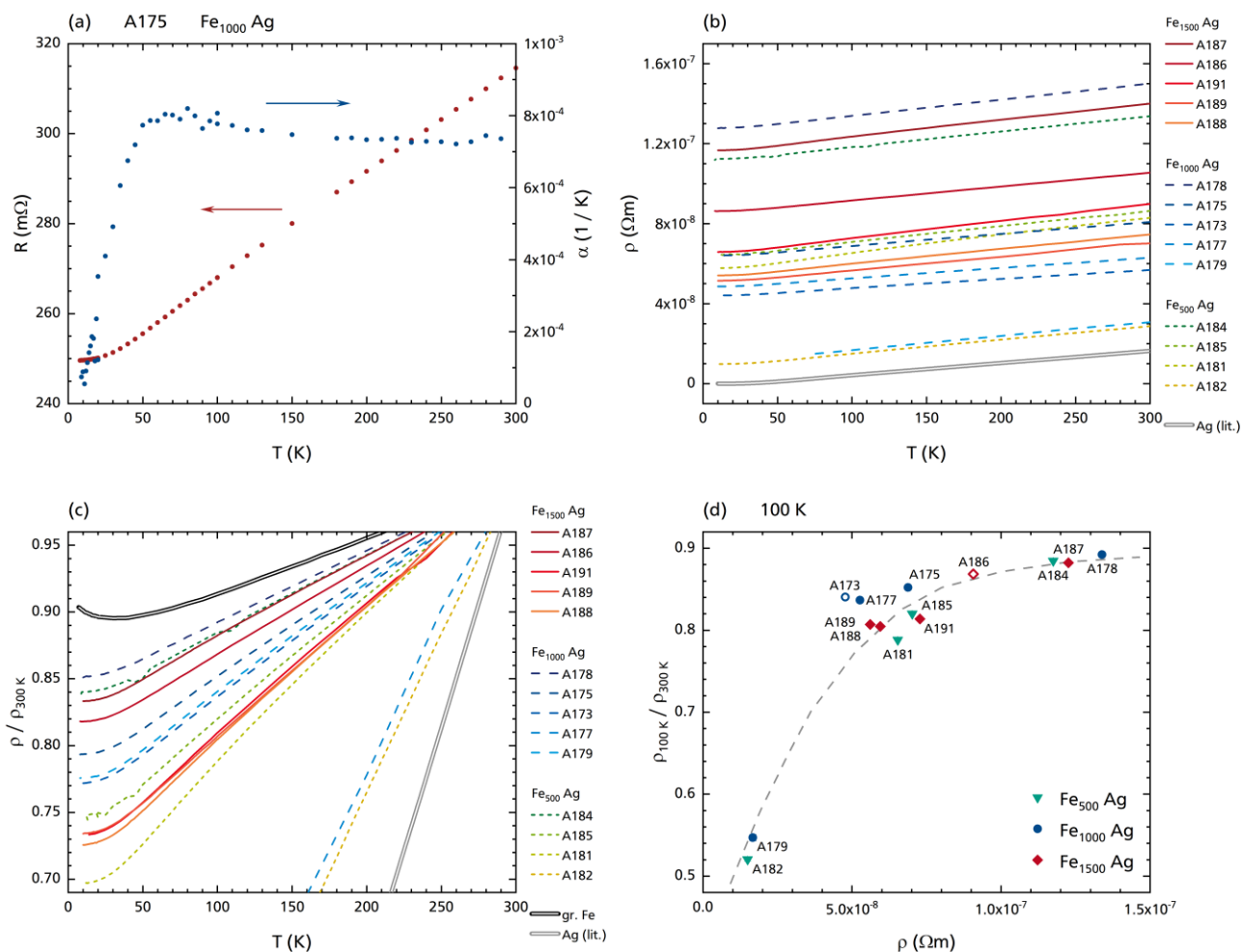
Figure 5-3: Transport Measurement Results of Fe-Ag Nanocomposite Samples

(a) Exemplary resistance (red) and temperature coefficient of resistivity (blue) vs. temperature curves of sample A175.
(b) Absolute resistivity vs. temperature curves of all Fe-Ag samples.
(c) Relative resistivity vs. temperature curves of all Fe-Ag samples.
(d) Relative resistivity vs. absolute resistivity. The dashed gray line is an intuitively drawn trend interpolating between the pure Ag and granular metal limits. All data points support the suggested trend.

Reference data of pure Ag from literature, Reference [234], are added to plots (b),(c) as gray double-line. Fe_{1000} granular film data (sample (G128)) are added to plot (c) as black double-line. The order of appearance is similar to that given in Table 5-1, i.e., by decreasing relative resistivity.

nanocomposite samples were synthesized with. The relative resistivity reflects the relative change of the absolute resistance of a sample under measurement while it remains uninfluenced by any correction factors, i.e., the XRR calibration factor of the crystal balance measuring the amount of deposited Ag, see Section 3.3, the Fe concentrations determined via EDX, and geometry correction factors for absolute resistivity calculations. The reason is that both the nanocomposite thickness t and the geometry correction factor λ reduce from the fraction $\rho_{100\,K}/\rho_{300\,K}$ according to Equation [5-3].

Figure 5-3(d) relates the relative resistivities of the samples to the absolute ones at 100 K. It can be seen that samples with a larger relative change in resistivity show lower absolute resistivities, yet they are still well above that of pure Ag. Starting from the low-resistivity side, i.e., at low Fe concentration, and moving to higher resistivity, A179 and A182 are the first samples to appear in the plot. Their relative resistivities change much stronger compared to the other Fe-Ag samples. This is most likely because of a much lower Fe concentration in these films.

Then, the relative resistivity approaches the granular metal limit, specified with $\rho_{100\,K}/\rho_{300\,K} \approx 0.9$ in the text above, quite soon with increasing resistivity. It is already close to it when the absolute resistivity reaches the 10^{-7} Ωm range, which is still two orders of magnitude below the resistivity of a granular metal. Therefore, nanocomposite properties caused by the embedded Fe clusters, i.e., granular giant magnetoresistance, are expected to be present for samples with a relative resistivity close to the granular metal limit.

An intuitively drawn trend interpolating between the argued limits according to the data points is added to graph (d) as gray dashed line. The data points of all samples support the suggested trend. However, no dependence on Fe cluster size can be identified from the plot. The data points of samples A173 and A186 are represented by open symbols for reasons that are explained and discussed in steps in the further course of this chapter.

5.2.2.2 Magnetoresistance Measurement Results

Magnetoresistance curves were recorded at several temperatures in the temperature range mentioned above. As an example, the data of sample A175 are plotted in Figure 5-4(a) as example. Similar to tunneling magnetoresistance, the strength of the magnetoresistance is determined by the degree of alignment between the surface moments of neighboring clusters. Accordingly, the measured magnetoresistance curves exhibit a quick increase of magnetoresistance at low fields, followed by a small negative field-dependent magnetoresistance. Anomalous behavior of magnetoresistance curves—no saturation despite a saturating magnetization—was found in other Fe-X systems, as well [237,238]. Because the variation with magnetic field is small compared to the low-field drop, magnetoresistance $\Delta\rho/\rho_0$ is henceforth defined via its value at maximum field $(\Delta\rho/\rho_0)_{6\,T}$. As it is shown in Figure 5-4(b) the magnetoresistance increases in magnitude with decreasing temperature, and saturates or even reduces again a bit at low temperatures. In general, negative magnetoresistance of several percent was observed for the Fe-Ag samples.

Figures 5-4(a)–(c) reveal that the magnetoresistance curves of Fe-Ag nanocomposites exhibit a saturating behavior similar to that observed for the Fe-Ge nanocomposites, i.e., the magnitude of the effect depends on temperature in a similar way. It increases with decreasing temperature and saturates
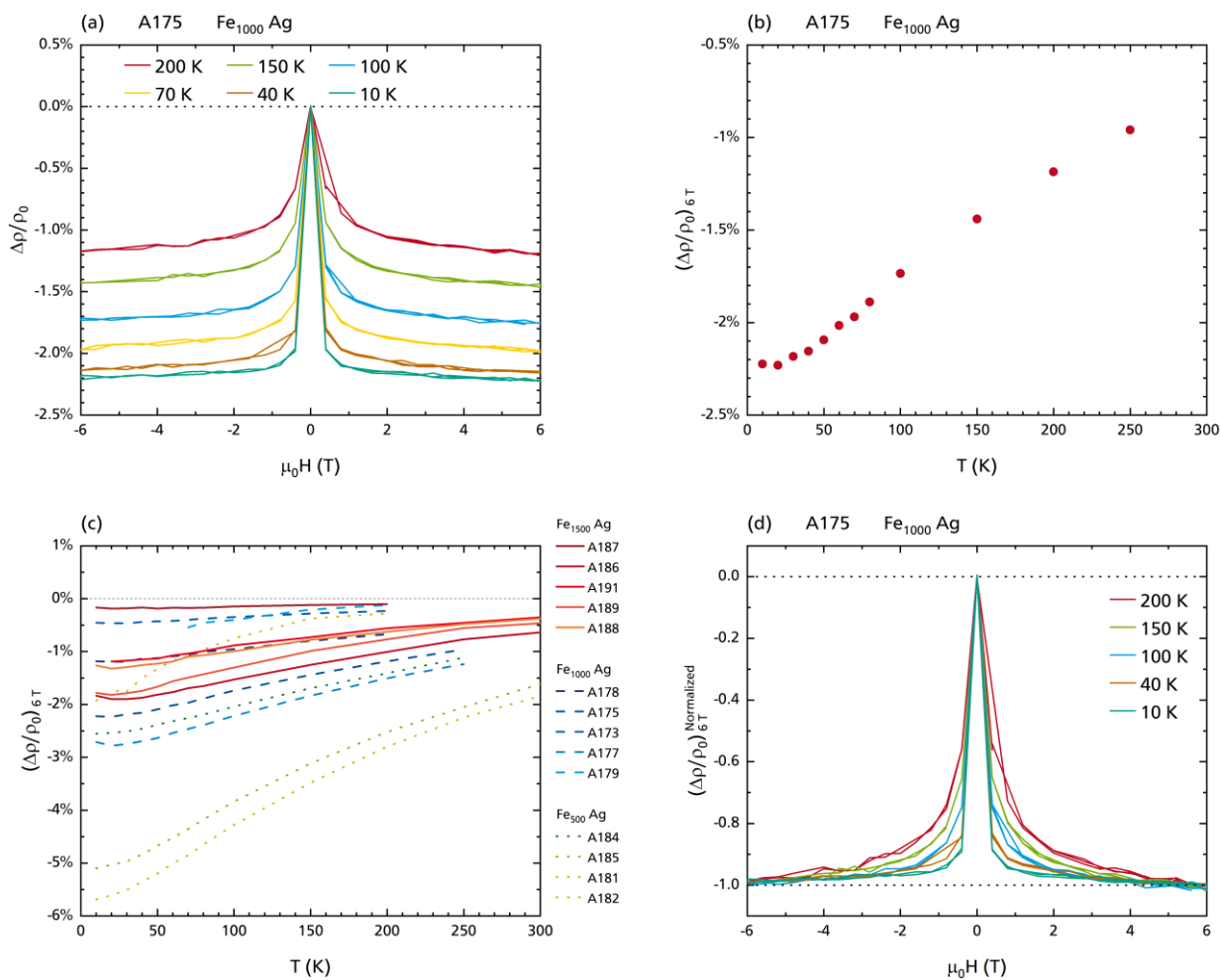
Figure 5-4: Magnetoresistance Measurements Results of Fe-Ag Nanocomposite Samples

(a) Magnetoresistance curves of sample A175 at various temperatures recorded in perpendicular sample orientation.
(b) Magnetoresistance at maximum field (± 6 T) of sample A175 vs. temperature.
(c) Magnetoresistance vs. temperature curves of all Fe-Ag nanocomposite samples.
(d) Magnetoresistance curves of sample A175 normalized to their maximum values at ± 6 T.

at low temperatures. It turned out that the magnetoresistance curves are reversible only at 200 K and below, however, not at 300 K. Two non-reversing magnetoresistance curves recorded at 300 K are presented in Figure D-5 in Appendix D. A summary of the magnetoresistance vs. temperature curves of all samples is given in Figure 5-4(c). The magnetoresistance curves of all Fe-Ag samples at 200 K, 100 K, 40 K, and 10 K are attached in Appendix C.

Figure 5-4(d) presents the same magnetoresistance data as Figure 5-4(a) but now with the magnetoresistance curves normalized each to the maximum-effect value at ± 6 T. From this plot it can be concluded that the low-field magnetoresistance evolves quicker, i.e., at progressively smaller field
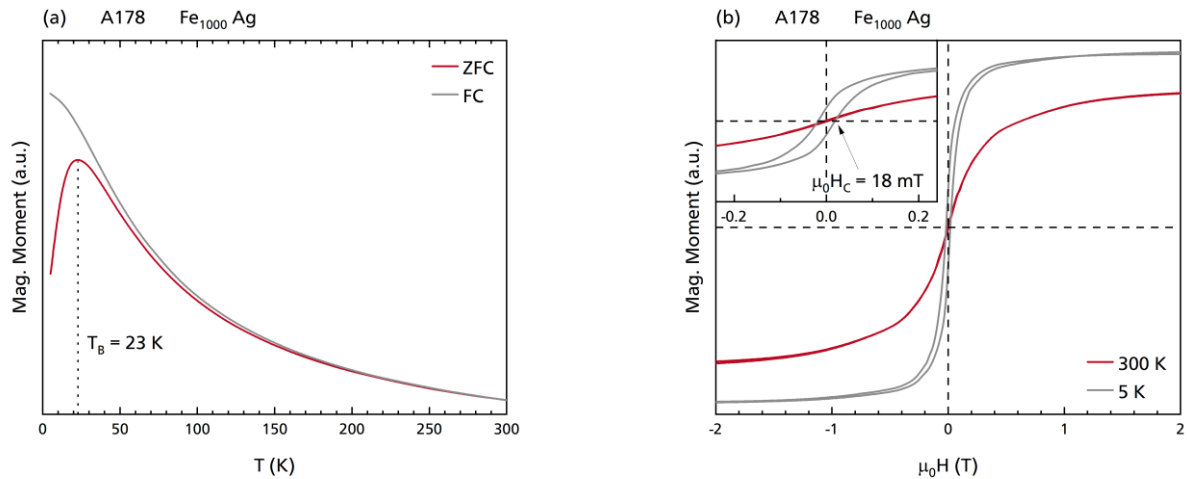
Figure 5-5: Magnetization vs. Temperature and Magnetic Field Curves of Fe_{1000}-Ag Sample A178

(a) ZFC/FC magnetization curves recorded in a 20 mT field.
(b) Magnetization curves at 300 K (red) and 5 K (gray).

ranges, with decreasing temperature. This is, as it is in the case of tunneling magnetoresistance, accounted to the rate at which the magnetic moments of the superparamagnetic clusters are aligned.

5.2.3 Magnetic Properties

ZFC/FC magnetization vs. temperature and magnetization vs. magnetic field data recorded at 300 K and 5 K curves of Fe_{1000}-Ag sample A178 are shown in Figures 5-5(a),(b). The superparamagnetic blocking temperature of the sample is measured to be 23 K. The small offset between ZFC and FC curve up to approximately 150 K already hints to the existence of ferromagnetic agglomerates of Fe clusters. As expected for a superparamagnetic ensemble, the saturation magnetization is higher at lower temperatures. Moreover, hysteretic behavior is evident at 5 K as can be seen best from the inset of graph (b). Nevertheless, the data prove that superparamagnetic clusters are dominating the magnetic properties of the films. As expected for superparamagnetic particles, and as it was found for Fe-Ge nanocomposites as well, see Section 4.5.2, the saturation magnetization is larger at the lower temperature, i.e., in the temperature regime where the magnetization of the film exhibits ferromagnetic field dependence.

At 5 K all Fe-Ag samples exhibited hysteretic behavior with coercivities $\mu_0 H_C$ in the range of 5.5 mT to 31.5 mT. However, at 10 K, i.e., the lowest temperature resistivity data were recorded at, no hysteresis in resistivity data was observed for any of the examined Fe-Ag samples.

5.3 Analysis

5.3.1 Granular Giant Magnetoresistance as a Function of Temperature

The evolution of granular giant magnetoresistance with temperature observed for Fe-Ag nanocomposites is discussed by Alonso et al. [237,239]. The recorded evolutions of the present samples are summarized in Figure 5-4(c).

Alonso et al. prepared Fe-Ag nanocomposite films by dc-magnetron sputtering, the samples contain Fe clusters with diameters from 2.5 nm to 3.0 nm and possess Fe concentrations between 20 at. % and 50 at. %. From magnetic property measurements the authors identified a crossover of the collective magnetic behavior of their nanocomposites at 35 at. %. Below this concentration threshold, i.e., the magnetic percolation threshold, where dipolar forces between isolated clusters and aggregates of clusters are dominating, the authors find their samples to be in a superspin glass state when at low temperatures; misaligned but correlated magnetic moments are collectively frozen here. Above a concentration-dependent transition temperature nanocomposite films of this kind are in an interacting superparamagnetic regime [25]. At a concentration higher than 35 at. % exchange interaction dominates, the nanoparticles lose their individuality, and the superspins start to form a superferromagnetic state.

In the articles by Alonso et al. [237,239], the changes between magnetic states observed from analyzing the magnetization data of the nanocomposites are also reflected as changes in the slopes of the resistance vs. temperature curves of the samples and, especially, in the magnetoresistance vs. temperature curves. Starting at low temperature, the granular giant magnetoresistance effect reduces in magnitude with increasing temperature both for samples below and above 35 at. % of Fe. When reaching about 50 K the magnetoresistance vs. temperature curves flatten and remain constant until the magnetic transition temperature of a sample is reached in case the concentration of a sample is $\geq$ 35 at. %. The initial decrease of the effect is assigned to the increasing importance of exchange interaction that correlates the magnetic moments to higher degrees with increasing temperature as well as with increasing Fe concentration. As the interaction defines the degree of alignment in the ensemble of moments when no external magnetic field is applied, the magnetoresistance effect is larger when less exchange interaction is present, i.e., the system has more freedom to adapt to an external magnetic field out of its superspin glass state.

Alonso et al. [237,239] propose that ferromagnetic alignment as a change away from the superspin glass state makes the magnetoresistance become temperature independent because the ferromagnetic

ordering is also independent from temperature when it orders the system as a whole. At the concentration-dependent transition temperature the interparticle exchange coupling vanishes and the ensemble becomes a set of interacting superparamagnets. With the change of the magnetic state the granular giant magnetoresistance effect further reduces in magnitude. When a sample is below the magnetic percolation threshold interparticle exchange coupling has only a minor effect. Therefore, the magnetic transition temperature moves towards the temperature where the low-temperature superspin state becomes collectively unblocked when the system is warmed up from very low temperatures. The former plateau phase in the magnetoresistance vs. temperature curve then reduces to a shoulder for their lowest-concentration sample (25 at. %). It can be assumed to fully disappear for samples with even lower Fe concentrations.

Further, Granovskii et al. [240] conclude from anomalous Hall effect data that skew scattering of electrons is the type of spin-dependent scattering happening at the interfaces between the magnetic clusters and the nonmagnetic matrix.

The lack of a shoulder in the magnetoresistance vs. temperature curve as observed by Alonso et al. [237,239] and as discussed above is what was found for all Fe-Ag nanocomposite samples of the present work. Therefore, from the discussion of the findings by Alonso et al. the following conclusion can be drawn. All Fe-Ag nanocomposite samples of the present work are ensembles of interacting superparamagnetic moments of mainly isolated clusters and to a small amount also of exchange-coupled cluster aggregates that are correlated by magnetic dipole-dipole interaction. This is supported by the hyperbolic shape of the magnetization vs. temperature ZFC/FC curves that was found for all samples in their reversible temperature regimes, see Figure 5-5(a) for an exemplary data set. This is in good agreement with the range of Fe concentrations determined from EDX elemental mapping for the present set of Fe-Ag sample.

5.3.2 Magnetoresistance as a Function of Nanocomposite Resistivity

In Figure 5-6(a) magnetoresistance vs. absolute resistivity at 100 K data of all Fe-Ag samples are plotted. The colored lines connect samples that belong to one and the same series in the order of their relative resistivity according to Table 5-1, with exception of samples A173 and A186. As expected, the magnetoresistance approaches zero on the low absolute resistivity side because of the low concentration of Fe clusters. Also, the data suggest an optimum absolute resistivity, i.e., Fe concentration, since the magnetoresistance tends to decrease also with increasing resistivity. Seemingly, the giant magnetoresistance effect is larger when smaller clusters are embedded in a film. The same systematics are found when the magnetoresistance is plotted as a function of the temperature coefficient of resistivity α, see Figure 5-6(b), as an alternative indicator for the amount of Fe that is mixed into a Ag film. A film
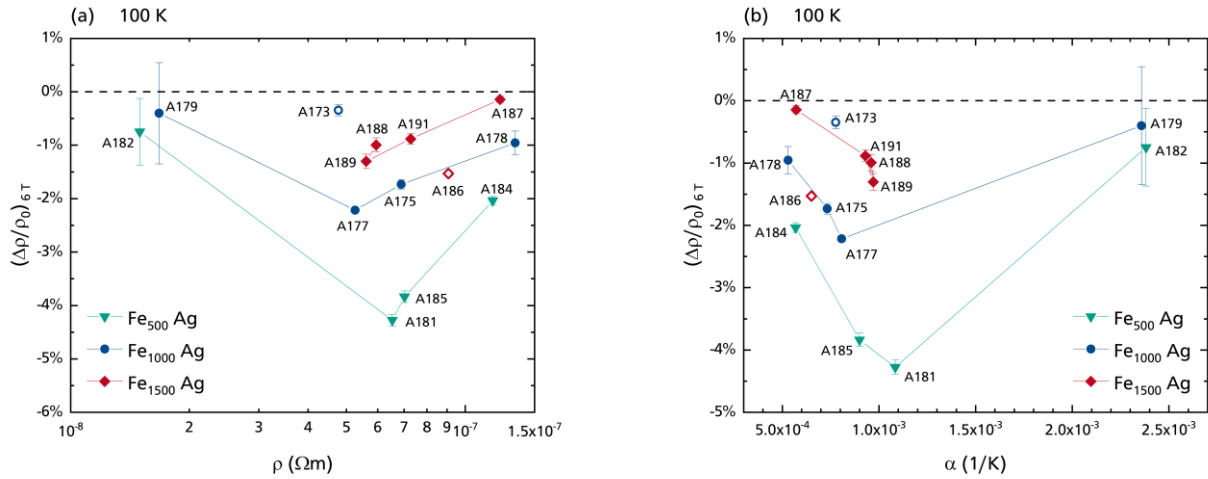
Figure 5-6: Magnetoresistance vs. Absolute Resistivity and Temperature Coefficient of Resistivity of all Fe-Ag Nanocomposite Samples

(a) Magnetoresistance vs. resistivity at $100\,\mathrm{K}$.
(b) Magnetoresistance at $100\,\mathrm{K}$ vs. temperature coefficient of resistivity.

On the low-resistivity side the pure Ag film with zero magnetoresistance defines the limit that is approached by samples A179 and A182. To the high-resistivity side an increasing degree of correlation of magnetic moments reduces the magnetoresistance. Between these limiting cases optimum conditions seem to exist. As can be seen, nanocomposites containing smaller clusters exhibit larger magnetoresistance. The data points of samples A173 and A186 are represented by open symbols for reasons that are explained in the text.

of pure Ag has $\alpha_{\mathrm{Ag}} = 3.7 \times 10^{-3}\,\mathrm{K}^{-1}$, which defines the high-α limit. Also, Ag films exhibit no magnetoresistance. On the low-α side, the Fe granular film (G128) with $\alpha_{(\mathrm{G128})} = 4.3 \times 10^{-4}\,\mathrm{K}^{-1}$ forms the other limit; the magnetoresistance is again zero. Samples A173 and A186 each deviate from the trends suggested by the other samples of the corresponding series. This is most likely because the voltage sensing during transport measurements was distorted by concentration fluctuations.

The appearance of a maximum between the high- and low-concentration limits is motivated by the assumption that there exists an optimum size of integrated Fe/Ag surfaces per unit volume to result in a largest possible magnetoresistance effect. At concentrations below the optimum, the scattering by the interfaces becomes less. At concentrations above, dipole-dipole interaction between the clusters may lead to an increasing degree of correlation of magnetic moments. As a consequence, the correlation of magnetic moments reduces the degree of misalignment and, hence, the effect induced by the application of a magnetic field. This is thought to be the driving effect as soon as agglomeration of clusters becomes relevant.

5.3.3 Blocking Temperature vs. Relative Resistivity and Magnetoresistance

The degree of agglomeration of clusters within a nanocomposite influences the magnetic properties of a sample. More precisely, the blocking temperature observed from ZFC/FC magnetization measurements of a film containing clusters of a well-known basic size. After a brief discussion of magnetic properties studies of Fe-Ag nanocomposites as found in the literature the blocking temperatures of the present Fe-Ag samples are related to their relative resistivity and magnetoresistance values at 100 K for this purpose.

Detailed studies on the magnetic properties of Fe-Ag nanocomposites were performed by Binns et al. [167]. The authors grew nanocomposite films by co-depositing preformed Fe clusters from a gas aggregation source, in which Fe was thermally evaporated from a crucible and where Fe clusters aggregated in He atmosphere [241], and where Ag was evaporated from a Knudsen cell. The size distribution of the clusters was of log-normal shape with a most probable diameter of 2.5 nm and a median diameter of 3.0 nm and, therefore, of a size comparable to that of the present Fe clusters. Binns et al. deposited films with concentrations ranging from < 1 vol. % up to 100 vol. % of Fe. The samples were exclusively prepared for magnetometer measurements, therefore, no magnetoresistance data are available for their samples.

To analyze and interpret their data Binns et al. [167] modeled Fe-Ag nanocomposites via Monte Carlo simulations. The Fe clusters were assumed to be spheres of equal size and to randomly occupy the sites of a sc lattice, whose lattice parameter was chosen to be equal to the diameter of these spheres. This was their way to assure that neighboring clusters touch each other in the simulation. Besides Zeeman energy, anisotropy energy, and dipolar interaction energy, Binns et al. [167] also included exchange interaction between clusters in their simulations in order to model the magnetic behavior as detailed as possible.

Their sample lowest in Fe concentration (0.8 vol. %) represents an ensemble of ideal noninteracting superparamagnets, since its magnetization vs. magnetic field curve perfectly scales with H/T well above the blocking temperature in accordance with the argument of the Langevin function (see Equation [2-9] and Section 2.3). From magnetization data recorded at 2 K the authors calculate an anisotropy constant $K = 2.41 \times 10^5$ J/m^3 and a single-particle blocking temperature $T_B \approx 5$ K from magnetization data fits for the above-mentioned particle size distribution. Binns et al. [167] used these two quantities further to simulate their samples with higher Fe concentrations.

Above the regime of ideal superparamagnetism, dipolar interaction starts to influence the arrangement of superparamagnetic moments by disordering them [25]. This regime of interacting superparamagnets is discussed by Allia et al. [25] by means of an apparent temperature in the argument
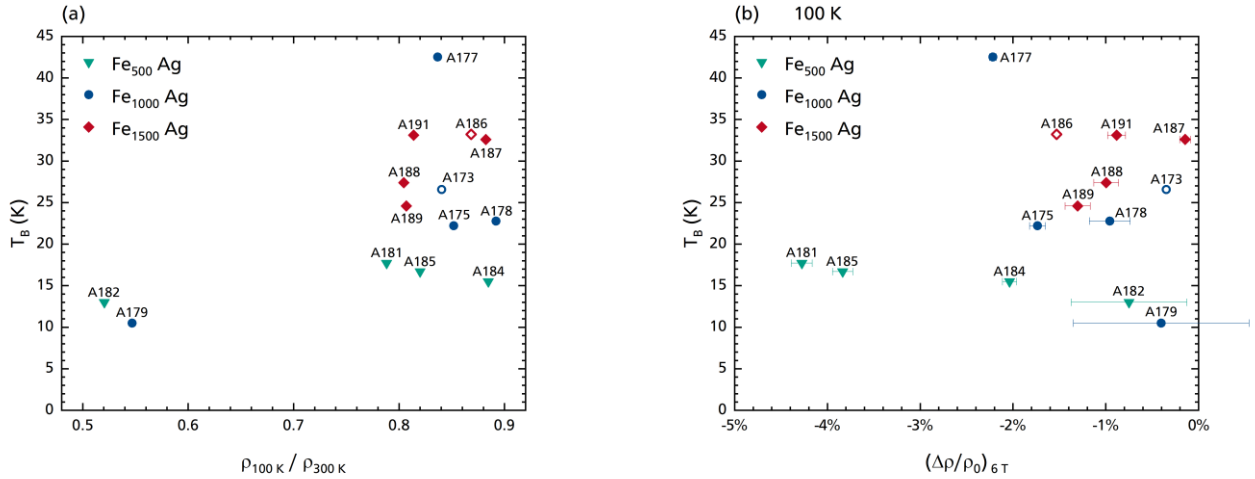
Figure 5-7: Blocking Temperature of Fe-Ag Nanocomposite Samples vs. Relative Resistivity and Magnetoresistance

(a) Blocking temperature vs. relative resistivity at 100 K.
(b) Blocking temperature vs. magnetoresistance at 100 K.

The average blocking temperature increases with increasing cluster size. Fe_{500}: 15 K; Fe_{1000}: 25 K; Fe_{1500}: 30 K.

of the Langevin function (see Equation [2-9]). The apparent temperature is the sum of the physical temperature of the system and a constant that is related to the dipolar interaction between the clusters. From this modification the true moments of the superparamagnetic base units can be calculated and, hence, their size estimated. For their sample containing 10 vol. % of Fe Binns et al. [167] find the superparamagnetic base units to consist of 6 to 7 agglomerated clusters. These clusters are exchange coupled and the aggregates in turn interact with each other via dipolar forces. Simulations of the ZFC/FC curves of their samples with concentrations ≥ 10 vol. % via Monte Carlo calculations confirm that exchange coupling of touching clusters is required to explain the observed ZFC/FC temperature evolution of magnetization in this magnetic regime. In particular, the shift of the blocking temperatures under magnetic field variations and the deviation of the magnetization from an ideal $1/T$ dependence towards a linear decay with increasing Fe concentration cannot be explained without exchange interaction.

As one consequence, the magnetic moments of exchange-coupled cluster aggregates freeze collectively at a temperature above the single-particle blocking temperature. In case of the present samples, the blocking temperature is determined by the magnetic properties of the entire sample and needs not exactly represent the magnetic properties present in the region sampled by the four-wire transport measurement excitation current.

Assuming a sample is measured across its region of highest concentration, i.e., maximum blocking temperature, this magnetic property can be carefully compared with transport data, i.e., with relative resistivity and magnetoresistance. In Figures 5-7(a),(b), the blocking temperatures are plotted vs.

relative resistivity and magnetoresistance, respectively. There, it can be seen that nanocomposites containing Fe_{500} clusters exhibit the lowest average blocking temperatures, about 15 K, and those containing the Fe_{1500} ones exhibit the highest, about 30 K. In between the data points of these series, three out of five Fe_{1000}-Ag data points are located—their blocking temperature is about 25 K on average.

Since the blocking temperature of every sample is higher than the one of a single cluster, see text above and Section 4.5.2.2, all samples are likely to consist of cluster aggregates rather than isolated clusters according to the results of Binns et al. [167]. This holds also for samples A173 and A186, whose magnetotransport properties are thought to be distorted by concentration fluctuations. Large agglomerates would yield large blocking temperatures. However, since the blocking temperature of each sample is consistent with the average blocking temperature of the corresponding cluster series there do not seem to be larger-than-average agglomerates within these two samples.

The transport measurements of sample A177, which is one of the deviating Fe_{1000}-Ag samples, were executed across a region apart from that of highest Fe concentration as was found by means of EDX. Additionally, A177 is the only sample with a thickness below 100 nm. These differences may be the reason why A177 exhibits the highest blocking temperature of all Fe-Ag samples while it does not fit to the trend given by all other data points in the same turn. Sample A179, the other Fe_{1000}-Ag one that deviates, is very low in Fe concentration. This explains the lower-than-average blocking temperature that was observed.

The Fe_{500}-Ag sample A182 was measured far beside the cluster spot as well and, moreover, was synthesized with a very low concentration of Fe anyway. However, the blocking temperature of A182 is on the same order as that of the other Fe_{500}-Ag samples. Preliminary EDX Fe concentration and two-wire resistance data of samples A177 and A182, similar to these discussed in Section 4.5.1.1, are presented in Figure D-6 in Appendix D.

It can be concluded that the blocking temperature is dominated by the cluster size rather than by magnetic dipole-dipole interaction between the clusters. This means agglomeration of clusters determines the properties of the Fe-Ag nanocomposites only to a small degree within the present samples. This can be seen best from the Fe_{500}-Ag series, where the blocking temperature, a quantity representing the size of superparamagnetic particles in the film and the strength of interaction between them, is constant to good approximation, while transport properties vary from sample to sample within the series.

One reason for the blocking temperature to vary only slowly with the relative quantities surely is the immiscibility of Fe and Ag, which makes it harder for Fe clusters to merge or agglomerate as long as they are kept separated by the Ag matrix between them.
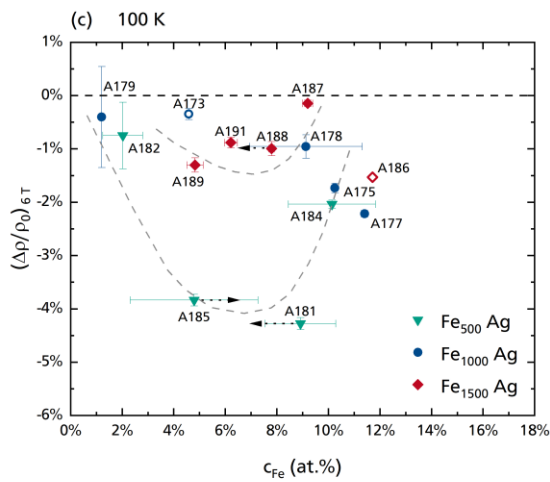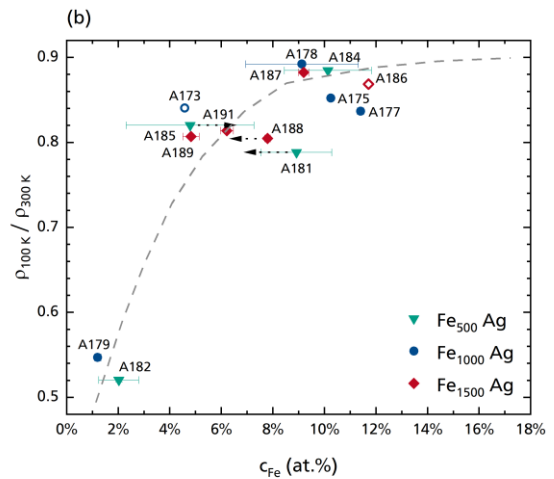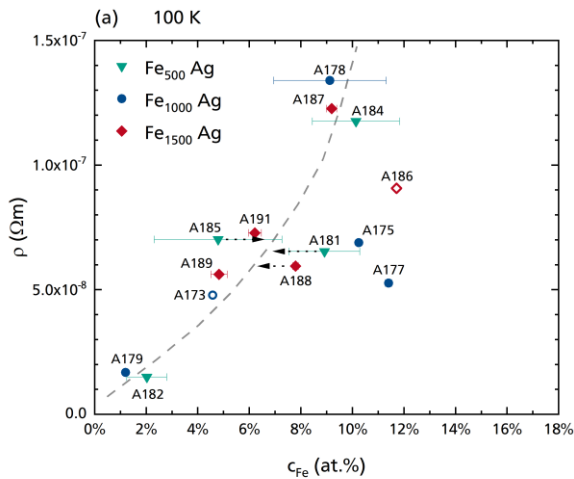
Figure 5-8: Transport Properties vs. Fe Concentration

(a) Resistivity vs. Fe concentration.
(b) Relative resistivity vs. Fe concentration.
(c) Magnetoresistance vs. Fe concentration.

The gray dashed lines represent the suggested trends. Their motivations are given in the text.

Also, the good thermal and electric conductivity of Ag makes the deposition energy and the charge of soft-landing cluster ions dissipate much faster compared to a-Ge matrix samples. The same holds for the thermal energy of the deposited Ag atoms coming from the effusion cell. The surface mobility of the Fe clusters is expected to be reduced quicker in case of Ag matrix samples compared to the a-Ge matrix films. The benefit of a quicker reduction is a better isolation of the Fe clusters.

5.3.4 Comparison on Iron Concentration

The concentration and the size of the embedded clusters are the basic quantities that determine the transport properties of the nanocomposites. In Figures 5-8(a)–(c), absolute resistivity, relative resistivity, and magnetoresistance are plotted as a function of the Fe concentration determined from EDX elemental mapping. However, there are no straight-forward correlations of these quantities with concentration. The local variations in the cluster concentrations across the measured film areas are most likely the reason for this. Nevertheless, there must exist a biunique relation between the absolute resistivity and

the Fe concentration of the nanocomposites at least well below the percolation threshold. Similar to Figure 5-3(d), intuitively drawn trends, drawn as dashed lines, are added to the plots of Figure 5-8. They are motivated as follows.

The trend suggested in graph (a) starts at the resistivity of pure Ag, i.e., at $c_{Fe} = 0\%$. With increasing Fe concentration the absolute resistivity first increases strongly and then saturates in the granular metal limit, $\sim 10^{-5}$ Ωm, well above the percolation threshold. According to the Monte Carlo simulations by Binns et al. [167] the percolation threshold estimated in Reference [171] for a random distribution of spheres (see Section 4.7.2.1) is 29 vol. %, which may be caused by the strict sc lattice of touching spheres that was used by the authors for their simulations. The percolation threshold found by Allia et al. [46] is about 20 vol. %. Both values are higher than the value of 15.4 vol. % given by Scher & Zallen [170] for random distributions of spheres, see also Section 4.7.2.1. The concentrations determined via EDX elemental mapping all range below these concentration values.

In fact, no effect of percolation is visible in any of the plots of Figure 5-8. This is most likely because percolation of clusters plays a minor role in the Fe-Ag system in comparison with the Fe-Ge system. The conduction through a nanocomposite of the latter system is governed by the amount of percolating clusters, i.e., the tunneling barriers between well-conducting chains of percolating clusters. However, this is not the case in the Fe-Ag nanocomposites, where conduction is always of metallic kind. Instead, it is the amount of Fe-Ag interfaces that determine the resistivity of a nanocomposite through the scattering caused by them. The trend suggested in graph (b) is motivated similarly to the one drawn into Figure 5-3(d) and follows from the arguments given in Section 5.2.2.1.

Since the Fe_{500}- and Fe_{1500}-Ag series were all measured using the same contact geometry '40' (see Table 5-1 and Section 5.1.3.3) and since they are of comparable thickness (about 140 nm to 190 nm), the samples of these series can be compared on Fe concentration both within each series and with each other. For this reason, these two series are discussed first.

For sample A188 only an Fe concentration averaged across the full film width could be determined from EDX data. The Fe concentration map of the sample (see Figures D-7(a),(b) in Appendix D) indicates that the Fe concentration increases from the left-hand to the right-hand side of the film. Therefore, since the film was contacted from its left-hand side it is justified to assume an Fe concentration lower than the one listed in Table 5-1. Because sample A188 is close to sample A189 in terms of its resistivity, see Figure 5-3(d), assuming a similar Fe concentration of about 6 at. % is justified. This would move the data point of sample A188 to positions in the plots Figures 5-8(a)–(c) so that it supports the suggested trends; the according shifts are indicated by dashed arrows.

One data point with a seemingly too high Fe concentration is that of sample A186. An assumed concentration of about 8 at.% would move the data points belonging to A186 towards the suggested trends. However, an Fe concentration of about 12 at.% was found from an EDX analysis of the region close to the contacted film edge. Unlike A188, A186 was connected at the side exhibiting the higher-than-average concentration (see Figures D-7(c),(d)). Therefore, assuming a lower concentration remains unjustified for this sample. Also, the much lower magnetoresistance of sample A173 cannot be explained this way.

On first sight, the Fe_{500}-Ag data represented by green triangles seem to form a trend in the magnetoresistance vs. Fe concentration plot Figure 5-8(c) that exhibits a maximum in magnetoresistance, and the reduction to zero magnetoresistance at 0 at.% and at about 11 at.% of Fe concentration. However, since the relative resistivity of sample A181 is lower than that of A185 it should have a similar but lower average concentration than A185. Also, a similar magnitude in magnetoresistance suggests a similar concentration; about 7 at.% may suit both of them. Dashed arrows are added to the plots accordingly.

Especially the Fe_{500}-Ag data suggest there is an optimum concentration at which the giant magnetoresistance has a maximum within the examined concentration range. This maximum is thought to be of global kind. For a second maximum or even oscillating behavior to appear a well-controlled periodic distribution of clusters would be needed to yield periodicity. In contrast to this, the transport measurements of the present samples are averages across wide ranges in which clusters are distributed in a completely random manner.

The data also show that a larger granular giant magnetoresistance is achieved when smaller clusters are embedded. The maximum magnetoresistance is reached at a concentration of about 8 at.% in case of the present samples according to Figure 5-8(c). Two dashed lines are added for the Fe_{500}-Ag and the Fe_{1500}-Ag series in order to represent the suggested dependence of the magnetoresistance on the Fe concentration.

In principle, it is expected that the magnetoresistance values of the Fe_{1000}-Ag series should follow a similar trend located between these of the Fe_{500}-Ag and Fe_{1500}-Ag series. One possible reason for the observed deviation is that, except sample A179, the samples of the Fe_{1000}-Ag series were recorded in different contact geometries (see Table 5-1). For this reason A179 is the only sample of the Fe_{1000}-Ag series which is directly comparable to the samples of the other series discussed above.

All of the samples discussed so far were measured in the '40' geometry. Moreover, the majority of these films were contacted at that side of the film stripe that may have exhibited a thin region where no Fe clusters were deposited. According to the definition given in Section 4.2.1 the side with a thin region

free of Fe clusters is the right-hand one. See also Figure 4-7. This Fe-free region results from the different directions of incidence of cluster ion and effusion cell beam in the deposition chamber of the CIBD system, see Section 3.3. Only samples A179, A182, A188, and A189 were contacted at the opposite side. The region of pure Ag may have been expected to result in the measurement of systematically lower absolute resistivities and smaller magnetoresistance effects. On the other hand, the better conductivity of pure Ag may have been countered by the porousness caused by the lack of the Ta adhesion layer, which is missing for the same directions of incidence reason.

Sample A178 was measured in the '31' geometry, i.e., at least the voltage drop for resistivity measurements was sensed along one and the same film edge. Therefore, it is comparable to the other samples to sufficient approximation. This may be the reason why samples A179 and A178 fit well to the argued trends and the data of the other samples.

The remaining two samples A175 and A177 were measured in the '22' geometry. Since the excitation current, which crosses the entire film from one side to the other in this contact geometry, prefers regions of lower resistivity, it favors paths with a lower-than-average Fe concentration. Therefore, the average concentrations used to characterize these two films are an upper limit for the concentration effectively experienced by the excitation current. Samples A175 and A177 would join the trends if their Fe concentrations were roughly between 4 at. % and 8 at. %.

One factor that may have influenced the properties of the nanocomposites as well is the oxidation of Fe clusters. Indeed, two samples, A177 and A182, showed a number ratio of O to Fe atoms larger than 10 in their EDX elemental analyses, while the ratios of all other samples varied around 3. In the case of sample A177 this is accounted to the small thickness of the film. This allows for a higher relative O signal from the SiO_2 surface layer. For sample A182 the high ratio may be due to the low absolute Fe content itself, which again yields an increased ratio. However, both samples exhibit plausible magnetotransport behavior according to Figures 5-8 and 5-9. Therefore, the Fe-Ag films with their only 10 nm thick protection layers seem to be well protected against oxidation.

5.3.5 Comparison of Relative Quantities

With embedding Fe clusters into Ag matrices the excellent conductivity of pure Ag is diminished by the scattering of conduction electrons at the interfaces between the clusters and the matrix, and by the higher resistivity of Fe itself. This worsening of conduction can be characterized by the relative resistivity as presented in Figures 5-3(c),(d). The quantity is independent of correction factors, measured film thicknesses, and absolute sample resistances, see Sections 5.1.3.3 and 5.2.2.1. In particular, the relative resistivity is independent of systematic errors potentially introduced by these quantities since these are
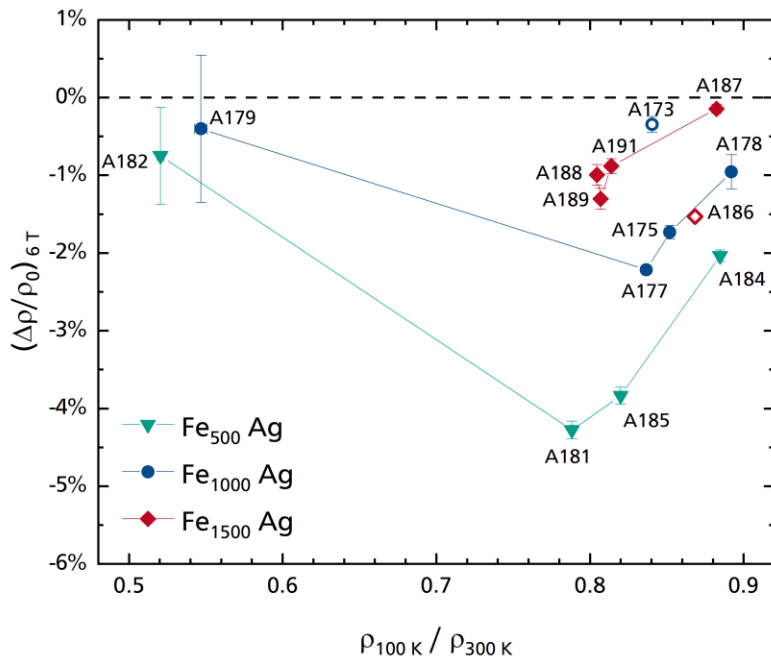
Figure 5-9: Correlation of Magnetoresistance and Relative Resistivity

Magnetoresistance and relative resistivity do not depend on film thicknesses and correction factors. Accordingly, their correlation can be used to identify whether the data of a sample are plausible or not. Samples A173 and A186 do not integrate into the trends given by the other samples.

reduced when the fraction of the quantity is calculated. For the same reason, the magnetoresistance is a relative quantity, which is independent of these potential sources of error, too.

However, as was discussed in Section 5.3.4, no straight-forward systematic dependence of absolute resistivity, relative resistivity, and magnetoresistance on Fe concentration was found. Since both magnetoresistance and resistivity are determined simultaneously, at least magnetoresistance and relative resistivity are expected to be correlated. Therefore, a potential correlation of these two relative quantities is examined as a last point. Accordingly, magnetoresistance data are plotted as a function of the corresponding relative resistivities at 100 K in Figure 5-9.

As was discussed in Section 5.2.2.1, pure Ag has a relative resistivity of 0.26 at 100 K. Therefore, samples low in Fe concentration should also exhibit a large temperature-caused change in resistivity because scattering by Fe-Ag interfaces becomes very unlikely here. In the same measure, the magnetoresistance is expected to vanish for these samples. Indeed, this situation is represented by the two samples lowest in relative resistivity in Figure 5-9, A182 and A179.

On the other side of the plot the magnetoresistance decreases as the nanocomposite becomes more and more of a granular metal with increasing Fe concentration. This limit is characterized by a relative resistivity of about 0.9 at 100 K as was discussed in Section 5.2.2.1. It was found from Figure 5-3(d) that

the relative resistivity approaches this limit quite quickly, i.e., already when the absolute resistivity is about 10^{-7} Ωm. Assuming there is only one maximum of magnetoresistance between these two limits, consequently, the limit should appear closer to the right-hand side of the plot. Figure 5-9 can misleadingly be interpreted to show this optimum. However, since none of the nanocomposites exhibited a relative resistivity in the range $0.6 < \rho_{100\,K}/\rho_{300\,K} < 0.8$ there are no data available to support this argumentation. Nevertheless, the data suggest again that the granular giant magnetoresistance effect can take larger values when smaller clusters are embedded in the films. Also in this last comparison plot the data points of A173 and A186 deviate from the trends suggested by all other Fe-Ag nanocomposite samples.

5.4 Conclusions

In this chapter, the transport and magnetic properties of cluster-assembled Fe-Ag nanocomposite films that were synthesized with the CIBD system reviewed in Chapter 3 were studied. In addition to Fe_{500} and Fe_{1000} clusters, Fe_{1500} ones were used to create a third series of nanocomposite samples. The main difference in transport properties with respect to semiconductor matrix nanocomposites is that no longer chains of percolating Fe clusters, i.e., the tunneling contacts between them, define the paths of charge transport through the nanocomposites. Instead, the nanocomposites are fully metallic since the matrix is made of Ag, and it is now the electron scattering at the Fe/Ag interfaces that determines the resistivities of the Fe-Ag nanocomposites. Except of two samples that contain only a small amount of Fe clusters, the absolute resistivities of the Fe-Ag nanocomposites were all found to be within 0.5×10^{-7} Ωm and 1.5×10^{-7} Ωm in the present study.

The granular metal limit, representing the high Fe concentration limit, was argued to be reached at an absolute resistivity on the order of 10^{-5} Ωm. Since no straight-forward dependence on Fe concentration was observed, neither for the resistivity nor for the magnetoresistance, the relative resistivity at 100 K was used as an alternative characteristic quantity for sample comparison. The relative resistivity was found to be about 0.5 for the two samples very low in Fe concentration and to vary between 0.8 and 0.9 for the other samples. Approximating the granular Fe film limit with the measured properties of an Fe-Ge sample with a very high Fe concentration, 83 at.%, it was argued that 0.9 is the relative resistivity that is approached in the granular metal limit. When plotting the relative resistivity as a function of the absolute resistivity, indeed, the data of all three series suggest that the relative resistivity quickly increases from the value of pure Ag, 0.26, and is already close to its upper limit when the absolute resistivity is on the order of 1×10^{-7} Ωm.

The idea to compare the magnetoresistance of the Fe-Ag nanocomposites on the relative resistivity of the samples is based on the fact that both relative quantities are determined under identical conditions right after another. Multiplicative sources of error such as calibration and geometry correction factors are reduced from the fractions representing these two relative quantities. Therefore, relative resistivity and magnetoresistance are expected to be correlated, independent of the Fe concentrations determined from EDX elemental mapping on which the measured data were compared, too. As expected, the magnetoresistance is small for samples both with a relative resistivity tending towards that of pure Ag and with one that is close to the value taken in the granular metal limit. Accordingly, the data show that the giant magnetoresistance becomes zero in both limits. Also, the data imply the existence of a maximum of the magnetoresistance effect in the range $0.6 < \rho_{100\,K}/\rho_{300\,K} < 0.8$.

Magnetoresistance as a function of temperature data implicates that the fabricated Fe-Ag nanocomposites are ensembles of isolated exchange-coupled agglomerates, which in turn interact via magnetic dipole-dipole interaction. This means the present samples are all settled in the interacting superparamagnets regime. Therefore, the Fe concentrations determined for the Fe-Ag samples can be assumed to be on the correct order. Concentration data suggest the maximum magnetoresistance effect to appear already at an Fe concentration of < 10 at. %. The absolute resistivity is on the order $\leq 10^{-7}$ Ωm there. Also, the magnetoresistance effect of the nanocomposite increases when the clusters contained in the film are smaller. This is assigned to the larger surface-to-volume ratio coming along with smaller clusters. A larger integrated Fe/Ag interface allows for a higher rate of spin-dependent scattering and, consequently, for a larger giant magnetoresistance.

For future generations of Fe-Ag nanocomposites the granular giant magnetoresistance samples need to be synthesized with a better control of cluster isolation and homogeneity of cluster distribution. However, it is difficult to distribute cluster ions homogeneously over several square millimeters by manipulating the cluster ion beam of the CIBD system only.

Another option is to restrict the sample to the stripe and only four contact terminals, and to form the contact pattern of nanocomposite rather than Pt. Besides the stripe, there may also be other suitable geometries, e.g., the van der Pauw cloverleaf [242,243]. However, this approach is complicated by the different directions of incidence of cluster ion beam and matrix material. This difference led to the systematic mismatch of cluster and matrix deposition areas observed for the present samples, see Figure 4-7. The cause of the systematic mismatch can only be removed by using two separate masks in parallel, one for the cluster ion beam and one for the matrix material. However, this solution is thought to be very challenging. Further, it would not prevent the clusters from agglomerating, i.e., would not improve the isolation of the clusters.

To also improve the isolation of clusters it is thinkable to deposit sub-monolayer amounts of clusters and enough matrix material to fully cover the previous layer of newly deposited clusters in an alternating order. With an appropriate sample holder setup a sample may be moved between the alternating deposition steps such way to alternatingly point towards the cluster ion beam and the source of matrix material. This would reduce the mismatch of the film components to a minimum. However, the thicknesses of the nanocomposites would be smaller because of the much lower effective deposition rate. Moreover, the limiting factor for the maximum deposition time is the amount of LN_2 that can be stored in the dewar used to supply both the CIBD source and the deposition stage with cooling fluid.

A third approach is to structure the pattern to be used for magnetotransport measurements from a selected region of homogeneous cluster concentration by removing parts of the deposited nanocomposite film. A picosecond laser, i.e., the one that was used to cut, e.g., the shadow deposition mask parts (see Section 4.2), may be suitable for this task. With a picosecond laser, a sufficiently wide rim of the nanocomposite could be removed such that the structure to be used for transport measurements remains separated and, hence, isolated from the rest of the deposited nanocomposite film. This approach can be applied to co-deposited samples, samples that are deposited in an alternating order, and maybe even to the already existing samples of the present work.

To monitor the homogeneity, i.e., to record an intensity profile of the cluster ion beam in the deposition chamber of the CIBD right before and also during deposition it is thinkable to install a detector to the sample arm of the deposition chamber as another cluster ion beam analysis tool. Thought of as an array of 'pixel' electrodes, such a detector must allow to read out small and equidistantly installed parts of the sample electrode separately and quickly in sequence in order to obtain a 2D beam profile within an acceptable time span.

6 Outlook: Construction of a Pulsed Laser – Buffer Gas Condensation Cluster Source Setup

In addition to the research performed with the CIBD system, see Chapters 3–5, a UHV cluster deposition setup based on a laser ablation source was developed and assembled. The setup uses pulsed laser ablation to remove material from the surface of a target in order to obtain vaporized material for the subsequent cluster condensation [244–246]. Ablation and cluster condensation take place in a buffer gas atmosphere. The design of the setup aims for a beam of neutral clusters to be used for matter-wave interference experiments [48–51]. However, it may also be modified so that it can used for the growth of cluster-assembled materials.

One advantage of pulsed laser ablation is that it can be applied to almost every material. This is because of the wide range of laser wavelengths available. In the current setup, second-harmonic Nd:YAG laser light is used. A Cu target and a Ag target were used during test runs and for test depositions.

The principle of laser ablation with the focus on nanosecond pulsed laser ablation in an inert gas atmosphere is given at the beginning of the chapter in Section 6.1. The pulsed laser – buffer gas condensation (PL-BGC) setup is discussed in detail in Section 6.2. Results from an SEM analysis of a Ag cluster deposition test sample are presented in Section 6.3.

6.1 Nanosecond Pulsed Laser Ablation

The method of laser ablation makes use of the property of a target material to absorb light in order to locally deposit an amount of energy sufficient to melt or even evaporate a small part of a target. The energy density required for evaporation is high, therefore, it is usually provided by means of a focused, pulsed laser beam.

In a metal, like Ag, which is used for demonstration purposes in the present work, it is the gas of quasi-free electrons that absorbs the light emitted by the laser source, as only the electrons can follow the oscillation frequency of the incident electro-magnetic waves. This is because of their comparatively very high charge-to-mass ratio e/m_e. The ion cores forming the lattice, in turn, are much too inert to follow the oscillations of the electro-magnetic waves since the charge-to-mass ratio is several orders of magnitude smaller here.

The energy absorbed by the electron gas is redistributed among the electrons by electron-electron collisions within a time span on the order of 100 fs [245,246]. Subsequently, electron-phonon interaction causes a transfer of thermal energy to the atomic lattice. The much higher mass of the ion cores occupying the lattice sites elongates the time scale of energy transfer to picoseconds [244–246]. When the duration of the laser pulse is in the range of pico- or even femtosecond, different temperatures T_i and T_e have to be ascribed to lattice and electron gas, respectively. This is respected in the 1D two-temperature diffusion model of laser interaction with solids [244,247–250]. The model is 1D since it only respects the distance measured from the surface of the target as spatial parameter. Let it be the z-direction here.

However, when the duration of the laser pulse is on the order of nanoseconds, electron and lattice system are in thermal equilibrium $T_i = T_e = T$. For the equilibrium case, the equation of thermal diffusion is [244,247–250]

$$C_i \frac{\partial T}{\partial t} = \frac{\partial}{\partial z}\left(k_0 \frac{\partial T}{\partial z}\right) + I(t)\,(1-R)\,\alpha\,e^{-\alpha z}. \qquad \text{[6-1]}$$

Here, C_i is the heat capacity per unit volume of the lattice. The first term on the right-hand side describes the dissipation of thermal energy into the bulk of the ablation target, the second term is the laser heating source term. The main drain of thermal energy is heat dissipation into the bulk [245,246,251]. k_0 is the thermal conductivity of the target material, $I(t)$ is the intensity of the laser at the target surface, R is the according reflectivity, and α is the absorption coefficient. The optical penetration depth is the inverse of the absorption coefficient α^{-1}.

Under the influence of a nanosecond laser pulse the irradiated area of the target is melted rather than sublimated. Evaporation of liquid target material sets in when the deposited energy becomes comparable to the latent heat of vaporization H_v [246]. The required threshold laser fluence is

$$F_{th} \approx \rho\,H_v\,l_T, \qquad \text{[6-2]}$$
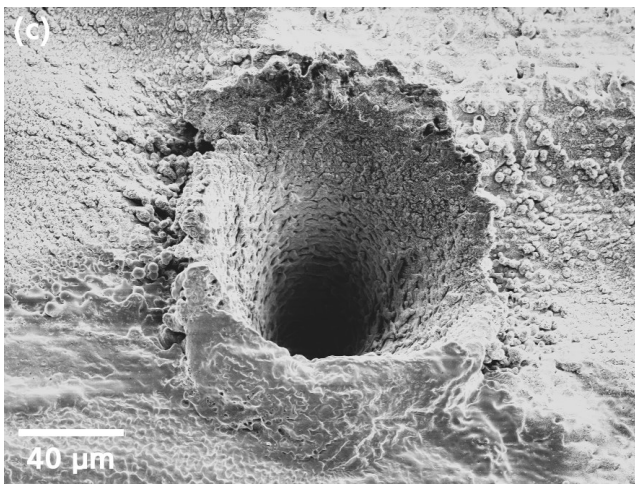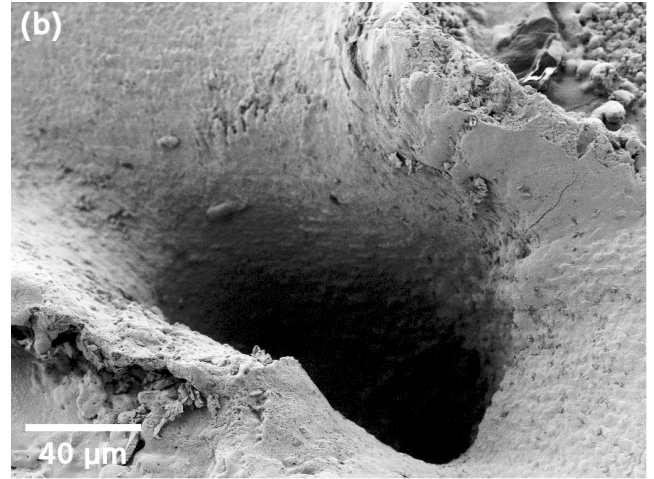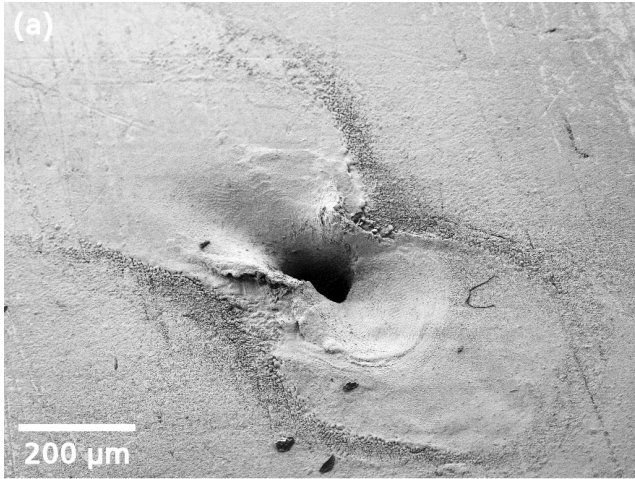
Figure 6-1: SEM Micrographs of Holes Drilled by Laser Ablation

The SEM micrographs show two different holes, images (a) and (c), that were drilled into a 0.5 mm thick Cu sheet during laser focus and power tests of the used PL-BGC setup. Image (b) provides a close-up view of the hole depicted in image (a). The tests were performed at room temperature and in ambient atmosphere. Unfortunately, number of shots and laser power remain unknown. The formation of a corona—at least in parts—can be identified in every image.

where ρ is the density of the target material, $l_T = 2\sqrt{D\tau_L}$ is the heat diffusion length with the thermal diffusivity D, and τ_L is the laser pulse duration. After irradiation by the laser the material remains molten for several tens of nanoseconds [246].

For Ag, the latent heat of vaporization is 254 kJ/mol [252] (which equals 2.35 kJ/g), the density of liquid Ag at the melting point is 9.3 g/cm^3 [253], and with $k_0 = 1.75$ W/(cm K) [254] and specific heat $C_p = 33.35$ J/(mol K) [255] (which equals 0.309 J/(g K)) for Ag at the melting point the diffusivity calculates to $D = k_0/\rho C_p = 60.9$ mm^2/s. For a 5 ns laser pulse (which is the pulse duration of the laser used in the present setup), Equation [6-2] yields a threshold fluence of $F_{th} = 2.4$ J/cm^2. As will be shown later, this threshold is overcome during the present experiments when the laser is focused to a spot of 0.7 mm in diameter or less.

During the ablation process, atoms evaporated from the molten layer of target material cause a recoil that is absorbed by the melt. Therefore, small droplets of liquid target material are ejected in addition to vaporized target material [244]. A corona of resolidified melt surrounding the area the laser beam

interacted with the target material is a characteristic feature of laser ablation in the nanosecond regime [244]. Three SEM micrographs of holes that were laser-drilled into a 0.5 mm thick Cu sheet during laser focus and laser power adjustment and calibration tests are presented in Figure 6-1, where graph (b) shows the same hole as depicted in graph (a) at a higher resolution. The tests were performed at room temperature and in ambient atmosphere. A corona around the hole, which is characteristic for nanosecond laser ablation, can be clearly identified in graph (c), and in parts also in graphs (a),(b).

Generally, ablated material is ejected with a velocity vector oriented perpendicular to the target surface. The plume of ablated material is mostly neutral. Usually, it carries less than 5% of ions and charged particles [246]. The temperature and the velocity of the plume particles are on the order of 10^5 K and 10^4 m/s, respectively, and the pressure within the plume is on the order of 10 GPa in the moment the plume starts to expand from the surface of the target [245].

The distribution of the velocity and the mass of the plume particles leads to a high rate of particle collisions, causing the plume to also expand vertically to its major direction of ejection. Electrical interaction between the low in amount but when charged mostly positive plume particles contribute to the plume expansion only at the early stage, usually within the first 100 fs [246,251]. After this time span, the negatively charged electrons did spatially separated from the positively charged plume particles because of their much higher velocity [246].

As soon as target material evaporates, i.e., forms an ablation plume, the incident laser beam interacts with it. When a metal is ablated by nanosecond laser pulses a plasma of evaporated material is produced when the laser fluence is larger than about 2 J/cm². Above this threshold, there exists a significant amount of ionized particles in the vapor by which a mentionable amount of energy is absorbed. This results in the formation of a plasma above the target surface that can even shield the target from further laser irradiation at higher fluences [246,250].

When laser ablation happens in a gaseous atmosphere instead of vacuum, the rate of collisions among the plume particles reduces with further progressing plume expansion since collisions with the ambient gas become more probable. These collisions dominate over collisions of plume particles at the later stage when the plume expanded to several centimeters [246]. Besides a deceleration of the plume particles, here, cooling of ablated target material is effective. Consequently, clusters of ablated target material can aggregate, where the heat due to aggregation is again taken away by the ambient buffer gas. When the plume particles are decelerated to a velocity that allows them to drift with the stream of buffer gas the resulting plume particles are taken away from the aggregation zone. This technique is called pulsed laser – buffer gas condensation (PL-BGC).

The growth of clusters is a complex process, see, e.g., References [110,111] for classical nucleation theory. Nuclei have to form on the one hand, while the clusters have to grow to a desired size on the other. These processes are competing with each other since both of them consume vapor particles [246]. The parameter with the highest influence is the cooling speed of the particles forming the ablation plume. Variation of growth can be achieved by regulating the ambient buffer gas pressure, or by changing its type or composition in case it is a mixture of gases, but also by changing the amount of ablated material via changing the laser power or even the laser spot size on the ablation target by (de)focusing the beam [246].

6.2   Pulsed Laser – Buffer Gas Condensation Setup

The PL-BGC setup designed and constructed in this thesis is illustrated by its digital CAD twin (created with Autodesk Inventor) in Figure 6-2. It consists of a laser setup, a UHV source chamber, a beam selection, a Faraday cup, and a separately pumped chamber that can be disconnected from the source chamber by means of a gate valve. The latter chamber is currently only meant to be used for the collection of beam particles by means of an inserted sample. The PL-BGC setup is installed on an optical table (Newport RS2000-48-12) with a 4.8 m × 1.2 m measuring table top. The table top comes with an array of M6 threaded holes, which is used to fix all the components to the table. The damping function of the stabilizers (Newport S-2000A-416) is not used. Two photographs of the real setup are attached in Appendix E, see Figure E-1.

A laser beam enters the source chamber from the left-hand side. Applying laser ablation, a beam of particles that leaves the source through an exit aperture into the right-hand direction is created. Subsequently, the beam of particles enters the beam section. With the help of a Faraday cup, which can be moved into the beam right behind the beam section assembly, charged beam particles can be detected. The UHV chamber following the beam section is currently only used to move a deposition sample into the nominal path of the particle beam at the end of the setup.

UHV conditions in the two separable vacuum sections of the setup are established by turbomolecular pumps (Pfeiffer HiPace 300 and TMU 261). Each section is equipped with a pressure gauge and so is the (not shown) backing vacuum line that is pumped by a scroll vacuum pump (Leybold Scrollvac SC 5 D). Laser setup, cluster source, and beam section plus Faraday cup are described in the following subsections.
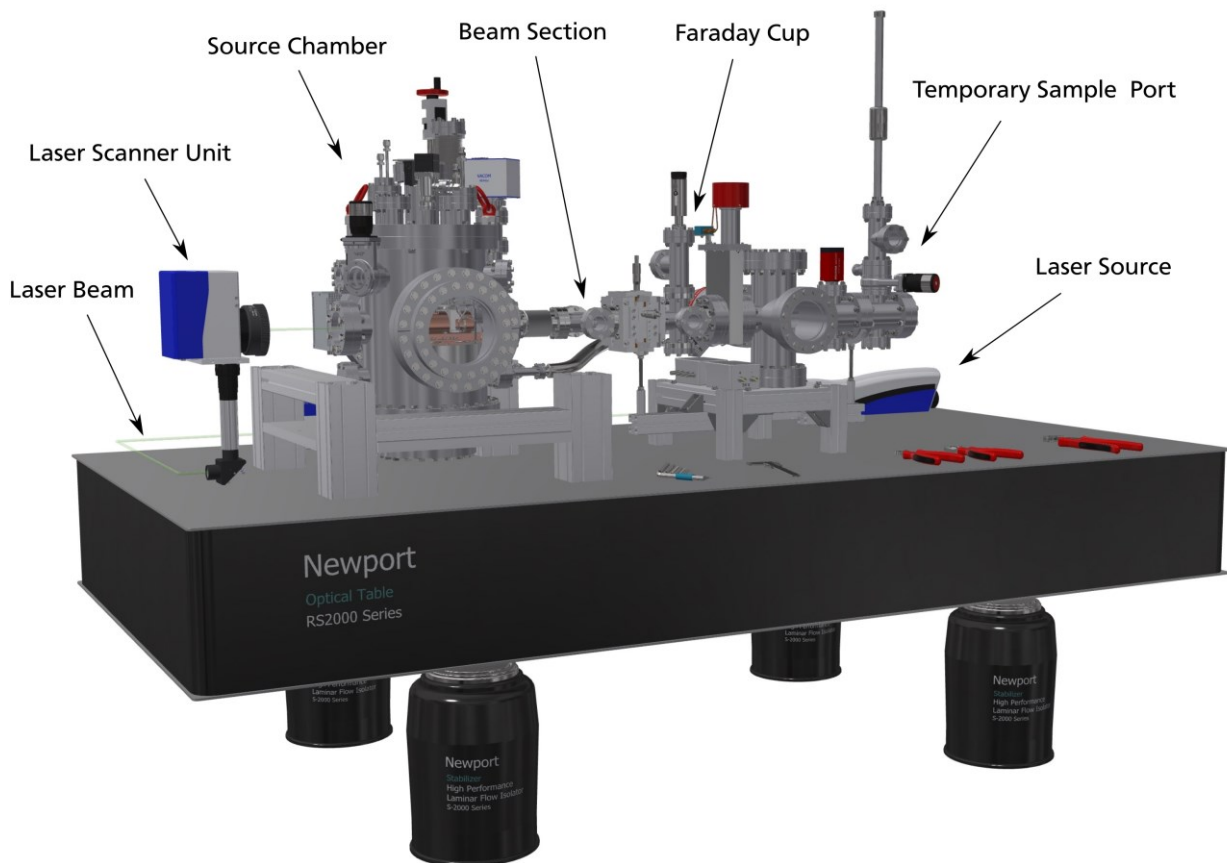
Figure 6-2: CAD Drawing of the PL-BGC Setup

The PL-BGC system is installed on an optical table. An Nd:YAG laser is directed into the UHV source chamber of the system from the left-hand side by means of a laser scanner unit. The beam of particles created in the source chamber is directed towards the right-hand side. It enters the beam section right next to the exit aperture of the source, at the end of which charged particles can be detected with a Faraday cup. The following chamber is currently used to move a deposition sample into the nominal path of the particle beam at the end of the system.

Except the MFC, whose control unit cannot be accessed remotely, and the laser source, because of safety reasons, all electronic components of the PL-BGC setup can be remote operated via RS-232 interfaces. Remote operation is implemented by means of a LabVIEW environment.

6.2.1 Laser Setup

In contrary to the illustrated setup where the laser source is placed into the right-hand corner at the back side of the table, the laser source is located at the left-hand side of the laser scanner unit in the real setup, as depicted correctly in Figure 6-3.

In the used PL-BGC setup, second-harmonic laser light ($\lambda = 532\,\text{nm}$) of a nanosecond pulsed Nd:YAG laser source (Quantel Brilliant with beam attenuator module and second-harmonic generator)

Laser Scanner

$f\theta$-Lens

Beam Attenuator Module

Second-Harmonic Generator

Nd:YAG Laser

Beam Expander

2ω

Brilliant

(Beam Splitter, Power Detector & Beam Shutter)
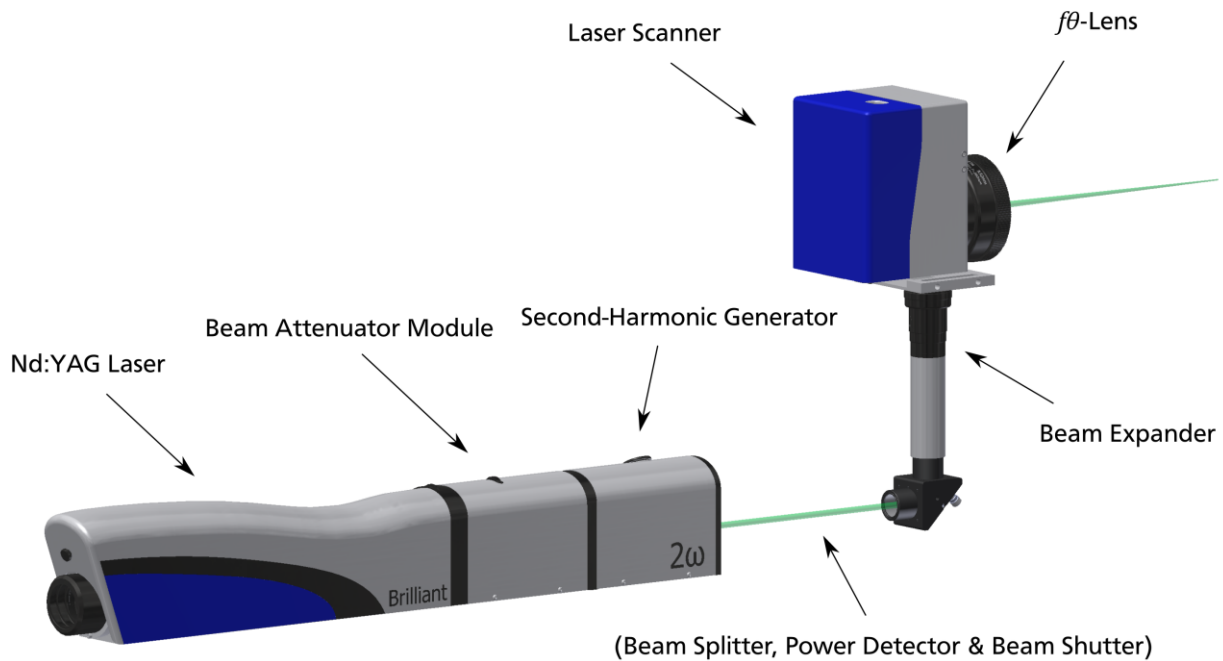
Figure 6-3: CAD Drawing of the Laser Setup

The laser setup consists of a laser source, which itself consists of three elements, and a scanner unit. The laser source consists of a nanosecond pulsed Nd:YAG laser, whose output beam is first attenuated by a corresponding module and then transformed by a second-harmonic generator. The Nd:YAG laser and the modules are installed with tight fitting.

The scanner unit is used to move the laser spot over the surface of the target that is installed inside the aggregation tube of the UHV source chamber. The beam expander is also capable of modifying the divergence of the laser beam. This option can be used to adapt the working distance of the scanner unit to the variable target position, or to explicitly defocus the laser in order to reduce the energy density on the surface of the ablation target.

Between laser source and scanner unit a microscopy slide, applied as a beam splitter, and a beam shutter are installed. The split-off beam is used to continuously monitor the laser power by means of a power meter. Beam splitter, beam shutter, and power sensor are not shown in the drawing.

is used for the ablation of target material. The as-used laser setup is illustrated in Figure 6-3. The real laser setup is completely confined in a laser housing. Operated at a repetition rate of 50 Hz, the laser source has a FWHM pulse duration of 5 ns and a nominal maximum energy of 65 mJ per pulse. The working principle of the used laser is reviewed separately in Section 6.2.1.1.

To continuously measure the output laser power, the laser beam is split by a microscopy slide. The deflected part of the beam is directed towards a thermopile power detector (Gentec UP19K-30H-VR-D0, read out by a Gentec Maestro), while the transmitted beam is used for the ablation of target material. Calibration measurements yielded that the power of the transmitted beam is 4.7 times larger than the power of the deflected beam. Microscopy slide and power detector are not included in Figure 6-3 and so is a beam shutter (Thorlabs SH05) that is located right behind the microscopy slide.

The PL-BGC setup has its ablation target installed at a fixed position, hence, the laser beam has to be scanned across the target in order to evenly ablate material from its surface. The installed deflection unit (Raylase Superscan II-15) is equipped with a non-telecentric $f\theta$-lens (Sill Optics S4LFT3260/121 with an appropriate spacer ring) that offers a scan field diameter of 162 mm at a working distance of 325.5 mm and a zoom beam expander (Sill Optics S6EXZ5311-328). The latter offers the opportunity to change the divergence of the laser beam. This way, the working distance of the setup can be adapted to varying target positions, or to explicitly defocus the laser beam in order to reduce the energy density of the laser beam at the surface of the target.

The deflected laser beam enters the UHV source chamber via a DN 63 CF laser transmission viewport and the aggregation chamber of the source via a high-transmittance laser windows, see Figure 6-6.

During sample preparation a maximum possible power of 120 mW was recorded with the power detector. However, the samples presented here were prepared at measured laser powers of about 90 mW. With the splitting ratio of the microscopy slide given above this calculates to a maximum laser spot diameter on the target with a diameter of 0.7 mm in order to reach the threshold fluence calculated in Section 6.1. The minimum possible spot size observed in calibration experiments with a piece of thermal paper was 0.1 mm.

6.2.1.1 Working Principle of the Installed Nd:YAG-Laser

Besides the manuals of the installed laser source, the textbooks by M. W. Sigrist [256], Stafe et al. [246], and H. Sun [257] were consulted for the brief review given here.

The Quantel Brilliant uses yttrium-aluminum-garnet ($Y_3Al_5O_{12}$, YAG) as host crystal. In an Nd:YAG crystal typically about 1% of the Y sites are occupied by Nd^{3+} dopant ions, which are the laser-active component of the crystal. The Nd:YAG laser is a four-level laser, where the ground state of the Nd^{3+} ion is $^4I_{9/2}$. From this state the Nd^{3+} ions are excited to mainly $^4F_{5/2}$, $^2H_{9/2}$, $^4S_{3/2}$, and $^4F_{7/2}$ states, absorbing light in the 700 nm and 800 nm ranges of wavelength. The excited ions relax to a $^4F_{3/2}$ excited state via quick nonradiative transitions. With its long lifetime of 240 µs the $^4F_{3/2}$ state forms the upper laser level of the Nd:YAG crystal. The majority of excited ions, about 60%, relax to an $^4F_{5/2}$ state under the emission of a photon with the well-known primary wavelength of 1064 nm. The coupling of this lower laser level to the ground state is again via quick nonradiative transitions.

The optical pumping inducing the occupation inversion that is required to make the stimulated emission dominate the relaxation of the excited Nd^{3+} ions is performed by a pulsed Xe flash lamp. A too early start of stimulated emission is prohibited by an electro-optical quality switch consisting of a polarizer, a Pockels cell, and a $\lambda/4$-plate. The quality switch is kept in the low quality factor state when the laser crystal is pumped by the flash lamp in order to maximize occupation inversion. In this state,

light passing the polarizer in the direction from the Nd:YAG crystal towards the back side mirror of the laser resonator is linearly polarized by this very element. Then, the Pockels cell and the $\lambda/4$-plate cooperatively rotate the polarization of the photons by $\pi/2$ before the reflected beam reaches the polarizer again on its way back. Consequently, the photons cannot pass the polarizer and, hence, cannot trigger stimulated emissions in the crystal. The fully reflecting mirror is installed at the back side of the laser resonator while a graded reflectivity output mirror is installed at its front side.

The birefringence of the crystal inside the Pockels cell can be changed by a voltage that is applied to it, i.e., the voltage can be set to a value so that the resulting polarization is oriented exactly parallel to the direction required for maximum transmission through the polarizer. Nanosecond electronics ensure that the switching happens within a few nanoseconds only. When switched to the high quality factor state, light emitted from the Nd:YAG crystal starts to resonate in the laser cavity. Now, the excited Nd^{3+} ions relax via stimulated emission of radiation within nanoseconds and generate a very intense pulse of laser light.

The time delay between firing the gas discharge in the Xe flash lamp for pumping purposes and the quality switching in order to trigger laser activity were carefully tuned from factory side. Hence, the Nd:YAG laser itself runs always at maximum power output. To control the output energy of the laser source without changing neither the pulse length nor the quality switch timing, the Brilliant is equipped with a beam attenuator module. The module consists of a rotatable $\lambda/2$-plate, which is located between two fixed polarizers. The rotatable $\lambda/2$-plate tilts the direction of the linear polarization of the laser beam such that it exactly matches the direction of the second polarizer for maximum transmissivity, or that it arrives with the polarization tilted by $\pi/2$ for zero transmissivity. The beam fractions deflected by the polarizers are absorbed by beam dumps.

Finally, a second-harmonic generator transforms a fraction of the infrared primary laser light into light of half the wavelength, i.e., 532 nm. Remnant radiation of 1064 nm is absorbed by a beam dump; only second-harmonic laser light leaves the laser source.

6.2.2 Cluster Source Setup

The in-vacuum components of the laser ablation source, in particular, the aggregation chamber (AC), are installed on the top face of a UHV-compatible LN_2 tank, which is referred to as component (a) in Figure 6-4(a). As graph (a) shows, the inside of the source chamber is constructed in a hanging way: The whole assembly is attached to a DN 250 CF multiport flange. This flange forms both the base of the in-vacuum constructions and the top flange of the accordingly sized UHV chamber, see Figure 6-2. In particular, the LN_2 tank (a) is connected to a stainless steel adapter plate (b) via four M4

(a)

(h)

(g)

(e)

(k)

(d)

(c)

(f)

(l)

(i)

(j)

(b)

(a)
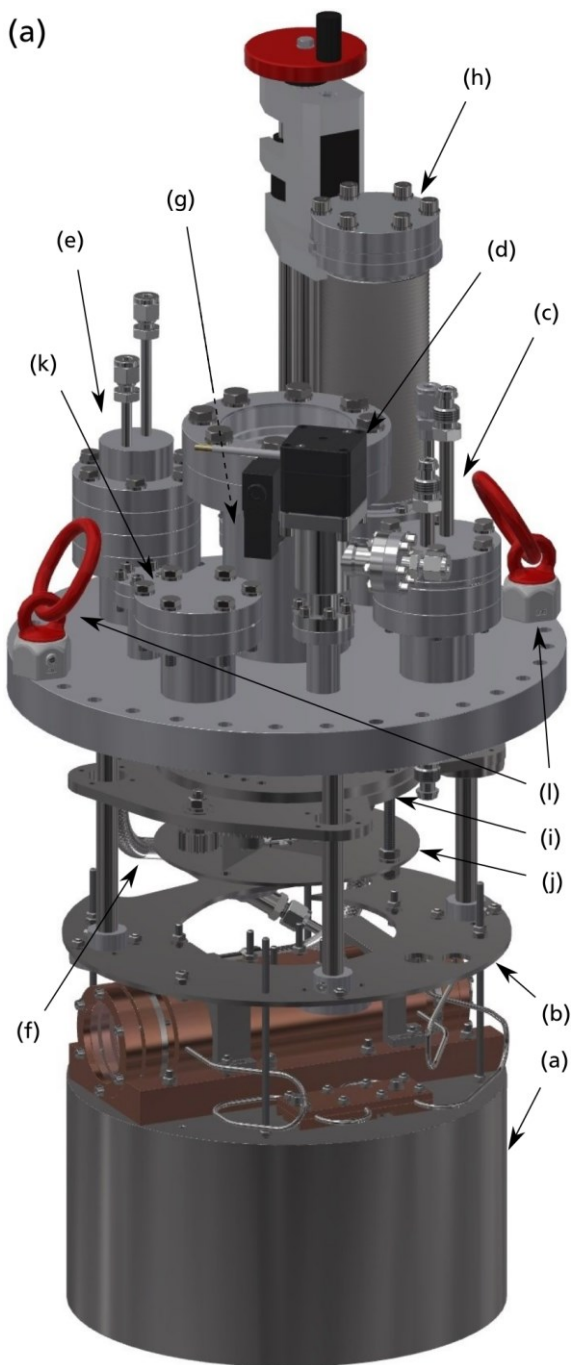
Figure 6-4: CAD Drawings of the Cluster Source Assembly

(a) Source chamber assembly.

(b) Vacuum parts of the laser ablation source.

See text for detailed descriptions of the labeled components.

All in-vacuum parts are attached to the top flange in a hanging way; the LN_2 storage tank with the AC sitting on its top form the lowest element. The top flange assembly can be lifted out of the source chamber, hence, it can be accessed from all sides when outside. Moreover, the hanging construction reduces mechanical stress due to thermal contraction when cooled with LN_2.

(b)

(c)

(e)

(f)

(d)

(b)

(a)
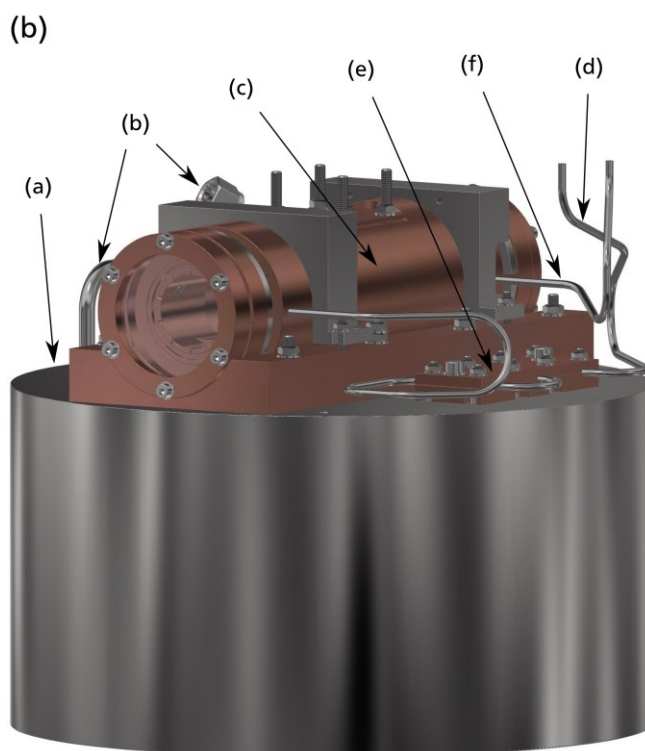
threaded rods. This way, the source can be easily aligned horizontally. The adapter plate, in turn, is connected to the base flange via four rods.

The base flange provides nine CF ports: Four DN 16 CF and four DN 40 CF ports are welded to the base plate flange in an alternating order around a central DN 63 sized one (one port every 45°). One of the DN 40 CF ports is equipped with a double tube fluid feedthrough (c) that is used to supply buffer gas via one of the tubes and for gauging the static pressure in the cavity of the AC via the other. For the latter purpose, an absolute capacitance manometer with 100 mbar full scale pressure range

(MKS Baratron Type AA02A12MCDS44B000000 with MKS Type 651C pressure controller) is installed to the second tube (not shown). Also, the second tube is connected to the source chamber vacuum via a UHV angle valve (d) (VAT 28424-GE41) flanged to the neighboring front side DN 16 CF port. Another double tube fluid feedthrough (e), in this case a thermally insulated one, is used to connect the in-vacuum tubing of the LN_2 tank with the outside. The in-vacuum coolant tubing (f) is made of flexible hoses (Swagelok FJ series), which can be identified at the back side of the CAD model illustrated graph (a). Flexible tubing was chosen in order to reduce the mechanical stress on the LN_2 tank, especially the thermally caused stress present when the source is cooled to the temperature off LN_2. Last, a feedthrough for two type K thermocouples (g) is installed at the DN 16 CF port located at the back side of the base flange. The two connected thermocouples, their positions of sensing are given later, are connected to a LabJack U6 for temperature calculation and computer-assisted readout.

The central DN 63 CF port is sealed with a viewport, a third DN 40 CF port is equipped with a linear shift mechanism (h), which is connected to components (i) and (j). (i) is the base plate of a sample carousel and (j) is its bottom plate. Rotation of the sample carousel located between components (i) and (j) is transduced via a rotary feedthrough (not shown) installed at the remaining DN 40 CF port (k), which is sealed by a blank flange in graph (a). Components (h)–(k) are relics of a previous version of the setup and are not discussed further. The remaining two DN 16 CF ports are sealed with blank flanges.

Two rotatable lifting points (l) are screwed into threaded holes of the base flange. With the help of these, the entire in-vacuum assembly can be lifted out of the vacuum chamber with a chain hoist for maintenance and construction purposes. A Viton® gasket is used between the source chamber and the base flange.

The UHV chamber containing the source assembly, see Figure 6-2, offers various side ports. Referring to the orientation of the model as depicted in Figure 6-2, these are two DN 63 CF ports, one at the left-hand and one at the right-hand side, and two DN 160 CF ports, one at the front and one at the back side. A laser window is flanged onto the left-hand side one, the right-hand side port is the one the particle beam is directed into. It is reduced to size DN 40. The parts that are installed beyond this port belong to the beam section and are discussed in Section 6.2.3. Front and back side flanges are reduced to size DN 100. A viewport seals the front side of the chamber, to its back side the HiPace 300 is installed. Last, a pressure gauge is installed to one of the eight additional DN 40 CF side ports.

Figure 6-4(b) displays the in-vacuum parts of the laser ablation source, i.e., the LN_2 tank and the AC. The LN_2 tank (a) consists of a bottom plate, a sheet that is bended to a tube in order to form the side wall, and a top plate. These three components are made of stainless steel and are connected by welding seams. Bottom plate and side wall have a thickness of 2 mm each, while the top plate is made of 8 mm thick stainless steel since it is a load-bearing component. The LN_2 tank contains ten Cu pillars that are
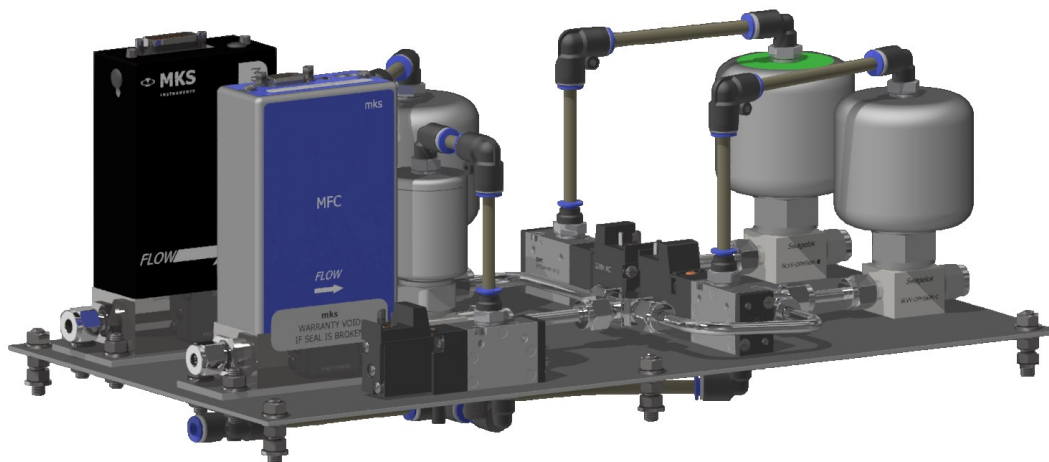
Figure 6-5: CAD Drawing of the Buffer Gas Board

Both MFCs are equipped with a downstream shut-off valve. Two other control valves regulate whether the MFCs are connected to the backing vacuum (on idle) or to the buffer gas feeding line (during operation). So far, only the black MFC has been in use.

pressed against the inner side of the top plate by screwed connections. When the tank is filled, the pillars are immersed in LN_2 and, this way, guarantee excellent thermal contact between the top plate and the cooling fluid for several hours without refilling. The tank is filled via one of the coolant tubing lines (b) hidden behind the AC assembly (c), while exhaust gas is released via the other. The AC is discussed separately in the context of Figure 6-6.

Besides the M4 threaded rods and the coolant tubing lines that are actively cooled by exhaust gas, the AC is in thermal contact with the outside only via the buffer gas tubing and two thermocouples. To prohibit a direct transfer of heat to the AC, the buffer gas feeding line (d) meanders through a Cu made cooling block (e) that is attached to the cooled surface of the LN_2 tank. This measure is not taken for the second buffer gas tubing line (f), which is only used to gauge the pressure present in the AC. Hence, there is no transfer of heat due to gas flow via this line. Another source of heating is, of course, the laser beam.

The delivery of buffer gas to the AC via the feeding line is managed by the 'buffer gas board' illustrated in Figure 6-5. It is equipped with two MFCs (MKS Mass-Flo Controller Type 1179A11CW3BV, black, 10 sccm maximum N_2 flow, with MKS Type 247D four-channel readout; and MKS GV50A013500M5V020, blue, 5 sccm maximum N_2 flow, each with a downstream shut-off valve). Both Ar and He (Air Liquide, N6 Purity) are available as buffer gas. Since the RS485 connection to the GV50A has not yet been set up, currently, only the 1179A can be used, i.e., either Ar or He but no mixtures can
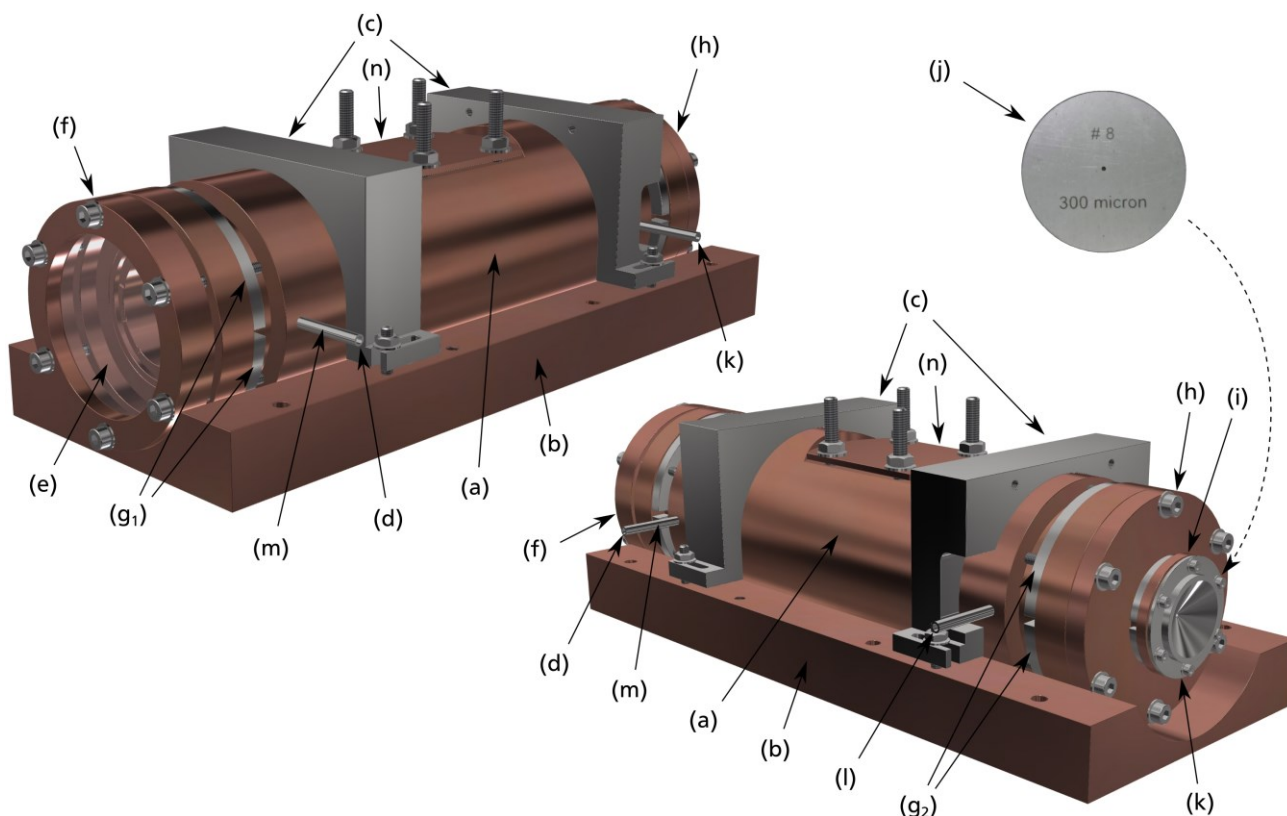
Figure 6-6: CAD Drawings of the AC Assembly

A high-transmittance laser window seals the left-hand side of the AC. It is pressed onto the Cu made AC with a Cu ring element. The right-hand side is closed with a Cu cap that carries the nozzle plate through which aggregated particles and buffer gas leave the AC. The cylindrical AC is pressed onto a Cu made base element, which, in turn, is tightened onto the top of the LN_2 tank. Specific information on components (a)–(n) is given in the text.

be delivered to the AC. The gas correction factor to be used with the 1179A by the four-channel controller is set to that of Ar; the maximum possible flow of Ar gas is 14.9 sccm. The MFCs are connected to the backing vacuum when the setup is on idle and to the buffer gas feeding line when it is operating. The switching is performed by the two control valves on the right-hand side of the buffer gas board.

The central component of the source chamber, the Cu made AC, is the hollow cylinder that is mounted onto the LN_2 tank as illustrated in Figure 6-4. It has an outer diameter of about 62 mm, an inner diameter of 40 mm, and a length of about 20 cm. Two detailed views are presented in Figure 6-6. The interior is discussed separately in the context of Figure 6-7.

Since the AC (a) itself is of cylindrical, i.e., round, shape, another Cu made base element (b) supports the AC in order to achieve good thermal contact between the AC and the surface of the LN_2 tank. The base element is tightened to the surface of the LN_2 tank, while the AC is pressed onto the base element by two stainless steel clamps (c). The contact faces between AC, base element, and LN_2 tank are lined with In foil to optimize thermal contact.

Buffer gas is fed into the AC via the 3 mm Swagelok tube (d) that is soldered to the left-hand side of the AC. The laser beam enters the AC from this side as well. Accordingly, a high-transmittance laser window (e) is pressed against the AC in order to seal it, where In foil was put as gasket between touching faces. In the same turn, the In foil protects the laser window from taking damage due to being pressed against the AC. A Cu made ring element (f) is carefully tightened via six M4 screws that are screwed into two stainless steel half rings with threaded bore holes (g_1), working as plate nuts. The laser window is wrapped with PTFE tape from this side to protect it from taking damage.

A similar design was chosen for the back side cap (h) that seals the right-hand side of the AC. On this side, a blank-flange-like Cu cap is extended to the outside in order to form a port (i) to which a nozzle plate (j) can be installed. For this reason, the cap has a hole drilled through its center. To be explicit, the functional components (h) and (i) belong to one and the same piece, the back side cap. The back side cap is tightened to the AC with another pair of half ring plate nuts (g_2).

A nozzle plate requires a diameter of about 10 mm in order to fit inside the port. The one depicted in Figure 6-6 is made of stainless steel and has a circular hole with a diameter of ~300 μm drilled through its center. A nozzle plate is pressed against the port from the outside by a stainless steel nozzle cap (k). The cap has a hole drilled through its center as well. Tightening of the nozzle cap is again performed by six screws, now M1.6 sized, that are screwed into two half ring plate nuts. Again, In foil is used as gasket between Cu back side cap and AC, and back side cap and nozzle plate.

In order to precisely align the holes of the nozzle and the nozzle cap, the complete back side cap needs to be dismounted from the AC. Moreover, the design allows to use various nozzles of different materials and with different thicknesses. In the present thesis, nozzles made of thin stainless steel sheet and nozzles made of ~1 mm thick PTFE sheet were fabricated and tested. PTFE was chosen as an alternative nozzle material because of its antiadhesive property. Metal-made nozzles had a tendency to get cloaked during ablation experiments.

When thin stainless steel nozzle plates are used, an M6 washer needs to be added as a spacer element. The stainless steel made nozzle plates were cut with the picosecond infrared laser mentioned earlier, the PTFE ones were cut from a larger sheet and the holes were machined with fine drill bits.

A second 3 mm Swagelok tube (l) is soldered to the right-hand side of the AC. It is connected to the pressure gauge located outside of the UHV chamber, see text above. Currently, there is no gas flow through this tube, however, it may be used to reduce the flow through the nozzle by releasing gas from the AC through this tube via a regulation valve to the backing vacuum. This way, buffer gas pressure and buffer gas flow through the nozzle would be decoupled.
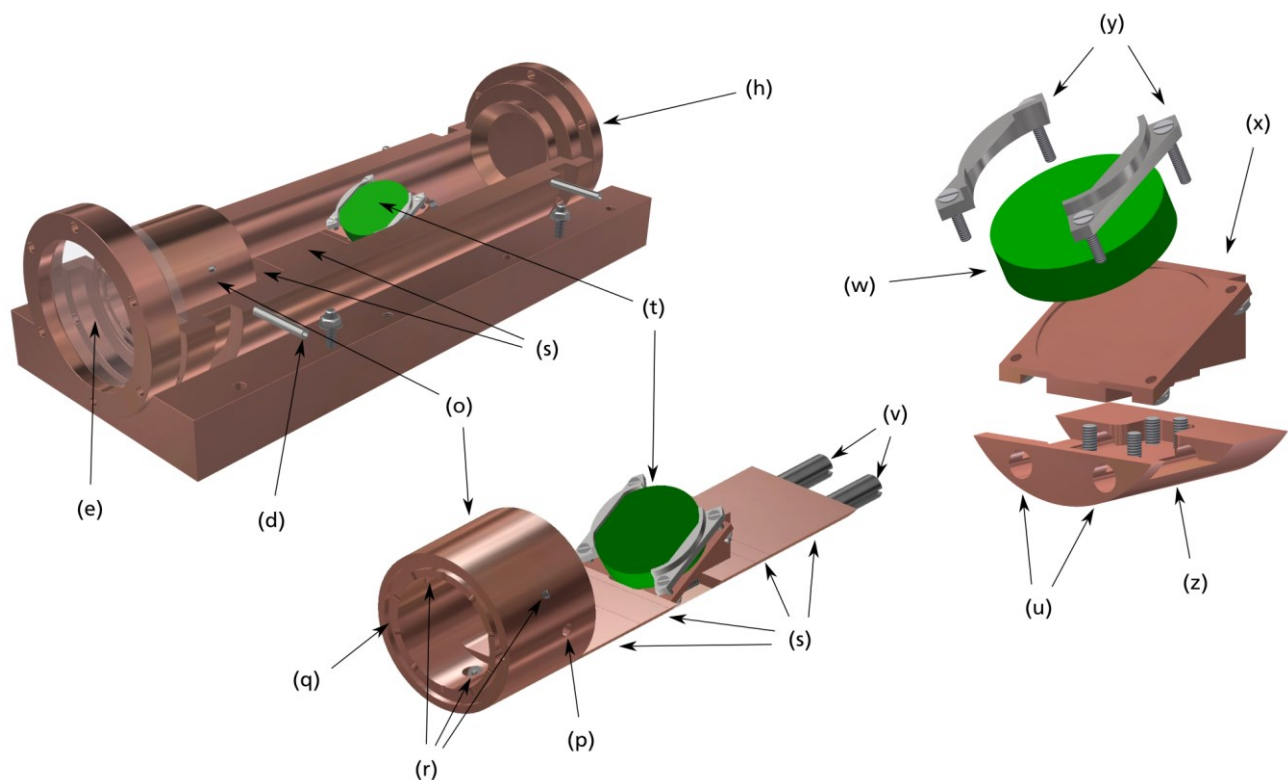
Figure 6-7: CAD Drawings of the Components Inside the AC

The first element of the inside assembly is the shower head sitting right behind the laser window. It is the only part that is anchored in the AC. All other parts, the spacer elements and the target holder, are pushed against it. Specific information on components (o)–(z) is given in the text.

The temperature of the source is measured using two type K thermocouples. One of them is fixed to the buffer gas inlet tube with adhesive Kapton® tape close to the AC cylinder; the position is indexed by (m) in Figure 6-6. The second thermocouple is attached to the top face of the LN$_2$ tank at the back side of the AC. The top side cap of the AC (n) with the four threaded rods seals a top side nozzle port of the AC, which is another relict of a previous version of the setup.

Last, the interior of the AC illustrated in Figure 6-7 is discussed. There, the indexing used in Figure 6-6 is continued. The indexing of buffer gas inlet (d), laser window (e), and back side cap (h) are repeated to clarify the orientation of the internal components with respect to the parts that are visible from the outside, i.e., in Figure 6-6. To access the internal parts, i.e., the ablation target holder, the nozzle cap has to be dismounted.

The first, leftmost component (o) that is installed in the cavity of the AC fulfills two purposes. Its shape is based on that of a cylinder shell. A construction drawing of this complicated part is attached in Appendix E, see Figure E-2. First, this component releases the buffer gas that enters the AC via inlet tube (d) into the AC. To do so, the incoming buffer gas is collected by the part with a bore hole (p) that

is drilled from the outside wall in radial direction. This hole does not penetrate the complete wall but connects the inlet tube (d) to another bore hole that is drilled into the shell of the cylinder from the laser window side, i.e., the front side (q) of the part. The so created pipe guides the buffer gas to the front face of the cylinder shell. There, the buffer gas streams into a ring-shaped groove in the front face of the cylinder shell. This groove resembles a ring tube since the front face of the part is in touch with the laser window. Finally, the buffer gas is released from this distribution ring into the AC via ten equally spaced openings, this way forming a shower head. Secondly, this first component is the only component that is in fix contact with the AC. It is kept in position by three set screws that penetrate the cylinder shell at positions (r) and that push against the inner wall of the AC when tightened. The corresponding screw holes are drilled under an angle so that the set screws can be accessed from the laser window side.

All other components that are installed inside the AC, the spacer elements (s) and the target holder (t), are slid into the AC guided by two of threaded rods that are screwed into the back side of the anchored shower head (o). The parts provide two correspondingly drilled holes (u). One cylinders with a female thread (v) on each rod pushes the inserted elements against the anchored shower head. This way, the position of the target holder (t) can be varied. With the available spacer elements, the target holder can be installed in steps of 5 mm away from the anchored shower head. All elements have to be inserted, otherwise, the assembly cannot be tightened from the back side in the way explained above. All components are in good thermal contact with the AC.

The depicted target holder (t) is used to install a 1″ ablation target (w) in a tilted way. To do so, the target is pressed onto a wedge (x) by two clamps (y). The construction is carried by a sleigh (z) that is slid onto the threaded rods just like the spacer elements are. Photographs of the target holder are presented in Figures 6-8(a),(b). There, the ablation areas the laser was scanned across are clearly visible.

When installed in a tilted way, the plume of ablated target material is directed towards the inner wall of the AC rather than the laser window. The advantage is a reduced pollution of the laser window and that the laser beam is not reflected back into the direction of incidence, i.e., into the optical setup. However, the volume into which the ablation plume expands is limited by the wall of the AC.

The assembly can also be used to bring preformed clusters into a gaseous atmosphere inside the AC by thermal activation. To do so, a glass substrate that carries the preformed clusters is installed onto the wedge, where a piece of Cu (here, the available Cu target) is needed to put the glass substrate to the distance required by the target clamps in order to fix the ablation target.

Alternatively, an ablation target can be installed standing upright, i.e., with the ablation surface directed towards the laser window. To do so, the ablation target is clamped between two spacer

(a)

(b)

(c)
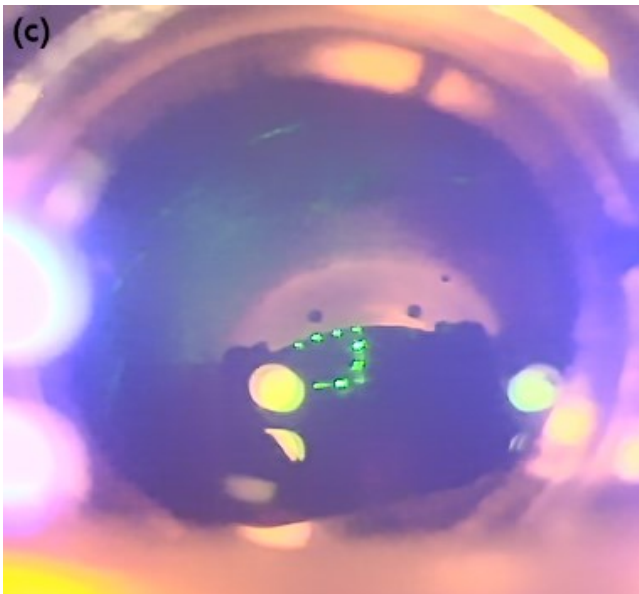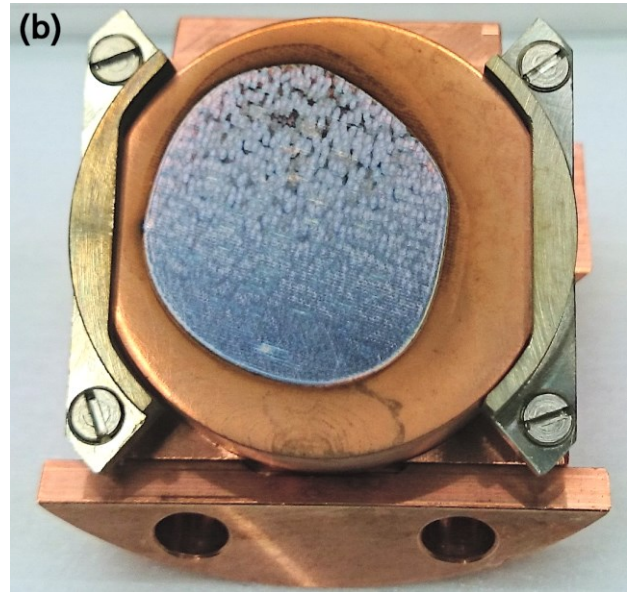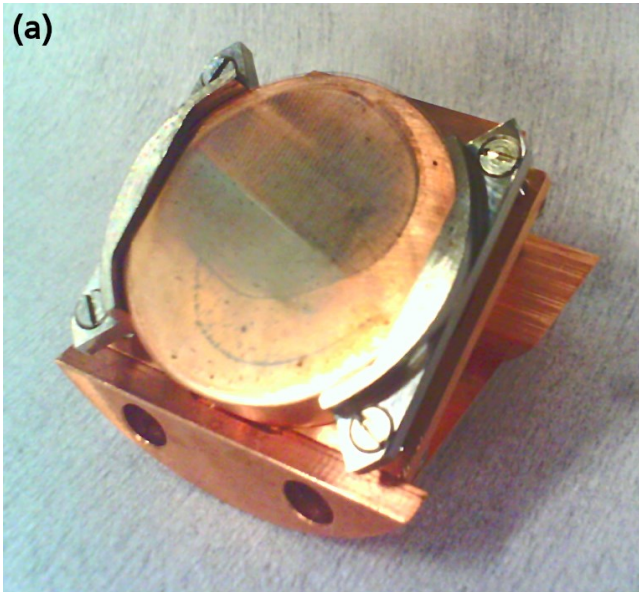
Figure 6-8: Photographs of the Ablation Target Holder

(a) Side view, where a glass substrate carrying preformed clusters is installed as target.
(b) Front view. Here, a Cu target is installed.
(c) Photograph of the interior of the AC, taken with the installed webcam.

In images (a) and (b) the area the laser was scanned across is clearly visible.

In Image (c) the target holder appears almost black but can be easily identified by its silhouette. The green laser spot is scanned along the upper left edge of the target for testing purposes. Multiple laser spots are visible because of the slow repetition rate of the installed webcam.

elements. Furthermore, to optimize the gas flow through the AC, holes can be drilled through the center of an installed target.

In either way, the area the laser is to be scanned across has to be manually defined within the laser scanner software (Raylase weldMARK 3D). To see at least parts of the interior of the AC, i.e., the laser spot on the target, a webcam is installed between laser scanner and CF laser window. Using the view provided by this webcam the edges of the installed target can be translated into laser scanner coordinates by moving the laser spot step by step across the surface of the target. A webcam image of the laser spot following the upper left edge of the target for testing purposes is presented in Figure 6-8(c).

6.2.3 Beam Section

As mentioned in the introduction of Section 6.2, the beam of particles is directed into the right-hand side DN 63 CF side port of the UHV source chamber. Here, the beam section branches off. Accordingly, the beam propagates to the right-hand side. A CAD image of the in-vacuum assembly of the beam section is illustrated in Figure 6-9. A detailed description of the parts is given in Appendix F, where also the steps of assembly of the beam section are reviewed. Furthermore, a photograph that demonstrates the size of the assembly, Figure F-1, is shown.

In brief, the assembly consists of a shielding plate (y) and a skimmer (x) on its left-hand side. The particle beam enters the section through the latter. In the following, tube-like parts (w$_2$,w$_1$,g,o,s) surround the particle beam and shield it from ground potential all the way through the section, except at about the middle of the section, where a capacitor unit (f,i,k) is installed. The capacitor unit can be used to deflect charged beam particles. All parts are installed to a framework (a,b,c,e,r) that is fixed to the DN 40 CF 4-way cross carrying most of the assembly. Last, a Faraday cup (parts (1)–(8), only discussed in Appendix F, not shown in Figure 6-9) can be moved into the path of the beam right behind tube (s).

In the following, the principle of operation of the beam section is explained. As stated in Section 6.1, most of the particles in a laser ablation plume are uncharged. Consequently, most of them are still neutral when they leave the AC through the nozzle plate. For this reason, the PL-BGC setup was designed to deposit particles from a neutral beam. Nonetheless, the net charge of the beam particles has to be different from zero in order to monitor the intensity of the beam by means of the installed Faraday cup. The corresponding electronics, consisting of a picoampere meter (Keithley 6485) and a battery pack ($\pm$52 V) just as used in the CIBD system, can also be connected to the tube assembly of the beam section. In this case, shield (y) and skimmer (x) are functionalized as the electrode the beam current is measured with. In case the beam current is measured with the Faraday cup, a shielding potential is applied to tubes (w$_{12}$,g,o,s), to electrodes (f), and to the outer cup (1) and the connected shielding grid (6) of the Faraday cup by means of a power supply (FuG HCP 35-6500). A second power supply (FuG HCP 35-6500) is used to apply a voltage to the retarding grid of the Faraday cup (7).

To obtain a beam of neutral particles only, one of the electrodes (f) is disconnected from the potential of the tubes and set to a different potential with the second power supply. This way, the charged particles in the beam are deflected from a straight path. Since charged particles only have to be shielded until they reach the Faraday cup no further shielding tubes are installed beyond this point.

Beam particles can be collected at three positions in the setup. The one most far away from the AC is the one inside the last 4-way reducing cross, see 'temporary sample port' in Figure 6-2. There,
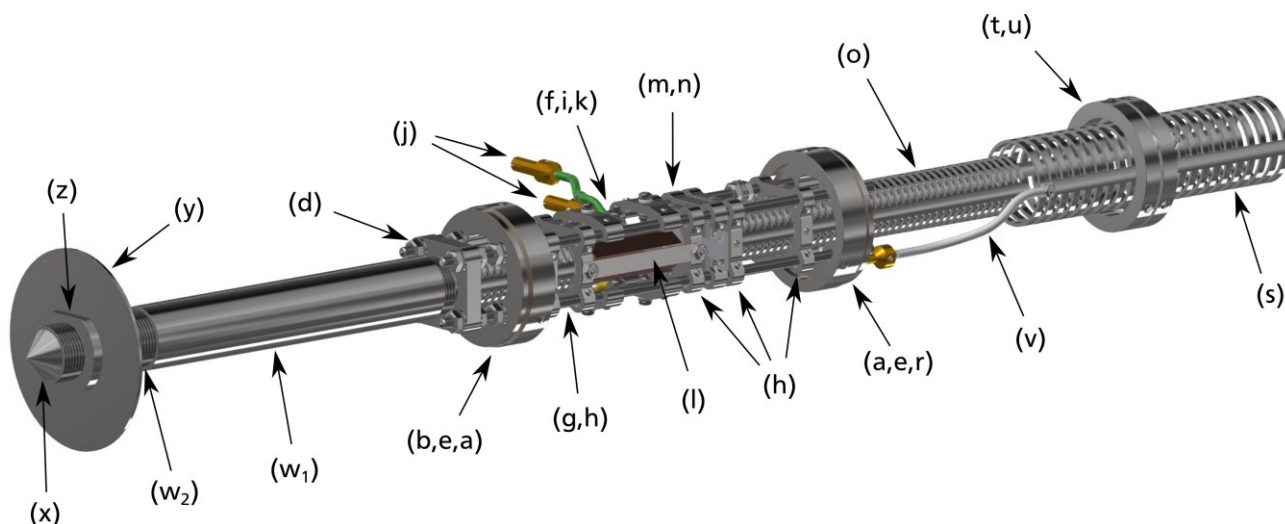
Figure 6-9: CAD Drawing of the Beam Section of the PL-BGC

The depicted parts are discussed in detail in the text.

a substrate connected to a sample transfer arm can be inserted into the setup. This option is labeled 'temporary' as no sample holder is installed inside the UHV part. The advantage of this position is that the arm with the attached sample is inserted into a load lock that is first evacuated with the backing pump and then pumped with the second turbomolecular pump before it is connected to the source chamber and beam section vacuum.

The second option is to insert a sheet of metal into the specialized slider (m) onto which a piece of substrate can be fixed with glue. Since the sheet has to be inserted and removed via the front side port of the corresponding 4-way cross, source and beam section have to be vented in case this option is used.

The last option is to remove the skimmer from tube (w_2) and to directly install a piece conducting substrate to its front face. In case this option is chosen, the entire source has to be lifted out of the source chamber. Then, the substrate can be installed through the front port of the UHV source chamber. This option provides the highest yield of collected nanoparticles.

6.3 Test Results

As stated above, gluing a piece of conducting substrate to the front face of tube (w_2) provides the highest yield of deposited beam particles. For this reason, this configuration was chosen for initial ablation tests. Several samples of output material were collected on 2 cm × 2 cm indium tin oxide (ITO)
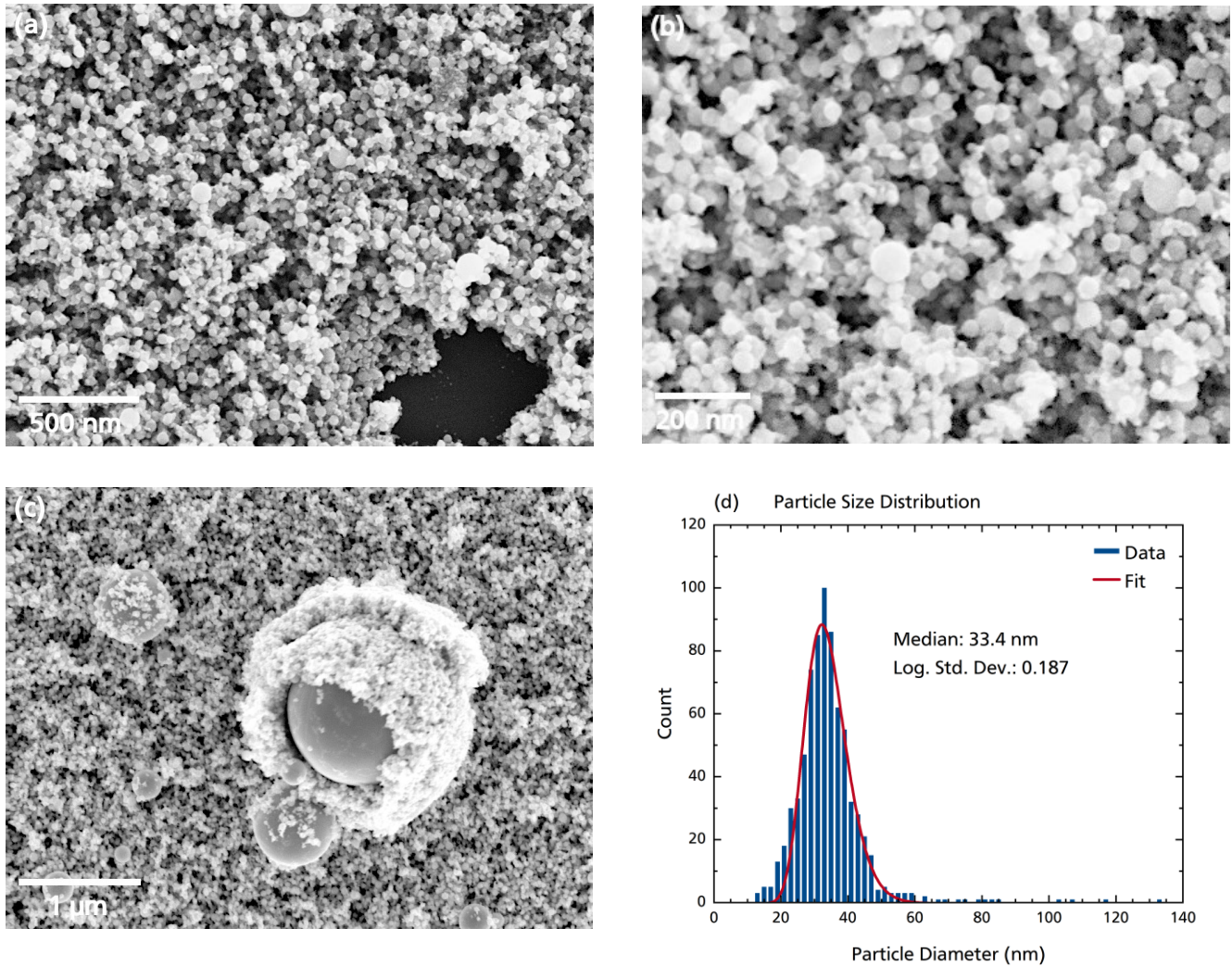
Figure 6-10: SEM Micrographs and Particle Size Distribution of the ITO Test Sample

(a) SEM micrograph of the test sample deposited onto ITO substrate.
(b) Detailed view of a section of graph (a). A spherical shape of the particles is evident.
(c) SEM micrograph that shows the largest particle (~1 µm) detected during analysis. Obviously, it is surrounded by a shell of smaller particles.
(d) Particle size distribution of 747 hand-measured particles of graph (a). Every column represents a 2 nm wide interval. A log-normal distribution function is fitted to the data.

substrates at this deposition option. The samples were then analyzed by means of an SEM. Testing of the other components, e.g., the Faraday cup, had to be postponed indefinitely, in favor of the experiments described in Chapters 4 and 5.

One test sample was deposited with the AC settled at room temperature, where a Ag target was installed standing upright 6 cm behind the shower head (see Figure 6-7). The measured laser power during deposition was 80 W $\pm$ 10 W and 14.9 sccm of Ar buffer gas streamed through the AC in order to cool and carry the ablated material. A PTFE nozzle with a hole diameter of ~400 µm was installed for

this experiment, which led to a pressure of 10.6 mbar in the AC. Output material was collected for 1 h, where the average current recorded with the picoampere meter was +2.5 pA.

SEM micrographs of this sample are depicted in Figures 6-10(a)–(c), where graph (b) provides a detailed view of a section of graph (a). The detailed view allows to easily recognize single particles and proves their spherical shape. Graph (a) was used for a 'by hand' particle size analysis, where 747 particles were measured. The resulting particle size distribution is illustrated in graph (d). Most of the particles have diameters between about 20 nm and 50 nm. The median of the fitted log-normal distribution is ~33 nm. Additionally, a few larger particles are present in the analyzed region; for the largest one a diameter of ~130 nm was measured. The number of small particles, i.e., of particles with diameters of about 20 nm, is assumed to be higher than indicated by the data. The reason is that the resolution limit of the SEM is reached at this length scale so that smaller particles can hardly be identified among the larger candidates from the recorded images. The largest particle found during the analysis is depicted in graph (c). It has a diameter of ~1 μm and is surrounded by a shell of 'regularly sized' particles.

Three more samples using ITO substrate were fabricated under different conditions. To optimize the flow of buffer gas in the AC a conical hole (front side diameter: 12 mm, back side diameter: 6 mm) was drilled through the used Ag target. After this, a different nozzle, made of stainless steel sheet and with a hole diameter of ~500 μm, was installed. Last, the setup was tested with the previously used PTFE nozzle reinstalled and the source being cooled to the temperature of LN_2. The drilled-through Ag target was installed even more far away from the shower head. For this reason, the laser beam was defocused when scanned across the target. Even then, an energy density sufficient for the ablation of target material was achieved. In case of all three samples comparable spots of cluster material were collected substrates.

6.4 Conclusions

A PL-BGC setup based on a nanosecond pulsed Nd:YAG laser source was presented. First, the principles of operation of laser ablation, more precisely, nanosecond pulsed laser ablation in a gaseous atmosphere, and the used Nd:YAG laser were reviewed. Subsequently, the laser setup that makes use of a laser scanner and an $f\theta$-lens was presented.

The PL-BGC setup consists of two main sections: the source section and the beam section. The source section has an AC sitting on a tank that can be filled with LN_2 for cooling purposes as its central element. Material is ablated from a target inside the AC and diluted by buffer gas that enters the AC via a shower

head. The mixture leaves the AC through an exchangeable nozzle. The beam of particles is directed into the beam section.

The in-vacuum assembly of the beam section is designed to measure the intensity of the beam by measuring the current of charged beam particles by means of a picoampere meter. It can be connected to a Faraday cup at the end of the section or to the shielding parts of the assembly in order to obtain a larger signal. Further, a capacitor unit can be applied to deflect charged particles in order to obtain a beam of neutral particles only. The original purpose of the designed setup is to perform matter-wave interference experiments with neutral cluster beams in the future.

In its current state of assembly, substrates can be inserted into the PL-BGC setup at three positions differing in distance from the AC. The one closest to the AC was used to collect output material on ITO substrates. SEM micrographs of one of these samples are presented together with a particle size distribution obtained from one of these graphs. Further, the spherical shape of the beam particles is proven.

More work is required in order to find parameter sets for reliable operation. Also, the setup may require additional components in order to achieve a higher degree of beam control and particle detection. For example, a higher amount of charged particles would increase the signal detected with the picoampere meter. Increasing the amount of charged beam particles may be done by irradiating the beam particles with a laser. Moreover, the setup may require an electrostatic lens setup similar to the CIBD system in order to achieve a collimated beam of ionized particles that can be directed into the Faraday cup. Then, and because of its compact size, it is also thinkable to integrate the setup into or to combine it with an existing deposition system. Another option is to collect aggregated clusters on a substrate in order to serve as target material in a different system where the clusters are brought into the gas phase again.

To perform cluster-based matter-wave interference experiments with the PL-BGC setup, a way to reliably produce clusters that are smaller by about one order of magnitude in size compared to the Ag test depositions discussed in this chapter has to be found. One step into the direction of a higher degree of control is to decouple the pressure in the AC from the applied flow of buffer gas and the hole in the used nozzle plate. This can be achieved by pumping the AC in a controlled way via the tubing that is currently used for pressure gauging only, e.g., by installing an exhaust throttle valve. This would decrease the gas flow through the nozzle and, in the same turn, prevent it from cloaking. Then, nozzles with even smaller openings than currently used may be installed. However, fine but regularly shaped holes through PTFE sheet are hard to fabricate. The use of an exhaust throttle valve would also require larger flows of buffer gas. To be able to also use mixtures of Ar and He as buffer gas, the second, already

installed MFC has to be put into operation. Also, a sample holder to be installed at the end of the beam section has to be developed.

The deposition sample setup to be used for matter-wave interference experiments [51] is quite similar to the one used for nanocomposite depositions (see Section 4.2.2). A piece of Si substrate is kept in place by stainless steel frames, where the number of which is chosen to match the thickness of the framed substrate. Instead of a co-deposition mask, a TEM grid (Plano G2785C) that carries free-standing diffraction obstacles is locked in between stainless steel masks with appropriate circular cutouts at a known distance in front of a substrate. Submicron SiO_2 Stöber particles [258] that are attached to Ag nanowires (Blue Nano, Inc.) serve as diffraction objects. Diffraction patterns are then recorded in form of spatial variations of the amount of material deposited onto the substrate. In particular, a Poisson spot [259–261] is expected to be observed in the centers of the shadows cast by the spherical Stöber particles.

7 Concluding Remarks and Outlook

Several approaches are available for the synthesis of granular nanocomposites. For the case of combining immiscible elements, the simultaneous deposition of these elements or ion implantation are approaches to obtain a granular phase-segregated structure. For the case of two at least partially miscible elements, simultaneous deposition of preformed clusters and matrix material is one strategy to grow nonequilibrium composition films. Ultimate control over composition and concentration is achieved in case of size-selective cluster deposition, which is the approach followed in the present thesis. The employed CIBD system makes use of a sector magnet acting as a mass selector element for the beam of cluster ions to achieve a narrow size distribution of embedded clusters. In particular, cluster-assembled nanocomposite films containing magnetic Fe clusters of 500 ± 50, 1000 ± 100, or 1500 ± 150 atoms were synthesized. These clusters were embedded into amorphous, semiconducting Ge (Fe_{500} and Fe_{1000}) and metallic, crystalline Ag matrices (Fe_{500}, Fe_{1000}, and Fe_{1500}) to create nanocomposite samples for the study of size and concentration dependence of transport and magnetoresistive properties.

Fe-Ge nanocomposite samples with concentrations between $15\,at.\%$ and $83\,at.\%$ of Fe were synthesized. It was found that Ge grows in an amorphous structure under the experimental conditions.

A sample layout consisting of a suitable co-deposition mask and a sample chip layout featuring ten parallel contact lines used to electrically connect the deposited films was developed. From the ten available equidistant contact lines a quadruple of neighboring lines was chosen individually for each sample to contact the deposited nanocomposite films by means of wire bonding in a four-wire configuration. This way, transport and magnetoresistive properties were measured. In addition, SQUID magnetometry, scanning electron microscopy, and EDX elemental analysis were applied to characterize the prepared samples.

A percolation threshold of about $30\,at.\%$ of Fe was observed from resistivity vs. Fe concentration data for the Fe-Ge nanocomposites. Furthermore, absolute and relative resistivity were found to be a function of the average distance between the surfaces of neighboring clusters independent of the size of the deposited clusters. This fact was interpreted as a hint for the existence of tunneling transport. Accordingly, resistivity data of the Fe-Ge samples were analyzed for temperature dependence signatures characteristic for tunneling and VRH transport, where the latter is the type of transport inherent to a-Ge. It can be assumed that generally both types of transport happen in parallel. The domination of tunneling

transport was found to be compatible with the temperature scaling of the resistivity for some samples within certain temperature ranges. Generally, the ratio of tunneling and VRH transport depends on temperature.

In accordance with tunneling transport and the existence of a percolation threshold the low-field magnetoresistive behavior of the Fe-Ge nanocomposites was identified as tunneling magnetoresistance caused by tunneling of electrons between aggregates of superparamagnetic clusters. Seemingly, nanocomposites containing the larger cluster species showed larger tunneling magnetoresistance. In addition, at least one field-dependent magnetoresistance effect that is linear in the examined magnetic field range to good approximation is present in the Fe-Ge nanocomposite films. In sum, the observed magnetoresistance is on the order of 1%. Magnetoresistive behavior is limited to samples below the percolation threshold.

To alter the structure of the Fe-Ge nanocomposite films some of the samples were annealed in vacuum and in 5 vol. % H_2, 95 vol. % Ar atmosphere at 220 °C. The resistivities of these films decreased by about one order of magnitude in this course. The resulting magnetoresistance curves were negative and of the same shape as these recorded from the as-deposited samples. However, the magnetoresistance became less in effect in the temperature range down to at least 40 K. Below 40 K, the magnetoresistance started to strongly increase, in particular, it overcame that of the as-deposited samples and increased to several percent in effect in the examined magnetic field range (± 6 T). The hydrogen gas present during annealing was not found to affect the properties of the annealed nanocomposite films.

One of the Fe-Ge samples was subsequently annealed also at 700 °C in another step. In this course, both the transport and magnetoresistive properties of the sample completely changed. The resistivity of the sample decreased by two more orders of magnitude, and the dependence of its resistivity on temperature became metal-like, i.e., $dR/dT > 0$, for temperatures ≥ 90 K. Below 90 K the resistivity quickly increased by two orders of magnitude with decreasing temperature and exhibited a maximum at about 30 K. The magnetoresistive behavior became positive, anisotropic, and much larger compared to the as-deposited and 220 °C annealed state: The maximum observed magnetoresistance was ~800% (see Figures 4-40(e),(f)).

Furthermore, the Fe cluster species used for the Fe-Ge nanocomposites and clusters consisting of 1500 ± 150 Fe atoms were embedded into Ag matrices with the same CIBD system and analyzed using the same techniques as were used for the research of Fe-Ge nanocomposites. As expected for the Fe-Ag nanocomposite system granular giant magnetoresistance of several percent was observed. The sample chip layout originally developed for Fe-Ge nanocomposite samples was used for the Fe-Ag ones as well. However, it was necessary to multiply correction factors to the recorded absolute resistance data owing to the different four-wire contact point geometries of contact lines and nanocomposite films. For this

reason, the focus of the analysis of the Fe-Ag nanocomposites was on the comparison of relative quantities: magnetoresistance (relative change of resistivity due to a magnetic field) and relative resistivity (relative change of resistivity due to temperature variation). Nevertheless, a dependence of giant magnetoresistance on particle size was revealed. However, no straightforward dependence of magnetotransport properties on neither Fe concentration nor average surface-to-surface distance was observed. This is assigned to the use of the sample chip layout that was designed for four-wire transport measurements of semiconductor-based nanocomposites and that was now used to measure nanocomposites with metallic matrices.

By comparing magnetoresistance and relative resistance data it can be concluded that nanocomposites containing smaller clusters exhibit larger magnetoresistance. The data also indicate that there is an optimum composition of clusters and matrix material at which maximum magnetoresistance is observed. Seemingly, the optimum composition is below 10 at.% of Fe. For future experiments, the evolution of granular giant magnetoresistance with decreasing cluster size would be of great interest: Down to what cluster size does the effect continue to increase, and when does it begin to decrease again?

In addition to the research on Fe-cluster-based nanocomposites a pulsed laser – buffer gas condensation setup was designed and assembled. The setup has been developed to be used for matter-wave diffraction experiments in the future. However, it can also be modified to be used for the growth of cluster-assembled materials. After optimizing the cluster aggregation source of the UHV setup, a beam section was developed, assembled, and installed to the setup. On the one hand, the pulsed laser – buffer gas setup is meant to provide a cluster beam of mostly uncharged particles for deposition. On the other hand, the few percent of charged particles in the beam are crucial for the detection of the particle beam and for measuring its intensity by means of a Faraday cup or, more general, by a conducting electrode that is connected to a picoampere meter. An example sample of aggregated Ag particles indicates that the aggregated particles are of spherical shape and mostly have diameters on the order of 10 nm to 100 nm.

Appendices

Appendix A — PPMS Example Sequences

Below, two example sequences used within the MultiVu software of the PPMS are presented. The example code shown in A.1 produces a $R(T)$ curve, the code in A.2 magnetoresistance curves at various temperatures.

A.1 Resistance vs. Temperature Example Sequence

The following example sequence measures the resistance of the sample connected to *Channel 1* between 300 K and 10 K, where the measurement is divided into three steps (breaks at 100 K and 40 K). Each step comes with a different cooling rate, a different temperature step width (5 K, 2 K, and 1 K, respectively) and different excitation currents.

```
// Example Code

   Scan Temp from 300 K to 100 K at 5 K/min in 41 steps, Uniform, Fast
      Scan Excitation Ch 1 0.050 µA to 0.200 µA, Ch 2 Off, Ch 3 Off, Ch 4 Off
   End Scan

   Scan Temp from 100 K to 40 K at 2 K/min in 31 steps, Uniform, Fast
      Scan Excitation Ch 1 0.020 µA to 0.200 µA, Ch 2 Off, Ch 3 Off, Ch 4 Off
   End Scan

   Scan Temp from 40 K to 10 K at 1 K/min in 31 steps, Uniform, Fast
      Scan Excitation Ch 1 0.010 µA to 0.050 µA, Ch 2 Off, Ch 3 Off, Ch 4 Off
   End Scan
```

A.2 Resistance vs. Magnetic Field Example Sequence

With the following example code magnetoresistance curve data at 300 K, 250 K, 200 K, 150 K, and 100 K are recorded, where the maximum magnetic field is ± 6 T. The measurements start after a delay of 10 min after the set temperature was reached to ensure the sample and the system were in thermal equilibrium. Then, data points are recorded in three different steps from zero to maximum field. Different step widths of the magnetic field were chosen in the different steps in order to record the curves with a higher resolution at lower fields.

The 'Scan Temp' loop also contains the parts completing the field scan loop, i.e., the scan from maximum field to maximum field in reverse direction and back to maximum field. These parts consist of steps similar to the shown ones. They are abbreviated by '[...]' for that reason.

```
// Example Code

  Scan Temp from 300 K to 100 K at 10 K/min in 5 steps, Uniform, Fast
    Wait For Temperature, Delay 600 s, No Action

    Scan Field from 0 Oe to 2000 Oe at 100 Oe/s in 6 steps, Uniform, No O'Shoot, Persistent
      Scan Excitation Ch 1 0.050 µA to 0.200 µA, Ch 2 Off, Ch 3 Off, Ch 4 Off
    End Scan

    Scan Field from 2000 Oe to 20 000 Oe at 100 Oe/s in 10 steps, Uniform, No O'Shoot, Persistent
      Scan Excitation Ch 1 0.050 µA to 0.200 µA, Ch 2 Off, Ch 3 Off, Ch 4 Off
    End Scan

    Scan Field from 20 000 Oe to 60 000 Oe at 100 Oe/s in 10 steps, Uniform, No O'Shoot, Persistent
      Scan Excitation Ch 1 0.050 µA to 0.200 µA, Ch 2 Off, Ch 3 Off, Ch 4 Off
    End Scan

    [...]

    Set Magnetic Field 0 Oe at 100 Oe/s in 5 steps, Oscillate, Persistent
    Wait For Field, Delay 10 s, No Action

  End Scan
```

Appendix B — Fe-Ge Magnetoresistance Curves

Summary of the magnetoresistance curves recorded at 200 K, 100 K, and 40 K of all Fe-Ge samples.
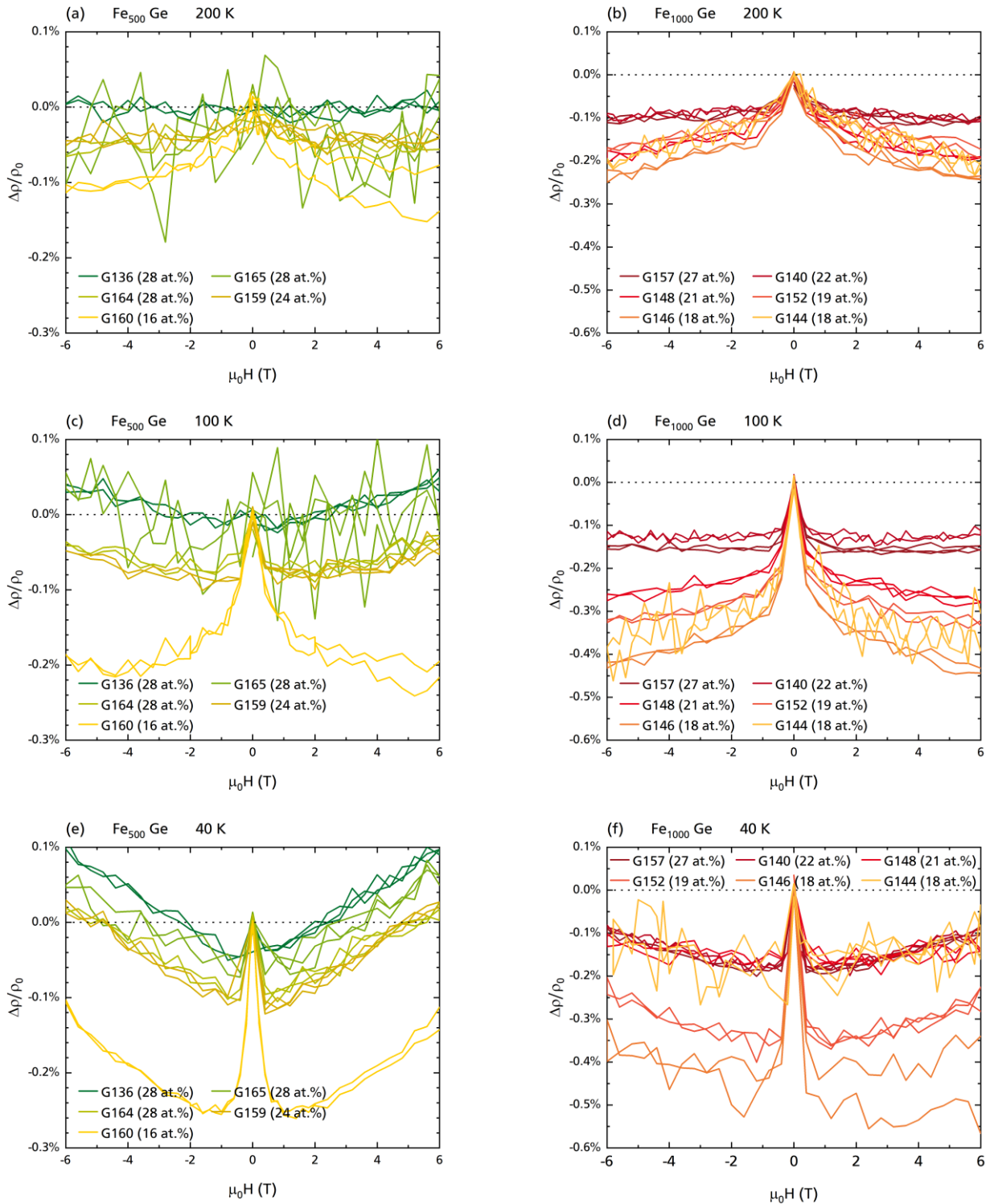
Figure B-1: Comparison of the Magnetoresistance Curves of all Fe-Ge Nanocomposite Samples at 200 K, 100 K, and 40 K

Appendix C — Fe-Ag Magnetoresistance Curves

Summary of the magnetoresistance curves recorded at 200 K, 100 K, 40 K, and 10 K of all Fe$_{500}$-Ag samples.
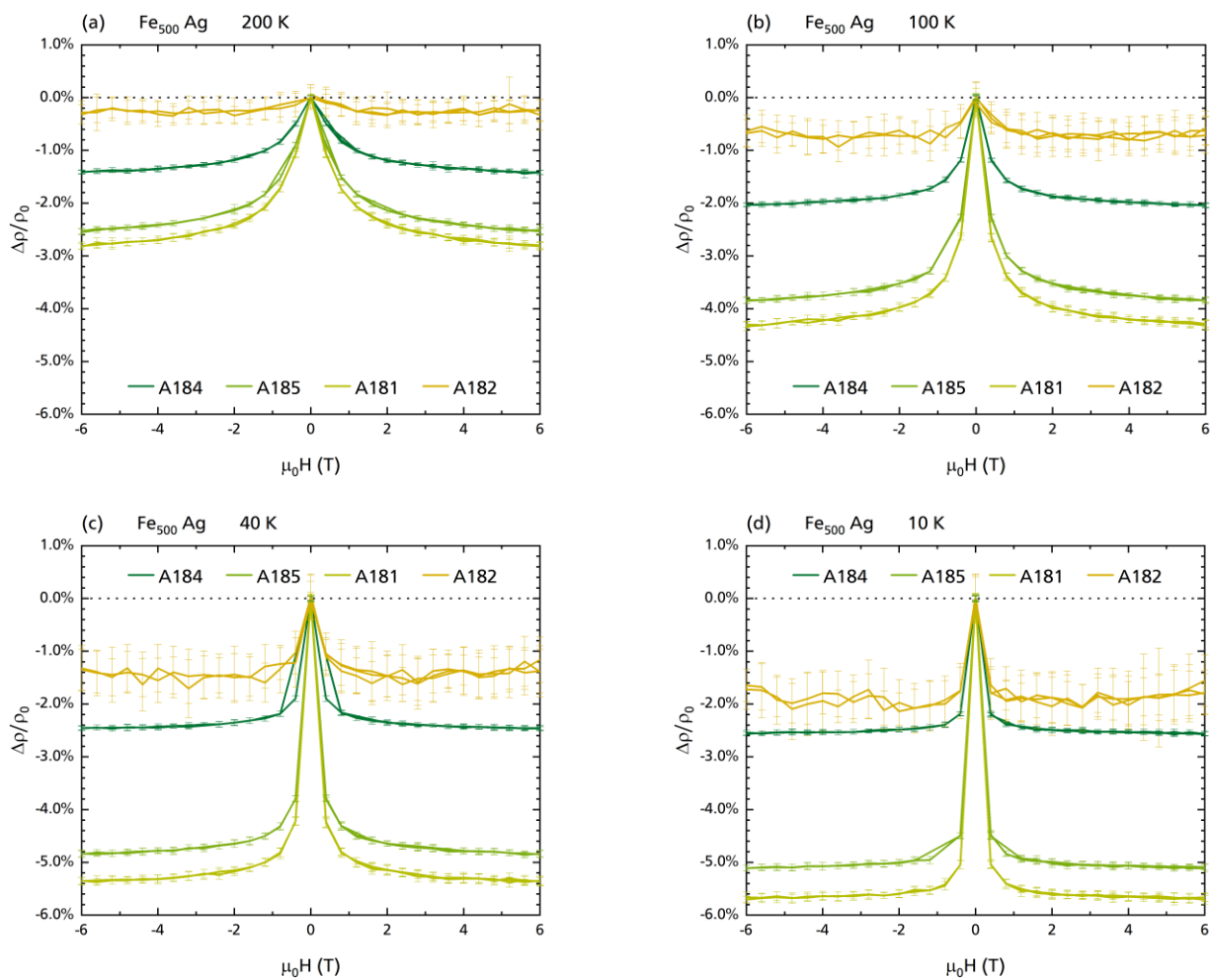
Figure C-1: Comparison of all Fe$_{500}$-Ag Nanocomposite Sample Magnetoresistance Curves at 200 K, 100 K, 40 K, and 10 K

Summary of the magnetoresistance curves recorded at 200 K, 100 K, 40 K, and 10 K of all Fe_{1000}-Ag samples.
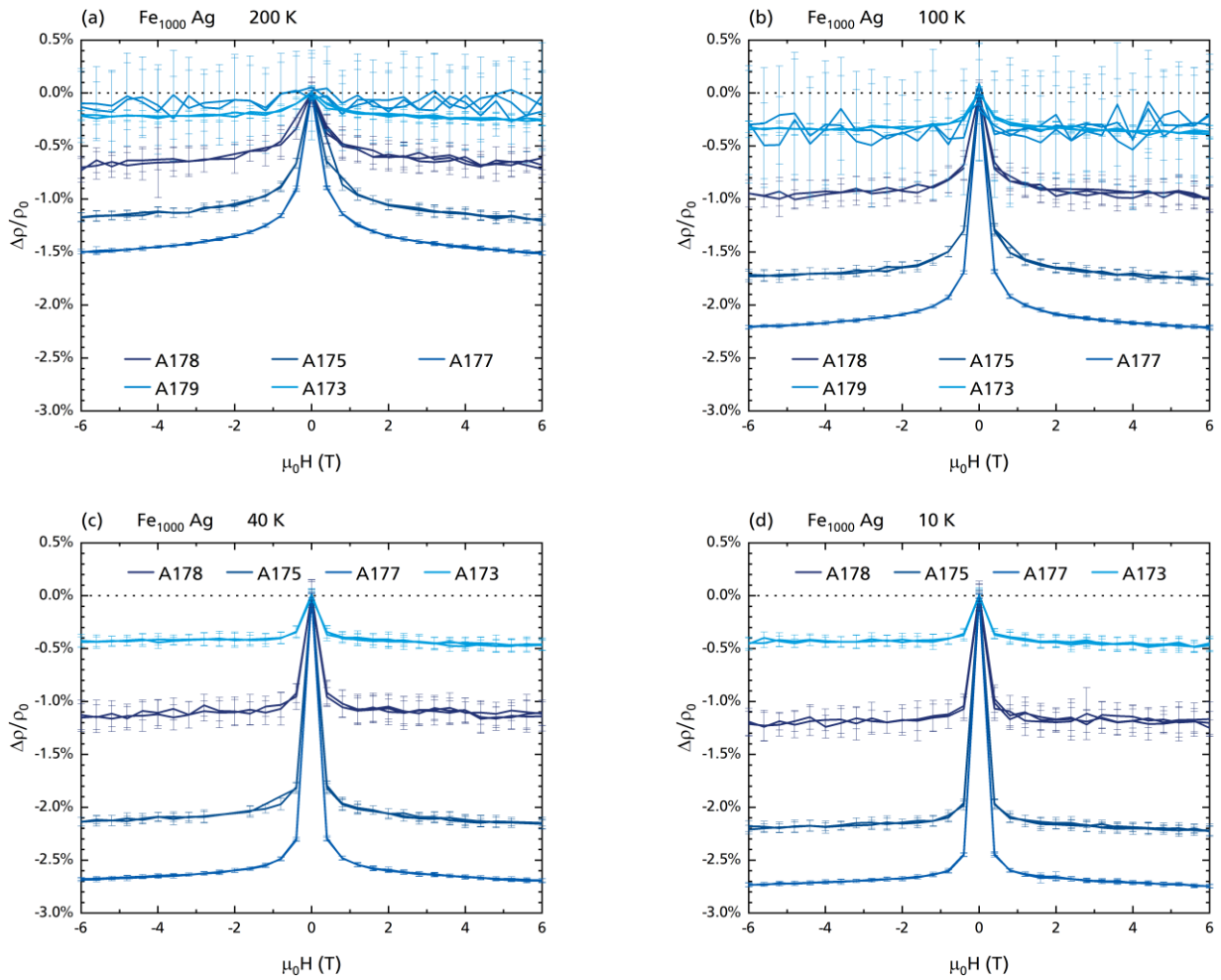
Figure C-2: Comparison of all Fe_{1000}-Ag Nanocomposite Sample Magnetoresistance Curves at 200 K, 100 K, 40 K, and 10 K

Summary of the magnetoresistance curves recorded at 200 K, 100 K, 40 K, and 10 K of all Fe_{1500}-Ag samples.
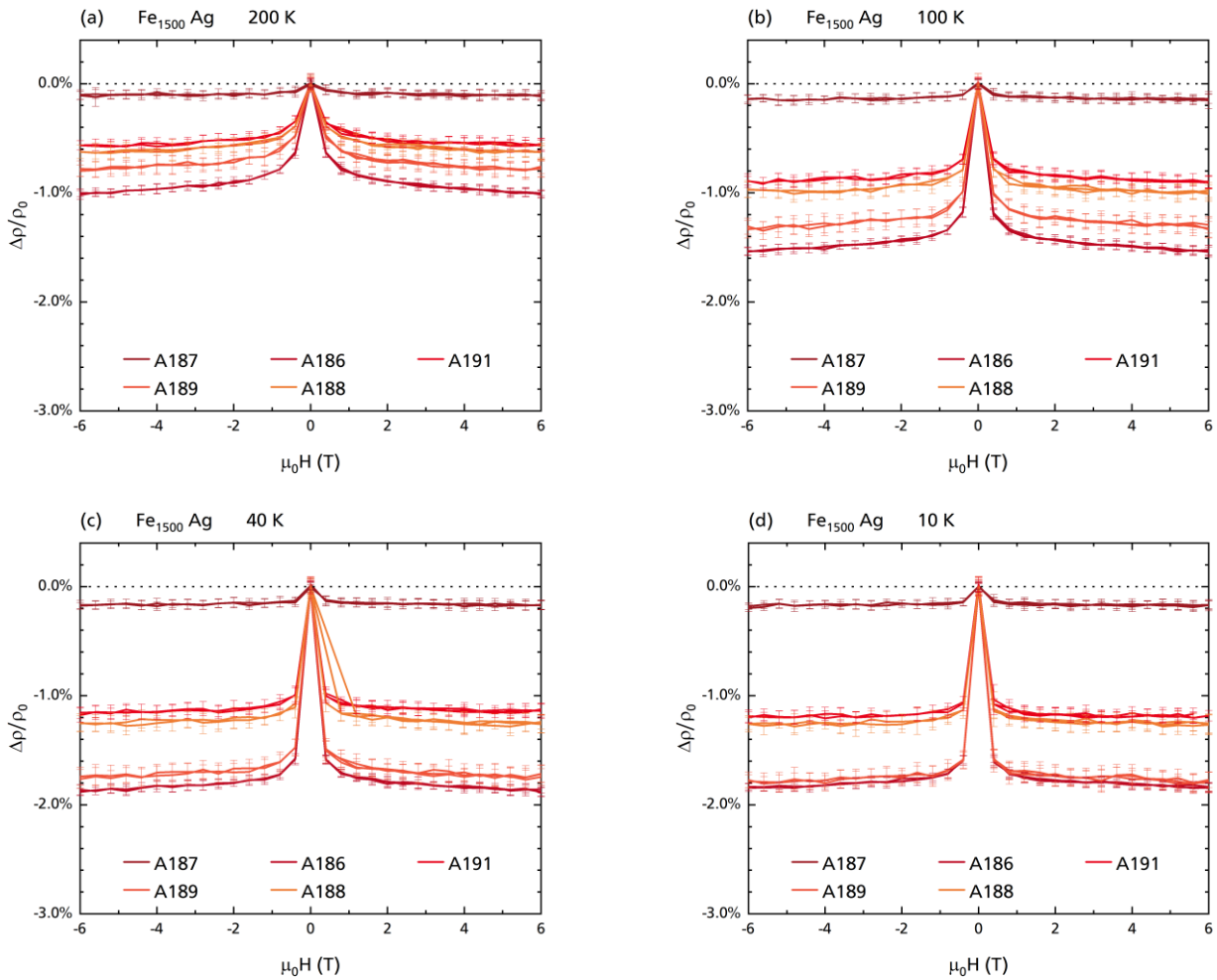
Figure C-3: Comparison of all Fe_{1500}-Ag Nanocomposite Sample Magnetoresistance Curves at 200 K, 100 K, 40 K, and 10 K

Appendix D — Additional Images Related to Fe-Ge and Fe-Ag Nanocomposites

Monte Carlo simulation of the trajectories of electrons penetrating into a CIBD sample during EDX analysis. The simulation was computed with CASINO v3.3 software [262,263]. Evidently, high-energy electrons propagate deeper than 1 µm, i.e., reach deep into the Si substrate.
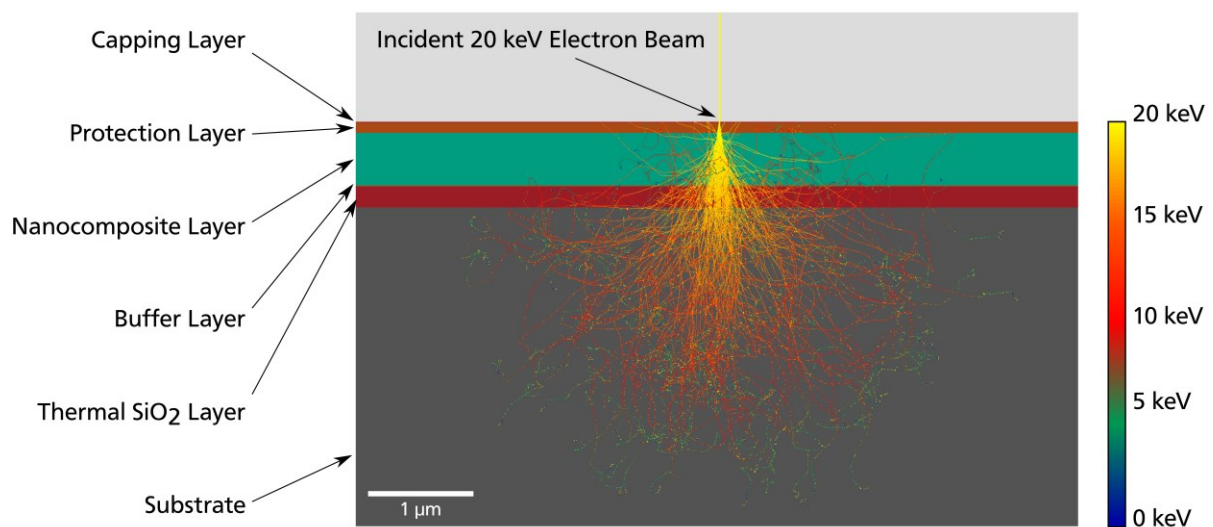
Figure D-1: Monte Carlo Simulation of Electron Trajectories in an Fe-Ge Example CIBD Sample

The layers of the shown example sample have the following thicknesses, compare Figure 4-6. Si capping: 10 nm, Ge protection: 100 nm, Fe-Ge nanocomposite: 500 nm, Ge buffer: 1 nm, thermal SiO_2: 200 nm, Si substrate: 4 µm. The image has a width of 7 µm. The initial electron energy was 20 keV.

It can be seen that electrons with high energy propagate deeper than 1 µm into the Si substrate.

Raw Concentrations of C, O, Si, Ti, Ge, Fe, and Pt as observed from preliminary EDX point spectra.
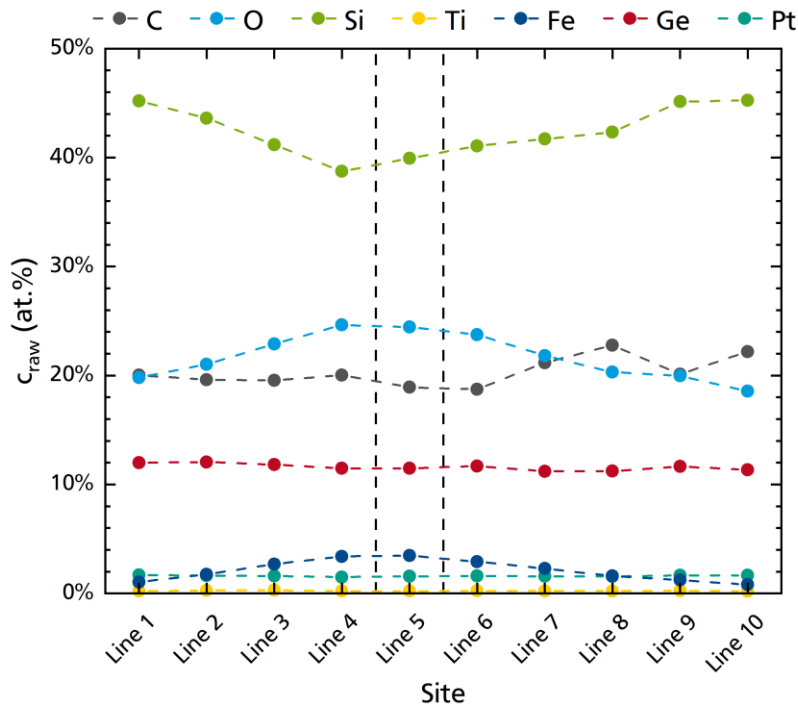
Figure D-2: Preliminary EDX Point Spectra Data of Sample G157

> The signals of Ti, Pt, and Ge remain constant to good approximation. Furthermore, the Gaussian-like distribution of Fe is visible. In the same turn, the Si signal reduces and the O signal increases.

Low-temperature part of the resistance curve of 700 ℃ annealed sample G152 and resistivity curve of sample (G128).
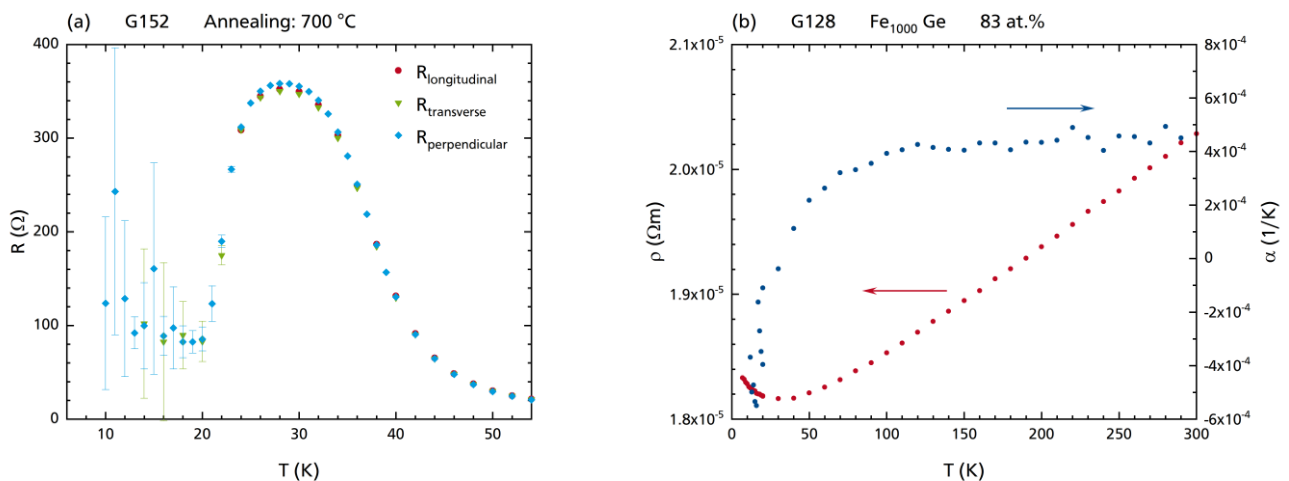
Figure D-3: Resistivity and Resistance Curve of 700 ℃ Annealed GeFe Sample G152 and Fe-Ge Sample (G128)

> (a) Low-temperature part of the $R(T)$ curve of the 700 ℃ annealed GeFe sample G152. All three measurement orientations are plotted. The full data set is plotted in Figure 4-40(a).
> (b) Metal-like shaped $\rho(T)$ (red, left scale) and $\Delta\rho/\Delta T\ (T)$ (blue, right scale) curves of Fe-Ge sample (G128).

Temperature coefficient of resistivity vs. temperature curves of all Fe-Ag samples, see Section 5.2.2.1.
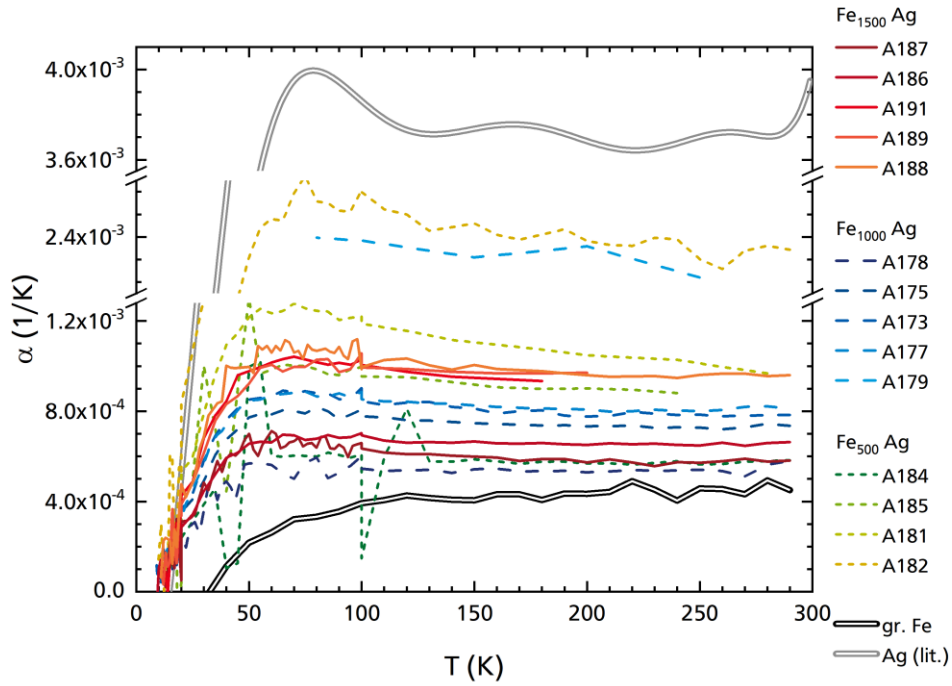
Figure D-4: Temperature Coefficient of Resistivity vs. Temperature Curves of all Fe-Ag Samples

The black and gray double-lines represent data of the (quasi-)granular Fe film Fe-Ge sample (G128) and of Ag data taken from literature [234].

Non-reversing magnetoresistance curves of two Fe-Ag samples, see Section 5.2.2.2.
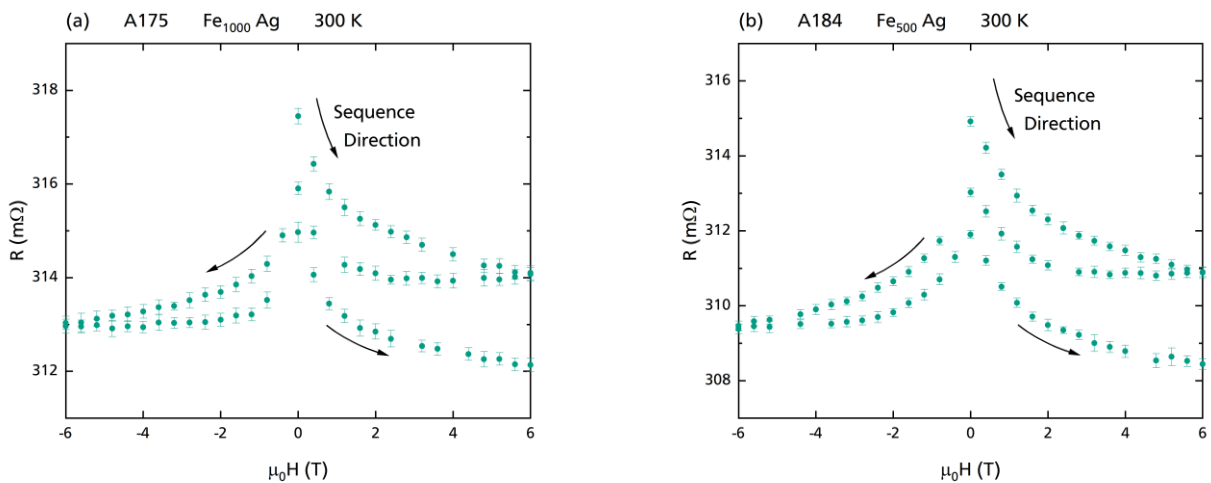
Figure D-5: Non-reversing Magnetoresistance Curves of Two Fe-Ag Samples Recorded at 300 K

(a) Sample A175.

(b) Sample A184.

The black arrows indicate the order the data points were recorded in (zero → maximum → zero → reverse maximum → zero → maximum).

Preliminary EDX point measurements (red data points) and two-wire resistance data (blue columns) determined as explained in Section 4.5.1.1.
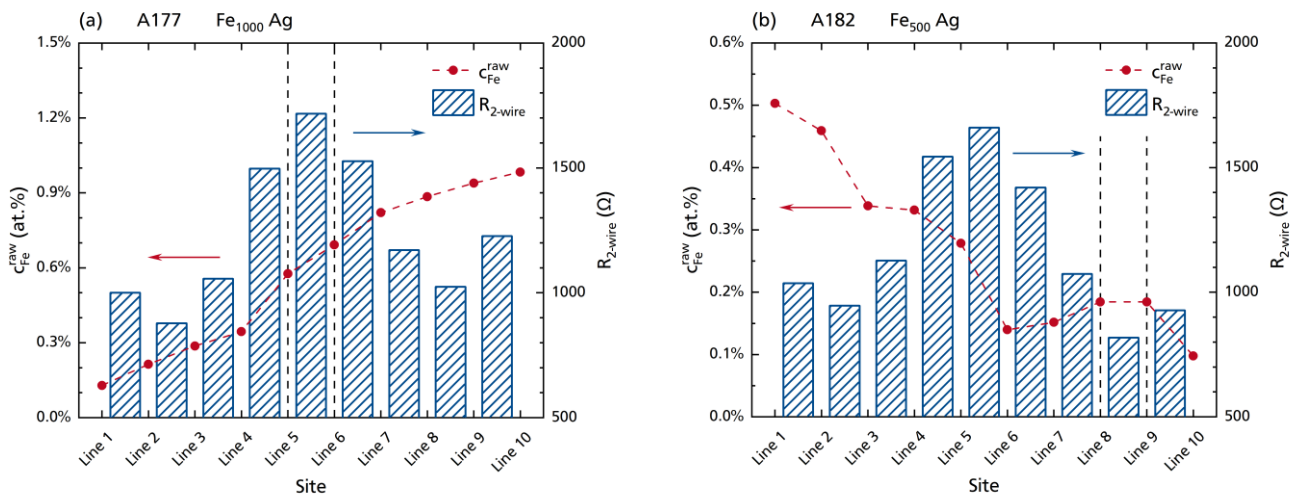
Figure D-6: Preliminary EDX Fe Concentration and Two-Wire-Resistance Data of Samples A177 and A182

  (a) Sample A177.
  (b) Sample A182.

  See Section 4.5.1.1 for details. Four-wire measurements were performed between the dashed lines.

Fe concentration mapping via EDX. EDX elemental analyses were performed in the area limited by the white rectangles in the SEM micrographs. The respective Fe signals are depicted beside each SEM micrograph on white background in order to visualize the Fe concentration gradient. A gradient, i.e., an increase of the concentration from the left-hand to the right-hand side of the film, is present in both samples as indicated by the percentage of colored pixels.

(a) A188

(b)

33.4%

31.0% 34.0% 37.0%

(c) A186

(d)

54.5%

49.5% 53.2% 59.0%
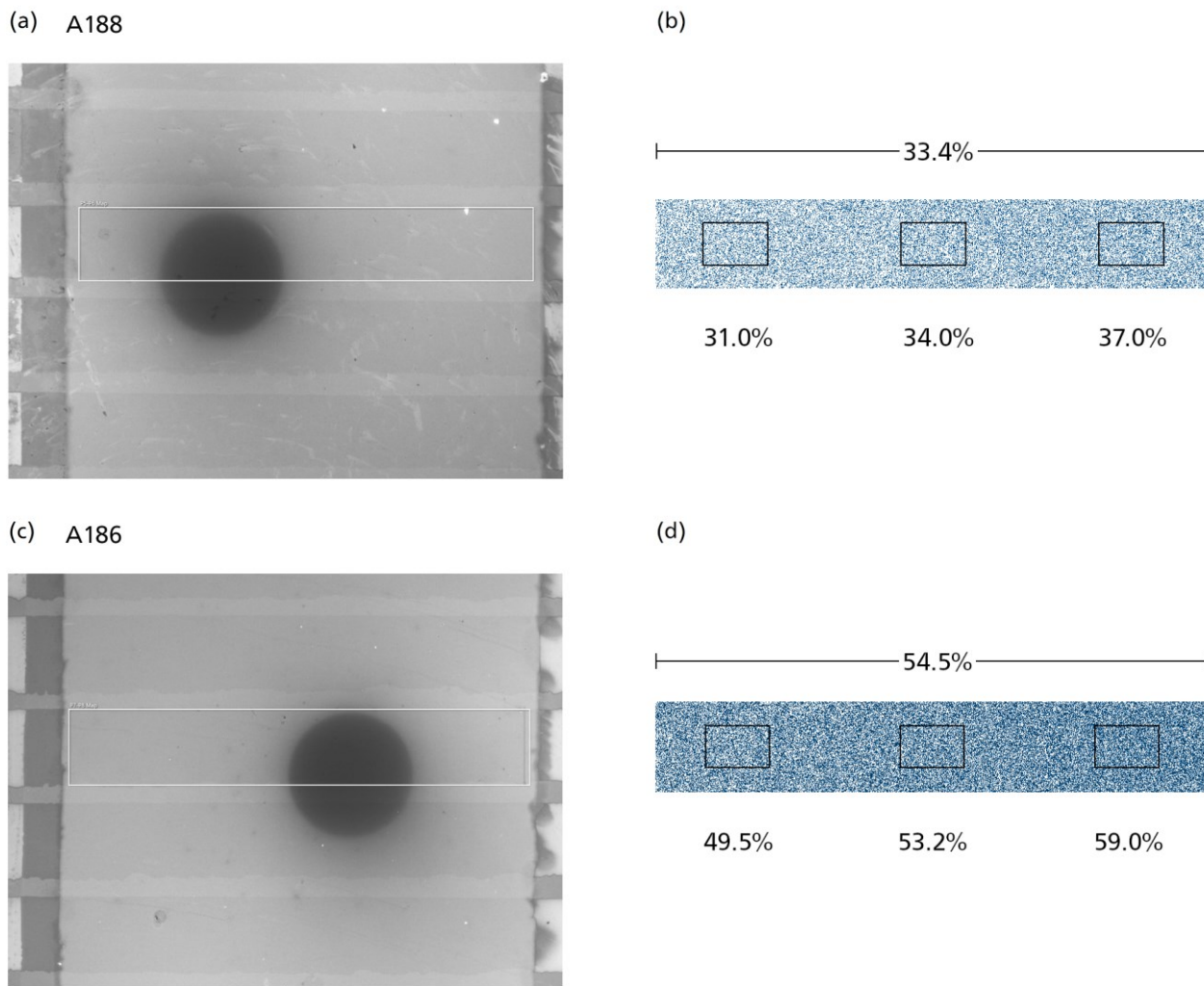
Figure D-7: EDX Fe Maps of Samples A188 and A186

(a) & (c) SEM micrographs. EDX elemental analyses were performed in the area limited by the white rectangles. The width of each micrograph is about 1 mm.

(b) & (d) EDX Fe maps recorded from the white rectangles in graphs (a) and (c). The lower-row numbers in graphs (b),(d) give the percentage of blue pixels in the equally sized frames, the upper row number gives the average over the full map. For both samples the percentage, i.e., the concentration of Fe, increases from the left-hand to the right-hand side. To be precise, a concentration gradient is present.

A188 was connected from its left-hand side, i.e., its low-concentration side. A186 was connect from the right-hand side, i.e., its high-concentration side.

Appendix E — Additional Images Related to the PL-BGC Setup

Two photographs of the PL-BGC setup presented in Section 6.2.
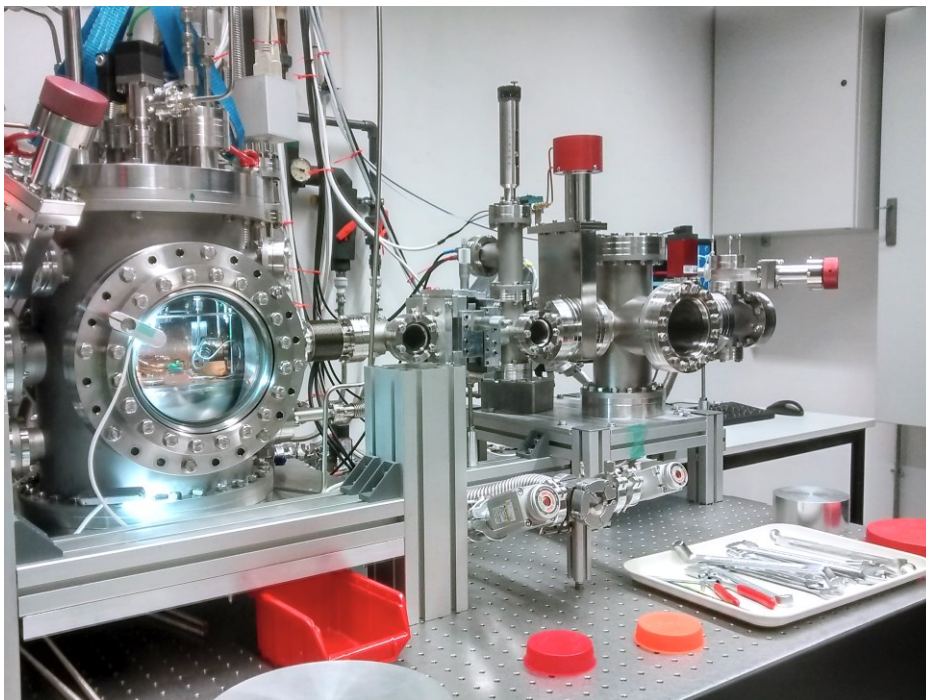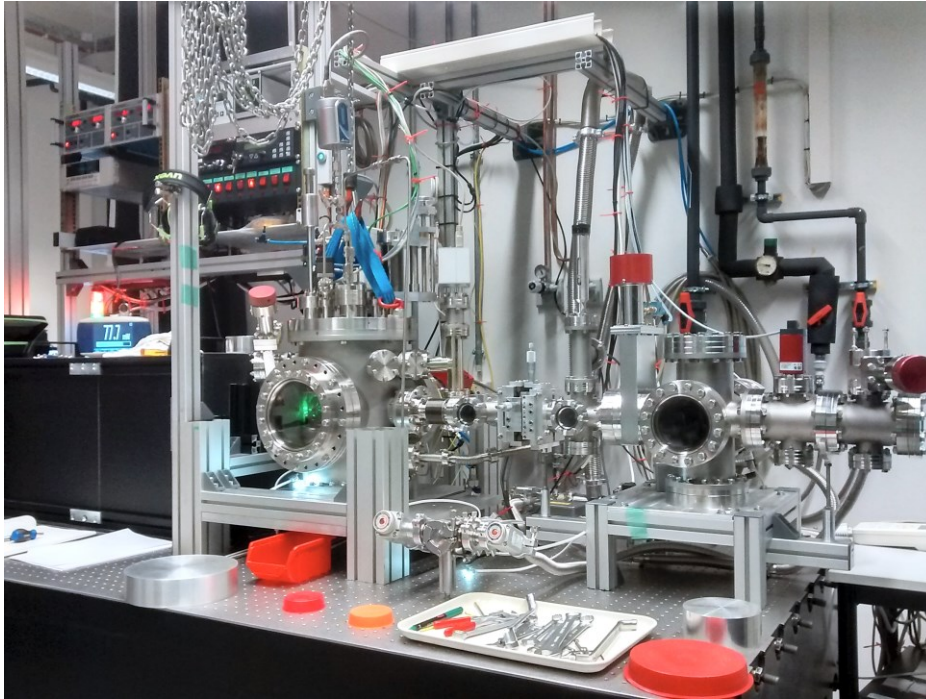
Figure E-1: Two Photographs of the PL-BGC Setup Presented in Section 6.2

Construction drawing of the shower head inside the AC. The part is also shown in illustrations of the according CAD model, see Figure 6-7.
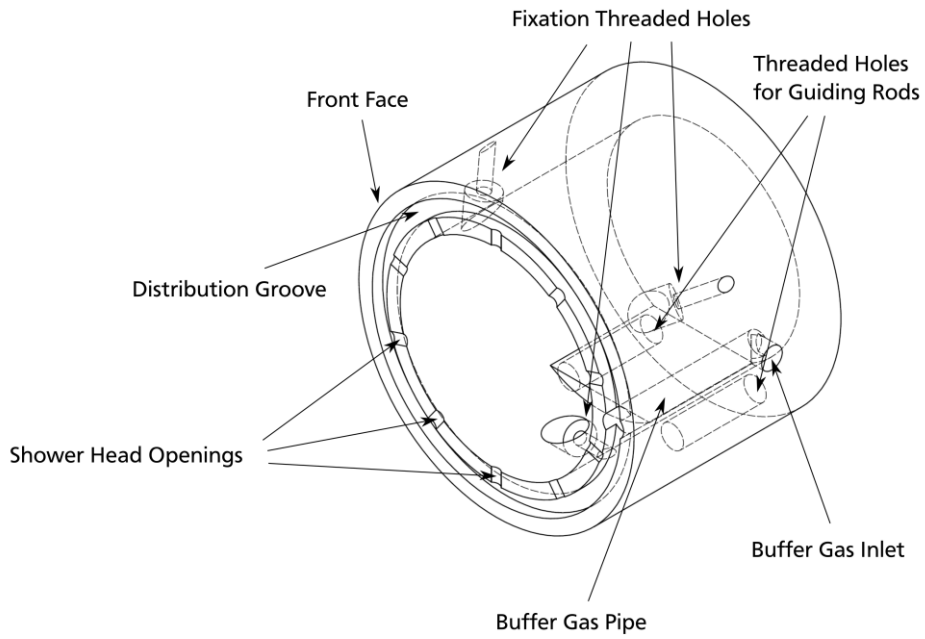
Figure E-2: Construction Drawing of the Shower Head Part inside the AC

The functional elements are labeled according to their function. The part has a diameter of ~40 mm.

Appendix F — Assembly of the Beam Section of the PL-BGC

A photograph of the assembled beam section of the PL-BGC setup is presented in Figure F-1. Details of the beam section are shown in Figures F-2 and F-4. Some of the in-vacuum parts of the beam section are arranged in Figure F-3 together with two building units of the beam section, framework and capacitor unit, in order to provide a clearer view of the designed parts.

One requirement that has to be fulfilled by the beam section is the ability to be moveable in the plane perpendicular to the direction of the beam in order to adjust the beam section to the exit aperture of the AC, i.e., the opening of the nozzle, see Figure 6-6. For this reason, most of the depicted parts, i.e., all components except (s)–(v), are fixed to a movable DN 40 CF 4-way cross or are in connection with it. The 4-way cross is installed between two DN 40 CF edge welded bellows, one at its left-hand side and one at its right-hand side. Translation of the movable components is performed by an xy-stage that is combined with the right-hand side bellow. The xy-stage, the cross-flange, and the bellow at its left-hand side can be identified in Figure 6-2, where they are highlighted as 'beam section'.

The components of the beam section are assembled and inserted into the setup as follows. They are made of stainless steel if not stated otherwise. First, two outer ring elements (a) are fixed inside the two CF ports of the 4-way cross the edge welded bellows will be attached to. This is done by a trio of set screws that are seated in threaded holes drilled through the walls of the ring elements. A trio is tightened such way that the set screws do not only push against the inner wall but, in the same turn, align the ring element concentrically to the CF port. The inner faces of the ring elements are of conical shape, i.e., their inner diameters narrow. The direction of narrowing is towards the middle of the 4-way cross.

Accordingly, there exist two inner ring elements (b,r) with appropriately conically shaped outer faces as well. One of them, the one that is put onto the left-hand side outer ring, (b), serves as base element for the framework of M4 threaded rods (c) that carries all the components to be inserted into the 4-way cross all in one piece. These components are assembled ex-situ and then inserted into the 4-way cross all in one piece. A photograph of the ex-situ assembled piece is presented in Figure F-1.

Starting with the framework, four 150 mm long M4 threaded rods are screwed through four correspondingly threaded holes in the first inner ring element (b). They are each locked in position with a nut from the left-hand side so that about 15 mm of each threaded rod jut out of the inner ring in this direction. Here, part (d) that will later carry the shielding tube that extends to the left-hand side and reaches into the UHV source chamber will be installed.
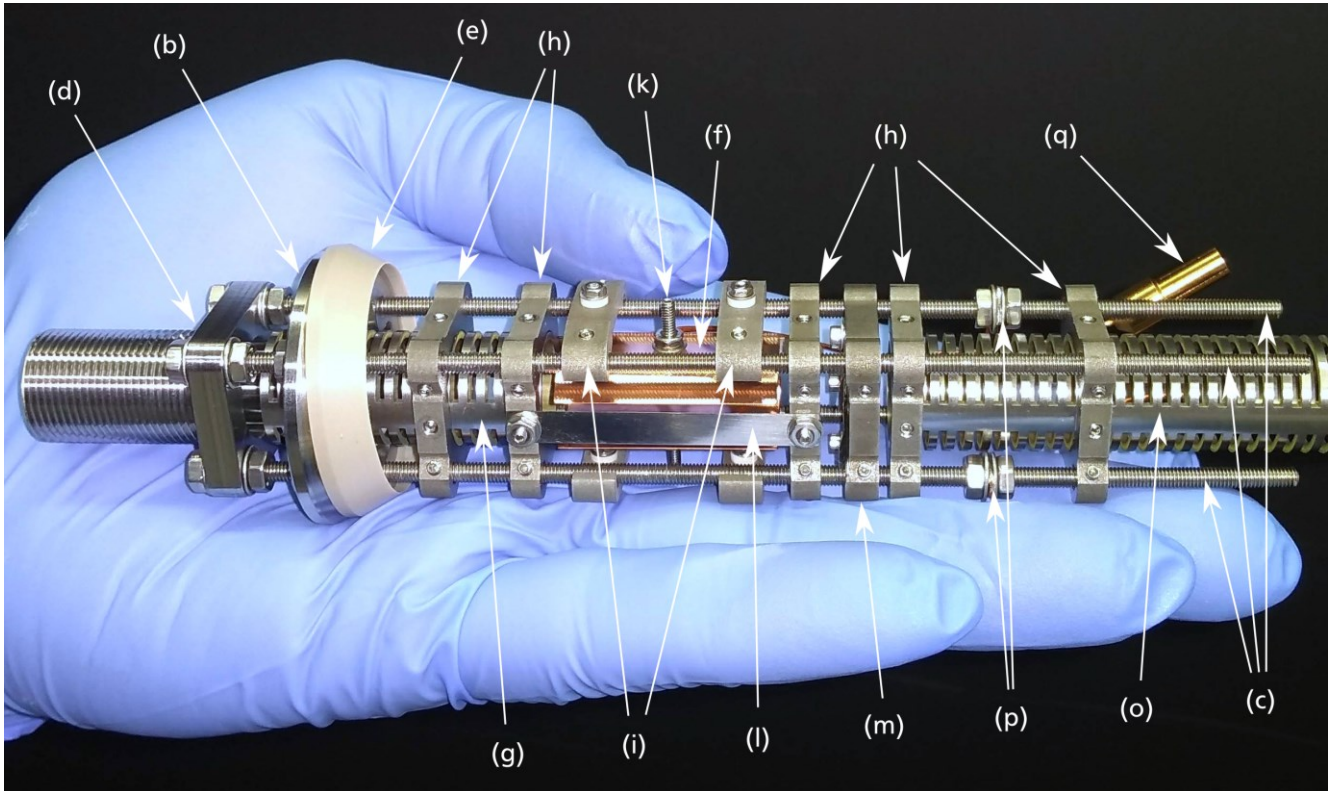
Figure F-1: Photograph of a Part of the Beam Section

The labeled parts are discussed in detail in the text.

From the right-hand side, first, an insulating ring made of polyether ether ketone (PEEK) (e) is slid onto the inner ring (b). The PEEK ring has the same conical shape as the inner and the outer ring in order to fit in between them. A second PEEK ring and the second inner ring (q) are slid onto the completely assembled beam section unit from the right-hand side after it is inserted into the 4-way cross. The PEEK rings ensure that all components installed to the framework are insulated from ground potential. The CAD model of the framework, consisting of the rings plus the threaded rods, is illustrated in Figure F-3.

The components located inside the 4-way cross can be divided into four subsection, with a pair of Cu made electrodes (f) that form a capacitor unit as its central element. The three other subsections are tube elements that shield the fraction of charged beam particles from ground potential. First, tube (g) that has an inner diameter of 14 mm and that is carried by a pair of sliders (h) is slid onto the framework. Both the tube to the sliders and the sliders to the M4 threaded rods are locked in position by tightening set screws in the sliders that push onto the tube and the threaded rods, respectively.

The electrodes of the capacitor (f) are carried by a second type of sliders (i) that allow to install the Cu electrodes in an insulated way so that each Cu electrode can be set to an individual potential. For
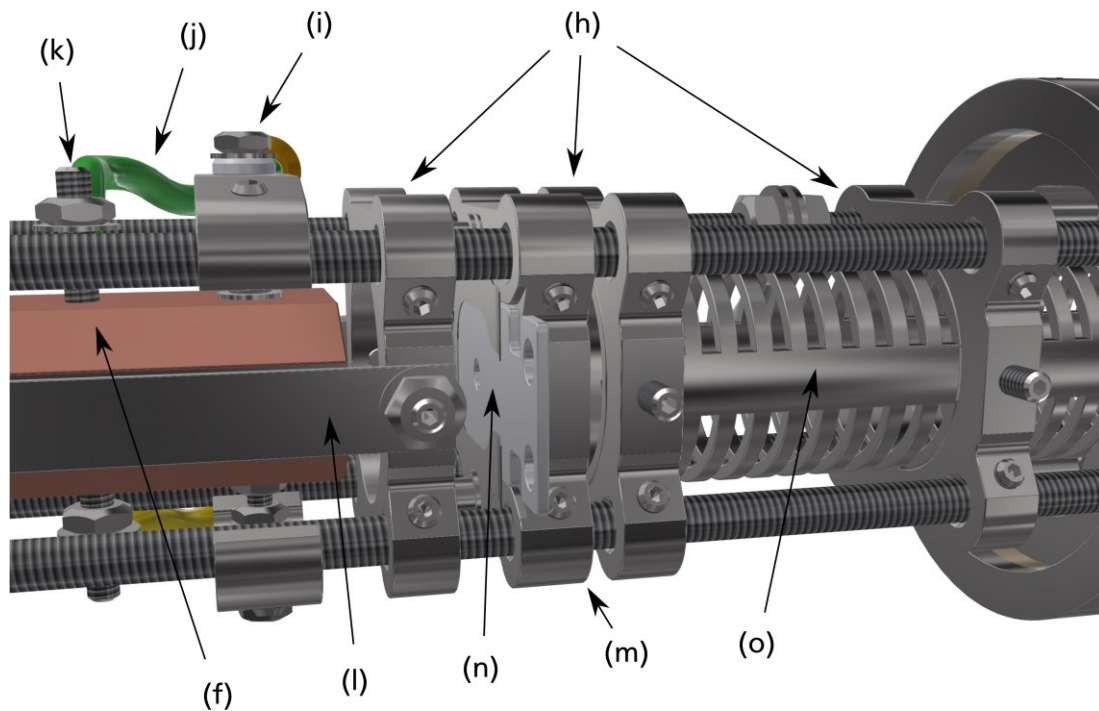
Figure F-2: Detailed View of the CAD Model of the Beam Section

In this detailed view, the aperture sheet (n) can be recognized.

this reason, the Cu electrodes work as a capacitor unit, with the purpose to deflect charged beam particles in order to obtain a beam of neutral particles only. Each electrode is contacted by a piece of UHV-compatible electric wire (j), only shown in Figure 6-9, that is tightened (k) to the outer side of a Cu electrode. At their inner sides the electrodes are plane and were polished by hand prior to installation. The plate capacitor that is formed this way is 30 mm long and 20 mm wide. The capacitor unit is also illustrated in Figure F-3.

The particle beam is not open to ground potential at the sides but is shielded by a pair of stainless steel stripes (l) in range of the capacitor unit that are tightened to the slider in front and at the back side of the capacitor unit. Note that only parts belonging to the upper capacitor element and only the front side stripe are indexed in Figures F-1 and F-2.

The capacitor unit, more precisely, the slider at its back side, is followed by a specialized slider (m) into which aperture sheets (n) can be inserted in order to restrict the diameter of the transmitted beam. The aperture sheet is only visible in Figure F-2. Also, sheets without an opening can be inserted in order to collect a sample of beam particles with an attached piece of substrate. The sheets are cut with the picosecond infrared laser that was mentioned earlier several times and are inserted into the setup through the front port of the 4-way cross. The front port is sealed with a viewport when the setup is under vacuum.
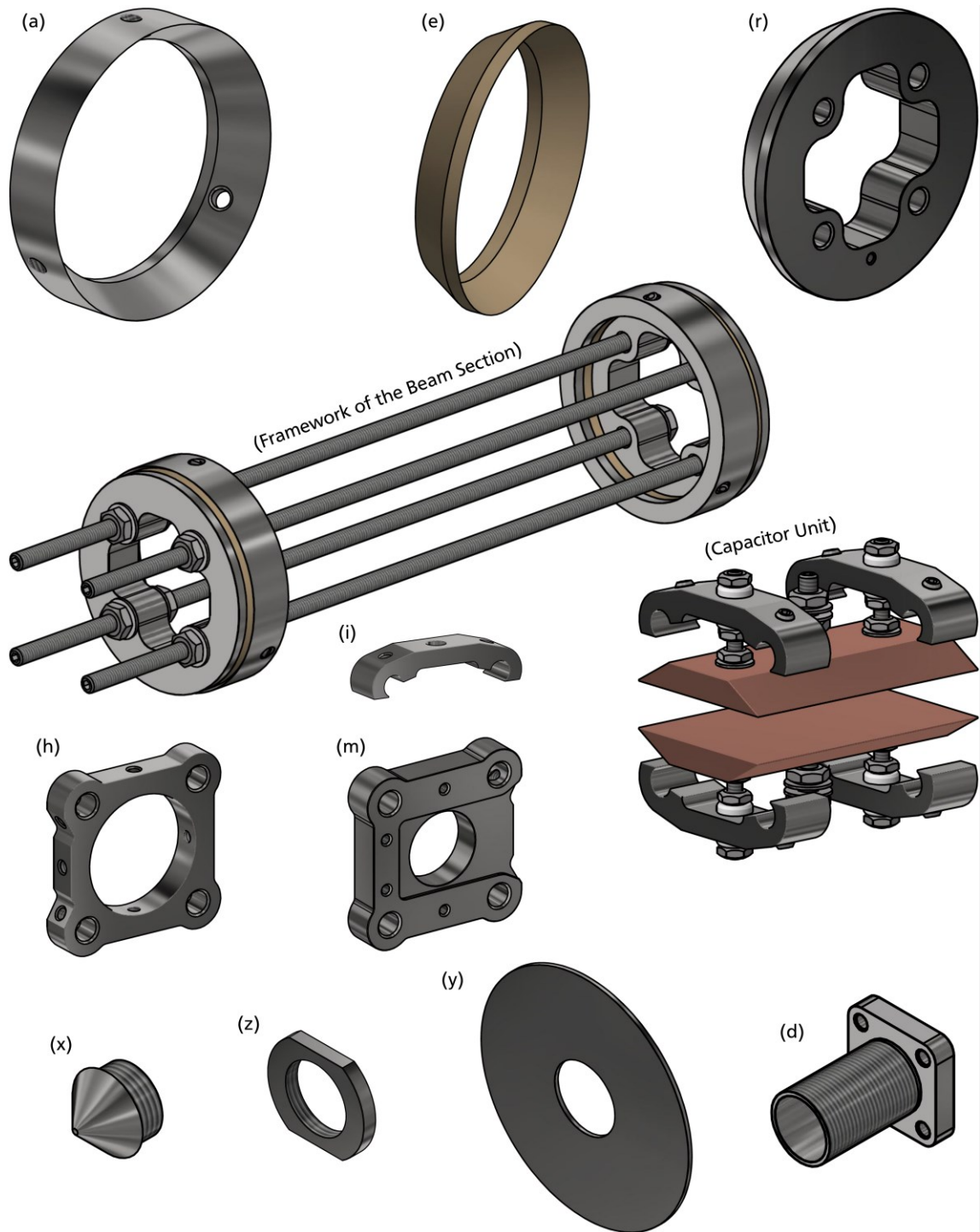
Figure F-3: Arrangement of Some Beam Section Elements
The indexing corresponds to the one used in the text.

Finally, a longer tube (o) similar to tube (g) that is kept in place by another pair of sliders (h) is slid onto the framework. This tube is about twice as long as depicted in Figure F-1 and reaches almost to the not moving right-hand side CF port of the right-hand side edge welded bellow. The two pairs of washers

and nuts (p) between the sliders of the right-hand side tube are used to clamp another pair of wires to the framework. These are used to apply an electric potential to the shielding tubes. All wires, also these connecting the Cu electrodes, end in push-on connectors (q). When the ex-situ assembled piece is inserted into the 4-way cross the connectors are put onto the pins of a high voltage quadruple feedthrough flange sealing the back side port of the 4-way cross.

To finally install the assembly inside the 4-way cross it is inserted through the left-hand side port of the 4-way cross. The M4 threaded rods were chosen long enough to reach throughout the right-hand side outer ring element. The second inner ring element (r) with the second PEEK ring on top is then moved onto the M4 threaded rods. To be able to do so, the second ring(r) comes with blank holes instead of threaded holes. Then, the assembly is carefully tightened with washers that are put onto the M4 threaded rods. While doing so, the conical shape of the ring elements helps to center the assembly inside the 4-way cross.

As can be seen in Figure 6-9, the right-hand side end of tube (o) does not mark the end of the beam section. Instead, shielding of the particle beam is taken over by tube (s) that is fixed inside the right-hand side CF port of the right-hand side edge welded bellow, which is the bellow that is combined with the xy-stage. Hence, tube (s) is not movable. Because the cross-sectional area of tube (s) has to cover the entire area the smaller yet movable tube (o) can be moved across, tube (s) has a larger diameter of 22 mm. Again, an outer ring element (t) is installed inside the hosting flange by pushing set screws against the inner wall of the flange. Since the tube is the only element to be carried it is directly inserted into an inner ring element (u) and locked in position by tightening set screws against it. Here, the ring elements (t,u) are not of conical but of cylindrical shape, and alumina split bushes are used instead of a PEEK ring to insulate the inner ring and the tube from ground potential. Tube and inner ring are connected to the shielding potential with a wire (v) that is tightened to tube (s) and connected to a pin sticking out of the inner ring (r).

After the movable 4-way cross is installed to the setup, the left-hand side tube assembly is installed as the last element. It is inserted through the UHV source chamber after the left-hand side edge welded bellow is attached to the corresponding port of the source chamber (via the mentioned DN 63/40 CF reducing flange). Before the bellow is connected to the movable 4-way cross—this is the step that closes the vacuum branch surrounding the beam section assembly—tube (w_1) is screwed onto holder (d), where the second part of the tube (w_2) is already screwed into the left-hand side of (w_1). To connect the parts, (d,w_2) each have a male and (w_1) has a female M16x1 fine thread cut into the corresponding faces. This thread also allows to screw the second part of the tube (w_2) into the first part. This way, the length of the tube can be adjusted. With the skimmer (x) screwed into the end of tube (w_2), the skimmer is a cone with a 1 mm hole through its tip, the length of the tube assembly is adjusted such way that the
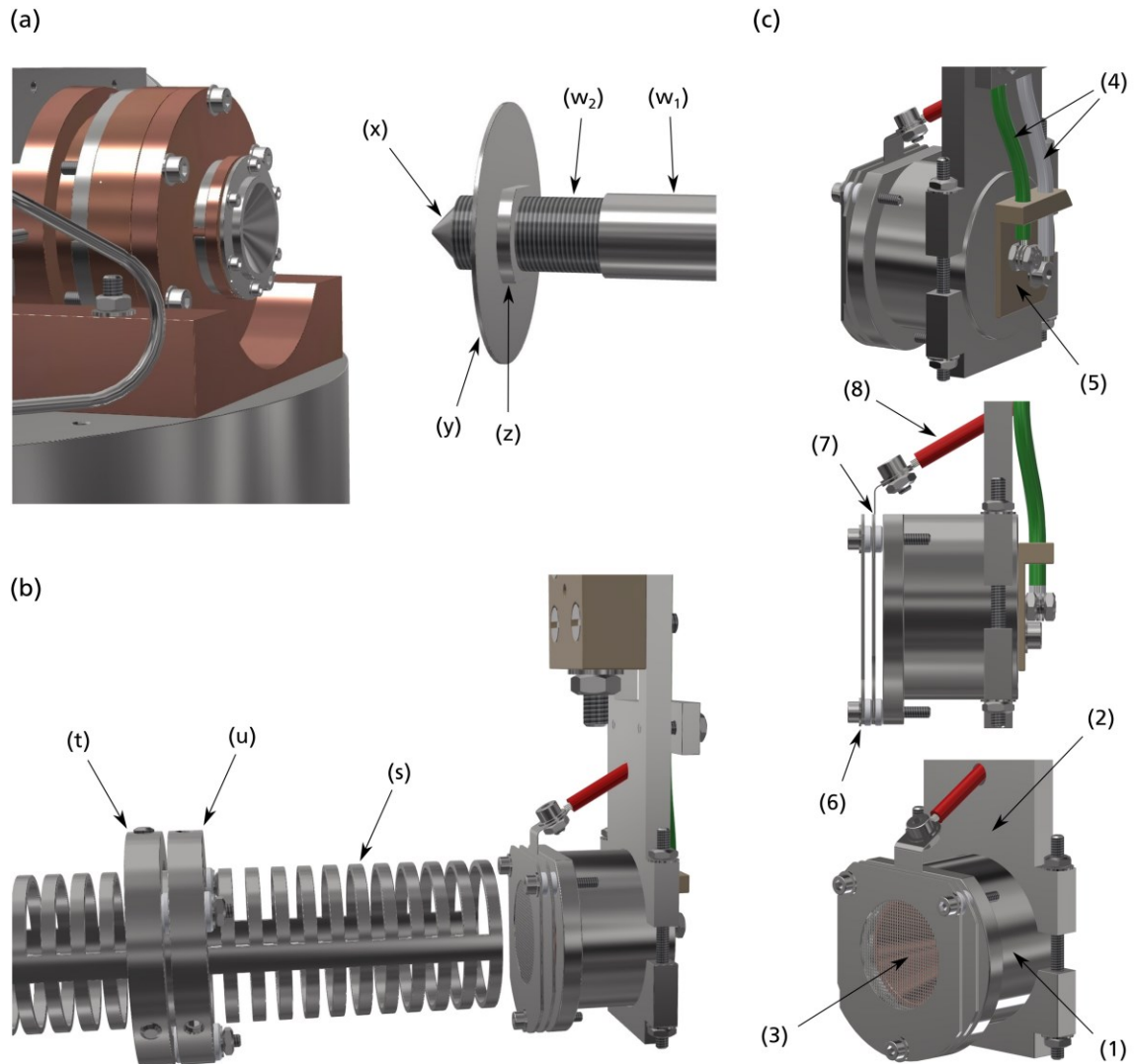
Figure F-4: Detailed View of Front and Back Side of the Beam Section and of the Faraday Cup

(a) The front side of the beam section is narrowed by a skimmer and. A disc surrounding the tube shields the branching off UHV chamber from the direct stream of particles and gas coming from the AC.
(b) At its back side the beam section ends abruptly. Here, a Faraday cup can be moved into the path of the beam.
(c) Detailed views of the installed Faraday cup. See text for description.

tip of the skimmer is close to the AC's exit but also at a safe distance from it so that it is not touched by the LN$_2$ tank when the source assembly is moved in or out of the source chamber. The resulting length of the left-hand side tube assembly is about 15 cm. The relative orientation of beam section and source assembly inside the vacuum setup is illustrated in Figure F-4(a).

To prevent the gas and the particles released by the AC from bypassing the skimmer at the front side of the beam, a circular shield (y) is installed to tube (w$_2$). Its diameter is chosen such that it is large enough to always cover the DN 40 hole through the DN 63/40 CF reducing flange on the one hand and small enough to allow a maximum of translation of the beam section on the other. Its diameter is 56 mm.

The shield is locked by two nut elements (z) with accordingly cut threads and installed at a position on (w$_2$) so that it moves inside the DN 63 CF port of the UHV source chamber right in front of the reducing flange from which the beam section branches off.

On its right-hand side end, the in-vacuum beam section ends abruptly. At the end of tube (s) the beam propagates into vacuum without further shielding. However, as illustrated in Figure F-4(b), a Faraday cup can be moved into the path of the beam right behind tube (s). Detailed views of the Faraday cup are depicted in Figure F-4(c). The design is inspired by the Faraday cups used in the CIBD system, see Chapter 3. However, the design was altered in order to build a Faraday cup assembly that fits through a size DN 40 tube.

The Faraday cup is attached to a manually operated linear bellows drive in an insulating way and it is pulled back into a DN 40 CF tee when not used. The outer cup (1) is clamped to a holder (2). Electrical connection to the outer and the inner cup (3) is made by clamping the corresponding wires (4) at the back side of the Faraday cup. There, a piece of insulating PEEK (5) guides the two cables to their contact terminals and separates the contact points from the back side of the outer cup. The front side of the Faraday cup is shielded by a grid (6) that is connected to the electric potential of the outer cup. In between the shielding grid and the cups a retarding grid (7) is installed. It can be set to an individual potential and is connected via a third wire (8). The three wires coming from the Faraday cup are connected to the outside via a high voltage quadruple feedthrough flange that is installed to the side port of the tee.

List of Abbreviations

AC	Aggregation Chamber
a-Ge	Amorphous Germanium
ARCAL™ 15	Gas Mixture by Air Liquide: Ar with (5 ± 0.5) vol. % H_2
bcc	Body-Centered Cubic
CAD	Computer-Aided Design
c-Ge	Crystalline Germanium
CIBD	Cluster Ion Beam Deposition
CIP	Current-in-Plane
CPP	Current-Perpendicular-to-Plane
EDX	Energy-Dispersive X-Ray Spectroscopy
EMR	Extraordinary Magnetoresistance
ESR	Electron Spin Resonance
FC	Field-Cooled
fcc	Face-Centered Cubic
Fe_x	Fe Cluster Consisting of x Fe Atoms
FWHM	Full Width at Half Maximum
hcp	Hexagonal Close-Packed
ITO	Indium Tin Oxide
LHe	Liquid Helium
LN_2	Liquid Nitrogen
LPMR	Linear Positive Magnetoresistance
MCD	Magnetic Circular Dichroism (Spectroscopy)
MFC	Mass Flow Controller
MPD	Mean Particle Distance: Average distance between the centers of two neighboring clusters.
MPS	Mean Particle Separation: Average distance between the surfaces of two neighboring clusters.

PEEK	Polyether Ether Ketone
PET	Polyethylene Terephthalate
PL-BGC	Pulsed Laser – Buffer Gas Condensation
PPMS	Physical Properties Measurement System by Quantum Design
PTFE	Polytetrafluoroethylene; also known as Teflon$^{®}$.
sc	Simple Cubic
SEM	Scanning Electron Microscope
SQUID	Superconducting Quantum Interference Device
TED	Transmission Electron Diffraction
TEM	Transmission Electron Microscopy
UHV	Ultra-high Vacuum
VRH	Variable-Range Hopping
YAG	Yttrium-Aluminum-Garnet
XRD	X-Ray Diffraction
XRR	X-Ray Reflectometry
ZFC	Zero-Field-Cooled
1D, 2D, 3D, 4D	One-, Two-, Three-, Four-Dimensional

List of Symbols

Mathematical Operators:

$\vec{\nabla}$	Nabla Operator
$\triangle$	Laplace Operator

Fundamental Physical Constants:

c	Speed of Light in Vacuum
e	Elementary Charge ($|e| = e$)
g_e	Electron g-Factor
$h, \hbar$	Planck Constant, Reduced Planck Constant
k_B	Boltzmann Constant
m_e	Electron Mass
ε_0	Vacuum Electric Permittivity
μ_B	Bohr Magneton
μ_0	Vacuum Magnetic Permeability

Latin Symbols:

A	Fraction of Misaligned to Well-Aligned Surface Magnetic Moments of a Cluster
A_S	Area of a CIBD Sample that Belongs to the Electric Potential U_S
$\vec{A}$	Vector Potential of the Magnetic Field
B	Absolute of the Magnetic Flux Density, of the 'Magnetic Field'
$\vec{B}$	Magnetic Flux Density, 'Magnetic Field'
$\mathcal{B}_J(x)$	Brillouin Function
C	(1) Curie Constant,
	(2) Tunneling Constant,
	(3) Mathematical Constant

C_i	Heat Capacity of the Ion Lattice
C_p	Specific Heat
C_{sph}	Capacity of a Spherical Capacitor
c_{dep}	Concentration of Cluster Material Calculated from Deposition Parameters
c_{Cl}	Concentration of Cluster Material
c_{Fe}	Concentration of Fe
c_M	Concentration of Matrix Material
c_3	VRH Numeric Factor
D	Diffusivity, Thermal Diffusivity
$D(E), D_\sigma(E)$	Total and Spin-Polarized Density of States
d	(1) Spacing of the Contact Lines of a CIBD Sample Chip,
	(2) Diameter,
	(3) Grain Size
d_{Cl}	Diameter of a Cluster
E	(1) Energy,
	(2) Absolute Value of the Electric Field
E_A	(1) Magnetic Anisotropy Energy,
	(2) Conduction Band Tail Edge
E_{Act}	Activation Energy
E_B	Valence Band Tail Edge
E_C	(1) Charging Energy,
	(2) Conduction Band Edge
E_C^0	Charging energy to create a fully dissociated pair of singly and oppositely charged grains out of two neutral grains.
E_F	Fermi Energy
E_g	Energy Gap of a Semiconductor
E_i	Discrete energy of a quantum state Indexed by i.
E_m	Energy Width
E_V	Valence Band Edge
E_Z	Zeeman Energy
$\vec{E}$	Electric Field
F, F_{th}	Laser Fluence, Laser Fluence Threshold
$F(s/d)$	Function that Carries Geometric Information

$\vec{F}_L$	Lorentz Force
$f(E)$	Fermi Function, Fermi-Dirac Occupation Probability
$f(E,T)$	Fraction of misaligned surface magnetic moments to the number of surface magnetic moments of a cluster in total.
g	Landé g-Factor
H	Absolute Value of the Magnetic Field Strength, of the 'Magnetic Field'
H_C	Coercive Field
H_v	Latent Heat of Vaporization
$\vec{H}$	Magnetic Field Strength, 'Magnetic Field'
$\hat{\mathcal{H}}$	Hamilton Operator, Hamiltonian
I	(1) Electric Current,
	(2) Stoner Parameter,
	(3) Laser Intensity
I_{Cl}	Cluster ion current recorded from the surface with electric potential U_S.
I_{exc}	Four-Wire Measurement Excitation Current
I_{SE}	Cluster ion current recorded from the surface with electric potential U_{SE}.
I_{TBC}	Total Beam Current: Total cluster ion current hitting a deposition sample.
i	(1) Counting Index,
	(2) Index of a not further defined quantum state.
J	Total Angular Momentum Quantum Number of a Many-Particle System
$\vec{J}$	Total Angular Momentum of a Many-Particle System
j	(1) Counting Index,
	(2) Absolute Value of the Electric Current Density
$\vec{j}$	(1) Electric Current Density,
	(2) Total Angular Momentum of a Single Particle
K	Magnetic Anisotropy Constant
$K_{eff}, K_S, K_{sh}, K_1$	Effective, Surface, Shape, Magnetocrystalline Anisotropy Constant
K_0	Kinetic Energy
k	(1) Absolute Value of a Wave Vector, Crystal Momentum,
	(2) Exponent
k_0	Thermal Conductivity
k_F	Fermi Crystal Momentum

$\vec{k}$	Wave Vector, Crystal Momentum
L_{VRH}	Average VRH Hopping Distance
$\vec{L}$	Orbital Angular Momentum of a Many-Particle System
$\hat{L}$	Many-Particle Orbital Angular Momentum Operator
$\mathcal{L}(x)$	Langevin Function
l	(1) Orbital Angular Momentum Quantum Number,
	(2) Diffusion Length
l_{sf}	Average Spin Diffusion Length
l_T	Heat Diffusion Length
l_σ	Spin-Polarized Diffusion Length
$\vec{l}$	Orbital Angular Momentum of a Single Particle
$\hat{l}$	Single-Particle Angular Orbital Momentum Operator
M	Absolute Value of Magnetization
M_J	Total Angular Momentum Projection Quantum Number of a Many-Particle System
M_S	Saturation Magnetization
$\vec{M}$	Magnetization
m	(1) Mass,
	(2) Relative Magnetization
m_l	Angular Orbital Momentum Projection Quantum Number of a Single Particle, Magnetic Quantum Number
m_r	Relative Remanence
m_s	Spin Projection Quantum Number of a Single Particle
m^*	Effective Carrier Mass
$m_c^*, m_{long}^*, m_{trans}^*$	Conductivity, Longitudinal, Transverse Effective Electron Mass
MPD	Mean Particle Distance: Average distance between the centers of two neighboring clusters.
MPS	Mean Particle Separation: Average distance between the surfaces of two neighboring clusters.
N	Number, Total Number of Something
$N(E_F)$	Number of States Per Atom at the Fermi Level
$N_{at/Cl}$	Number of Atoms per Cluster

n	(1) Number Density (e.g., of Charge Carriers),
	(2) Exponent,
	(3) Index
n_W	Weiss Constant
P	Spin Polarization
$P_{Sputter}$	Plasma Sputter Power
p_{AT}	Pressure in the Aggregation Tube
Q_i	Critical Spanning Wave Vector
R	(1) Resistance,
	(2) Reflectivity
R_{meas}	Measured Value of the Resistance
r	Radius, Radial Distance
r_C	Cyclotron Radius
r_{ij}	Distance between Particles i and j
$\vec{r}_{I+,V+,V-,I-}$	Four-Wire Contact Positions
r_{SI}	Area Resistance
$\hat{S}$	Spin Angular Momentum Operator of a Many-Particle System
s	(1) Tunneling Barrier Width,
	(2) Grain Separation
s_{max}	Maximum Tunneling Distance
$\vec{s}$	Spin Angular Momentum of a Single Particle
$\hat{s}$	Single-Particle Spin Angular Momentum Operator
T	Temperature
T_B	Superparamagnetic Blocking Temperature
T_C	Curie Temperature
T_{dep}	Time of Deposition
T_e, T_i	Temperature of the Electron Gas in / of the ion lattice of a Crystalline Solid
T_0	(1) VRH Parameter,
	(2) Reference Temperature
t	(1) Thickness of a Nanocomposite Layer,
	(2) Time
t_B, t_P, t_M	Thickness of the Buffer Layer, the Protection Layer, of Pure Matrix Material in a Nanocomposite Layer

U_{beam}	Electric Potential of the Cluster Ion Beam
U_S	Electric Potential of the 'Sample' Surface of a CIBD Sample
U_{SE}	Electric Potential of the 'Sample Electrode' Surface of a CIBD Sample
V	(1) Volume,
	(2) Voltage
v_D	Drift Velocity
v_F	Fermi Velocity
ΔW	Hopping Energy
w	Width of a Nanocomposite Film
x	Fraction of Volume, Composition, etc.
Z	Charge Number of a Nucleus
$\mathcal{Z}$	Partition Function of the Canonic Ensemble

Greek Symbols:

α	(1) Temperature Coefficient of Resistivity,
	(2) Absorption Coefficient,
	(3) Inverse Localization Length
β	Spin Asymmetry
$\gamma_{kin}, \gamma_{slit}$	Maximum Mass Error Estimated from Cluster Ion Kinetic Energy, Slit Width
ε_r	Dielectric Constant
θ	(1) Relative Angle between Two Magnetic Moments,
	(2) Geometric Angle
λ	(1) Wavelength,
	(2) Areal Fraction
λ_0	Electron Mean Free Path
$\lambda_{cub}, \lambda_{22}, \lambda_{31}, \lambda_{40}$	Geometry Correction Factors
μ	(1) Absolute Value of the Magnetic Dipole Moment,
	(2) Mobility
μ_z	Z-Component of the Magnetic Dipole Moment
$\vec{\mu}$	Magnetic Dipole Moment
v	Frequency

ρ	(1) Volumetric Mass Density,
	(2) Electric Resistivity,
	(3) Electric Charge Density
ρ_0	Electric Resistivity in Zero Magnetic Field
$\rho_{100\,\mathrm{K}}, \rho_{300\,\mathrm{K}}$	Electric Resistivity at 100 K, 300 K in Zero Field
$\Delta\rho/\rho_0$	Magnetoresistance: Relative change of electric resistivity caused by a magnetic field.
σ	(1) Electric Conductivity,
	(2) Spin Orientation Index $\sigma \in \{\uparrow, \downarrow\}$
σ_T	Tunneling Conductivity
$\hat{\sigma}$	Spin Orientation Operator
τ	Relaxation Time
τ^{-1}	(1) Flipping Frequency,
	(2) Scattering Rate
τ_L	Laser Pulse Duration
τ_0^{-1}	Attempt Frequency
ϕ	(1) Tunneling Barrier Height,
	(2) Geometric Angle
φ_i	Single-Particle Wave Function
χ	(1) Magnetic Susceptibility,
	(2) Constant of Decay in the Tunneling Probability
χ_P	Pauli Susceptibility
Ψ_{ij}	Two-Particle Wave Function
ω_C	Cyclotron Frequency

List of Figures

List of Tables

Curriculum Vitae

Education

02/2016 – 02/2023   Doctoral candidate at the Department of Materials- and Geoscience of Technische Universität Darmstadt, working in the Cluster-Assembled Materials group of the research unit Nanostructured Materials at the Institute of Nanotechnology at Karlsruhe Institute of Technology,
Supervisor: Prof. Dr.-Ing. Horst Hahn

10/2007 – 04/2013   Diploma degree in physics from Karlsruhe Institute of Technology.
Title of the thesis: *Untersuchung des Einflusses der Kontaktgeometrie nanostrukturierter Pb/Fe-Punktkontakte auf deren Eigenschaften*"
("Investigation of the Influence of the Contact Geometry of Nanostructured Pb/Fe-Point-Contacts on their Properties")

09/1998 – 07/2007   High school: Albertus-Magnus-Gymnasium Ettlingen
Graduation: Abitur

Work Experience

10/2015–09/2020   Research scientist at the Institute of Nanotechnology of Karlsruhe Institute of Technology in the course of the present work as a doctoral candidate

List of Publications

Peer-Reviewed Publications:

N. Gack, G. Iankevich, C. Benel, R. Kruk, D. Wang, H. Hahn, and T. Reisinger, "Magnetotransport Properties of Ferromagnetic Nanoparticles in a Semiconductor Matrix Studied by Precise Size-Selective Cluster Ion Beam Deposition," Nanomaterials, vol. 10, no. 11, p. 2192, Nov. 2020, doi:10.3390/nano10112192.

N. Gack, C. Reitz, J. L. Hemmerich, M. Könne, R. Bennett, J. Fiedler, H. Gleiter, S. Y. Buhmann, H. Hahn, and T. Reisinger, "Signature of Short-Range van der Waals Forces Observed in Poisson Spot Diffraction with Indium Atoms," Phys. Rev. Lett., vol. 125, no. 5, p. 050401, Jul. 2020, doi:10.1103/PhysRevLett.125.050401.

Conference Poster:

N. Gack, H. Gleiter, H. Hahn, and T. Reisinger, "Design and Characterization of a Source for Buffer Gas Cooled Atoms and Molecules," presented at the Frontiers of Matter-Wave Optics Conference 2016, Arcachon, France, Sep. 2016, Conference Website: https://www.matterwaveoptics.eu/fomo-2016/.

List of References

[1]   C. Benel, T. Reisinger, R. Kruk, and H. Hahn, "Cluster-Assembled Nanocomposites: Functional Properties by Design," Adv. Mater., p. 1806634, Dec. 2018, doi:10.1002/adma.201806634.

[2]   M. Hillenkamp, G. di Domenicantonio, and C. Félix, "Monodispersed Metal Clusters in Solid Matrices: A New Experimental Setup," Rev. Sci. Instrum., vol. 77, no. 2, p. 025104, Feb. 2006, doi:10.1063/1.2173051.

[3]   G. Schultes, M. Schmidt, M. Truar, D. Goettel, O. Freitag-Weber, and U. Werner, "Co-Deposition of Silver Nanoclusters and Sputtered Alumina for Sensor Devices," Thin Solid Films, vol. 515, no. 20–21, pp. 7790–7797, Jul. 2007, doi:10.1016/j.tsf.2007.03.183.

[4]   J. Zhao, L. Cao, R. E. Palmer, K. Nordlund, and F. Djurabekova, "Formation and Emission Mechanisms of Ag Nanoclusters in the Ar Matrix Assembly Cluster Source," Phys. Rev. Mater., vol. 1, no. 6, p. 066002, Nov. 2017, doi:10.1103/PhysRevMaterials.1.066002.

[5]   A. S. Fischer, "Crystalline and amorphous cluster-assembled nano-materials, synthesized with a novel cluster deposition system," PhD Thesis, TU Darmstadt, Darmstadt, Germany, 2015, https://tuprints.ulb.tu-darmstadt.de/id/eprint/4631.

[6]   A. Fischer, R. Kruk, D. Wang, and H. Hahn, "Magnetic Properties of Iron Cluster/Chromium Matrix Nanocomposites," Beilstein J. Nanotechnol., vol. 6, pp. 1158–1163, May 2015, doi:10.3762/bjnano.6.117.

[7]   A. Fischer, R. Kruk, and H. Hahn, "A Versatile Apparatus for the Fine-Tuned Synthesis of Cluster-Based Materials," Rev. Sci. Instrum., vol. 86, no. 2, p. 023304, Feb. 2015, doi:10.1063/1.4908166.

[8]   S. F. Marenkin, A. D. Izotov, I. V. Fedorchenko, and V. M. Novotortsev, "Manufacture of Magnetic Granular Structures in Semiconductor-Ferromagnet Systems," Russ. J. Inorg. Chem., vol. 60, no. 3, pp. 295–300, Mar. 2015, doi:10.1134/S0036023615030146.

[9]   M. Knobel, W. C. Nunes, L. M. Socolovsky, E. De Biasi, J. M. Vargas, and J. C. Denardin, "Superparamagnetism and Other Magnetic Features in Granular Materials: A Review on Ideal and Real Systems," J. Nanosci. Nanotechnol., vol. 8, no. 6, pp. 2836–2857, Jun. 2008, doi:10.1166/jnn.2008.15348.

[10]   P. N. Hai, S. Ohya, and M. Tanaka, "Long Spin-Relaxation Time in a Single Metal Nanoparticle," Nat. Nanotechnol., vol. 5, no. 8, pp. 593–596, Aug. 2010, doi:10.1038/nnano.2010.130.

[11]   R. C. Temple, M. McLaren, R. M. D. Brydson, B. J. Hickey, and C. H. Marrows, "Long Spin Lifetime and Large Barrier Polarisation in Single Electron Transport through a CoFe Nanoparticle," Sci. Rep., vol. 6, no. 1, p. 28296, Sep. 2016, doi:10.1038/srep28296.

[12]   K. Yakushiji, F. Ernult, H. Imamura, K. Yamane, S. Mitani, K. Takanashi, S. Takahashi, S. Maekawa, and H. Fujimori, "Enhanced Spin Accumulation and Novel Magnetotransport in Nanoparticles," Nat. Mater., vol. 4, no. 1, pp. 57–61, Dec. 2004, doi:10.1038/nmat1278.

[13]   H. Fujimori, S. Mitani, and S. Ohnuma, "Tunnel-Type GMR in Metal-Nonmetal Granular Alloy Thin Films," Mater. Sci. Eng. B, vol. 31, no. 1–2, pp. 219–223, Apr. 1995, doi:10.1016/0921-5107(94)08032-1.

[14]   A. E. Berkowitz, J. R. Mitchell, M. J. Carey, A. P. Young, S. Zhang, F. E. Spada, F. T. Parker, A. Hutten, and G. Thomas, "Giant Magnetoresistance in Heterogeneous Cu-Co Alloys," Phys. Rev. Lett., vol. 68, no. 25, pp. 3745–3748, Jun. 1992, doi:10.1103/PhysRevLett.68.3745.

[15]   J. Q. Xiao, J. S. Jiang, and C. L. Chien, "Giant Magnetoresistance in the Granular Co-Ag System," Phys. Rev. B, vol. 46, no. 14, pp. 9266–9269, Oct. 1992, doi:10.1103/PhysRevB.46.9266.

[16]   J. Q. Xiao, J. S. Jiang, and C. L. Chien, "Giant Magnetoresistance in Nonmultilayer Magnetic Systems," Phys. Rev. Lett., vol. 68, no. 25, pp. 3749–3752, Jun. 1992, doi:10.1103/PhysRevLett.68.3749.

[17]   A. Hirohata and K. Takanashi, "Future Perspectives for Spintronic Devices," J. Phys. D: Appl. Phys., vol. 47, no. 19, p. 193001, May 2014, doi:10.1088/0022-3727/47/19/193001.

[18]   E. C. Gingrich, B. M. Niedzielski, J. A. Glick, Y. Wang, D. L. Miller, R. Loloee, W. P. Pratt Jr, and N. O. Birge, "Controllable 0–π Josephson Junctions Containing a Ferromagnetic Spin Valve," Nat. Phys., vol. 12, no. 6, pp. 564–567, Jun. 2016, doi:10.1038/nphys3681.

[19]   M. Weides, M. Kemmler, H. Kohlstedt, R. Waser, D. Koelle, R. Kleiner, and E. Goldobin, "0−π Josephson Tunnel Junctions with Ferromagnetic Barrier," Phys. Rev. Lett., vol. 97, no. 24, p. 247001, Dec. 2006, doi:10.1103/PhysRevLett.97.247001.

[20]   M. L. Schneider, C. A. Donnelly, S. E. Russek, B. Baek, M. R. Pufall, P. F. Hopkins, P. D. Dresselhaus, S. P. Benz, and W. H. Rippard, "Ultralow Power Artificial Synapses Using Nanotextured Magnetic Josephson Junctions," Sci. Adv., vol. 4, no. 1, p. e1701329, Jan. 2018, doi:10.1126/sciadv.1701329.

[21]   L. B. Ioffe, V. B. Geshkenbein, M. V. Feigel'man, A. L. Fauchère, and G. Blatter, "Environmentally Decoupled Sds-Wave Josephson Junctions for Quantum Computing," Nature, vol. 398, no. 6729, pp. 679–681, Apr. 1999, doi:10.1038/19464.

[22]   T. Yamashita, K. Tanikawa, S. Takahashi, and S. Maekawa, "Superconducting π Qubit with a Ferromagnetic Josephson Junction," Phys. Rev. Lett., vol. 95, no. 9, p. 097001, Aug. 2005, doi:10.1103/PhysRevLett.95.097001.

[23]   X. Batlle and A. Labarta, "Finite-Size Effects in Fine Particles: Magnetic and Transport Properties," J. Phys. D: Appl. Phys., vol. 35, no. 6, pp. R15–R42, Mar. 2002, doi:10.1088/0022-3727/35/6/201.

[24] M. Holdenried, B. Hackenbroich, and H. Micklitz, "Systematic Studies of Tunneling Magnetoresistance in Granular Films Made from Well-Defined Co Clusters," J. Magn. Magn. Mater., vol. 231, no. 1, pp. 13–19, May 2001, doi:10.1016/S0304-8853(01)00143-3.

[25] P. Allia, M. Coisson, P. Tiberto, F. Vinai, M. Knobel, M. Novak, and W. Nunes, "Granular Cu-Co Alloys as Interacting Superparamagnets," Phys. Rev. B, vol. 64, no. 14, p. 144420, Sep. 2001, doi:10.1103/PhysRevB.64.144420.

[26] M. Jamet, W. Wernsdorfer, C. Thirion, D. Mailly, V. Dupuis, P. Mélinon, and A. Pérez, "Magnetic Anisotropy of a Single Cobalt Nanocluster," Phys. Rev. Lett., vol. 86, no. 20, pp. 4676–4679, May 2001, doi:10.1103/PhysRevLett.86.4676.

[27] C. Chappert, A. Fert, and F. N. Van Dau, "The Emergence of Spin Electronics in Data Storage," Nat. Mater., vol. 6, no. 11, pp. 813–823, Nov. 2007, doi:10.1038/nmat2024.

[28] A. Fert and F. N. Van Dau, "Spintronics, from Giant Magnetoresistance to Magnetic Skyrmions and Topological Insulators," C. R. Phys., vol. 20, no. 7–8, pp. 817–831, Nov. 2019, doi:10.1016/j.crhy.2019.05.020.

[29] A. Molinari, H. Hahn, and R. Kruk, "Voltage-Controlled On/Off Switching of Ferromagnetism in Manganite Supercapacitors," Adv. Mater., vol. 30, no. 1, p. 1703908, Jan. 2018, doi:10.1002/adma.201703908.

[30] L. V. Lutsev, A. I. Stognij, and N. N. Novitskii, "Giant Magnetoresistance in Semiconductor/Granular Film Heterostructures with Cobalt Nanoparticles," Phys. Rev. B, vol. 80, no. 18, p. 184423, Nov. 2009, doi:10.1103/PhysRevB.80.184423.

[31] L. V. Lutsev, L. A. Shelukhin, A. I. Stognij, and N. N. Novitskii, "Relaxation Processes of the Light-Induced Giant Injection Magnetoresistance in Semiconductor/Granular-Film Heterostructures with Cobalt Nanoparticles," Phys. Rev. B, vol. 99, no. 13, p. 134433, Apr. 2019, doi:10.1103/PhysRevB.99.134433.

[32] K. Takiguchi, L. D. Anh, T. Chiba, T. Koyama, D. Chiba, and M. Tanaka, "Giant Gate-Controlled Proximity Magnetoresistance in Semiconductor-Based Ferromagnetic–Non-Magnetic Bilayers," Nat. Phys., vol. 15, no. 11, pp. 1134–1139, Nov. 2019, doi:10.1038/s41567-019-0621-6.

[33] T. Dietl, "A Ten-Year Perspective on Dilute Magnetic Semiconductors and Oxides," Nat. Mater., vol. 9, no. 12, pp. 965–974, Dec. 2010, doi:10.1038/nmat2898.

[34] W. Liu, H. Zhang, J. Shi, Z. Wang, C. Song, X. Wang, S. Lu, X. Zhou, L. Gu, D. V. Louzguine-Luzgin, M. Chen, K. Yao, and N. Chen, "A Room-Temperature Magnetic Semiconductor from a Ferromagnetic Metallic Glass," Nat. Commun., vol. 7, no. 1, p. 13497, Dec. 2016, doi:10.1038/ncomms13497.

[35] N. Chen, K. Fang, H. Zhang, Y. Zhang, W. Liu, K. Yao, and Z. Zhang, "Amorphous Magnetic Semiconductors with Curie Temperatures above Room Temperature," J. Semicond., vol. 40, no. 8, p. 081510, Aug. 2019, doi:10.1088/1674-4926/40/8/081510.

[36] L. Chen, X. Yang, F. Yang, J. Zhao, J. Misuraca, P. Xiong, and S. von Molnár, "Enhancing the Curie Temperature of Ferromagnetic Semiconductor (Ga,Mn)As to 200 K via Nanostructure Engineering," Nano Lett., vol. 11, no. 7, pp. 2584–2589, Jul. 2011, doi:10.1021/nl201187m.

[37] M. Jamet, A. Barski, T. Devillers, V. Poydenot, R. Dujardin, P. Bayle-Guillemaud, J. Rothman, E. Bellet-Amalric, A. Marty, J. Cibert, R. Mattana, and S. Tatarenko, "High-Curie-Temperature Ferromagnetism in Self-Organized $Ge_{1-x}Mn_x$ Nanocolumns," Nat. Mater., vol. 5, no. 8, pp. 653–659, Aug. 2006, doi:10.1038/nmat1686.

[38] S. S. Yu, T. T. L. anh, Y. E. Ihm, D. Kim, H. Kim, S. K. Hong, C. S. Kim, and H. Ryu, "Magnetic and Magnetotransport Properties of Annealed Amorphous $Ge_{1-x}Mn_x$ Semiconductor Thin Films," in *2007 2nd IEEE International Conference on Nano/Micro Engineered and Molecular Systems*, Bangkok, Thailand, Jan. 2007, pp. 618–621, doi:10.1109/NEMS.2007.352094.

[39] S. Sugahara, K. L. Lee, S. Yada, and M. Tanaka, "Precipitation of Amorphous Ferromagnetic Semiconductor Phase in Epitaxially Grown Mn-Doped Ge Thin Films," Jpn. J. Appl. Phys., vol. 44, no. No. 48, pp. L1426–L1429, Nov. 2005, doi:10.1143/JJAP.44.L1426.

[40] K. Potzger, S. Zhou, H. Reuther, A. Mücklich, F. Eichhorn, N. Schell, W. Skorupa, M. Helm, J. Fassbender, T. Herrmannsdörfer, and T. P. Papageorgiou, "Fe Implanted Ferromagnetic ZnO," Appl. Phys. Lett., vol. 88, no. 5, p. 052508, Jan. 2006, doi:10.1063/1.2169912.

[41] S. Zhou, K. Potzger, G. Talut, H. Reuther, J. von Borany, R. Grötzschel, W. Skorupa, M. Helm, J. Fassbender, N. Volbers, M. Lorenz, and T. Herrmannsdörfer, "Fe-Implanted ZnO: Magnetic Precipitates versus Dilution," J. Appl. Phys., vol. 103, no. 2, p. 023902, Jan. 2008, doi:10.1063/1.2828060.

[42] I. V. Fedorchenko, A. N. Aronov, S. F. Marenkin, N. P. Simonenko, N. M. Boeva, A. V. Kochura, and E. Lahderanta, "Phase Diagram of the $ZnSnAs_2$–MnAs System," J. Alloys Compd., vol. 626, pp. 9–15, Mar. 2015, doi:10.1016/j.jallcom.2014.11.147.

[43] I. V. Fedorchenko, L. Kilanski, I. Zakharchuk, P. Geydt, E. Lahderanta, P. N. Vasilyev, N. P. Simonenko, A. N. Aronov, W. Dobrowolski, and S. F. Marenkin, "Composites Based on Self-Assembled MnAs Ferromagnet Nanoclusters Embedded in $ZnSnAs_2$ Semiconductor," J. Alloys Compd., vol. 650, pp. 277–284, Nov. 2015, doi:10.1016/j.jallcom.2015.08.006.

[44] V. G. Myagkov, I. A. Tambasov, O. A. Bayukov, V. S. Zhigalov, L. E. Bykova, Yu. L. Mikhlin, M. N. Volochaev, and G. N. Bondarenko, "Solid State Synthesis and Characterization of Ferromagnetic Nanocomposite $Fe-In_2O_3$ Thin Films," J. Alloys Compd., vol. 612, pp. 189–194, Nov. 2014, doi:10.1016/j.jallcom.2014.05.176.

[45] C. Alof, B. Stahl, M. Ghafari, and H. Hahn, "Interface Contribution to Giant Magnetoresistance in Granular AgFe Studied with Mössbauer Spectroscopy," J. Appl. Phys., vol. 88, no. 7, p. 4212, 2000, doi:10.1063/1.1289232.

[46] P. Allia, M. Coisson, F. Spizzo, P. Tiberto, and F. Vinai, "Magnetic Correlation States in Cosputtered Granular $Ag_{100-x}Fe_x$ Films," Phys. Rev. B, vol. 73, no. 5, p. 054409, Feb. 2006, doi:10.1103/PhysRevB.73.054409.

[47] S. M. Thompson, "The Discovery, Development and Future of GMR: The Nobel Prize 2007," J. Phys. D: Appl. Phys., vol. 41, no. 9, p. 093001, May 2008, doi:10.1088/0022-3727/41/9/093001.

[48] A. D. Cronin, J. Schmiedmayer, and D. E. Pritchard, "Optics and Interferometry with Atoms and Molecules," Rev. Mod. Phys., vol. 81, no. 3, pp. 1051–1129, Jul. 2009, doi:10.1103/RevModPhys.81.1051.

[49] K. Hornberger, S. Gerlich, P. Haslinger, S. Nimmrichter, and M. Arndt, "*Colloquium*: Quantum Interference of Clusters and Molecules," Rev. Mod. Phys., vol. 84, no. 1, pp. 157–173, Feb. 2012, doi:10.1103/RevModPhys.84.157.

[50] T. Reisinger, P. M. Leufke, H. Gleiter, and H. Hahn, "On the Relative Intensity of Poisson's Spot," New J. Phys., vol. 19, no. 3, p. 033022, Mar. 2017, doi:10.1088/1367-2630/aa5e7f.

[51] N. Gack, C. Reitz, J. L. Hemmerich, M. Könne, R. Bennett, J. Fiedler, H. Gleiter, S. Y. Buhmann, H. Hahn, and T. Reisinger, "Signature of Short-Range van Der Waals Forces Observed in Poisson Spot Diffraction with Indium Atoms," Phys. Rev. Lett., vol. 125, no. 5, p. 050401, Jul. 2020, doi:10.1103/PhysRevLett.125.050401.

[52] J. M. D. Coey, *Magnetism and Magnetic Materials*. Cambridge, UK: Cambridge University Press, 2010, doi:10.1017/CBO9780511845000.

[53] W. Nolting, *Quantum Mechanics - Methods and Applications*. Cham, Germany: Springer, 2017, doi:10.1007/978-3-319-63324-4.

[54] T. Fließbach, *Elektrodynamik*. Heidelberg, Germany: Spektrum Akademischer Verlag, 2012, doi:10.1007/978-3-8274-3036-6.

[55] H. Ibach and H. Lüth, *Festkörperphysik*. Berlin, Heidelberg, Germany: Springer Berlin Heidelberg, 2009, doi:10.1007/978-3-540-85795-2.

[56] R. Gross and A. Marx, *Festkörperphysik*. München, Germany: Oldenbourg, 2012, doi:10.1524/9783486714869.

[57] P. Hadley, "Electron Density of States for Bcc Iron." http://lampx.tugraz.at/~hadley/ss1/materials/dos/iron.html (accessed June 6, 2023).

[58] F. Cardarelli, *Materials Handbook*. London, UK: Springer London, UK, 2008, doi:10.1007/978-1-84628-669-8.

[59] S. C. Abrahams, L. Guttman, and J. S. Kasper, "Neutron Diffraction Determination of Antiferromagnetism in Face-Centered Cubic (γ) Iron," Phys. Rev., vol. 127, no. 6, pp. 2052–2055, Sep. 1962, doi:10.1103/PhysRev.127.2052.

[60] P. Ehrhart, B. Schönfeld, H. H. Ettwig, and W. Pepperhoff, "The Lattice Structure of Antiferromagnetic γ-Iron," J. Magn. Magn. Mater., vol. 22, no. 1, pp. 79–85, Dec. 1980, doi:10.1016/0304-8853(80)90011-6.

[61] J. Kübler, "Magnetic Moments of Ferromagnetic and Antiferromagnetic Bcc and Fcc Iron," Phys. Lett. A, vol. 81, no. 1, pp. 81–83, Jan. 1981, doi:10.1016/0375-9601(81)90311-X.

[62] V. L. Moruzzi, P. M. Marcus, and J. Kübler, "Magnetovolume Instabilities and Ferromagnetism versus Antiferromagnetism in Bulk Fcc Iron and Manganese," Phys. Rev. B, vol. 39, no. 10, pp. 6957–6961, Apr. 1989, doi:10.1103/PhysRevB.39.6957.

[63] D. Bagayoko and J. Callaway, "Lattice-Parameter Dependence of Ferromagnetism in Bcc and Fcc Iron," Phys. Rev. B, vol. 28, no. 10, pp. 5419–5422, Nov. 1983, doi:10.1103/PhysRevB.28.5419.

[64] V. L. Moruzzi, P. M. Marcus, K. Schwarz, and P. Mohn, "Ferromagnetic Phases of Bcc and Fcc Fe, Co, and Ni," Phys. Rev. B, vol. 34, no. 3, pp. 1784–1791, Aug. 1986, doi:10.1103/PhysRevB.34.1784.

[65]   C. Gros, "Festkörpertheorie II, SS08, Skript 6, Magnetismus," 2008.
         https://itp.uni-frankfurt.de/~gros/Vorlesungen/FKT/FKT_6.pdf (accessed June 6, 2023).

[66]   E. C. Stoner and E. P. Wohlfarth, "A Mechanism of Magnetic Hysteresis in Heterogeneous
         Alloys," Phil. Trans. R. Soc. Lond. A, vol. 240, no. 826, pp. 599–642, May 1948,
         doi:10.1098/rsta.1948.0007.

[67]   S. A. Majetich and M. Sachan, "Magnetostatic Interactions in Magnetic Nanoparticle
         Assemblies: Energy, Time and Length Scales," J. Phys. D: Appl. Phys., vol. 39, no. 21,
         pp. R407–R422, Nov. 2006, doi:10.1088/0022-3727/39/21/R02.

[68]   S. Zhang, Q. Wu, Y. Liu, and O. V. Yazyev, "Magnetoresistance from Fermi Surface Topology,"
         Phys. Rev. B, vol. 99, no. 3, p. 035142, Jan. 2019, doi:10.1103/PhysRevB.99.035142.

[69]   J. Smit, "Magnetoresistance of Ferromagnetic Metals and Alloys at Low Temperatures,"
         Physica, vol. 17, no. 6, pp. 612–627, Jun. 1951, doi:10.1016/0031-8914(51)90117-6.

[70]   I. A. Campbell, A. Fert, and O. Jaoul, "The Spontaneous Resistivity Anisotropy in Ni-Based
         Alloys," J. Phys. C: Solid State Phys., vol. 3, no. 1S, pp. S95–S101, May 1970,
         doi:10.1088/0022-3719/3/1S/310.

[71]   O. Jaoul, I. A. Campbell, and A. Fert, "Spontaneous Resistivity Anisotropy in Ni Alloys,"
         J. Magn. Magn. Mater., vol. 5, no. 1, pp. 23–34, Mar. 1977,
         doi:10.1016/0304-8853(77)90193-7.

[72]   A. P. Malozemoff, "Anisotropic Magnetoresistance with Cubic Anisotropy and Weak
         Ferromagnetism: A New Paradigm," Phys. Rev. B, vol. 34, no. 3, pp. 1853–1863, Aug. 1986,
         doi:10.1103/PhysRevB.34.1853.

[73]   S. Kokado, M. Tsunoda, K. Harigaya, and A. Sakuma, "Anisotropic Magnetoresistance Effects
         in Fe, Co, Ni, Fe_4N, and Half-Metallic Ferromagnet: A Systematic Analysis," J. Phys. Soc. Jpn.,
         vol. 81, no. 2, p. 024705, Feb. 2012, doi:10.1143/JPSJ.81.024705.

[74]   M. Viret, D. Vignoles, D. Cole, J. M. D. Coey, W. Allen, D. S. Daniel, and J. F. Gregg,
         "Spin Scattering in Ferromagnetic Thin Films," Phys. Rev. B, vol. 53, no. 13, pp. 8464–8468,
         Apr. 1996, doi:10.1103/PhysRevB.53.8464.

[75]   M. Jullière, "Tunneling between Ferromagnetic Films," Phys. Lett. A, vol. 54, no. 3,
         pp. 225–226, Sep. 1975, doi:10.1016/0375-9601(75)90174-7.

[76]   J. C. Slonczewski, "Conductance and Exchange Coupling of Two Ferromagnets Separated by a
         Tunneling Barrier," Phys. Rev. B, vol. 39, no. 10, pp. 6995–7002, Apr. 1989,
         doi:10.1103/PhysRevB.39.6995.

[77]   R. Meservey and P. M. Tedrow, "Spin-Polarized Electron Tunneling," Phys. Rep., vol. 238,
         no. 4, pp. 173–243, Mar. 1994, doi:10.1016/0370-1573(94)90105-8.

[78]   J. S. Moodera and G. Mathon, "Spin Polarized Tunneling in Ferromagnetic Junctions,"
         J. Magn. Magn. Mater., vol. 200, no. 1–3, pp. 248–273, Oct. 1999,
         doi:10.1016/S0304-8853(99)00515-6.

[79]   S. Maekawa and U. Gäfvert, "Electron Tunneling between Ferromagnetic Films,"
         IEEE Trans. Magn., vol. 18, no. 2, pp. 707–708, Mar. 1982,
         doi:10.1109/TMAG.1982.1061834.

[80] T. Miyazaki and N. Tezuka, "Giant Magnetic Tunneling Effect in Fe/Al$_2$O$_3$/Fe Junction," J. Magn. Magn. Mater., vol. 139, no. 3, pp. L231–L234, Jan. 1995, doi:10.1016/0304-8853(95)90001-2.

[81] J. S. Moodera, L. R. Kinder, T. M. Wong, and R. Meservey, "Large Magnetoresistance at Room Temperature in Ferromagnetic Thin Film Tunnel Junctions," Phys. Rev. Lett., vol. 74, no. 16, pp. 3273–3276, Apr. 1995, doi:10.1103/PhysRevLett.74.3273.

[82] J. Inoue and S. Maekawa, "Theory of Tunneling Magnetoresistance in Granular Magnetic Films," Phys. Rev. B, vol. 53, no. 18, pp. R11927–R11929, May 1996, doi:10.1103/PhysRevB.53.R11927.

[83] G. Binasch, P. Grünberg, F. Saurenbach, and W. Zinn, "Enhanced Magnetoresistance in Layered Magnetic Structures with Antiferromagnetic Interlayer Exchange," Phys. Rev. B, vol. 39, no. 7, pp. 4828–4830, Mar. 1989, doi:10.1103/PhysRevB.39.4828.

[84] M. N. Baibich, J. M. Broto, A. Fert, F. N. Van Dau, F. Petroff, P. Etienne, G. Creuzet, A. Friederich, and J. Chazelas, "Giant Magnetoresistance of (001)Fe/(001)Cr Magnetic Superlattices," Phys. Rev. Lett., vol. 61, no. 21, pp. 2472–2475, Nov. 1988, doi:10.1103/PhysRevLett.61.2472.

[85] R. E. Camley and J. Barnaś, "Theory of Giant Magnetoresistance Effects in Magnetic Layered Structures with Antiferromagnetic Coupling," Phys. Rev. Lett., vol. 63, no. 6, pp. 664–667, Aug. 1989, doi:10.1103/PhysRevLett.63.664.

[86] P. M. Levy, S. Zhang, and A. Fert, "Electrical Conductivity of Magnetic Multilayered Structures," Phys. Rev. Lett., vol. 65, no. 13, pp. 1643–1646, Sep. 1990, doi:10.1103/PhysRevLett.65.1643.

[87] W. P. Pratt, S.-F. Lee, J. M. Slaughter, R. Loloee, P. A. Schroeder, and J. Bass, "Perpendicular Giant Magnetoresistances of Ag/Co Multilayers," Phys. Rev. Lett., vol. 66, no. 23, pp. 3060–3063, Jun. 1991, doi:10.1103/PhysRevLett.66.3060.

[88] T. Valet and A. Fert, "Theory of the Perpendicular Magnetoresistance in Magnetic Multilayers," Phys. Rev. B, vol. 48, no. 10, pp. 7099–7113, Sep. 1993, doi:10.1103/PhysRevB.48.7099.

[89] A. Fert and S.-F. Lee, "Theory of the Bipolar Spin Switch," Phys. Rev. B, vol. 53, no. 10, pp. 6554–6565, Mar. 1996, doi:10.1103/PhysRevB.53.6554.

[90] A. Fert, "Giant Magnetoresistance," Scholarpedia, vol. 6, no. 2, p. 6982, 2011, doi:10.4249/scholarpedia.6982.

[91] S. Zhang, P. M. Levy, and A. Fert, "Conductivity and Magnetoresistance of Magnetic Multilayered Structures," Phys. Rev. B, vol. 45, no. 15, pp. 8689–8702, Apr. 1992, doi:10.1103/PhysRevB.45.8689.

[92] S. S. P. Parkin, N. More, and K. P. Roche, "Oscillations in Exchange Coupling and Magnetoresistance in Metallic Superlattice Structures: Co/Ru, Co/Cr, and Fe/Cr," Phys. Rev. Lett., vol. 64, no. 19, pp. 2304–2307, May 1990, doi:10.1103/PhysRevLett.64.2304.

[93]   J. Unguris, R. J. Celotta, and D. T. Pierce, "Observation of Two Different Oscillation Periods in the Exchange Coupling of Fe/Cr/Fe(100)," Phys. Rev. Lett., vol. 67, no. 1, pp. 140–143, Jul. 1991, doi:10.1103/PhysRevLett.67.140.

[94]   S. S. P. Parkin, "Systematic Variation of the Strength and Oscillation Period of Indirect Magnetic Exchange Coupling through the 3d, 4d, and 5d Transition Metals," Phys. Rev. Lett., vol. 67, no. 25, pp. 3598–3601, Dec. 1991, doi:10.1103/PhysRevLett.67.3598.

[95]   M. A. Ruderman and C. Kittel, "Indirect Exchange Coupling of Nuclear Magnetic Moments by Conduction Electrons," Phys. Rev., vol. 96, no. 1, pp. 99–102, Oct. 1954, doi:10.1103/PhysRev.96.99.

[96]   T. Kasuya, "A Theory of Metallic Ferro- and Antiferromagnetism on Zener's Model," Prog. Theor. Phys., vol. 16, no. 1, pp. 45–57, Jul. 1956, doi:10.1143/PTP.16.45.

[97]   K. Yosida, "Magnetic Properties of Cu-Mn Alloys," Phys. Rev., vol. 106, no. 5, pp. 893–898, Jun. 1957, doi:10.1103/PhysRev.106.893.

[98]   P. Grünberg and D. E. Bürgler, "Metallic Multilayers: Discovery of Interlayer Exchange Coupling and GMR," in Handbook of Spintronics, Y. Xu, D. D. Awschalom, and J. Nitta, Eds. Dordrecht, Netherlands: Springer Netherlands, 2015, pp. 1–16, doi:10.1007/978-94-007-7604-3_6-1.

[99]   M. D. Stiles, "Interlayer Exchange Coupling," J. Magn. Magn. Mater., vol. 200, no. 1–3, pp. 322–337, 1999, doi:10.1016/S0304-8853(99)00334-0.

[100]   P. Bruno, "Theory of Interlayer Magnetic Coupling," Phys. Rev. B, vol. 52, no. 1, pp. 411–439, Jul. 1995, doi:10.1103/PhysRevB.52.411.

[101]   E. F. Ferrari, F. C. S. da Silva, and M. Knobel, "Theory of Giant Magnetoresistance in Granular Alloys," Phys. Rev. B, vol. 59, no. 13, pp. 8412–8415, Apr. 1999, doi:10.1103/PhysRevB.59.8412.

[102]   S. Zhang and P. M. Levy, "Conductivity Perpendicular to the Plane of Multilayered Structures," J. Appl. Phys., vol. 69, no. 8, pp. 4786–4788, Apr. 1991, doi:10.1063/1.348229.

[103]   S. Zhang, "Theory of Giant Magnetoresistance in Magnetic Granular Films," Appl. Phys. Lett., vol. 61, no. 15, pp. 1855–1857, Oct. 1992, doi:10.1063/1.108396.

[104]   S. Zhang and P. M. Levy, "Conductivity and Magnetoresistance in Magnetic Granular Films (Invited)," J. Appl. Phys., vol. 73, no. 10, pp. 5315–5319, May 1993, doi:10.1063/1.353766.

[105]   H. E. Camblong, P. M. Levy, and S. Zhang, "Electron Transport in Magnetic Inhomogeneous Media," Phys. Rev. B, vol. 51, no. 22, pp. 16052–16072, Jun. 1995, doi:10.1103/PhysRevB.51.16052.

[106]   E. F. Ferrari, F. C. S. da Silva, and M. Knobel, "Influence of the Distribution of Magnetic Moments on the Magnetization and Magnetoresistance in Granular Alloys," Phys. Rev. B, vol. 56, no. 10, pp. 6086–6093, Sep. 1997, doi:10.1103/PhysRevB.56.6086.

[107]   Yu. G. Pogorelov, M. M. P. de Azevedo, and J. B. Sousa, "Microscopic Theory of Magnetoresistance in Granular Materials," Phys. Rev. B, vol. 58, no. 1, pp. 425–431, Jul. 1998, doi:10.1103/PhysRevB.58.425.

[108] H. Haberland, M. Karrais, and M. Mall, "A New Type of Cluster and Cluster Ion Source," Z. Phys. D: At., Mol. Clusters, vol. 20, no. 1–4, pp. 413–415, Mar. 1991, doi:10.1007/BF01544025.

[109] H. Haberland, "History, Some Basics, and an Outlook," in *Gas-Phase Synthesis of Nanoparticles*, Y. Huttel, Ed. Weinheim, Germany: Wiley-VCH Verlag GmbH & Co. KGaA, 2017, pp. 1–21, doi:10.1002/9783527698417.ch1.

[110] D. W. Oxtoby, "Homogeneous Nucleation: Theory and Experiment," J. Phys.: Condens. Matter, vol. 4, no. 38, pp. 7627–7650, Sep. 1992, doi:10.1088/0953-8984/4/38/001.

[111] V. I. Kalikmanov, *Nucleation Theory*, vol. 860. Dordrecht, Netherlands: Springer Netherlands, 2013, doi:10.1007/978-90-481-3643-8.

[112] H. Haberland, M. Mall, M. Moseler, Y. Qiang, T. Reiners, and Y. Thurner, "Filling of Micron-sized Contact Holes with Copper by Energetic Cluster Impact," J. Vac. Sci. Technol. A, vol. 12, no. 5, pp. 2925–2930, Sep. 1994, doi:10.1116/1.578967.

[113] H. Haberland, Ed., *Clusters of Atoms and Molecules*, vol. 52. Berlin, Heidelberg, Germany: Springer Berlin Heidelberg, 1994, doi:10.1007/978-3-642-84329-7.

[114] J. Söderlund, L. B. Kiss, G. A. Niklasson, and C. G. Granqvist, "Lognormal Size Distributions in Particle Growth Processes without Coagulation," Phys. Rev. Lett., vol. 80, no. 11, pp. 2386–2388, Mar. 1998, doi:10.1103/PhysRevLett.80.2386.

[115] N. Gack, G. Iankevich, C. Benel, R. Kruk, D. Wang, H. Hahn, and T. Reisinger, "Magnetotransport Properties of Ferromagnetic Nanoparticles in a Semiconductor Matrix Studied by Precise Size-Selective Cluster Ion Beam Deposition," Nanomaterials, vol. 10, no. 11, p. 2192, Nov. 2020, doi:10.3390/nano10112192.

[116] P. Villars (Chief Editor) and H. Okamoto (Section Editor), "Fe-Ge Binary Phase Diagram 0–100 at.% Ge." SpringerMaterials Release 2016, Springer, Heidelberg, Germany, & Material Phases Data System (MPDS), Switzerland, & National Institute for Materials Science (NIMS), Japan. Database: Pauling File Multinaries Edition – 2012, Dataset: c_0901040, [Online]. Available: https://materials.springer.com/isp/phase-diagram/docs/c_0901040.

[117] K. Yasukōchi, K. Kanematsu, and T. Ohoyama, "Magnetic Properties of Intermetallic Compounds in Iron-Germanium System: $Fe_{1.67}Ge$ and $FeGe_2$," J. Phys. Soc. Jpn., vol. 16, no. 3, pp. 429–433, Mar. 1961, doi:10.1143/JPSJ.16.429.

[118] J. W. Drijver, S. G. Sinnema, and F. van der Woude, "Magnetic Properties of Hexagonal and Cubic Fe_3Ge," J. Phys. F: Met. Phys., vol. 6, no. 11, pp. 2165–2177, Nov. 1976, doi:10.1088/0305-4608/6/11/015.

[119] D. D. Vaughn, D. Sun, J. A. Moyer, A. J. Biacchi, R. Misra, P. Schiffer, and R. E. Schaak, "Solution-Phase Synthesis and Magnetic Properties of Single-Crystal Iron Germanide Nanostructures," Chem. Mater., vol. 25, no. 21, pp. 4396–4401, Nov. 2013, doi:10.1021/cm402795r.

[120] S. Choi, S. C. Hong, S. Cho, Y. Kim, J. B. Ketterson, C.-U. Jung, K. Rhie, B.-J. Kim, and Y. C. Kim, "Ferromagnetic Properties in Cr, Fe-Doped Ge Single Crystals," J. Appl. Phys., vol. 93, no. 10, pp. 7670–7672, May 2003, doi:10.1063/1.1558611.

[121] F. Tsui, L. He, L. Ma, A. Tkachuk, Y. S. Chu, K. Nakajima, and T. Chikyow, "Novel Germanium-Based Magnetic Semiconductors," Phys. Rev. Lett., vol. 91, no. 17, p. 177203, Oct. 2003, doi:10.1103/PhysRevLett.91.177203.

[122] W. S. Rasband, *ImageJ*. Bethesda, Maryland, USA: U. S. National Institute of Health, 1997, https://imagej.nih.gov/ij.

[123] A. H. Clark, "Electrical and Optical Properties of Amorphous Germanium," Phys. Rev., vol. 154, no. 3, pp. 750–757, Feb. 1967, doi:10.1103/PhysRev.154.750.

[124] P. A. Walley, "Electrical Conduction in Amorphous Silicon and Germanium," Thin Solid Films, vol. 2, no. 4, pp. 327–336, Nov. 1968, doi:10.1016/0040-6090(68)90038-2.

[125] P. A. Walley and A. K. Jonscher, "Electrical Conduction in Amorphous Germanium," Thin Solid Films, vol. 1, no. 5, pp. 367–377, Mar. 1968, doi:10.1016/0040-6090(68)90026-6.

[126] B. G. Streetman and S. Banerjee, *Solid State Electronic Devices*, 7th ed. Harlow, UK: Pearson Education Limited, 2015, ISBN 978-0-13-335603-8.

[127] S. M. Sze and K. K. Ng, *Physics of Semiconductor Devices*, 3rd ed. Hoboken, NJ, USA: Wiley-Interscience, 2007, doi:10.1002/0470068329.

[128] A. Rockett, *The Materials Science of Semiconductors*. New York, NY, USA: Springer, 2008, doi:10.1007/978-0-387-68650-9.

[129] H. Richter and G. Breitling, "Struktur des amorphen Germaniums und Siliciums," Z. Naturforsch., A: Astrophys., Phys. Phys. Chem., vol. 13, no. 11, Jan. 1958, doi:10.1515/zna-1958-1109.

[130] R. M. Mehra, R. Shyam, and P. C. Mathur, "Magnetoresistance in Amorphous Semiconductors," Thin Solid Films, vol. 100, no. 2, pp. 81–110, Feb. 1983, doi:10.1016/0040-6090(83)90464-9.

[131] F. Urbach, "The Long-Wavelength Edge of Photographic Sensitivity and of the Electronic Absorption of Solids," Phys. Rev., vol. 92, no. 5, pp. 1324–1324, Dec. 1953, doi:10.1103/PhysRev.92.1324.

[132] N. F. Mott, "Conduction in Non-Crystalline Materials: III. Localized States in a Pseudogap and near Extremities of Conduction and Valence Bands," Philos. Mag., vol. 19, no. 160, pp. 835–852, Apr. 1969, doi:10.1080/14786436908216338.

[133] S. Koc, O. Renner, M. Závětová, and J. Zemek, "Physical Properties of Sputtered Amorphous Ge: The Role of the Deposition Rate," Czech. J. Phys., vol. 22, no. 12, pp. 1296–1301, Dec. 1972, doi:10.1007/BF01689909.

[134] J. J. Hauser and A. Staudinger, "Electrical and Structural Properties of Amorphous Germanium," Phys. Rev. B, vol. 8, no. 2, pp. 607–615, Jul. 1973, doi:10.1103/PhysRevB.8.607.

[135] T. Unold, J. D. Cohen, and C. M. Fortmann, "Electronic Mobility Gap Structure and Deep Defects in Amorphous Silicon-germanium Alloys," Appl. Phys. Lett., vol. 64, no. 13, pp. 1714–1716, Mar. 1994, doi:10.1063/1.111814.

[136]   J. Tauc, R. Grigorovici, and A. Vancu, "Optical Properties and Electronic Structure of Amorphous Germanium," Phys. Status Solidi B, vol. 15, no. 2, pp. 627–637, 1966, doi:10.1002/pssb.19660150224.

[137]   M. H. Cohen, H. Fritzsche, and S. R. Ovshinsky, "Simple Band Model for Amorphous Semiconducting Alloys," Phys. Rev. Lett., vol. 22, no. 20, pp. 1065–1068, May 1969, doi:10.1103/PhysRevLett.22.1065.

[138]   P. C. Padhi, G. S. Tripathi, and P. K. Misra, "Theory of Magneto Resistance of Amorphous Semiconductors," Int. J. Mod. Phys. B, vol. 23, no. 22, pp. 4579–4587, Sep. 2009, doi:10.1142/S0217979209053461.

[139]   I. Kubelík and A. Tříska, "Two Types of Magnetoresistance in Amorphous Germanium," Czech. J. Phys., vol. 23, no. 1, pp. 123–129, Jan. 1973, doi:10.1007/BF01596886.

[140]   I. Kubelík and A. Tříska, "Magnetoresistance in Amorphous Germanium," Czech. J. Phys., vol. 23, no. 1, pp. 115–122, Jan. 1973, doi:10.1007/BF01596885.

[141]   H. Mell and J. Stuke, "Negative Magnetoresistance of Amorphous Semiconductors," J. Non-Cryst. Solids, vol. 4, pp. 304–310, Apr. 1970, doi:10.1016/0022-3093(70)90055-4.

[142]   E. A. Davis and N. F. Mott, "Conduction in Non-Crystalline Systems V. Conductivity, Optical Absorption and Photoconductivity in Amorphous Semiconductors," Philos. Mag., vol. 22, no. 179, pp. 0903–0922, Nov. 1970, doi:10.1080/14786437008221061.

[143]   N. Apsley and H. P. Hughes, "Temperature-and Field-Dependence of Hopping Conduction in Disordered Systems," Philos. Mag., vol. 30, no. 5, pp. 963–972, Nov. 1974, doi:10.1080/14786437408207250.

[144]   N. F. Mott, "Conduction in Non-Crystalline Systems: IV. Anderson Localization in a Disordered Lattice," Philos. Mag., vol. 22, no. 175, pp. 7–29, Jul. 1970, doi:10.1080/14786437008228147.

[145]   M. L. Knotek, M. Pollak, T. M. Donovan, and H. Kurtzman, "Thickness Dependence of Hopping Transport in Amorphous-Ge Films," Phys. Rev. Lett., vol. 30, no. 18, pp. 853–856, Apr. 1973, doi:10.1103/PhysRevLett.30.853.

[146]   G. A. Gibson and R. Meservey, "Properties of Amorphous Germanium Tunnel Barriers," J. Appl. Phys., vol. 58, no. 4, pp. 1584–1596, Aug. 1985, doi:10.1063/1.336045.

[147]   D. K. Paul and S. S. Mitra, "Evaluation of Mott's Parameters for Hopping Conduction in Amorphous Ge, Si, and Se-Si," Phys. Rev. Lett., vol. 31, no. 16, pp. 1000–1003, Oct. 1973, doi:10.1103/PhysRevLett.31.1000.

[148]   B. Movaghar and L. Schweitzer, "A Model for the Anomalous Magnetoresistance in Amorphous Semiconductors," J. Phys. C: Solid State Phys., vol. 11, no. 1, pp. 125–135, Jan. 1977, doi:10.1088/0022-3719/11/1/023.

[149]   B. Movaghar and L. Schweitzer, "ESR and Conductivity in Amorphous Germanium and Silicon," Phys. Status Solidi B, vol. 80, no. 2, pp. 491–498, Apr. 1977, doi:10.1002/pssb.2220800210.

[150] M. Abkowitz, P. G. Le Comber, and W. E. Spear, "A.C. Conductivity in Amorphous Silicon and Germanium and the Density of States at the Fermi Level," Comments Phys., vol. 1, p. 175, 1976, [Online]. Available: http://pascal-francis.inist.fr/vibad/index.php?action=getRecordDetail&idt=PASCAL7730078300 (accessed June 6, 2023).

[151] M. Ortuno and M. Pollak, "An Extended Theory for Hopping Transport in A-Ge and a-Si," J. Non-Cryst. Solids, vol. 59–60, pp. 53–56, Dec. 1983, doi:10.1016/0022-3093(83)90523-9.

[152] Y. Osaka, "Theory of the Anomalous Magnetoresistance in Amorphous Si and Ge," J. Phys. Soc. Jpn., vol. 47, no. 3, pp. 729–732, Sep. 1979, doi:10.1143/JPSJ.47.729.

[153] A. H. Clark, M. M. Cohen, M. Campi, and H. P. D. Lanyon, "Magnetoresistance in Amorphous Germanium," J. Non-Cryst. Solids, vol. 16, no. 1, pp. 117–127, Oct. 1974, doi:10.1016/0022-3093(74)90074-X.

[154] F. T. Hedgcock and T. W. Raudorf, "Two Band Model for Negative Magnetoresistance in Heavily Doped Semiconductors," Solid State Commun., vol. 8, no. 22, pp. 1819–1822, Nov. 1970, doi:10.1016/0038-1098(70)90324-8.

[155] R. M. Mehra, H. Kumar, S. C. Agarwal, S. Koul, and P. C. Mathur, "Magnetoresistance Measurements in the Bulk Amorphous Ge_xSe_{1-x} System," J. Mater. Sci., vol. 20, no. 7, pp. 2459–2463, Jul. 1985, doi:10.1007/BF00556074.

[156] M. Pollak, M. L. Knotek, H. Kurtzman, and H. Glick, "Dc Conductivity of Amorphous Germanium and the Structure of the Pseudogap," Phys. Rev. Lett., vol. 30, no. 18, pp. 856–859, Apr. 1973, doi:10.1103/PhysRevLett.30.856.

[157] V. N. Popok, I. Barke, E. E. B. Campbell, and K.-H. Meiwes-Broer, "Cluster–Surface Interaction: From Soft Landing to Implantation," Surf. Sci. Rep., vol. 66, no. 10, pp. 347–377, Oct. 2011, doi:10.1016/j.surfrep.2011.05.002.

[158] J. Bansmann, S. Baker, C. Binns, J. Blackman, J. Bucher, J. Dorantesdavila, V. Dupuis, L. Favre, D. Kechrakos, and A. Kleibert, "Magnetic and Structural Properties of Isolated and Assembled Clusters," Surf. Sci. Rep., vol. 56, no. 6–7, pp. 189–275, Feb. 2005, doi:10.1016/j.surfrep.2004.10.001.

[159] P. Sheng, B. Abeles, and Y. Arie, "Hopping Conductivity in Granular Metals," Phys. Rev. Lett., vol. 31, no. 1, pp. 44–47, Jul. 1973, doi:10.1103/PhysRevLett.31.44.

[160] B. Abeles, P. Sheng, M. D. Coutts, and Y. Arie, "Structural and Electrical Properties of Granular Metal Films," Adv. Phys., vol. 24, no. 3, pp. 407–461, May 1975, doi:10.1080/00018737500101431.

[161] S. Mitani, S. Takahashi, K. Takanashi, K. Yakushiji, S. Maekawa, and H. Fujimori, "Enhanced Magnetoresistance in Insulating Granular Systems: Evidence for Higher-Order Tunneling," Phys. Rev. Lett., vol. 81, no. 13, pp. 2799–2802, Sep. 1998, doi:10.1103/PhysRevLett.81.2799.

[162] H. Fujimori, S. Mitani, and S. Ohnuma, "Tunnel-Type GMR in Co–Al–O Insulated Granular System — Its Oxygen-Concentration Dependence," J. Magn. Magn. Mater., vol. 156, no. 1–3, pp. 311–314, Apr. 1996, doi:10.1016/0304-8853(95)00880-2.

[163]   R. F. Egerton, *Physical Principles of Electron Microscopy*. Cham, Germany: Springer International Publishing, 2016, doi:10.1007/978-3-319-39877-8.

[164]   J. I. Goldstein, D. E. Newbury, J. R. Michael, N. W. M. Ritchie, J. H. J. Scott, and D. C. Joy, *Scanning Electron Microscopy and X-Ray Microanalysis*. New York, NY, USA: Springer New York, 2018, doi:10.1007/978-1-4939-6676-9.

[165]   V. Franco, X. Batlle, and A. Labarta, "Evidence of Domain Wall Scattering in Thin Films of Granular CoFe-AgCu," Eur. Phys. J. B, vol. 17, no. 1, pp. 43–50, Aug. 2000, doi:10.1007/s100510070158.

[166]   B. Westerstrand, P. Nordblad, and L. Nordborg, "The Magnetocrystalline Anisotropy Constants of Iron and Iron-Silicon Alloys," Phys. Scr., vol. 11, no. 6, pp. 383–386, Jun. 1975, doi:10.1088/0031-8949/11/6/010.

[167]   C. Binns, M. J. Maher, Q. A. Pankhurst, D. Kechrakos, and K. N. Trohidou, "Magnetic Behavior of Nanostructured Films Assembled from Preformed Fe Clusters Embedded in Ag," Phys. Rev. B, vol. 66, no. 18, p. 184413, Nov. 2002, doi:10.1103/PhysRevB.66.184413.

[168]   K. P. Chik and P.-K. Lim, "Annealing and Crystallization of Amorphous Germanium Thin Films," Thin Solid Films, vol. 35, no. 1, pp. 45–56, Jun. 1976, doi:10.1016/0040-6090(76)90239-X.

[169]   A. J. Lewis, "Use of Hydrogenation in the Study of the Transport Properties of Amorphous Germanium," Phys. Rev. B, vol. 14, no. 2, pp. 658–668, Jul. 1976, doi:10.1103/PhysRevB.14.658.

[170]   H. Scher and R. Zallen, "Critical Density in Percolation Processes," J. Chem. Phys., vol. 53, no. 9, pp. 3759–3761, Nov. 1970, doi:10.1063/1.1674565.

[171]   I. Balberg, "Tunnelling and Percolation in Lattices and the Continuum," J. Phys. D: Appl. Phys., vol. 42, no. 6, p. 064003, Mar. 2009, doi:10.1088/0022-3727/42/6/064003.

[172]   S. Mitani, H. Fujimori, and S. Ohnuma, "Spin-Dependent Tunneling Phenomena in Insulating Granular Systems," J. Magn. Magn. Mater., vol. 165, no. 1–3, pp. 141–148, Jan. 1997, doi:10.1016/S0304-8853(96)00490-8.

[173]   G. A. N. Connell, R. J. Temkin, and W. Paul, "Amorphous Germanium III. Optical Properties," Adv. Phys., vol. 22, no. 5, pp. 643–665, Sep. 1973, doi:10.1080/00018737300101359.

[174]   I. Balberg and N. Binenbaum, "Invariant Properties of the Percolation Thresholds in the Soft-Core – Hard-Core Transition," Phys. Rev. A, vol. 35, no. 12, pp. 5174–5177, Jun. 1987, doi:10.1103/PhysRevA.35.5174.

[175]   B. J. Hattink, M. García del Muro, Z. Konstantinović, X. Batlle, A. Labarta, and M. Varela, "Tunneling Magnetoresistance in $Co-ZrO_2$ Granular Thin Films," Phys. Rev. B, vol. 73, no. 4, p. 045418, Jan. 2006, doi:10.1103/PhysRevB.73.045418.

[176]   M. G. Lukashevich, V. N. Popok, V. S. Volobuev, A. A. Melnikov, R. I. Khaibullin, V. V. Bazarov, A. Wieck, and V. B. Odzhaev, "Magnetoresistive Effect in PET Films with Iron Nanoparticles Synthesized by Ion Implantation," Open Appl. Phys. J., vol. 3, no. 1, pp. 1–5, Jan. 2010, doi:10.2174/1874183501003010001.

[177] D. L. Peng, K. Sumiyama, S. Yamamuro, T. Hihara, and T. J. Konno, "Characteristic Tunnel-Type Conductivity and Magnetoresistance in a CoO-Coated Monodispersive Co Cluster Assembly," Appl. Phys. Lett., vol. 74, no. 1, pp. 76–78, Jan. 1999, doi:10.1063/1.122956.

[178] C. A. Neugebauer and M. B. Webb, "Electrical Conduction Mechanism in Ultrathin, Evaporated Metal Films," J. Appl. Phys., vol. 33, no. 1, pp. 74–82, Jan. 1962, doi:10.1063/1.1728531.

[179] L. F. Schelp, A. Fert, F. Fettar, P. Holody, S. F. Lee, J. L. Maurice, F. Petroff, and A. Vaurès, "Spin-Dependent Tunneling with Coulomb Blockade," Phys. Rev. B, vol. 56, no. 10, pp. R5747–R5750, Sep. 1997, doi:10.1103/PhysRevB.56.R5747.

[180] J. G. Simmons, "Generalized Formula for the Electric Tunnel Effect between Similar Electrodes Separated by a Thin Insulating Film," J. Appl. Phys., vol. 34, no. 6, pp. 1793–1803, Jun. 1963, doi:10.1063/1.1702682.

[181] J. G. Simmons, "Low-Voltage Current-Voltage Relationship of Tunnel Junctions," J. Appl. Phys., vol. 34, no. 1, pp. 238–239, Jan. 1963, doi:10.1063/1.1729081.

[182] P. Sheng, "Fluctuation-Induced Tunneling Conduction in Disordered Materials," Phys. Rev. B, vol. 21, no. 6, pp. 2180–2195, Mar. 1980, doi:10.1103/PhysRevB.21.2180.

[183] N. W. Ashcroft and N. D. Mermin, *Festkörperphysik*, 4., verb. Aufl. München, Germany: Oldenbourg, 2013, ISBN 978-3-486-71301-5.

[184] J. G. Simmons, "Generalized Thermal J–V Characteristic for the Electric Tunnel Effect," J. Appl. Phys., vol. 35, no. 9, pp. 2655–2658, Sep. 1964, doi:10.1063/1.1713820.

[185] R. Stratton, "Volt-Current Characteristics for Tunneling through Insulating Films," J. Phys. Chem. Solids, vol. 23, no. 9, pp. 1177–1190, Sep. 1962, doi:10.1016/0022-3697(62)90165-8.

[186] Q. Q. Shu and W. G. Ma, "Barrier Parameter Variation in Al–Al_2O_3–Metal Tunnel Junctions," Appl. Phys. Lett., vol. 61, no. 21, pp. 2542–2544, Nov. 1992, doi:10.1063/1.108145.

[187] M. B. Stearns, "Simple Explanation of Tunneling Spin-Polarization of Fe, Co, Ni and Its Alloys," J. Magn. Magn. Mater., vol. 5, no. 2, pp. 167–171, Apr. 1977, doi:10.1016/0304-8853(77)90185-8.

[188] R. J. Soulen Jr., "Measuring the Spin Polarization of a Metal with a Superconducting Point Contact," Science, vol. 282, no. 5386, pp. 85–88, Oct. 1998, doi:10.1126/science.282.5386.85.

[189] R. Venugopal, B. Sundaravel, W. Y. Cheung, I. H. Wilson, F. W. Wang, and X. X. Zhang, "Magnetic Properties of Nanoclusters Formed by Implantation of Fe into Ge Using a Metal-Vapor Vacuum Arc Ion Source," Phys. Rev. B, vol. 65, no. 1, p. 014418, Dec. 2001, doi:10.1103/PhysRevB.65.014418.

[190] R. Venugopal, B. Sundaravel, I. H. Wilson, F. W. Wang, and X. X. Zhang, "Structural and Magnetic Properties of Fe–Ge Layer Produced by Fe Ion-Implantation into Germanium," J. Appl. Phys., vol. 91, no. 3, pp. 1410–1416, Feb. 2002, doi:10.1063/1.1427135.

[191] T. Thio and S. A. Solin, "Giant Magnetoresistance Enhancement in Inhomogeneous Semiconductors," Appl. Phys. Lett., vol. 72, no. 26, pp. 3497–3499, Jun. 1998, doi:10.1063/1.121639.

[192] S. A. Solin, T. Thio, D. R. Hines, M. Kawano, N. Oda, and M. Sano, "Large Enhancement of the Giant Magnetoresistance in Inhomogeneous Semiconductors: Dependence on Magnetic Field Direction," J. Appl. Phys., vol. 85, no. 8, pp. 5789–5791, Apr. 1999, doi:10.1063/1.369920.

[193] S. A. Solin, "Enhanced Room-Temperature Geometric Magnetoresistance in Inhomogeneous Narrow-Gap Semiconductors," Science, vol. 289, no. 5484, pp. 1530–1532, Sep. 2000, doi:10.1126/science.289.5484.1530.

[194] J. F. Gregg, W. Allen, K. Ounadjela, M. Viret, M. Hehn, S. M. Thompson, and J. M. D. Coey, "Giant Magnetoresistive Effects in a Single Element Magnetic Thin Film," Phys. Rev. Lett., vol. 77, no. 8, pp. 1580–1583, Aug. 1996, doi:10.1103/PhysRevLett.77.1580.

[195] S. Hamzaoui, M. Labrune, I. B. Puchalska, and C. Sella, "Influence of Oblique Incidence Anisotropy on Domain Structures in GdCo$_3$ Sputtered Amorphous Films," J. Magn. Magn. Mater., vol. 22, no. 1, pp. 69–78, Dec. 1980, doi:10.1016/0304-8853(80)90010-4.

[196] A. Gerber, I. Kishon, I. Ya. Korenblit, O. Riss, A. Segal, M. Karpovski, and B. Raquet, "Linear Positive Magnetoresistance and Quantum Interference in Ferromagnetic Metals," Phys. Rev. Lett., vol. 99, no. 2, p. 027201, Jul. 2007, doi:10.1103/PhysRevLett.99.027201.

[197] J. C. Phillips, "Fermi Surface of Ferromagnetic Nickel," Phys. Rev., vol. 133, no. 4A, pp. A1020–A1028, Feb. 1964, doi:10.1103/PhysRev.133.A1020.

[198] P. Sheng, "Feature Article: Electronic Transport in Granular Metal Films†," Philos. Mag. B, vol. 65, no. 3, pp. 357–384, Mar. 1992, doi:10.1080/13642819208207638.

[199] P. A. Lee and T. V. Ramakrishnan, "Disordered Electronic Systems," Rev. Mod. Phys., vol. 57, no. 2, pp. 287–337, Apr. 1985, doi:10.1103/RevModPhys.57.287.

[200] T. Yu and P. Chen, "Abnormal Resistance and Magnetoresistance Temperature Dependence in Fe-Semiconductor Granular Films," IEEE Trans. Magn., vol. 47, no. 10, pp. 3467–3469, Oct. 2011, doi:10.1109/TMAG.2011.2158302.

[201] N. Wiser, "Phenomenological Theory of the Giant Magnetoresistance of Superparamagnetic Particles," J. Magn. Magn. Mater., vol. 159, no. 1–2, pp. 119–124, Jun. 1996, doi:10.1016/0304-8853(95)00613-3.

[202] B. J. Hickey, M. A. Howson, S. O. Musa, and N. Wiser, "Giant Magnetoresistance for Superparamagnetic Particles: Melt-Spun Granular CuCo," Phys. Rev. B, vol. 51, no. 1, pp. 667–669, Jan. 1995, doi:10.1103/PhysRevB.51.667.

[203] L. Péter, Z. Rolik, L. F. Kiss, J. Tóth, V. Weihnacht, C. M. Schneider, and I. Bakonyi, "Temperature Dependence of Giant Magnetoresistance and Magnetic Properties in Electrodeposited Co-Cu/Cu Multilayers: The Role of Superparamagnetic Regions," Phys. Rev. B, vol. 73, no. 17, p. 174410, May 2006, doi:10.1103/PhysRevB.73.174410.

[204] I. Bakonyi, L. Péter, Z. Rolik, K. Kiss-Szabó, Z. Kupay, J. Tóth, L. F. Kiss, and J. Pádár, "Decomposition of the Magnetoresistance of Multilayers into Ferromagnetic and Superparamagnetic Contributions," Phys. Rev. B, vol. 70, no. 5, p. 054427, Aug. 2004, doi:10.1103/PhysRevB.70.054427.

[205]   J. S. Moodera, J. Nassar, and G. Mathon, "Spin-Tunneling in Ferromagnetic Junctions," Annu. Rev. Mater. Sci., vol. 29, no. 1, pp. 381–432, Aug. 1999, doi:10.1146/annurev.matsci.29.1.381.

[206]   Y. Shuto, M. Tanaka, and S. Sugahara, "Magneto-Optical Properties of Group-IV Ferromagnetic Semiconductor $Ge_{1-x}Fe_x$ Grown by Low-Temperature Molecular Beam Epitaxy," J. Appl. Phys., vol. 99, no. 8, p. 08D516, Apr. 2006, doi:10.1063/1.2172909.

[207]   Y. Shuto, M. Tanaka, and S. Sugahara, "Epitaxial Growth and Magnetic Properties of a New Group-IV Ferromagnetic Semiconductor: $Ge_{1-x}Fe_x$," Phys. Status Solidi C, vol. 3, no. 12, pp. 4110–4114, Dec. 2006, doi:10.1002/pssc.200672881.

[208]   Y. Shuto, M. Tanaka, and S. Sugahara, "Structural and Magnetic Properties of Epitaxially Grown $Ge_{1-x}Fe_x$ Thin Films: Fe Concentration Dependence," Appl. Phys. Lett., vol. 90, no. 13, p. 132512, Mar. 2007, doi:10.1063/1.2718270.

[209]   Y. Shuto, M. Tanaka, and S. Sugahara, "Epitaxial Growth and Magnetic Properties of Ferromagnetic Semiconductor $Ge_{1-x}Fe_x$ Thin Films Epitaxially Grown on Si(001) Substrates," Jpn. J. Appl. Phys., vol. 47, no. 9, pp. 7108–7112, Sep. 2008, doi:10.1143/JJAP.47.7108.

[210]   Y. K. Wakabayashi, S. Ohya, Y. Ban, and M. Tanaka, "Important Role of the Non-Uniform Fe Distribution for the Ferromagnetism in Group-IV-Based Ferromagnetic Semiconductor GeFe," J. Appl. Phys., vol. 116, no. 17, p. 173906, Nov. 2014, doi:10.1063/1.4901060.

[211]   Y. K. Wakabayashi, Y. Ban, S. Ohya, and M. Tanaka, "Annealing-Induced Enhancement of Ferromagnetism and Nanoparticle Formation in the Ferromagnetic Semiconductor GeFe," Phys. Rev. B, vol. 90, no. 20, p. 205209, Nov. 2014, doi:10.1103/PhysRevB.90.205209.

[212]   Y. K. Wakabayashi, S. Sakamoto, Y. Takeda, K. Ishigami, Y. Takahashi, Y. Saitoh, H. Yamagami, A. Fujimori, M. Tanaka, and S. Ohya, "Room-Temperature Local Ferromagnetism and Its Nanoscale Expansion in the Ferromagnetic Semiconductor $Ge_{1-x}Fe_x$," Sci. Rep., vol. 6, no. 1, p. 23295, Mar. 2016, doi:10.1038/srep23295.

[213]   S. Sakamoto, Y. K. Wakabayashi, Y. Takeda, S. -i. Fujimori, H. Suzuki, Y. Ban, H. Yamagami, M. Tanaka, S. Ohya, and A. Fujimori, "Origin of Robust Nanoscale Ferromagnetism in Fe-Doped Ge Revealed by Angle-Resolved Photoemission Spectroscopy and First-Principles Calculation," Phys. Rev. B, vol. 95, no. 7, p. 075203, Feb. 2017, doi:10.1103/PhysRevB.95.075203.

[214]   Y. Ban, Y. K. Wakabayashi, R. Nakane, and M. Tanaka, "Impurity Band Conduction in Group-IV Ferromagnetic Semiconductor $Ge_{1-x}Fe_x$ with Nanoscale Fluctuations in Fe Concentration," J. Appl. Phys., vol. 124, no. 11, p. 113902, Sep. 2018, doi:10.1063/1.5022543.

[215]   A. P. Li, J. F. Wendelken, J. Shen, L. C. Feldman, J. R. Thompson, and H. H. Weitering, "Magnetism in Mn_xGe_{1-x} Semiconductors Mediated by Impurity Band Carriers," Phys. Rev. B, vol. 72, no. 19, p. 195205, Nov. 2005, doi:10.1103/PhysRevB.72.195205.

[216]   R. Goswami, G. Kioseoglou, A. T. Hanbicki, O. M. J. van 't Erve, B. T. Jonker, and G. Spanos, "Growth of Ferromagnetic Nanoparticles in Ge:Fe Thin Films," Appl. Phys. Lett., vol. 86, no. 3, p. 032509, Jan. 2005, doi:10.1063/1.1854743.

[217]   E. Adelson and A. E. Austin, "Magnetic Structures of Iron Germanides," J. Phys. Chem. Solids, vol. 26, no. 12, pp. 1795–1804, Dec. 1965, doi:10.1016/0022-3697(65)90212-X.

[218] H. Bracht and N. A. Stolwijk, "Diffusion in Ge," in *Diffusion in Semiconductors*, vol. 33A, D. L. Beke, Ed. Berlin/Heidelberg, Germany: Springer-Verlag, 1998, pp. 222–240, doi:10.1007/10426818_8.

[219] A. C. H. Rowe and S. A. Solin, "Importance of Interface Sampling for Extraordinary Resistance Effects in Metal Semiconductor Hybrids," Phys. Rev. B, vol. 71, no. 23, p. 235323, Jun. 2005, doi:10.1103/PhysRevB.71.235323.

[220] J. Sun and J. Kosel, "Finite-Element Modelling and Analysis of Hall Effect and Extraordinary Magnetoresistance Effect," in *Finite Element Analysis - New Trends and Developments*, F. Ebrahimi, Ed. InTech, 2012, doi:10.5772/47777.

[221] J. Sun and J. Kosel, "Extraordinary Magnetoresistance in Semiconductor/Metal Hybrids: A Review," Materials, vol. 6, no. 2, pp. 500–516, Feb. 2013, doi:10.3390/ma6020500.

[222] L. M. Pugsley, L. R. Ram-Mohan, and S. A. Solin, "Extraordinary Magnetoresistance in Two and Three Dimensions: Geometrical Optimization," J. Appl. Phys., vol. 113, no. 6, p. 064505, Feb. 2013, doi:10.1063/1.4790503.

[223] S. Hunklinger, *Festkörperphysik*, 3., verb. und aktualisierte Aufl. München, Germany: Oldenbourg, 2011, doi:10.1524/9783486711547.

[224] W. R. Branford, A. Husmann, S. A. Solin, S. K. Clowes, T. Zhang, Y. V. Bugoslavsky, and L. F. Cohen, "Geometric Manipulation of the High-Field Linear Magnetoresistance in InSb Epilayers on GaAs (001)," Appl. Phys. Lett., vol. 86, no. 20, p. 202116, May 2005, doi:10.1063/1.1923755.

[225] R. Xu, A. Husmann, T. F. Rosenbaum, J. E. Enderby, and P. B. Littlewood, "Large Magnetoresistance in Non-Magnetic Silver Chalcogenides," Nature, vol. 390, pp. 57–60, Nov. 1997, doi:10.1038/36306.

[226] A. Husmann, J. B. Betts, G. S. Boebinger, A. Migliori, T. F. Rosenbaum, and M.-L. Saboungi, "Megagauss Sensors," Nature, vol. 417, no. 6887, pp. 421–424, May 2002, doi:10.1038/417421a.

[227] M. M. Parish and P. B. Littlewood, "Classical Magnetotransport of Inhomogeneous Conductors," Phys. Rev. B, vol. 72, no. 9, p. 094417, Sep. 2005, doi:10.1103/PhysRevB.72.094417.

[228] M. Lee, T. F. Rosenbaum, M.-L. Saboungi, and H. S. Schnyders, "Band-Gap Tuning and Linear Magnetoresistance in the Silver Chalcogenides," Phys. Rev. Lett., vol. 88, no. 6, p. 066602, Jan. 2002, doi:10.1103/PhysRevLett.88.066602.

[229] M. M. Parish and P. B. Littlewood, "Non-Saturating Magnetoresistance in Heavily Disordered Semiconductors," Nature, vol. 426, no. 6963, pp. 162–165, Nov. 2003, doi:10.1038/nature02073.

[230] J. Xu, D.-M. Zhang, Z.-W. Deng, and F.-X. Yang, "Quasi-Random Resistor Network Model for Linear Magnetoresistance of Metal–Semiconductor Composite," Chin. Phys. Lett., vol. 25, no. 11, pp. 4124–4127, Aug. 2008, doi:10.1088/0256-307X/25/11/078.

[231] J. Xu, D. Zhang, F. Yang, Z. Li, and Y. Pan, "A Three-Dimensional Resistor Network Model for the Linear Magnetoresistance of $Ag_{2+\delta}Se$ and $Ag_{2+\delta}Te$ Bulks," J. Appl. Phys., vol. 104, no. 11, p. 113922, Dec. 2008, doi:10.1063/1.3035834.

[232] T. A. Rabedeau, M. F. Toney, R. F. Marks, S. S. P. Parkin, R. F. C. Farrow, and G. R. Harp, "Giant Magnetoresistance and Co-Cluster Structure in Phase-Separated Co-Cu Granular Alloys," Phys. Rev. B, vol. 48, no. 22, pp. 16810–16813, Dec. 1993, doi:10.1103/PhysRevB.48.16810.

[233] L. J. Swartzendruber, "The Ag−Fe (Silver-Iron) System," Bull. Alloy Phase Diagrams, vol. 5, no. 6, pp. 560–564, Dec. 1984, doi:10.1007/BF02868316.

[234] R. A. Matula, "Electrical Resistivity of Copper, Gold, Palladium, and Silver," J. Phys. Chem. Ref. Data, vol. 8, no. 4, pp. 1147–1298, Oct. 1979, doi:10.1063/1.555614.

[235] P. D. Desai, T. K. Chu, H. M. James, and C. Y. Ho, "Electrical Resistivity of Selected Elements," J. Phys. Chem. Ref. Data, vol. 13, no. 4, pp. 1069–1096, Oct. 1984, doi:10.1063/1.555723.

[236] P. Hadley, "Four Point Resistivity Measurements." http://lampx.tu-graz.ac.at/~hadley/sem/4pt/4pt.php (accessed June 6, 2023).

[237] J. Alonso, M. L. Fdez-Gubieda, O. Montero, A. Svalov, and I. Orue, "Influence of the Interactions on the Magnetotransport Properties of Fe–Ag Granular Thin Films," J. Nanosci. Nanotechnol., vol. 12, no. 9, pp. 7473–7476, Sep. 2012, doi:10.1166/jnn.2012.6528.

[238] J.-Q. Wang and G. Xiao, "Transition-Metal Granular Solids: Microstructure, Magnetic Properties, and Giant Magnetoresistance," Phys. Rev. B, vol. 49, no. 6, pp. 3982–3996, Feb. 1994, doi:10.1103/PhysRevB.49.3982.

[239] J. Alonso, M. L. Fdez-Gubieda, J. M. Barandiarán, A. Svalov, L. Fernández Barquín, D. Alba Venero, and I. Orue, "Crossover from Superspin Glass to Superferromagnet in $Fe_xAg_{100−x}$ Nanostructured Thin Films ($20 \leq x \leq 50$)," Phys. Rev. B, vol. 82, no. 5, p. 054406, Aug. 2010, doi:10.1103/PhysRevB.82.054406.

[240] A. B. Granovskii, A. V. Kalitsov, and F. Brouers, "Field Dependence of the Anomalous Hall Effect Coefficient of Granular Alloys with Giant Magnetoresistance," JETP Lett., vol. 65, no. 6, pp. 509–513, Mar. 1997, doi:10.1134/1.567384.

[241] S. H. Baker, S. C. Thornton, K. W. Edmonds, M. J. Maher, C. Norris, and C. Binns, "The Construction of a Gas Aggregation Source for the Preparation of Size-Selected Nanoscale Transition Metal Clusters," Rev. Sci. Instrum., vol. 71, no. 8, pp. 3178–3183, Aug. 2000, doi:10.1063/1.1304868.

[242] L. J. van der Pauw, "A Method of Measuring Specific Resistivity and Hall Effect of Discs of Arbitrary Shape," Philips Res. Rep., vol. 13, no. 1, pp. 1–9, Feb. 1958.

[243] S. H. N. Lim, D. R. McKenzie, and M. M. M. Bilek, "Van Der Pauw Method for Measuring Resistivity of a Plane Sample with Distant Boundaries," Rev. Sci. Instrum., vol. 80, no. 7, p. 075109, Jul. 2009, doi:10.1063/1.3183503.

[244] B. N. Chichkov, C. Momma, S. Nolte, F. Alvensleben, and A. Tünnermann, "Femtosecond, Picosecond and Nanosecond Laser Ablation of Solids," Appl. Phys. A, vol. 63, no. 2, pp. 109–115, Aug. 1996, doi:10.1007/BF01567637.

[245] N. G. Semaltianos, "Nanoparticles by Laser Ablation," Crit. Rev. Solid State Mater. Sci., vol. 35, no. 2, pp. 105–124, May 2010, doi:10.1080/10408431003788233.

[246] M. Stafe, A. Marcu, and N. N. Puscas, *Pulsed Laser Ablation of Solids*, vol. 53. Berlin, Heidelberg, Germany: Springer Berlin Heidelberg, 2014, doi:10.1007/978-3-642-40978-3.

[247] P. B. Corkum, F. Brunel, N. K. Sherman, and T. Srinivasan-Rao, "Thermal Response of Metals to Ultrashort-Pulse Laser Excitation," Phys. Rev. Lett., vol. 61, no. 25, pp. 2886–2889, Dec. 1988, doi:10.1103/PhysRevLett.61.2886.

[248] M. B. Agranat, A. A. Benditskir, G. M. Gandel'man, P. S. Kondratenko, B. I. Makshantsev, G. I. Rukman, and B. M. Stepanov, "Inertialess Metal Glow Produced by Picosecond Pulses," JETP, vol. 52, no. 1, pp. 27–31, Jul. 1980, [Online]. Available: http://www.jetp.ras.ru/cgi-bin/dn/e_052_01_0027.pdf (accessed June 6, 2023).

[249] S. I. Anisimov, B. L. Kapeliovich, and T. L. Perel'man, "Electron Emission from Metal Surfaces Exposed to Ultrashort Laser Pulses," Sov. Phys. - JETP, vol. 39, no. 2, pp. 375–377, Aug. 1974, [Online]. Available: http://www.jetp.ras.ru/cgi-bin/dn/e_039_02_0375.pdf (accessed June 6, 2023).

[250] S. Amoruso, R. Bruzzese, N. Spinelli, and R. Velotta, "Characterization of Laser-Ablation Plasmas," J. Phys. B: At. Mol. Opt. Phys., vol. 32, no. 14, pp. R131–R172, Jul. 1999, doi:10.1088/0953-4075/32/14/201.

[251] P.-E. Nica, S. A. Irimiciuc, M. Agop, S. Gurlui, M. Ziskind, and C. Focsa, "Experimental and Theoretical Studies on the Dynamics of Transient Plasmas Generated by Laser Ablation in Various Temporal Regimes," in *Laser Ablation - From Fundamentals to Applications*, T. E. Itina, Ed. InTech, 2017, doi:10.5772/intechopen.70759.

[252] Y. Zhang, J. R. G. Evans, and S. Yang, "Corrected Values for Boiling Points and Enthalpies of Vaporization of Elements in Handbooks," J. Chem. Eng. Data, vol. 56, no. 2, pp. 328–337, Feb. 2011, doi:10.1021/je1011086.

[253] A. D. Kirshenbaum, J. A. Cahill, and A. V. Grosse, "The Density of Liquid Silver from Its Melting Point to Its Normal Boiling Point 2450°K," J. Inorg. Nucl. Chem., vol. 24, no. 3, pp. 333–336, Mar. 1962, doi:10.1016/0022-1902(62)80188-2.

[254] C. Y. Ho, R. W. Powell, and P. E. Liley, "Thermal Conductivity of the Elements," J. Phys. Chem. Ref. Data, vol. 1, no. 2, pp. 279–421, Apr. 1972, doi:10.1063/1.3253100.

[255] J. W. Arblaster, "Thermodynamic Properties of Silver," J. Phase Equilib. Diffus., vol. 36, no. 6, pp. 573–591, Dec. 2015, doi:10.1007/s11669-015-0411-5.

[256] M. W. Sigrist, *Laser: Theorie, Typen und Anwendungen*. Berlin, Heidelberg, Germany: Springer Berlin Heidelberg, 2018, doi:10.1007/978-3-662-57515-4.

[257] H. Sun, *Basic Optical Engineering for Engineers and Scientists*. Bellingham, Washington, USA: SPIE, 2019, doi:10.1117/3.2504404.

[258] W. Stöber, A. Fink, and E. Bohn, "Controlled Growth of Monodisperse Silica Spheres in the Micron Size Range," J. Colloid Interface Sci., vol. 26, no. 1, pp. 62–69, Jan. 1968, doi:10.1016/0021-9797(68)90272-5.

[259] E. Hecht, *Optik*. Berlin, Germany / Boston, MA, USA: De Gruyter, 2018, doi:10.1515/9783110526653.

[260] T. Reisinger, A. A. Patel, H. Reingruber, K. Fladischer, W. E. Ernst, G. Bracco, H. I. Smith, and B. Holst, "Poisson's Spot with Molecules," Phys. Rev. A, vol. 79, no. 5, p. 053823, May 2009, doi:10.1103/PhysRevA.79.053823.

[261] T. Reisinger, G. Bracco, and B. Holst, "Particle–Wave Discrimination in Poisson Spot Experiments," New J. Phys., vol. 13, no. 6, p. 065016, Jun. 2011, doi:10.1088/1367-2630/13/6/065016.

[262] R. Gauvin, P. Hovongton, D. Drouin, P. Horny, and H. Demers, "Monte Carlo Simulation of Electron Trajectory in Solids Software," *CASINO Hompage*. https://www.gegi.usherbrooke.ca/casino/index.html (accessed June 6, 2023).

[263] H. Demers, N. Poirier-Demers, A. R. Couture, D. Joly, M. Guilmain, N. de Jonge, and D. Drouin, "Three-Dimensional Electron Microscopy Simulation with the CASINO Monte Carlo Software," Scanning, vol. 33, no. 3, pp. 135–146, May 2011, doi:10.1002/sca.20262.